MONASH University

mm-wave EM-imaging Chipless RFID System

Mohammad Zomorrodi

DOCTOR OF PHILOSOPHY

A thesis submitted for the degree of *Doctor of Philosophy* at Monash University in 2015

Department of Electrical and Computer Systems Engineering,
Faculty of Engineering,

Monash University, Melbourne, Australia

Copyright notice

To

My wife
Fatemeh Sajjadi dokht

and my children
MohammadKasra and Zoha Zomorrodi

Abstract

A new mm-wave imaging chipless RFID system is proposed. The system comprises a multi-bit tiny chipless RFID tag, a double sided printed dipole array (DSPDA) as the reader antenna and the synthetic aperture radar (SAR) image processing algorithm. The multi-bit tags comprise a series of meander line and strip line polarizers on a paper substrate. A linearly polarized (LP) incident wave illuminates the tag surface at 60 GHz instrumentation scientific and medical (ISM) band. The DSPDA is a four-element linear array of DSPD elements. One DSPDA illuminates the tag in vertical polarisation and another DSPDA receives the backscattered signal in horizontal polarisation. The backscattered signal in the cross-polar radar cross section (RCS) of the tag contains the data contents. The reader synthetically processes the cross-polar RCS to construct the image of the tag surface. This data is decoded in the reader's synthetic aperture radar (SAR) processor. The developed mm-wave imaged tag is immune to noise and interference due to its cross polar nature of data processing. Since the tag does not operate on the frequency signature based principle as is for its predecessor tags, the new imaged tag provides high data capacity, compact design and immunity to printing errors.

To validate the concept of the electromagnetic (EM) polariser as the unit cell of the data encoding element, first, a 45° inclined thin strip line as an effective EM polariser is analysed using the diffraction theory. The design parameters of the strip line polariser are optimised for the maximum cross-polar RCS in Computer Simulation Technology (CST) Microwave Studio full-wave EM solver. The stripline polariser is used to design a few multi-bit first prototype chipless RFID tags. Knowing the fact that a 45° inclined meander line is an excellent polariser, secondly, the meander line polariser is investigated for the optimum cross-polar RCS. It is observed that the meander line polariser provides more compact design and higher cross-polar RCS compared to that for the stripline polariser. Finally, a few multi-bit second prototype tags are designed with a series of meander line polarisers.

The advantage of the cross-polar RCS data encoding over the conventional co-polar RCS data encoding is analysed and then verified through a series of experiments in different practical scenarios such as tags attached: (i) to an object in cluttered and interfering environments; (ii) on liquid containers; (iii) on metallic surfaces such as aluminium cans; and

finally, (iv) the tag is covered with thick paper, plywood and cardboard and read at non-line-of-sight (NLOS) conditions. Moreover, the radius of curvature of a bent tag is thoroughly investigated attaching the tag on tubes with varying radii. The proposed tag demonstrates robustness toward multipath and clutter interferences, provides a very reliable approach to tagging of bent surfaces and highly reflective items such as water bottles and aluminium cans. Moreover, the mm-wave tag can be read NLOS inside envelopes, cardboard and wooden boxes hence secure item tagging is also feasible in this approach.

The achieved data encoding capacity of the tag is 2 bits/cm^2 which is very promising for industrial applications. A credit card size tag offers more than 90 bits of data. This content capacity can be increased further with addition of range resolution image processing of the tag surface.

The SAR reading process requires movement of the reader antennas around the tag. The reader takes the snap shots of the whole tag surface at 125 view angles for SAR image processing. The requirement for relative movement of the reader with respect to the tag is also addressed with a new multiple input multiple output (MIMO)-based SAR technique. A limited number of fixed transmit and receive antennas is design based on the MIMO theory to provide a fast imaging processing for the proposed mm-wave EM-imaging chipless RFID system. The MIMO signal processing results in significant throughput enhancements in terms of tag reading time and least hardware requirement.

Finally, the salient features of the proposed system are: (i) a fully printable very compact tag which costs less than a barcode; (ii) printing error tolerant on-demand commercial production using a poor quality printer; (iii) low cost lossy substrate materials based commercial production; (iii) very robust system performance in multipath and cluttered environments; (iv) very reliable tag readings on liquid containers, reflective and curved surfaces; (v) the potential to read secured documents/objects hidden in envelopes, wooden and cardboard boxes; and finally, (vi) very high data encoding capacity. The proposed chipless RFID tag system finds potentials in low cost item level tagging. Recent success of Xerox, USA, University Affairs Committee (UAC) Grant of 115, 865 $ from 2015-2017 for investigations into the proposed tag to read secured documents inside envelops is an excellent testimonial of the potential of the proposed tag.

Declaration

This thesis contains no material which has been accepted for the award of any other degree or diploma at any university or equivalent institution and that, to the best of my knowledge and belief, this thesis contains no material previously published or written by another person, except where due reference is made in the text of the thesis.

Mohammad Zomorrodi

List of publications

Journals:

[1] **M.Zomorrodi,** and N.C.Karmakar, " A Low Cost Wideband Printed Dipole Array Antenna for 60 GHz Image-Based Chipless RFID Reader ", in *IEEE Antennas and Propagation Magazine*, accpeted on 1st Jan 2015, in printing process.

[2] **M.Zomorrodi,** N.C.Karmakar and J.Walker, " Fast Imaging Technique for Chipless RFID Tag ", submitted on 15th Jan 2015 to *IEEE Transactions on Microwave Theory and Techniques* as the extended version of IMaRC-2014 conference paper, under review process.

[3] **M.Zomorrodi,** and N.C.Karmakar, " Electromagnetic Imaging, a New Power for Chipless RFID System", in *Cambridge Press*, Submitted on Feb 2015.

[4] **M.Zomorrodi**, and N.C.Karmakar, "mm-Wave Cross-Polar EM-imaging for High Data Capacity Chipless RFID System ", to IEEE Transactions on Antennas and Propagation, submitted on 5th June 2015.

[5] **M.Zomorrodi**, and N.C.Karmakar, "Fast EM-imaging of Chipless RFID System Through MIMO-based Technique" to IEEE Transactions on Microwave Theory and Techniques as the extended version of IMS-2015 conference paper. submitted on 24th June 2015.

Conference papers:

[1] **M.Zomorrodi,** "Improved Genetic Algorithm Approach for Phased Array Radar Design", in *Asia-Pacific Microwave Conference*, APMC, Melbourne, Australia, 2011.

[2] **M. Zomorrodi** and N.C.Karmakar, "60 GHz Dipole Array Antenna for SAR-based Chipless RFID", in 13th *Australian Symposium on Antennas*, Sydney, 2013.

[3] **M.Zomorrodi,** N.C.Karmakar, and S.G.Bansal, "Introduction of Electromagnetic Image-based Chipless RFID System," in *Intelligent Sensors, Sensor Networks and Information Processing (ISSNIP-2013)*, Melbourne, 2013, pp. 443-448.

[4] **M.Zomorrodi** and N.C.Karmakar, "Cross-RCS Based, High Data Capacity, Chipless RFID System", in *International Microwave Symposium (**IMS-2014**)*, Tampa Bay, Flordia, US, 2014.

[5] **M.Zomorrodi** and N.C.Karmakar, "An Array of Printed Dipoles at 60 GHz", in *IEEE International Symposium on Antennas and Propagation*, Memphis, Tennessee, USA, July-2014, pp. 73-74.

[6] **M.Zomorrodi** and N.C.Karmakar, "On the Usage of Diffraction effect for Chipless RFID Systems", in *Australian Microwave Symposium (AMS)*, Melbourne, Australia, June 2014.

[7] **M.Zomorrodi** and N.C.Karmakar, "Cross-Polarized Printable Chipless RFID Tag with Superior Data Capacity", in *European microwave week, EuMW2014*, Rome, Italy, 2014.

[8] **M.Zomorrodi** and N.Karmakar, "Image-based Chipless RFID System with High Content Capacity for Low Cost Tagging", in *International Microwave and RF Conference (IMaRC)* Bangalore, India., 2014.

[9] **M. Zomorrodi** and N.C.Karmakar, " Fabrication Error Tolerant Array Antenna at 60 GHz", in 14th *Australian Symposium on Antennas*, Sydney, Feb-2015.

[10] **M.Zomorrodi** and N.C.Karmakar, " Novel MIMO-based Technique for EM-imaging of Chipless RFID", in *International Microwave Symposium (**IMS- 2015**)*, Phoenix, USA, May-2015.

[11] **M.Zomorrodi** and N.C.Karmakar, "On the Study of Fabrication Errors on mm-Wave Antenna", in IEEE International Symposium on Antennas and Propagation, Vancouver, BC, Canada, July-2015.

Grant:

Xerox, USA, University Affairs Committee (UAC) Grant, *mm-wave Chipless RFID tag*, $115,865 AUD, 2015-2017.

Investigators, A/P Nemai Chandra Karmakar and Mohammad Zomorrodi, Department of Electrical and Computer Systems Engineering, Monash University, Clayton, Australia,

Xerox, USA Investigator, Dr. Timothy Stowe, Program Manager, Xerox PARC, Inc, Palo Alto, CA, USA,

Remarks: Collaboration with Xerox Ltd, USA is based on the outcomes of this PhD research. The grant application was ranked in the top 3 proposals among more than 20 shortlisted applications from reputed universities from all over the world.

Patent:

M.Zomorrodi, N.Karmakar, "MM-Wave Image-based chipless RFID system" Australia provisional patent, Dec 2013. Patent number: 2013-071.

Book Proposal:

Karmakar, Nemai; **Zomorrodi, Mohammad**; Divarathne, Chamath, "Advanced Signal Processing Techniques for Chipless RFID Systems", John Wiley & Sons, Inc. (Submitted on September 2014 and approved by Wiley on *3rd July 2015*)

Project Awards and Achievements:

- Second place in 3 minutes thesis competition (3MT) at the Postgraduate Research Forum, Monash University, July 2012.
- Second place in poster competition at the Postgraduate Research Forum, Monash University.
- Recipient of the Post publication Award (PPA), Monash University 2015.

Acknowledgement

I would like to thank my supervisor A/Prof. Nemai Chandra Karmakar for providing me the opportunity to work under his supervision. He always provided me all kinds of supports to complete my PhD research. When I was exhausted, he was the person who generously supported me. Without his guidance and support, it was not possible to finish this thesis work. His generous effort on editing my thesis is also highly appreciated. I also thank my associate supervisor, Prof. Jeffery Walker, the head of Civil Engineering Department, to provide me the opportunity to get me involved in the SMAP project in the beginning of my PhD candidature that inspired me toward the EM-imaging technique. Also I thank him for his guidance during my PhD studies. I would also like to thank other members of my advisory committee, Prof. Emanuele Viterbo, Dr. Mehmet Rasit Yuce, and Dr. Jonathan Li for their help on completing my Ph.D. Special thanks also go to my external examiners Prof. Christophe Fumeaux from Adelaide University and A/Prof. Amin Abbosh from University of Queensland. Also I thank Dr. Jan Miller for proof reading this dissertation and her useful suggestions.

The research work and the scholarship have been fully supported by the Australian Research Council (ARC) Discovery Project Grant: DP110105606: Electronically Controlled Phased Array Antenna for Universal UHF RFID Applications. I acknowledge ARC's.

I also would like to express my appreciation to all my colleagues at Monash Microwave, Antenna, RFID and Sensors (MMARS) laboratory of Monash University. They helped me in many aspects of my PhD studies. I learnt so many things from them. The daily collaboration and discussion with my MMARS colleagues provided me tremendous opportunities to explore different areas of chipless RFID research. Thanks to , Mr. Chamath Divarathne, Drs. Aminul Islam, Shakil Bhuiyan, Prasanna Kalansuriya, Emran Amin, Mrs. Rubayet-e-azim Anee, Messer Shuvashis Dey, Muhsiul Hasan and Wan Wan Zamri for their assistances and pleasant.

My Special thanks to my wife, Mrs. Fatemeh Sajjadi dokht, whose kindness and support was the most inspirational factor during the PhD studies. It was absolutely her encouragement to finish my PhD with her love and continues support. I also shall express my special thanks to my children MohammadKasra and Zoha who endeavoured my absence during my PhD

studies and thesis writing. Continues supports and prayers of my beloved parents, Mrs. Fatemeh Eshraghi and Mr. Hossein Zomorrodi, encouraged me during my entire life especially during the four years of my PhD studies.

Contents

List of Figures

List of tables

List of Abbreviation

1D	One Dimensional
2D	Two Dimensional
ADC	Analog to Digital Converter
ADS	Advanced Design System
ARC	Australian Research Council
ASIC	Application Specific Integrated Circuit
BW	Bandwidth
cm	Centimetre
CP	Circular polarisation
CPL	Cross Polar Ratio
CPU	Central Processing Unit
CPW	Co-Planar Waveguide
CST	Computer Simulation Technology
CW	Continuous Wave
DAC	Digital to Analog Converter
dpi	Dot per inch
DSPD	Double side printed dipole
dB	Decibel
dBi	Gain Expressed in dB with Respect to an Isotropic Radiator
dB_m	Decibel with milli-watt reference
DGS	Defected Ground Structure
DSP	Digital Signal Processing/Processor
ECSE	Electrical and Computer Systems Engineering
EIRP	Equivalent Isotropic Radiated Power
EM	Electromagnetic
FCC	Federal Communications Commission
FM	Frequency Modulated
FSS	Frequency Selective Surface
G	Gain
GHz	Gigahertz
GO	Geometric Optic
GTD	Geometric Theory of Diffraction
H	Henry
HF	High Frequency
HPBW	Half Power Beamwidth
IC	Integrated Circuit
IDT	Interdigital Transducer
IF	Intermediate Frequency
IL	Insertion Loss
ISAR	Inverse Synthetic Aperture Radar
ISM	Industrial Scientific and Medical
ITU	International Telecommunication Union
kHz	Kilohertz
LED	Light Emitting Diode
LHCP	Left Hand Circular Polarisation
LNA	Low Noise Amplifier
LO	Local Oscillator

LOS	Line-of-Sight
LP	Linear Polarisation
mA	Milliampere
MEC	Method of Equivalent Current
MMARS	Monash microwave, Antenna, RFID and Sensor research group
MHz	Megahertz
MIMO	Multiple Input Multiple Output
mm	Millimetre
mV	Millivolts
nH	Nanohenry
PA	Power Amplifier
PC	Personal Computer
PCB	Printed Circuit Board
PCR	Pulse Compression Ratio
PO	Physical Optic
PNA	Performance Network Analyser
PTD	Physical Theory of Diffraction
Q	Quality Factor
RCS	Radar Cross Section
RF	Radio Frequency
RFID	Radio Frequency Identification
RHCP	Right Hand circular Polarisation
RL	Return Loss
RLC	Resistance-Inductor-Capacitor
RMA	Range Migration Algorithm
Rx	Receiver
SAR	Synthetic Aperture Radar
SAW	Surface Acoustic Wave
sec	Second
SEM	Singularity Expansion Method
SMAP	Soil Moisture Active Passive
SNR	Signal to Noise Ratio
SRR	Split ring Resonator
STD	Spectral Theory of Diffraction
TDMA	Time Division Multiple Access
TDR	Time Domain Reflectometry
TFTC	Thin Film Transistor Circuits
TWI	Through-to-Wall
Tx	Transmitter
UAD	Uniform Asymptotic Theory of Diffraction
UHF	Ultra-High Frequency
USA	United States of America
UTD	Uniform Theory of Diffraction
UWB	Ultra-Wide Band
V	Volt
VCO	Voltage Controlled Oscillator
VNA	Vector Network Analyser
W	Watts

List of Major Symbols

α	Weighting aperture coefficient
B	Bandwidth
$¢$	Cent
D	Antenna aperture size
F	Fourier transform
λ	Wavelength
k_r	Wave number
ρ_r	Range resolution
ρ_{gr}	Ground range resolution
ρ_a	Azimuth resolution
$\theta_{3\text{-}dB}$	3-dB bandwidth
ε_r	Relative dielectric constant
k_0	Wave number
J_m	Bessel function of order m
σ	Scattering parameter
c	Velocity of Light in Free Space
T_p	Pulse width
γ	Chirp rate

Chapter 1 Introduction

The area of contactless identification systems is growing rapidly into a multi-billion dollar market. It covers a broad range of applications including supply chain management, manufacturing and distribution services. Examples of these applications include consumer packaged goods, postal items, drugs, books, airbag management, animal tracking, pharmaceuticals, waste disposal, clothes, defence, smart tickets, people tracking such as prisoners, hospital patients, patients in care homes, leisure visitors, etc as shown in Figure 1-1. Tough trading conditions due to the global competition strives industries to attain more process efficiencies. Effective goods tracking systems are required to assist the implementation of the modern management system.

In general terms, any application that involves object identification, tracking, navigation or surveillance would benefit from an identification system. Several hundred billion tags per year is required by this wide area of applications [1].

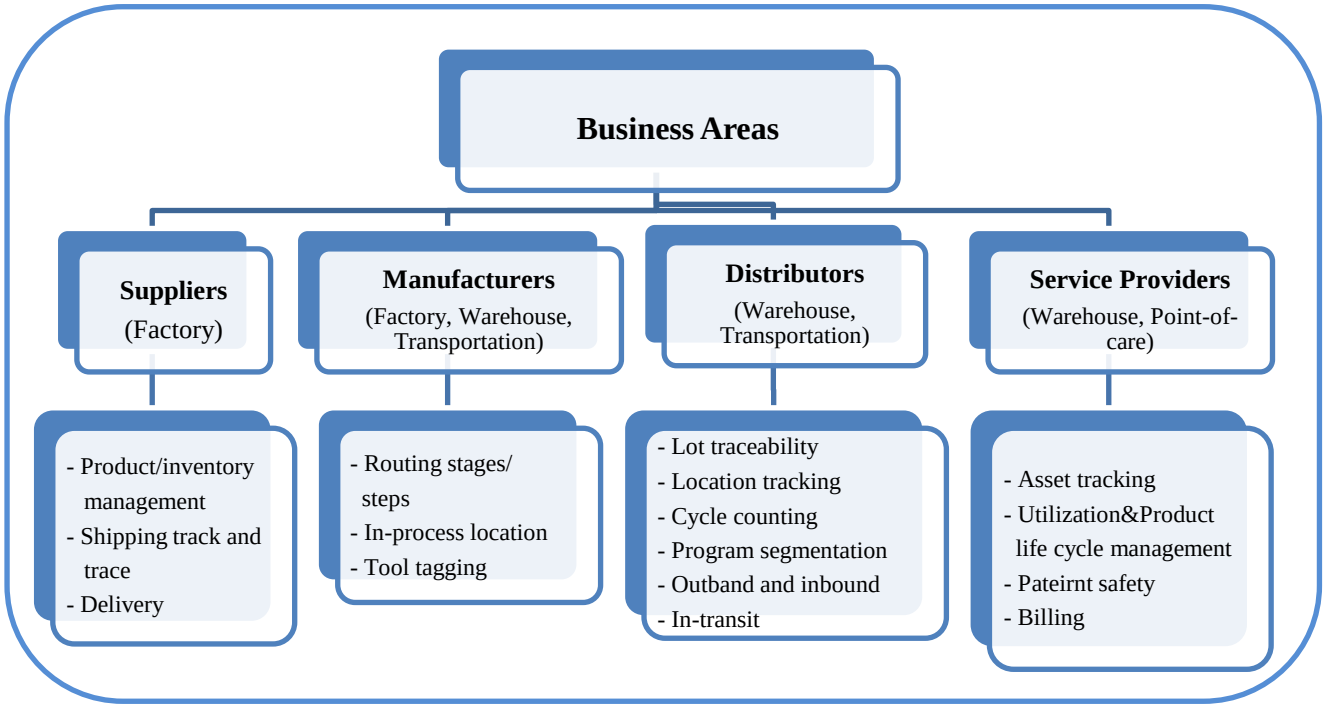

Figure 1-1 Application areas of identification systems.

In this market, every application has its own technical and financial specifications. Main applications, those that need a huge number of tags, require high data encoding capacity and survive only with a very cheap tag solution. For others, secure identification and anti-theft tagging is more important. In some cases, the tag size is a key factor and for some others proper identification of highly reflective items like liquid containers or metal objects has more priority. Reading range is also another important factor for many applications.

Irrespective of all priorities, there are two main factors which matter in all applications, the **data encoding capacity** and the **system cost**. For applications with millions of items for tagging, high data capacity of the identification system is a must. However, for applications with a limited number of objects, high data encoding capacity may be utilised for secure and higher reading reliability by sacrificing some of the available data bits. Moreover, cost reduction is the main initiative for the usage of identification systems in industry. Obviously, the cost of the identification system and its tagging price must be low and competitive enough to initiate the request for the system. Otherwise, there would be no demand for such systems.

The cost of identification systems, like any other broadcasting service, has two parts: the reader and the tag. The reader cost is normally a fixed cost irrespective of the number of tags. However, the price of the tag attached to every individual item is the most costly part of the whole system. Specifically when the number of items are in the order of millions, then the tag cost plays a major role in the system's total cost. For such applications, a tag cost of only one dollar would increase the total cost of the system to a level that restricts the usage of identification systems. Therefore, the tag price should be kept as small as possible to offer a reasonably low identification system cost.

1.1 Barcodes as identification technology

The barcode is an optical-based, machine-readable technique for identification purposes. It has been established in various industries for many decades with proven applicability. It provides an **extremely low cost** solution for identification of items to which it attaches. Originally, barcode tags are comprised of many parallel printed dark lines. The tag's data are systematically represented by varying the widths and spacing of those parallel lines. This type of barcode, dominant in many applications, is normally referred to as a linear or one dimensional (1-D) barcode. Data encoding capacity of the barcode tag is restricted by the

diffraction of light through the edges of the lines, the reader sensitivity, and the reading distance, as shown in Figure 1-2. Diffraction restricts the minimum detectable line width as well as the minimum distance between two adjacent lines. This means that for increasing the data encoding capacity of the barcode, the only way is to increase the length of the tag. As the data encoding capacity of barcodes is proportional to the tag's size, it may result in an unreasonable tag size for many applications. This issue is considered as a main limitation of barcode systems. The 1-D barcodes have evolved into rectangles, circles, dots, hexagons and other two dimensional (2-D) geometric patterns to enhance the data encoding capacity. This resulted in new machine-readable optical labels known as quick response (QR) code. QR codes use four standardized encoding modes to efficiently store data. The maximum storage capacity of QR codes can be up to 7,000 characters that is better than that of barcodes [2]. However, barcodes and QR have many operational limitations. They are very labour intensive as every tag needs to be read/scanned individually. Moreover, being an optical-based system, a clear line-of-sight (LoS), known as optical LoS, is also necessary for proper reading. This means that the tag shall be always printed and exposed on the products and the scanner requires clear LoS to read the barcodes or QR codes. Even, barcodes inside clear polyethylene bags cannot not be read due to the light reflection of the bags. Any damage or dirt on the barcode results in improper reading. The reading distance between the optical scanner and the tag is also limited when considering the light dispersion/attenuation in free space and diffraction effect on the tag surface. Normal reading distance in optical systems is limited to few millimeters to a few centimetres. Moreover, the barcode is not a secure means of communication as tags can be easily reproduced by a cheap inkjet printer. The reading errors of barcodes are depends on applications and many industries loss billions of dollars as compensations and damages each year. For example, optical barcode based luggage handling has approximately 20% reading errors and airlines are paying more than $2 bn/yr as compensations to passengers.

To address positive aspects of barcodes, no doubt a very cheap tag solution and proven applicability in identification systems are the most important factors. Its few cents tagging solution is very attractive for many applications, specifically for industries with millions of products. Being accepted globally for almost half a century also provides it a unique superior

Figure 1-2 Data encoding limitation of a 1-D barcode tag due to diffraction effect.

opportunity that makes it very difficult for other technologies to compete. The globally accepted international barcode quality specification standards, ISO/IEC-15416 (linear) and ISO/IEC 15415 (2-D) [3], and no privacy issues involved with the barcodes usage are highly regarded by many users. Moreover, barcode systems provide a fairly good reading accuracy that is almost comparable with what other new techniques are offering [3]. Another good aspect of the barcode is that the accuracy of the reading process is almost independent of the items on which tags are placed.

1.2 RFID systems

The usage of light waves as a communication means between the reader and the tag in barcode systems causes many technical and operational limitations. Diffraction of light waves by the barcode lines restricts the data encoding capacity and its reading distance. Barcodes also require a clear LoS for proper reading. Labour intervention is another major limitation of the barcodes systems. As an alternative approach, the use of EM-waves for identification and tracking of objects was first proposed by Watson-Watt in 1935 [4] and coined as the Radio Frequency Identification (RFID) system. In an RFID system, the reader sends an EM-wave interrogating signal toward the tag. This signal is then processed by the tag's microchip unit and backscattered towards the reader. This backscattered signal carries the tag identification information and is received and processed by the reader to retrieve the data.

Error! Reference source not found. shows the generic configuration of the RFID system. s the EM-wave is not obstructed by barriers, then the system doesn't need a LOS link between the reader and tag. This provides a number of opportunities for an RFID system. For example, the tag may hide inside the item and not necessarily be exposed on the object as the barcode system does. Moreover, many reader antennas are omni-directional hence they can

detect tags irrespective of their position with respect to the reader. Multiple tag reading is also feasible in an RFID system, bulk detection scenario. The RFID reading distance may be much greater than that of barcodes as the EM-waves are much less attenuated in free space than light waves. The more attractive part of an RFID system is its higher data encoding capacity, which is not comparable to the barcode, as the data are encoded by a microchip. Moreover, many security codes can be easily manipulated inside the microchip to provide more secure communication.

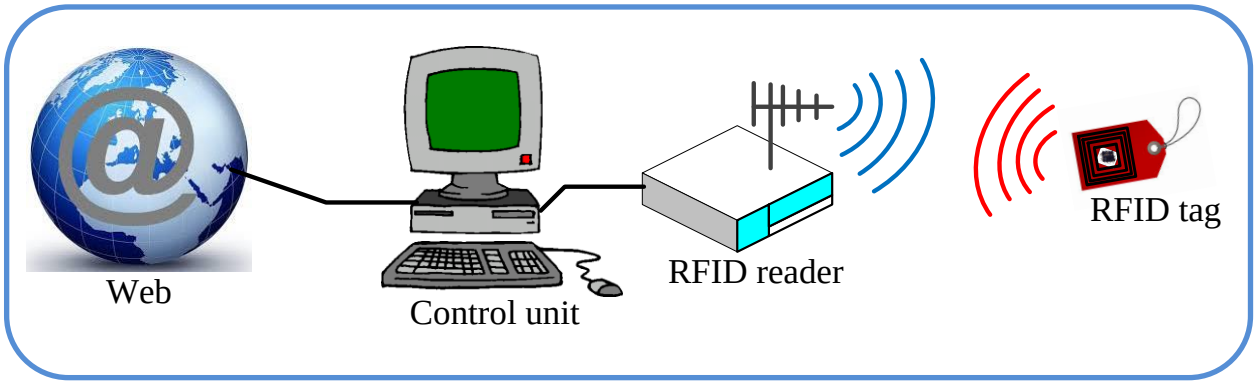

Figure 1-3 RFID general system structure.

1.3 Barcodes vs RFID

Optical based identification systems such as barcodes and QR Codes, and RFID systems all have their own advantages and limitations. This means that each system would be suitable for different purposes and under different circumstances. Although majority of users still consider barcode systems as the most cost effective way to handle the circulation and inventory management of equipment, the indication of changing market occurred in 2003, when Walmart adopted and mandated RFID tagging for all its suppliers. Walmart's motto of mandating RFID is to obtain seamless information from the manufacturing point to the ends of sales when the goods are sold and the boxes are crashed. There are numerous discussions and studies in industry and academia about the suitability of these three systems [5-9]. It is almost agreed that there is no clear superiority of one technology over other technology when the cost and operational flexibility both are considered simultaneously. In general, it is upon each specific industry to select the most suitable technology based on their needs and budgets. The benefit of barcode technology comes from their low cost implementation. It is well established in industry and has fairly enough content capacity for many industrial and

commercial applications. QR codes offering higher data encoding capacity while working almost on the same basis as barcodes. RFID are popular and appropriate technology than barcodes for many industries as it can provide higher content capacity and much more operational flexibilities. As for example, Cisco recently announced its new idea of internet-of-everything (IoE) based on RFID systems [10]. However, conventional RFID systems are associated with limitations too. The main issue for RFID is that many industries cannot afford the cost. To alleviate the potentials of RFID systems to compete with optical barcodes and being accepted by more applications, it is required to reduce the cost of the RFID tag to a level similar to optical barcodes, say less than a cent. A fully printable tag which is still able to provide the same or higher data encoding capacity compared to 1-D barcodes with more operational flexibility would be highly welcomed by industries.

A fair comparison among barcode, QR codes and RFID systems is provided in Table 1-1. For comparison purposes, the specifications of the proposed technology in this dissertation are also included in the table.

Table 1-1 Barcode, QR codes and RFID [8, 9]

	Data capacity (max)	**tag cost (¢)**	**Reading speed**	**Unique advantage**	**Operational limitation**	**Reading distance**
Barcodes	20 bits	0.5	Relatively quick	Cheap& accurate	Optical LoS	few cm
QR codes	7000 character	1	Relatively quick(depends on device)	Versatile	Optical LoS	few cm
RFID	4 million character	>30	Very fast	Many technical superiorities	EM LoS or NLoS	Tens of meter
Image-base	93 bits	<0.5	Relatively quick	Secure identification	EM LoS	50 cm

1.4 Chipless RFID systems

As addressed in previous section, RFID systems show many technical and operational superiorities over barcodes and therefore, are suggested as the most promising technique for barcode replacement. However, to date this has not happened for main applications with billions of yearly tag requirements because of the higher cost of an RFID system. The RFID system cost mainly depends on its tag expense like any other broadcasting system. Based on **Error! Reference source not found.**, the total cost of any identification system is mainly governed by the tag's cost and the reader system does not contribute significantly in operational cost as it is a fixed cost.

$$\begin{aligned}&\text{System cost} = \text{Fixed cost} + \text{N} \times \text{tag cost},\\&\text{N: number of tags ; Fixed cost} = \text{Reader electronic} + \text{Middleware costs}\\&\textit{if } \text{N} \to \infty\\&\text{then: Total system cost} \approx \textit{tag cost} \times \text{N}\end{aligned} \quad \textbf{(1.1)}$$

In RFID systems, every tag needs a silicon chip to encode data. This results in an RFID tag cost that is many times more expensive than the barcodes. Significant investments and research have been spent on lowering the price of microchips to below a cent and thus make it comparable with barcodes. However, the application specific integrated circuit (ASIC or IC for short) design and testing along with the tag antenna and ASIC assembly still result in a costly manufacturing process [11-13]. Furthermore, as the price of every silicon chip directly depends on its size on the wafer, the minimum predictable cost of an RFID chip with the quantity of billion cannot be less than five cents which is still not competitive with one cent tag price of barcodes [11, 14]. Despite all recent improvements in silicon chip technology, silicon chips remain too expensive to be part of every RFID tag [15]. Considering the minimum predictable cost of a chipped-tag, the total cost of an RFID system in applications with millions of tagging requirements, would be much higher than that of barcodes. Therefore, RFID tags without a chip, named as chipless tags, appear to be necessary for the commercialisation of RFID systems in main applications with billions of yearly tag requirements [1]. However, the way the data can be encoded in a chipless tag is a big challenge that opens a new area of research. To date, many techniques and approaches have been proposed for a data encoding scheme in a chipless tag structure [11, 16-18], however there are very few available products on the market.

One of the reasons for unsuccessful chipless tag-based RFID system commercialisation is that the chipless tag does not necessarily mean a cheap tag solution for RFID systems. Radio frequency surface acoustic wave (RFSAW) [19] for instance is a chipless tag structure that works based on surface acoustic wave (SAW) theory. However, the tag price is even higher than the chipped tags. This is because of RFSAW's requirements for a piezoelectric component in the tag structure. Therefore, the chipless tag structure should avoid expensive materials. This normally includes the usage of meta-materials as proposed [20, 21], however meta-materials which can be produced cheaply are excepted. Moreover, the fabrication cost of the tag should also be considered in any proposed solution for chipless RFID system, as it may increase the tag cost beyond expectations. Hence, it could be a general conclusion that the commercialisation of RFID systems would be fully addressed if the tag price drops to

below one cent, including the cost of fitting them in place. This encourages researchers to work on the printable tag structure for reduction of the fabrication cost to the barcode level. However, any proposed tag structure must be able to provide the required encoding capacity in a small tag size. There are examples of chipless and printable tag solutions but the expected data capacity leads to an un-reasonable tag size [22].

The last but very important criterion for a successful chipless RFID system is its proven performance based on the commercialised tag structure. There are many proposed prototypes available in the open literature with very good performance that is based on the precisely fabricated tag and through using high quality copper and low loss materials as the substrate. However, if the proposed tag structure is printed on paper by a low cost conductive inkjet printer, the overall performance of the tag drops significantly. Normally, the frequency domain-based chipless RFID systems fall in this category [22-26]. Any proposal for a chipless tag with proven performance and high data encoding capacity, based on the printed version of the tag structure, would revolutionise the multi-billion dollar market of the identification and tracking industries.

1.5 Proposed chipless RFID system

This research introduces a new data encoding scheme for the chipless RFID systems. The EM-imaging in the mm-wave range is proposed for data retrieval from a chipless tag. The tag is comprised of tiny conductive printable strip or meander lines as EM-polarisers. The EM-polarisers on the tag surface create a high cross-polar radar cross section (RCS) on the backscattered signal while being interrogated by a linearly polarised signal. The reader utilises two orthogonally oriented arrays of double side printed dipole (DSPD) antennas [27, 28]. The reader moves around the tag to create a synthetic aperture and provides a fine EM-image of the tag using synthetic aperture radar (SAR) signal processing. Figure 1-4 shows the general structure of the reader, the tag and the movement requirement in the proposed system.

In comparison to other techniques in chipless RFID systems, the tag structure is fully passive and printable. The expected tag printing cost is even less than that of barcodes as the tag size in the proposed technique is smaller than the barcodes. The system does not require any calibration or reference tag. Changing the background of the environment around the tag has no effect on the performance of the proposed system.

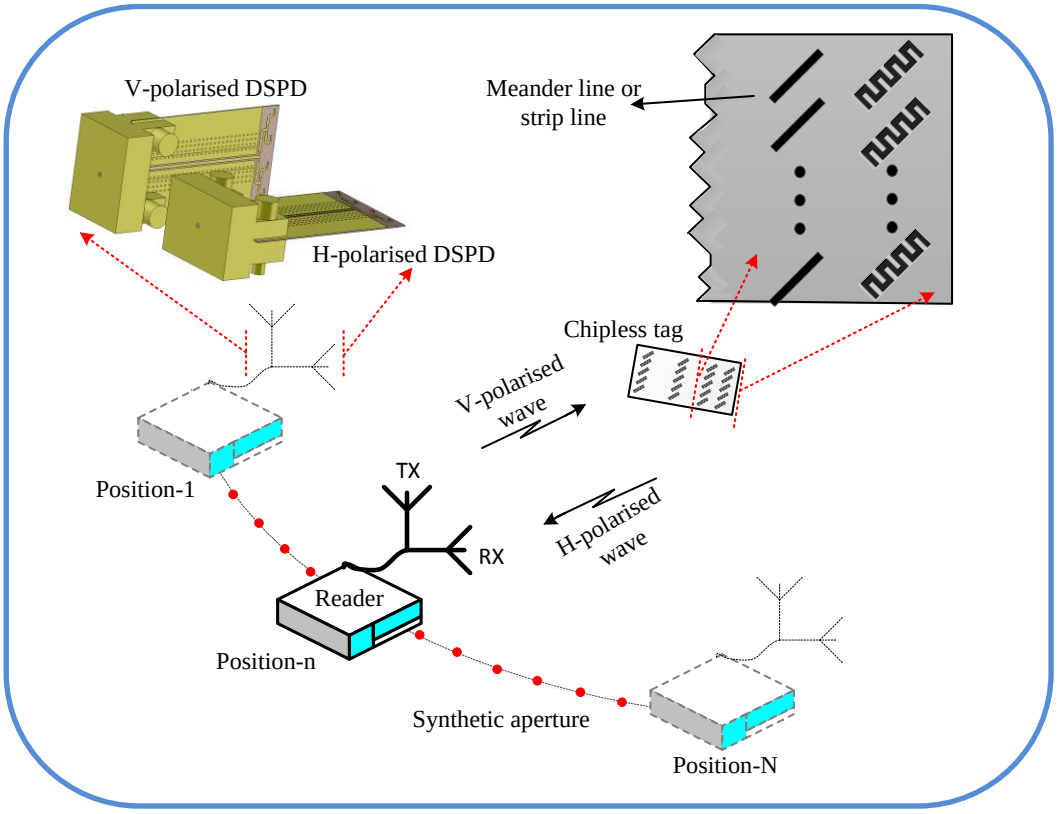

Figure 1-4 Block diagram of proposed image-based cross-polar chipless RFID system.

It also provides higher data encoding capacity in a smaller tag size as reported to date by other chipless RFID systems [18, 29, 30]. The system is very robust to multipath and clutter interference as it is a cross-polar based system. Moreover, the highly reflective items tagged with the proposed tag structure show a very satisfactory result. All printing inaccuracies are also considered in the proposed system and appropriate solutions are suggested. All the measurements of the system are based on the printed tag structure in a highly reflective lab environment with no calibration process.

The proposed frequency band of operation is the licence free band of 57-64 GHz. However, working on higher frequency bands is also possible. The global regulatory freedom [31-34] of the 57-64 GHz, equivalent isotropic radiated power (EIRP) < 40 dBm, provides a unique opportunity for a reading distance of up to one metre. This is again an enhancement compared with other available chipless RFID techniques. The system does not require any ultra wide band (UWB) reader as the data are not encoded in the frequency domain of the backscattered signal. Moreover, no narrow pulsed shape for the interrogation signal is needed as the data are not encoded in the time response of the tag. The receiver simply sends a chirped wave signal and the detection of the tag's ID is based on the EM-image of the tag in a cross-polar direction. This suggests a simple receiver structure; however the physical

movement of the reader and SAR-based signal processing are required at this stage of the research.

The tag in the proposed image-based cross polar-RCS system consists of small conductive objects printed on a paper base without any ground plane at the back of the tag. Every conductive object is designed in a special way to show unique polarisation behaviour in the backscattered direction. The tag structure is shown in Figure 1-5 in which the polariser element is a type of meander line. The meander line is specifically designed to show a high cross polar-RCS in the backscattered direction when illuminated by a linearly polarised interrogation signal. This is a unique characteristic of the obliquely oriented meander line on the tag surface. It is also possible to use a strip line as the EM-polariser on the tag surface.

The tag comprises a matrix of $m \times n$ pixels. Every pixel with an approximate dimension of 2×2 mm^2 may include one polariser. The reader ability to provide a high resolution EM-image of the tag specifies the final data encoding capacity of the system. If enough frequency band is available, every pixel may separately carry one bit hence huge data capacity is expected. However, for a limited frequency band, only a column of EM-polarisers is detectable by the reader. In this scenario, the tag's width depends on the number of rows, *m*, in the matrix.

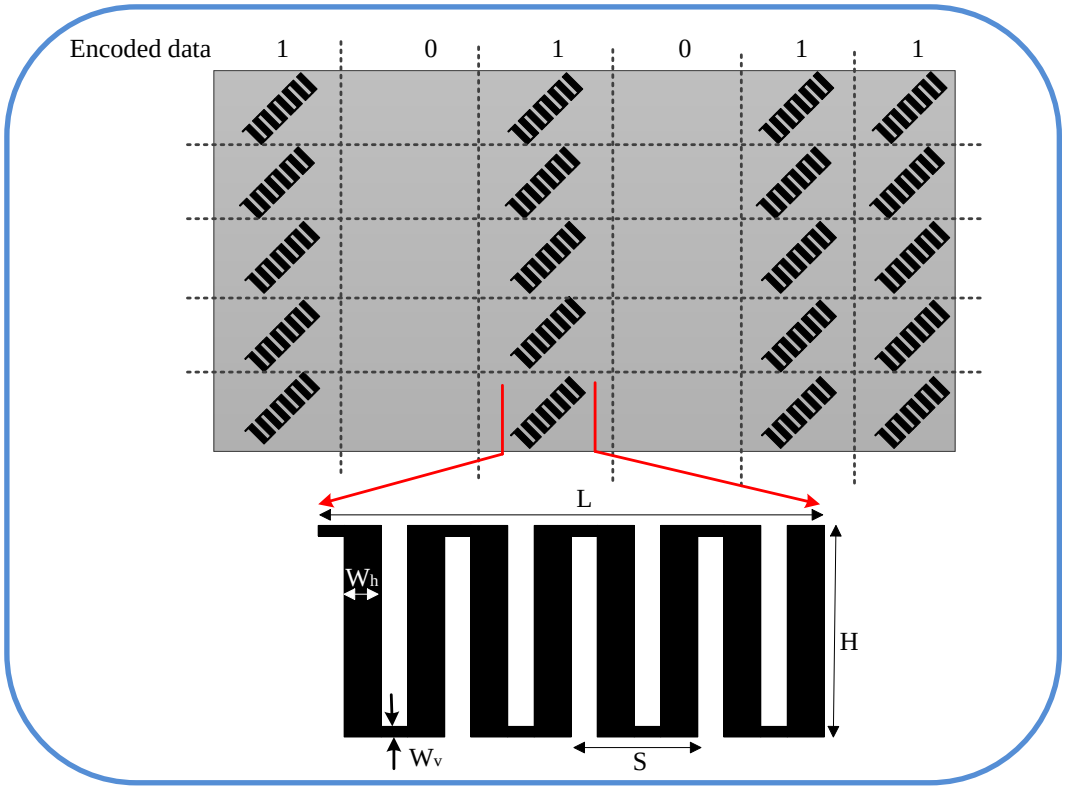

Figure 1-5 Tag structure in image based chipless system.

Normally, 5~10 polarisers are required to produce adequate RCS levels for 50 cm to 100 cm reading distance. However the reading distance also depends on the transmit power and reader sensitivity. Consequently, the tag's width is fixed and varies between 5-15 mm. Every column of the tag surface may include the total number of m polarisers for data bit "1" or it may have no polariser for data bit "0". Figure 1-5 shows the structure of a tag with the data content of "101011". When the moving reader finishes a full synthetic aperture scan, the effect of each vertical slice of the tag is separately analysed by the signal processing. Based on the presence or absence of the polarisers, the reader then receives a significantly different power level, ΔRCS = 20 dB for example, on the cross-polar RCS.

This RCS difference ensures data encoding at this mm-wave frequency band. Absence or presence of vertical polariser-strips yields RCS variation that represents " 0 " and " 1 " binary bits respectively as the encoding algorithm. The received power level on the cross-polar direction is shown in Figure 1-6 that depends on the presence or absence of polariser(s) on each vertical slice of the tag surface. The 20 dB different level is the minimum measured level for a printed tag structure. This detected power level difference is reliably transferable to the EM-image of the tag. The calculated EM-image of the tag through SAR-based signal processing is also shown in Figure 1-6(c).

The width of each vertical slice of the tag structure which carries one bit of data is only 2 mm. Multiple vertical columns of polariser-strips in a matrix configuration yield a multi-bit tag design. This means that encoding capacity of the system is proportional to the tag's length while its width is fixed and depends mainly on the expected reading distance. Since 60 GHz strips are mini-scale structures, large data bits can be included in a credit card size chipless tag. As for example, a 100×7 mm^2 tag area is capable of encoding up to 50 or more bits of binary data.

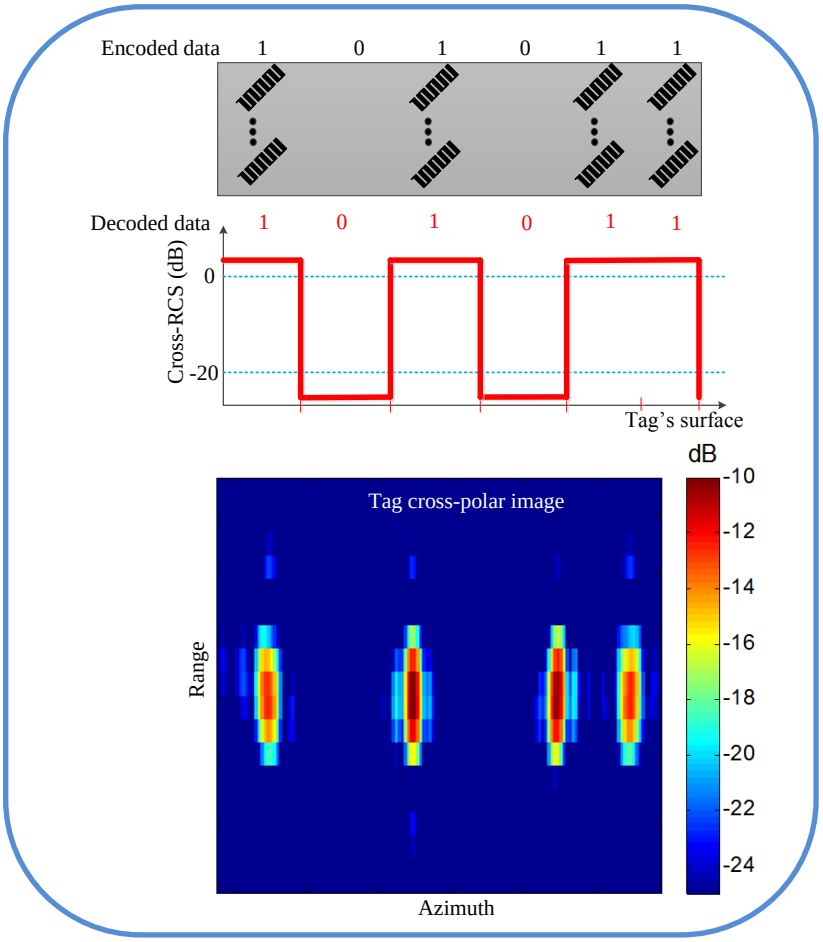

Figure 1-6 (a) tag configuration, (b) data encoding method, (c) SAR focused tag image of 101011 tag data.

1.6 Hypothesis and goals of the research

A quick review of the identification technologies mainly barcodes, QR codes and RFID systems (chipped and chipless) were provided in previous sections. It was shown that each technique has its own advantages and limitations. The proposed image-based chipless RFID system is not also an exception in this regard. The proposed image-based technique suggests a practical approach for data encoding in a fully printable chipless tag structure while all effects of low grade materials and printing errors are considered in the approach. It also provides high data encoding capacity compared with 1-D barcodes and other reported chipless RFID systems. The 93 bits content capacity in a credit card size tag suggested by the image-based technique adequately satisfy the UTC standard [35]. The operational flexibility mainly on none optical LoS is its main advantages over barcodes. This provides the secure identification flexibility with the same or even less tag cost of barcodes. This would enable RFID systems to cover broader applications and supersede the optical-based systems.

The main technical goal of this thesis is to develop a fully printable mm-wave cross-polar RCS imaging chipless RFID tag, related reader antennas and signal processing algorithm for the reader. The milestones and tasks that have been envisaged during the research can be described as follows:

1. A comprehensive literature review in chipless RFID systems to find the bottle neck of chipless RFID systems for being fully accepted by the identification industries. A research gap is identified to develop a fully printable chipless RFID system with high data encoding capacity.

2. The theoretical and practical fundamentals of novel EM-polarisers that yield strong cross-polar RCS while illuminated by a linearly polarised incident signal. An inclined strip line and meander line polarisers are interrogated and the co- and cross-polar RCSs are extracted. The differential RCS level between the two scenarios represents the data content.

3. An in-depth review of the available techniques and algorithms in SAR-based image signal processing. The appropriate signal processing strategy is identified and applied for imaging of the RFID tags.

4. An image-based mm-wave chipless RFID tag is developed using cascade of the polarisers developed earlier and multi bit data are extracted in both simulation and measurement.

5. A DSPD antenna is developed to read the multi-bits tag with high cross polar level (CPL) and wide azimuth beamwidth while being very small and light.

6. An image signal processing algorithm and the related code are developed to extract and illustrate the multi-bits data from the tag.

7. A fast imaging approach is suggested and proved to be effective through MIMO-based array antenna.

The stream of the activities and research during the PhD period can be presented as follow: First, a comprehensive literature review was accomplished to explore the main obstacle(s) for commercialisation of the chipless RFID systems in the main RFID applications with billions of yearly tag requirements. It was found that the very low data encoding capacity of the printed version of any proposed tag is the critical drawback of the current techniques in chipless RFID systems. In the meantime, being involved with the international soil moisture

active passive (SMAP) earth remote sensing project suggested a new approach for data retrieval from the tag. After some research on the basics of earth imaging techniques and doing calculations and simulations, the appropriate system specifications for the RFID application, including the reader antenna, reading distance, feasible encoding capacity and the proper frequency band(s), were found and the idea of tag imaging for data retrieval was proposed [36]. It was shown that with proper frequency band selection, it is possible to scan the tag surface in millimetre order and significantly enhance the data encoding capacity of the chipless RFID tags. Then the idea of a polariser-based tag was developed based on diffraction theory and the resonance behaviour of the shorted dipole [37]. The simulation result by computer simulation technology (CST) microwave studio proved the concept of a strip line as an EM-polariser. Then the idea of a meander line as a more effective polariser at mm-wave was developed. The cross-polar RCS-based tag was designed and fabricated by the printed circuit board (PCB) technology. This tag showed a very good result on the field trial to prove the concept of the proposed theory.

The tag showed high robustness towards multipath interferences and ambient noises in the measurement phase. It also performed very well on highly reflective item tagging. In the next phase, the tag was printed by SATO inkjet printer [38] to address the expected tag price of one cent. The printing inaccuracy changed the cross polar RCS response of the tag. This issue was also considered in the proposed approach. The final printed tag was tested in a highly reflective environment to demonstrate the potentials of the proposed theory in a real scenario. The printed tag showed all positive aspects of the precisely fabricated tag while it was also very robust to the effect of tag bending [39, 40]. Finally, the chipless tag printed on paper by conductive ink was tested in field trials in order to validate its successful operation for addressing the high data encoding capacity in a credit card size tag. As the cross polar level of the reader antenna plays a major role in the proposed cross-polar RCS tag detection technique, an appropriate antenna was designed, fabricated and tested. The antenna was an array of double side printed dipoles (DSPD) that covered the whole frequency band of 57-64 GHz yielding 12% bandwidth. The antenna was used for field trials of printed tags and showed very good results.

As the final step, signal processing based on the SAR technique was performed to fulfil the final goal of the thesis. It was shown that SAR-based signal processing with a proper system specification is capable of retrieving the data content through its EM-imaging.

In summary, the tasks that have been performed to fulfil the requirements of this research are shown in Figure 1-7, including: *i)* Proposing the new idea of tag EM-imaging for data retrieval purposes in RFID systems; *ii)* Tag design for the cross-polar RCS-based approach and its fabrication process including the printing phase; *iii)* Reader antenna design, fabrication and testing; and finally *iv)* SAR-based signal processing for final data retrieval from the tag surface in a real environment.

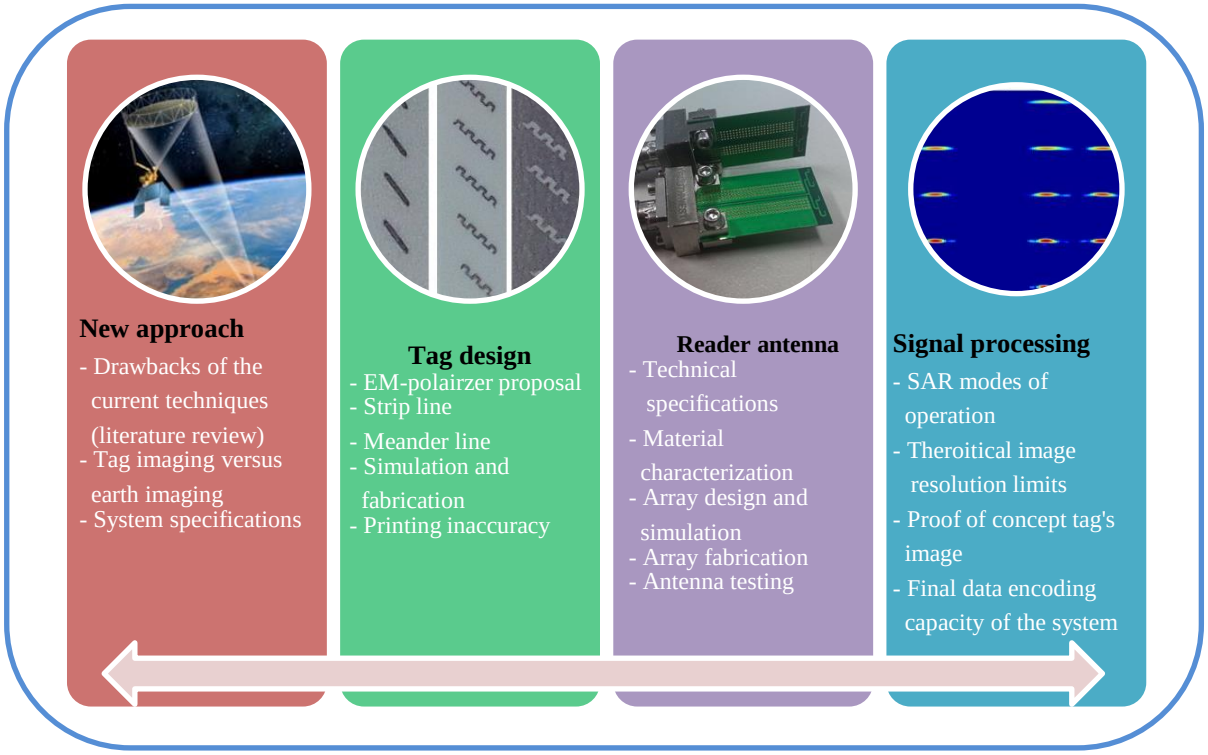

Figure 1-7 Fulfilling thesis goal.

1.7 Original contributions

Fulfilling the thesis goal and tasks performed have yielded the following original contributions of the thesis:

1. Image-based mm-wave encoding for the chipless RFID system. The new encoding scheme enhances the data encoding capacity of the chipless system suitable for many commercial applications.

2. The new cross-RCS level working basis that is immune to multipath interferences and ambient noises hence works better in harsh industrial environments.

3. mm-wave EM-polariser chipless tag that provides a very small tag size with high data encoding capacity.

4. Design and optimisation of two EM-polarisers, strip line and meander lines, with excellent performance based on the printed version of the polarisers utilising conductive ink and paper substrate.

5. Novel tag design, based on the printed polarisers, that is chipless, fully printable, low cost, robust, and is of high data capacity, small size and cross polarised–based.

6. A new matrix-based tag structure for a proper reading process based on the proposed SAR theory.

7. Design, optimisation and fabrication of new array antennas with 12% bandwidth and very high CPL that is suitable for the application of the cross-polar RCS EM-image based chipless RFID system.

8. The proven concept of MIMO-based array antenna for fast imaging purpose.

The aforementioned original contributions, in the field of research result in: *i)* four referred journal papers (one accepted and three under review), *ii)* 11 refereed conference papers, *iii)* one Australian provisional patent application and a successful grant of US$ 90,000 from the Xerox, USA. The full list of publications can be found on pages *v* to *vi* of this dissertation.

1.8 Thesis outline

The research embodied in this thesis is divided into nine chapters. Each chapter aims to provide a smooth transition from the start of the research to its final goal.

Chapter 1 Introduction

A brief overview of the industries with identification and tracking requirements is provided in this chapter. High data encoding capacity and low system cost are appeared as the top priorities of the industries for identification purpose. The barcode system as a well-stablished identification technique is then reviewed regarding its ultimate potentials for addressing the current demands of industries. It is shown that the limitations of the barcodes on providing enough content capacity and also their high labour costs are not compatible with the needs of industries in the modern international trading market. The RFID system as an alternative solution is introduced and its main limitation on providing cheap tagging solution is presented. Conventional techniques in the chipless RFID systems are reviewed. Finally, the mm-wave image based chipless RFID system is briefly introduced and its salient attributes are highlighted.

Chapter 2 High data capacity, printable chipless RFID tag

The literature review related to the proposed technique of cross-polar image-based chipless RFID systems is provided in Chapter 2. It first considers the potentials of the chipless RFID system to fulfil the requirements of the main industries with billions of yearly tag usage. A fully printable chipless tag structure is suggested as the only option to satisfy the tag expectation by industries. Conventional techniques in the chipless RFID systems are reviewed and their final capabilities based on a fully printable tag are fully investigated. Potentials of the proposed technique, specifically regarding the tag cost and content capacity, are introduced then.

Chapter 3 EM-imaging through reflective EM-polariser

This chapter shows the possibility of EM-imaging for data encoding purposes in the chipless RFID tag. It first highlights the main difference between the proposed approach of EM-imaging and other conventional techniques in RFID systems. Then the chapter is divided into two almost separate parts. In the first part the millimetre scanning of the tag surface is considered. Then the novel idea of a strip line and a meander line as effective polarisers are

introduced and the working basis of these two elements based on diffraction theory and resonance is presented. Finally, the technical and regulatory situation of the 60 GHz band is also covered in this section.

Chapter 4 Practical data encoding EM-polariser

The fabrication process of the proposed strip line and meander line EM-polarisers is discussed in this chapter. Both polarisers are fabricated through two different technologies. First, the costly but accurate approach of a photolithographic process that utilises annealed copper and high quality substrate is considered. Then the same tags are printed through a commercial printing process that is very cheap but includes many printing inaccuracies. Two samples are measured in real scenario for their final performance. While precise fabricated tags show similar results as expected by simulation, the printed version of the tags lose their resonance behaviour though still creating high cross-polar components. Based on the printed tag performance, then an on/off data encoding algorithm is proposed.

Chapter 5 Printed EM-polariser performance

The actual performance of the printed polariser-based tag is considered in Chapter 5. First an analytical model of the reading scenario for the chipless RFID system is developed based on radar theory. Based on this analytical model, the performance of co- and cross-polar RCS-based systems are compared. Different measurement scenarios are considered for confirmation of the analytical assumptions. The printed tags are measured against their performance in severe multipath scenarios, tagging of highly reflective items, bending effects, and barrier effects. Based on the successful measurement results, it is concluded that the proposed tag structure provides a very robust, reliable and fully practical solution for the industrial applications.

Chapter 6 Reader antenna

The reader antenna is discussed in Chapter 6. It first reviews the technical and operational necessities of reader antennas for the image-based chipless RFID system. Then an array of double side printed dipole (DSPD) antennas is proposed to satisfy the required technical specifications. The substrate characterisation is performed through a substrate integrated waveguide (SIW) resonant technique at 60 GHz. Finally the array is fabricated through standard printed circuit board (PCB) technology and tested. The array adequately covers the

whole frequency range of operation 57-64 GHz. The antenna provides a uniform radiation pattern in the azimuth direction with a limited pattern on the elevation angle. The measured CPL is below -20 dB. The measured gain of the array is 5.5-7 dBi over the entire frequency range of operation. The size of the array is 22×14 mm^2.

Chapter 7 Electromagnetic imaging

This chapter briefly reviews the SAR theory. The necessity of SAR for the chipless RFID application is shown. Then three modes of operation in SAR theory are discussed and the suitable scenario for the chipless RFID is proposed. The range and azimuth image resolutions are introduced and it is discussed that only azimuth resolution of few millimetre is feasible. Then appropriate tag structure is designed for high data encoding capacity and reliable reading process. In the final stage of this chapter, the EM-images of some sample tags with different data encoding capacity are shown which successfully reveals the tag's data. A tag with 8.5 cm length encodes 17 bits of data while the tag width is only one cm. This step fulfils the main goal of the research on proposing a new approach to data encoding algorithm based on a fully printable tag structure.

Chapter 8 MIMO-based array antenna for fast imaging

The requirement for physical movement of the reader and tag is considered in this chapter. The novel idea of MIMO-based system is suggested to eliminate this necessity and suggest a very fast imaging algorithm. The theory of MIMO-based array antenna is comprehensively introduced. The proposed approach is considered for providing a fast imaging means through utilising only 55 physical elements .This new system structure is used in a simulation step to provide an EM-image of the tag. The characteristics of the provided image through new technique of MIMO-based reader are then compared with the conventional SAR technique results.

Chapter 9 Conclusion and future works

The conclusions focus on the important findings and outcomes of this research project and highlight the key aspects of the work. A brief review of each chapter is also discussed in conclusion. Moreover, the proposal for enhancing the data encoding capacity through three-level data encoding and the tag orientation sensitivity are introduced as the future work of this research.

1.9 Communications of results

The outcomes of this research have been divided in the following categories:

Grant Success:

Xerox, USA, University Affairs Committee (UAC) Grant, *mm-wave Chipless RFID tag*,

Investigators, A/P Nemai Chandra Karmakar and Mohammad Zomorrodi, Department of Electrical and Computer Systems Engineering, Monash University, Clayton, Australia,

Xerox, USA Investigator, Dr. Timothy Stowe, Program Manager, Xerox PARC, Inc, Palo Alto, CA, USA, $115,865 AUD from 2015-2017

Remarks: Collaboration with Xerox Ltd, USA is based on the outcomes of this PhD research. The grant application was ranked in the top 3 proposals among more than 20 shortlisted applications from reputed universities from all over the world.

Journals papers:

[1] **M.Zomorrodi,** and N.C.Karmakar, " A Low Cost Wideband Printed Dipole Array Antenna for 60 GHz Image-Based Chipless RFID Reader ", in *IEEE Antennas and Propagation Magazine*, accpeted on 1st Jan 2015.

[2] **M.Zomorrodi,** N.C.Karmakar and J.Walker, " Fast Imaging Technique for Chipless RFID Tag ", submitted on 15th Jan 2015 to *IEEE Transactions on Microwave Theory and Techniques* as the extended version of IMaRC-2014 conference paper, under review process.

[3] **M.Zomorrodi,** and N.C.Karmakar, " Electromagnetic Imaging, a New Power for Chipless RFID System", in *Cambridge Press*, Submitted on Feb 2015.

[4] **M.Zomorrodi**, N.C.Karmakar and J.Walker, "mm-Wave Cross-Polar EM-imaging for High Data Capacity Chipless RFID System ", to IEEE Transactions on Antennas and Propagation, submitted on 5th June 2015.

[5] **M.Zomorrodi**, N.C.Karmakar and J.Walker, "Fast EM-imaging of Chipless RFID System Through MIMO-based Technique" to IEEE Transactions on Microwave Theory and Techniques as the extended version of IMS-2015 conference paper. submitted on 24th June 2015.

Conference papers:

[1] **M.Zomorrodi,** "Improved Genetic Algorithm Approach for Phased Array Radar Design", in *Asia-Pacific Microwave Conference,* APMC, Melbourne, Australia, 2011.

[2] **M. Zomorrodi** and N.C.Karmakar, "60 GHz Dipole Array Antenna for SAR-based Chipless RFID", in 13th *Australian Symposium on Antennas*, Sydney, 2013.

[3] **M.Zomorrodi,** N.C.Karmakar, and S.G.Bansal, "Introduction of Electromagnetic Image-based Chipless RFID System," in *Intelligent Sensors, Sensor Networks and Information Processing (ISSNIP-2013)*, Melbourne, 2013, pp. 443-448.

[4] **M.Zomorrodi** and N.C.Karmakar, "Cross-RCS Based, High Data Capacity, Chipless RFID System", in *International Microwace Symposium (**IMS-2014**)*, Tampa Bay, Flordia, US, 2014.

[5] **M.Zomorrodi** and N.C.Karmakar, "An Array of Printed Dipoles at 60 GHz", in *IEEE International Symposium on Antennas and Propagation*, Memphis, Tennessee, USA, July-2014, pp. 73-74.

[6] **M.Zomorrodi** and N.C.Karmakar, "On the Usage of Diffraction effect for Chipless RFID Systems", in *Australian Microwave Symposium (AMS)*, Melbourne, Australia, June 2014.

[7] **M.Zomorrodi** and N.C.Karmakar, "Cross-Polarized Printable Chipless RFID Tag with Superior Data Capacity", in *European microwave week, EuMW2014*, Rome, Italy, 2014.

[8] **M.Zomorrodi** and N.Karmakar, "Image-based Chipless RFID System with High Content Capacity for Low Cost Tagging", in *International Microwave and RF Conference (IMaRC)* Bangalore, India., 2014.

[9] **M. Zomorrodi** and N.C.Karmakar, " Fabrication Error Tolerant Array Antenna at 60 GHz", in 14th *Australian Symposium on Antennas*, Sydney, Feb-2015.

[10] **M.Zomorrodi** and N.C.Karmakar, " Novel MIMO-based Technique for EM-imaging of Chipless RFID, " in *International Microwace Symposium (**IMS- 2015**)*, Phoenix, USA, May-2015.

[11] **M.Zomorrodi** and N.C.Karmakar, "On the Study of Fabrication Errors on mm-Wave Antenna", in IEEE International Symposium on Antennas and Propagation, Vancouver, BC, Canada, July-2015.

Patent:

M.Zomorrodi, N.Karmakar, "MM-Wave Image-based chipless RFID system", Australia provisional patent, Dec 2013, Patent number: 2013-071.

Book Proposal:

Karmakar, Nemai; **Zomorrodi, Mohammad**; Divarathne, Chamath, "Advanced Signal Processing Techniques for Chipless RFID Systems", John Wiley & Sons, Inc. (Submitted on September 2014 and approved by Wiley on *3rd July 2015*)

Project Awards and Achievements:

- Second place in 3 minutes thesis competition (3MT) at the Postgraduate Research Forum, Monash University, July 2012.

- Second place in poster competition at the Postgraduate Research Forum, Monash University, July 2012.

- Recipient of the Post publication Award (PPA), Monash University 2015.

Chapter 2 High data capacity, printable chipless RFID tag

2.1 Introduction

Identification systems were introduced in Chapter 1, and the reasons why barcodes are unable to satisfy the current requirements of main stream industries was described. Chipped RFID systems were considered as an alternative approach to barcodes. It was shown that they are not able to meet the requirements of main stream applications due to their higher tag cost. Then chipless RFID systems were considered as a solution for low cost item tagging. However, the developed and reported chipless RFID tags have limitations in terms of number of data bits, costs, reading methods and collision avoidance in multiple tag reading scenarios. As a solution to some of these limitations, high data capacity mm-wave chipless RFID tag is proposed. Finally, the basics of the proposed cross polar-RCS based approach were presented, together with some of its potential advantages with respect to other chipless techniques.

This chapter focuses on the importance of a printable tag solution for chipless RFID systems. It discusses how the main stream application of identification systems will be satisfied with a printable tag solution alone, at less than one cent (1¢) final tag cost. A review of the current techniques in chipless RFID systems is provided, and their final data encoding capacity based on the printable version of their proposed tag structures is considered. The idea of EM-imaging for data encoding in a chipless tag is also presented along with a review of EM-imaging in other applications. Finally, it is shown that the imaging is applicable to chipless RFID systems, and that it has potential to enhance the capabilities of current techniques in the chipped or chipless RFID systems.

2.2 Tag price sensitivity versus applications

Tough trading conditions due to global competition means that organisations and companies need to attain more process efficiencies. This would enable them to drive down their product costs and provide competitive advantages. Just-in-time retailing was introduced as an effective model for many organisations instead of traditional logistic procedures. Although retailers benefit from lower stock levels through new management systems, more pressure is experienced by manufacturers and distributors to address the retailers' requirements in a shorter time frame. Effective goods tracking systems are then required to assist the implementation of the new management systems through the supply chain [41]. Barcodes, as a well-established identification system, are unable to address the new

requirements due to their technical limitations. The requirements for line-of-sight reading and the non-flexible automatic reading scheme of barcodes drive up tracking cost due to labour intervention. Moreover, its limited data capacity, as discussed in Chapter 1, limits the new supply chain environment. For example, Walmart has mandated RFID technology for their thousands of manufacturers for goods flow visibility from manufacturer to the crashing point of boxes when the goods are sold [42].

RFID systems are an emerging tracking system with many advantages over barcodes. They have appealed to many organisations as an effective identification means for fulfilling the requirements of the modern supply chain. Unlike barcodes, RFID tags are robust and do not need a line-of-sight reading scenario, hence removing the need for labour intervention. RFID tags are also capable of carrying information about the location, destination, and product identification number as their data encoding capacity is much higher than that of barcodes. However, the price of these RFID tags remain as the first and foremost hurdle for their deployment in applications with low product costs; groceries for example. As discussed in Chapter 1 (1.1), the identification system cost linearly depends on the tag cost for large quantity tagging requirements. Based on the company's potential and system affordability, the relation between the tag cost and its volume is shown in Figure 2-1 [1]. Based on this model the RFID tag cost would be a large barrier in organisations with a high tagging requirements. As shown in Figure 2-1, the chipless tags are necessary to satisfy the requirements of medium to large-sized organisations, with a tag price to be down to 1¢. Although the chipless tags eliminate the need for the silicon chip, as the most expensive element of the tag structure, there are other factors which may surge the tag cost. The tag fabrication technique and its possible requirements to other elements rather the silicon chip along with heir installation process may elevate the tag cost higher than the targeted value of 1¢. Therefore, based on the worldwide well accepted model shown in Figure 2-1, the main stream industries with billions of yearly tag requirements will only be satisfied through a **fully printable chipless** tag structure. Any technique or suggested solution for a chipless RFID system, must consider this critical point of the industries for a printed tag, otherwise the proposed technique finds no place in the identification market or at least in main stream industries.

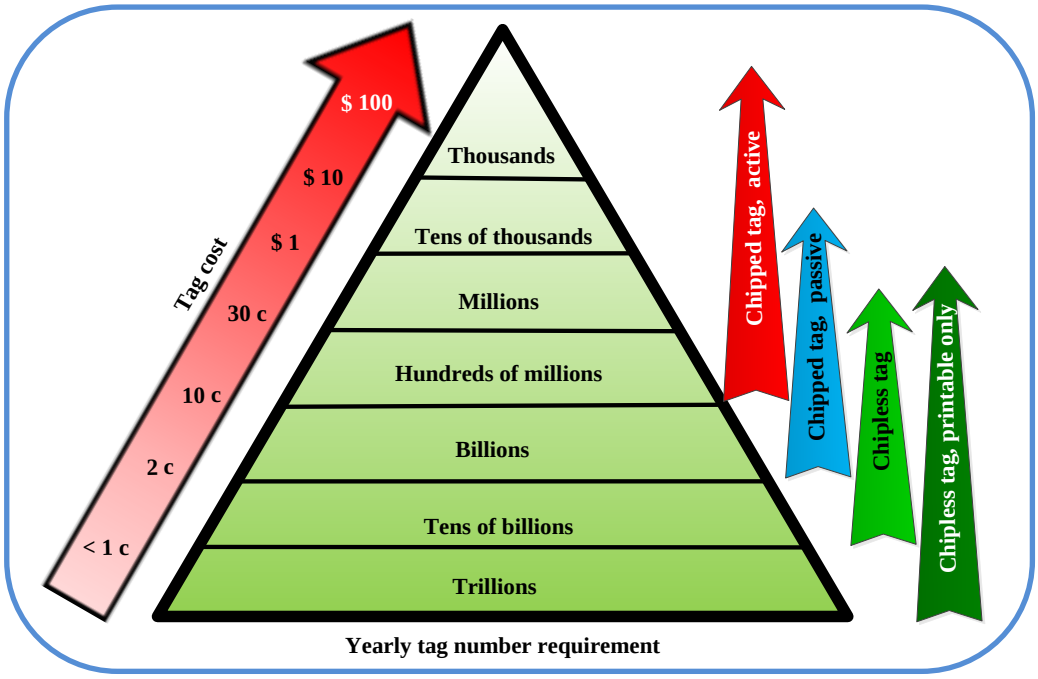

Figure 2-1 Expected tag volume versus tag cost. Source: IDTechEx [1].

2.3 Strengthened RFID systems by chipless tags

Successful deployment of RFID systems in main stream applications requires significant tag cost reduction. There is much effort around the world to drop the chip cost [13, 43, 44]. However, it appears that the silicon chip is too expensive to be a part of every RFID tag. This guides research towards designing an RFID tag without any embedded silicon chip, named as chipless RFID systems. There are many proposed techniques in the open literature on designing a chipless and passive tag structure with the mandated data encoding capability for identification purposes. This chapter mainly focuses on reviewing those techniques and approaches and exploring their potential advantages and limitations.

The communication between the RFID reader and the tag is accomplished through the use of EM waves. For the RFID chipless systems, the tag does not require any processor unit. Hence all the reading and coding processes are accomplished in the reader. The basis of the chipless system is that the reader receives the tag's backscattered signal in different domains and processes the signal to retrieve its encoded data. This leads to the time domain-based, frequency domain-based, phase-based or hybrid systems [45-47]. In the following sections, these systems are reviewed. Figure 2-2 shows the classifications of the empowered chipless RFID systems that are reviewed in this chapter.

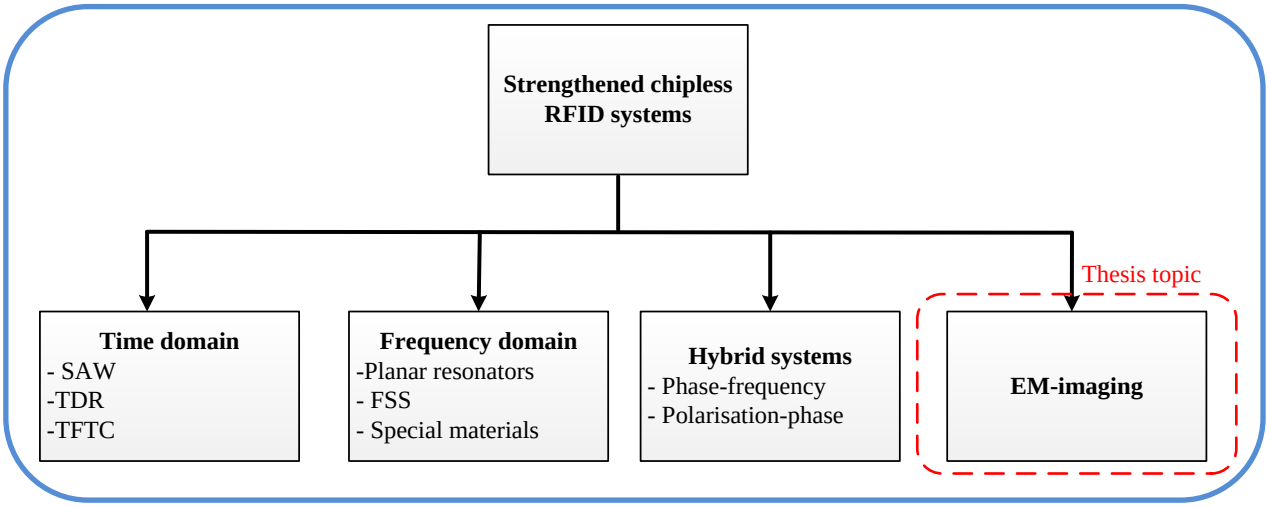

Figure 2-2 General classifications of chipless RFID systems.

2.3.1 Time domain-based chipless RFID systems

In a time domain-based system, the reader interrogates the tag with a series of pulses [48, 49]. The tag then re-transmits the signal as a train of echoes with some time delays with the data encoded in the delayed responses. Manipulation of the delays can be handled directly on the EM-waves domain, or it is possible to convert the EM-wave to another type of medium, acoustic wave for example, and then delays are deployed in the signal. After manipulation of the data as delayed responses, the EM-wave is re-transmitted to the reader. When an alternative medium is used for data encoding purposes other than the EM-wave, then extra elements are needed for conversion [50]. For instance, in the surface acoustic wave (SAW) technique the inter-digital transducer element is used to convert an electromagnetic wave to a mechanical wave which travels much slower than EM-waves. This surface acoustic wave propagates through a piezoelectric element and then it is reflected back by a number of reflectors towards the reader.

Figure 2-3 shows the general structure of a SAW tag [50]. Although the SAW tag has a fairly high data encoding capacity [19, 50], its requirement for an expensive piezoelectric component and its costly non-printable production process increase the SAW tag expense, to normally higher than that of many chip-based tags. Irrespective of the satisfactory performance of the SAW systems for some applications, the high tag cost prevents the SAW technique to fulfil main stream industries' requirements. To convert this idea for a multi-billion dollar business, several scientific and technological challenges must be solved and the fabrication cost of the tag and its related reader expense must be decreased drastically [50].

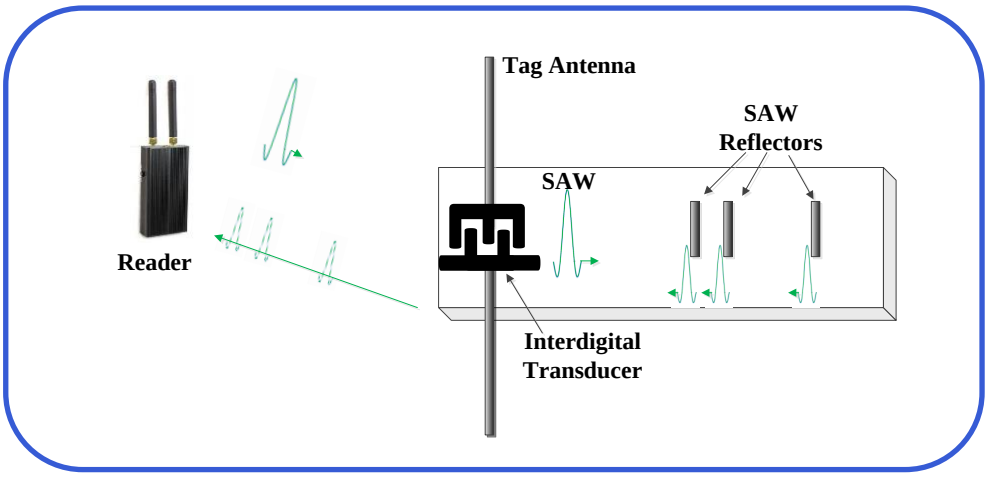

Figure 2-3 Time domain-based chipless RFID system, surface acoustic wave (SAW).

Therefore, it appears that the SAW-based RFID systems would be unable to address the required expectations of RFID systems for main applications. Lowering the tag cost in the time domain-based systems requires a printable tag structure without conversion of EM-waves to other types of media. In this approach, the tag operates on the time domain reflectometry (TDR) principle. The TDR tag normally consists of different types of transmission lines with multiple discontinuities [29, 48, 49, 51, 52]. Every discontinuity creates a reflection in the passing signal that shall be detected by the reader as the encoding technique. This approach provides the planar version of the tag structure, hence a very low tag cost expectation through direct printing is claimed to be feasible. There are however, some basic limitations which restrict their usage in real scenarios. Considering the much higher speed of EM-waves than mechanical/acoustic waves, the required circuit length is remarkably large in creating detectable delays in the backscattered signal. For example, almost an 80 × 30 mm^2 board size is required to encode only 4-bits of data, with the tag size rapidly increased with a higher amount of data [49]. Moreover, the claimed 4-bits capacity is also based on the fabricated tag structure with PCB technology and no information on the printed tag using conductive ink on paper were declared. The structure also includes some via holes which are not possible to mount on the commercial tag structure that is fully printable. In another work, the use of a transmission line of two metres is reported to have a 4-bit coding capacity [53], which results in a tag size of 112 × 53 mm^2 while the FR9151, Dupont was used as the substrate. The tag also includes the ground plane which increases the tag cost. No information was revealed on the performance of such a printed tag. There are some

techniques proposed by other researchers to decrease the tag size in time domain-based systems, however the total performance of the system was significantly degraded [54, 55].

In summary, it can be concluded that the time domain-based systems have major limitations in tag cost reduction and on providing enough data encoding capacity in a reasonable tag size. Although SAW tag, as the most successful chipless RFID product available in the market [56] is time domain-based, it appears that the main application of RFID systems will not be solely satisfied by the time domain-based approaches.

2.3.2 Frequency domain-based chipless RFID systems

A reader in a frequency domain-based RFID system normally interrogates the tag with a wide band signal. The interrogation signal is reflected back towards the reader, while specific resonances based on the tag structure are manipulated in the frequency domain of the backscattered signal. Alteration of the frequency domain of the interrogation signal is normally known as the tag's frequency signature. This process is figuratively shown in Figure 2-4. The reader then extracts the encoded data on the tag structure based on the detected resonances of the tag frequency signature [16, 57, 58]. To create specific resonances on the frequency domain of the interrogation signal, there are different types of approaches:

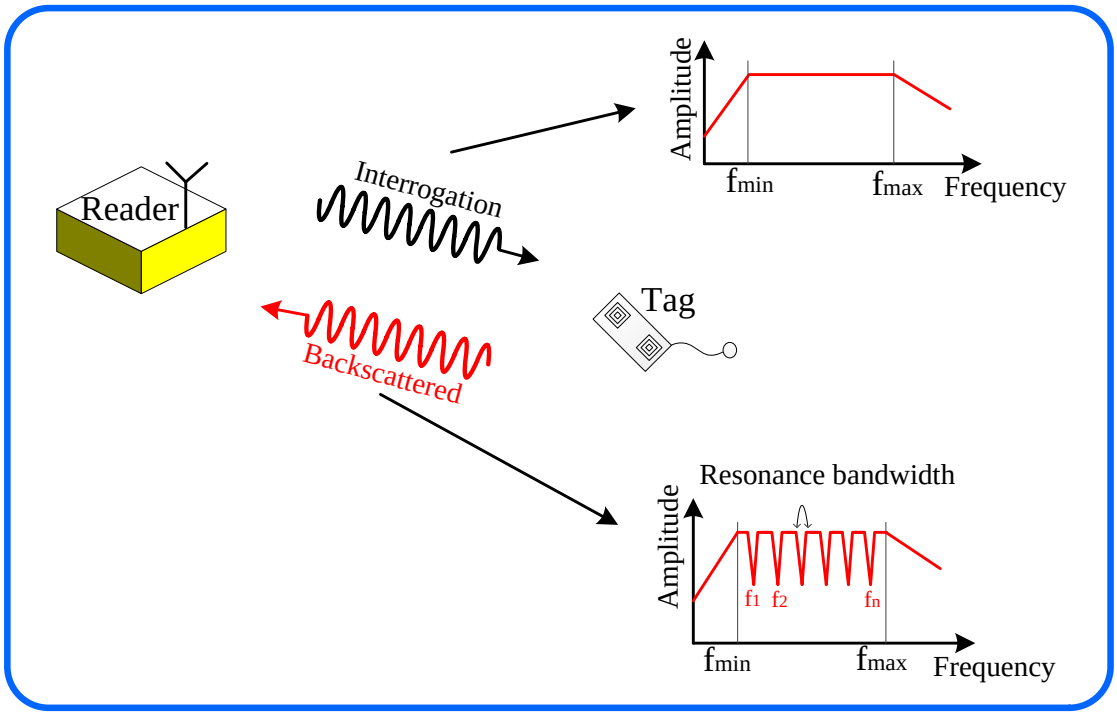

Figure 2-4 Working basis of the frequency domain chipless RFID systems.

i. Planar structure resonators [16]
ii. Frequency-selective surface (FSS) based resonators [59, 60], and
iii. Special materials usage for resonant purposes [20, 21, 61-64].

2.3.2.1 Planar structure resonators

Jalaly *et al.* [65] proposed some RF barcode type structures for data encoding. The structure is composed of planar dipoles, similar to barcodes that resonate at different frequency bands. To enhance the content capacity of the tag, it was proposed to use all available industrial, scientific and medical (ISM) radio frequency bands. Based on the proposal, every ISM band is capable of encoding a maximum of five bits. This expectation is based on simulation results. The precisely fabricated tag on the Taconic-TLY (ε_r = 2.2) substrate creates detectable resonances. However, based on the simulation results, the occurred resonances have 4 to 6 dB resonance deep that would be difficult for detection purposes in real scenario. It is very obvious that the same structure is not capable of creating detectable resonances if the tag is printed on a lossy paper substrate with low conductive ink. Moreover, system reliability decreases when multipath and clutter interferences are considered. The effect of printing inaccuracy on the length of the dipoles, which creates a resonance shift, is also another factor which affects the consistency of the system performance.

Microstrip spiral resonators were proposed to create sharp resonances on the frequency domain of the backscattered signal [16]. The chipless tag also comprises a cross-polarised transmitting and receiving microstrip ultra-wideband (UWB) disc loaded monopole antenna. It was shown that the system is capable of encoding up to 35 bits at 4 GHz frequency bandwidth. This is a significant success in the content capacity of the chipless RFID systems. However, certain circumstances were considered for the measured data capacity. First, the tag was fabricated through a costly process using PCB technology on the low loss material of Taconic TLX-0 (ε_r = 2.45). Moreover, the printed tag with conductive ink on a paper base will experience significant Q-factor drop due to the printing errors, high loss of the paper and low conductivity of the ink. These factors may limit the actual data encoding capacity of the proposed structure. However, the proposed idea in this work suggests a wide range of potentials for chipless RFID systems.

Fractal structures, as the load section of a wideband monopole antenna with encoding capability, were proposed by Balbin [66]. Based on the type and length of the fractal structures, multiple resonances would be detectable in the backscattered signal. However, due to the complex coupling behaviour among the branches of a fractal structure, the resonance frequencies alteration seems to be unpredictable. This may restrict the actual usage of the fractal structure for the RFID applications. Moreover, in the proposed work, the behaviour of precise fabricated structures was only considered and there was no study on the printable version of the fractal resonators. Considering the very tiny and complex shape of fractal structures, it is suggested that printing issue may cause more complexity on the frequency resonances of the tag. No further results have been reported on the fractal resonators for the RFID applications.

Using split ring resonators (SRRs) was also proposed for the data encoding purposes on the chipless RFID systems [67]. The proposed tag structure was printed on the poly carbonate (ε_r = 3.25) material and measured on the frequency range 8-12 GHz. The tag was capable of encoding four bits of data on a 4 GHz spectrum bandwidth. The authors suggested using waveguide antennas to create a small illumination zone. By repeating the split ring resonators on the tag surface, more encoding capacity would be feasible. The proposed technique would be suitable for security of credit/personnel cards. However, due to the low encoding capacity the proposed approach is not practical for identification purposes.

As an advanced approach, the usage of complex natural resonances was proposed to enhance the content capacity of a chipless RFID system [30]. Based on the singularity expansion method (SEM), complex natural resonances are aspect-independent parameters which include some structural information of the scattering target. This technique suggests encoding of up to 24 bits in a small area of 24 × 24 mm^2 that would be an extensive encoding enhancement compared with other available approaches in the chipless RFID systems. However, the system requires complex signal processing as multiple switching between time and frequency domain are required to decode the tag's content. Moreover, the performance of the printed tag was not shown in the proposed communication. The limited conductivity of the conductive ink and high loss tangent of the paper significantly changes the poles' positions of the tag responses, hence the proposed data encoding scheme is challenged. Additionally, the tag structure is very tolerance dependent as it comprises the line width and gaps in sub-millimeter (0.2~0.7 mm). This precise structure cannot be manipulated successfully through commercial printing facilities for low cost tag production purposes. The

effect of printing inaccuracy was not also considered in the proposed approach. However, the SEM approach opens a new area of research for chipless RFID systems and may be combined with other conventional techniques for enhancing their potentials for massive commercialisation.

2.3.2.2 Frequency-selective surface based resonators

Frequency selective surfaces (FSSs) are constructed as the rows and columns of a particular resonant structure designed to perform a (or a combination of) lowpass, bandpass, highpass and bandstop filtering functions on the incident plane wave passing through, in a measurement known as 'transmittance' [65, 68]. Although, barcodes and RFID systems are reflection–based structures, sometimes the FSS are used for creating resonances in the reflection direction and hence are suitable for RFID applications.

Costa *et al.* [59] proposed the usage of high-impedance surface-based multi-resonators. The structure is based on a finite metallic FSS comprising of several concentric square loop resonators. The reported tag structure occupies 45 × 45 mm^2 area and is capable of encoding five bits of data content. Therefore, the data encoding density is 0.25 bit/cm^2 that is very low considering the requirements of the main RFID applications. The tags are readable from 55 cm distance with zero dBm transmit power. The system had a good performance for different tag orientation scenarios. However, the system needs a calibration measurement process for proper reading to cancel out the effect of multipath interference and the effect of antennas; otherwise the system fails to read and detect the tag's data. Moreover, all measured data in the published work is based on the fabricated tag structure with PCB standards on a FR4 substrate. No result based on the printed tag structure was revealed.

In another work a stacked multilayer patch antennas is used as an all-pass network to provide more robustness with respect to multipath and clutter interferences [60]. In the proposed theory, instead of relying on an amplitude-frequency response of the multilayer structure, the phase-frequency response is considered. A three-layer structure with 18 × 18 mm^2 area is able to decode two bits of data content based on the simulation results. No measurement of the proposed tag structure was shown in that communication. However, the performance of the proposed structure is directly linked to the conductivity and loss tangent of the substrate. This suggests that the fabricated and printed tag may show significant performance degradation with respect to the simulation result. Moreover, printing of a three-

layer structure increases the tag fabrication cost and may not meet the low cost expectation of the RFID tag for the main industries.

2.3.2.3 Material-based resonators

CorssID [61], a telecommunication company, has reported developing a chipless RFID system that provides a reliable authentic approach for valuable documents, such as intelligence agency reports, financial securities and banknotes. The system uses "nanometric" materials, tiny particles of chemicals with varying degrees of magnetism, that resonate when bombarded with electromagnetic waves from a reader. Each chemical emits its own distinct radio frequency, or “note”, that is picked up by the reader, and all the notes emitted by a specific mix of different chemicals are then interpreted as a binary number. Since the system uses up to 70 different chemicals, each chemical is assigned its own position in a 70-digit binary number [61]. No further information about the working prototype and its applicable tag cost have been released since it was introduced in 2004.

In 2007 Somark Innovation declared that it has a special readable ink as a chipless RFID tag that can be used to track animals, cattle for example, or even human beings. No further discussion is disclosed by the company and no information is also available on its encoding capacity or the ink (tag) cost [62, 63].

A fair comparison among different chipless RFID system techniques with or without meta-materials are provided by Mandel *et al.* [20]. In this communication, various approaches were studied in terms of their merits, frequency band usage, and tag size for one bit of content, then they concluded that the meta-materials can shrink the tag size hence enhancing the merits of the structure. Although in their study, the time and frequency based systems were considered with the application of meta-materials, no information about the tag cost utilizing meta-materials was provided.

2.3.3 Phase-domain based and hybrid chipless RFID systems

Phase-domain based system is proposed as a method of data encoding to rely on the phase information of the backscattered signal. In one proposal, the tag consists of some plurality of antenna elements with different dimensions and orientations that provide polarisation and

phase information [69]. The interrogator device scans the area and uses radar imaging techniques to create an image of the scanned scene. The re-radiated RF signals of the tag preferably include polarisation and phase information of each antenna element. The proposed tag shapes are presented in Figure 2-5 with dipoles of different length and width. Four different orientations are suggested for each antenna size at angles 0°, +/- 45°, and 90°, which control their particular phase and polarisation responses. It has been also proposed to use some reflective rectangles with two (or more) reactive stub loading which are extended from rectangle antennas. One is perpendicular to the antenna and the other is parallel to the antenna polarisation. In this case, the length and position of the reactive stub elements control the phase and polarisation parameters of the reflected signal respectively. It is claimed that the proposed system has the ability to read and track chipless tags from 100 m away and to read thousands of tags per second [1, 69]. However, no commercial product is available on the market based on this approach yet. This is probably because the content encoding in RFID systems through phase and polarisation is very expensive and sometimes impractical. The phase of the reflection by a given element is dependent on its distance to the reader. This means that a slight bending of the tag surface causes a significant phase shift specifically in higher frequencies. There are suggestions to mitigate the phase ambiguity, however the solutions only apply to chipped-tags for low frequencies, below 1 GHz, and no work is reported on chipless systems [70, 71].

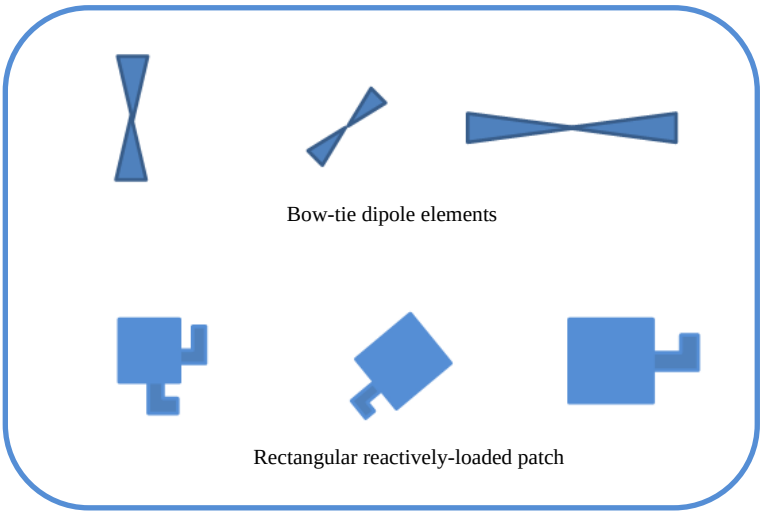

Figure 2-5 Phase-domain based chipless RFID tags.

As a hybrid based system, the combination of phase deviation and frequency position of the resonances was proposed as the data encoding approach in a chipless RFID system [72]. The tag consists of multiple "C" shaped resonators which are interrogated through a wideband signal in the band 2.5-7.5 GHz. The claimed content encoding capacity is 23 bits with five "C" shape resonators. The encoding is based on a matrix of frequency and phase shift deviation. However, the tag was tested in the anechoic chamber and no further discussion was communicated to explore the effect of multipath interference on the system performance. This would be an important aspect of the proposed approach as the reflection from other objects will cause significant effects on the phase shift. There is a need for pre-measurement of the scene to calibrate the system as well. This means that the system is vulnerable to errors if any changes happen in the surrounding area of the tag. Moreover, the performance of the tag is not clear regarding to the bending effect. The performance of a real printed tag structure was also not discussed.

In another work, the amplitude and frequency-based encoding scheme is proposed as a new encoding approach for enhancing the content capacity of the chipless RFID systems [73]. The split ring resonator (SRR) is the proposed resonator type, and based on the received signal level and the position of the resonances, the data can be encoded. Although system content capacity is increased, the system complexity and also its sensitive performance towards noise and multipath interference may prevent its actual usage.

2.4 EM-imaging in various applications

Carl A. Wiley, a mathematician at Goodyear Aircraft Company in Litchfield Park, Arizona, invented synthetic-aperture radar (SAR) in June 1951 while working on a correlation guidance system for the Atlas IBM program [74]. Nowadays, electromagnetic imagery based on SAR theory is of widespread interest and is extensively used in military and civil applications. In the SAR-based system, a large synthetic aperture antenna is formed by a moving antenna over the target region. The target is repeatedly illuminated with radio waves pulses at different frequencies, and the echo waveforms received successively at the different antenna positions are coherently detected and stored, and then post-processed together to resolve elements in an image of the target region. The obtained EM-image of the target scene through SAR technique acquires much finer spatial resolution than is possible with

conventional beam-scanning means. For applications like earth imaging, the SAR technique is the only option as carrying a large antenna over the earth is not practical. There are however other applications on which the usage of large antennas is feasible for imaging purposes, but the SAR technique is preferred for different reasons. For instance, in the body imaging application, it is possible to use a large antenna providing a high resolution EM-image of the body; however the SAR technique is much preferred as it minimises the amount of radiation on the body. Most body imaging systems nowadays use the SAR-based technique to comply with EM-radiation regulations [75-77]. Through-to-wall imaging (TWI) based on the SAR technique is also extensively used in construction activities [78] as well as intelligence and security applications.

2.5 Potential advantages of the proposed tag structure

The literature review and analysis shows that the identification market in main stream applications with billions of yearly tag requirements still requires an RFID product whose technical specifications are adequately matched with industry expectations mainly on:

i. Tag cost of below one cent,
ii. Enough data content capacity in a reasonable tag size,
iii. Consistent performance based on the printed tag structure, and
iv. Reliable performance in an industrial environment.

It appears that the proposed technique of the cross-polar image-based chipless RFID system promisingly addresses the aforementioned technical requirements and hence is capable of significantly influencing the RFID market. The key potential advantages of the proposed tag are as follows:

i. **Printing and cost issue.** The tag structure in the proposed technique utilises a tiny conductive component which acts as effective EM-polariser. The tag is fully printable through a low cost inkjet printer and the cost of the required ink is lower than that of a barcode for the same content capacity as will be shown in Chapter 3 (3.3.2). All the measurements and results in this dissertation are based on the printed tag structure which provides satisfactory performance for the proposed system in its commercial phase. Hence, it can be concluded that the tag cost in the proposed technique meets industry criteria as it is less expensive than a barcode.

ii. **High content capacity.** As briefly addressed in Chapter 1, the data content capacity of the proposed EM-imaging approach depends on the available frequency band and the system complexity. For a fairly simple reader structure and limited bandwidth, the tag's encoding capacity is proportional to the tag's length, see Figure 2-6. However, even based on the simplicity assumptions, the proved data encoding capacity through EM-imaging in a small tag size is much higher than of shown by other techniques to date for a printed tag. Normally, five vertical polarisers are assumed on every vertical slice of the tag surface, to yield a reading range of 10-30 cm. These five polarisers provide approximately five times larger RCS than that of a single polariser. Based on this assumption, the width of the tag is fixed at almost 10 mm. On the other hand, every 2 mm of the tag length has the potential to encode one bit of data, Figure 2-6. Hence the data encoding capacity is one bit per 0.2 cm^2 or equivalently 5 bits/cm^2. This is a revolutionary improvement in the content capacity of the chipless RFID systems based on a fully printable tag [1, 47]. The credit card size, 55 × 85 mm^2, as discussed before is considered as the maximum acceptable size of any RFID tag for main stream applications. The ultimate goal of the chipless RFID systems is to reach 35~50 bits content capacity [11, 47]. As results at the end of this thesis show, the proposed theory of cross-polar image-based chipless system provides 17 bits of data in a strip of 8.5 × 1 cm^2 that is 5.5 times narrower than a credit card size. Therefore, the content capacity of 93 bits is easily feasible for the credit card size tag surface.

iii. **Mitigation of the printing errors and performance.** Many proposed chipless RFID systems fail to address industry requirements because of the anomalies that occur during the printing of the tag fabrication. As discussed earlier, the printed tag structure generally suffers from two major limitations. First, the lossy characteristics of the paper and low conductivity of the ink adversely affect the Q factor of the resonances, hence the encoding capacity significantly reduces [79]. Second, the random anomalies occurring during the printing process, create noticeable frequency shifts and other unexpected effects on the tag responses, hence no reliable reading process is feasible.

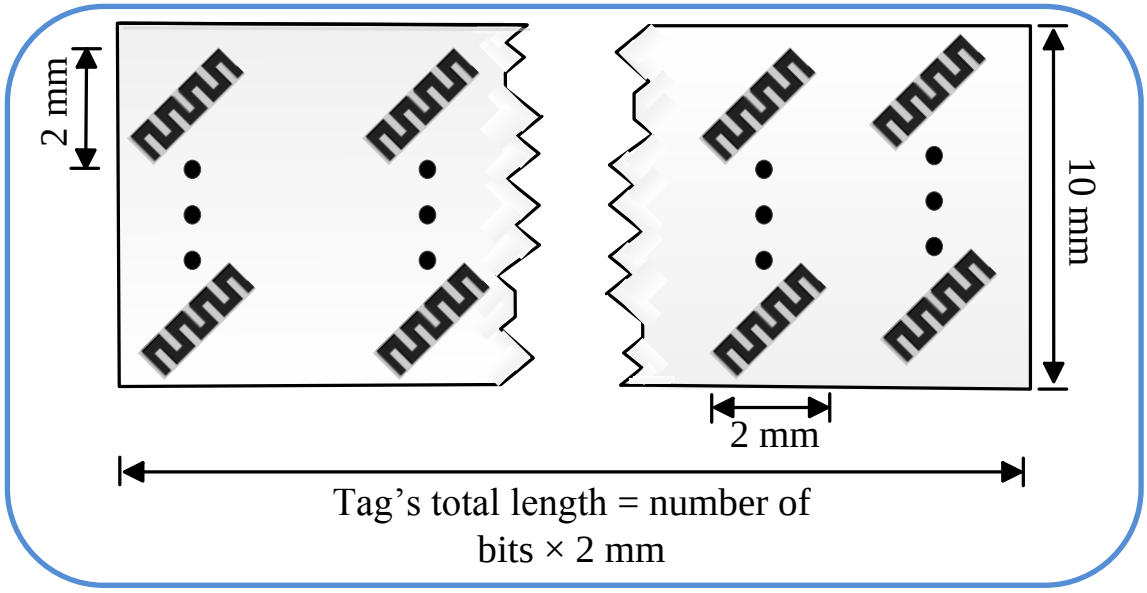

Figure 2-6 Maximum theoretical tag content capacity.

In the proposed technique of the cross-polar image-based chipless RFID system, both limitations occurring during the printing process have been considered and the system is capable of reading the tag and extracting its encoded content in a reliable manner. The tag structure considered during this research is a printed structure with all its anomalies. Figure 2-7 shows a sample of the considered tag that presents significant degradation of the tag structure during the printing process. Irrespective of these anomalies and the low Q factor of the structure, the data decoding process is fulfilled successfully in the proposed approach.

iv. **Mitigation of propagation issues in industrial environments.** There are many available approaches for chipless RFID systems with satisfactory performance when considered in an anechoic chamber condition. Elimination of background clutter, reduction of external noise, mitigation of multipath interferences and other considerations may result in a satisfactory tag performance. However, if the system is tested in real environment, its potential advantages for proper data communication are significantly challenged. Any successful product must consider the harsh industrial environments and provide solution based on those conditions. The performance of the proposed tag structure has been considered in laboratory conditions with many reflective items and other sources of interference. No calibration or reference tag has been considered for the entire measurement process.

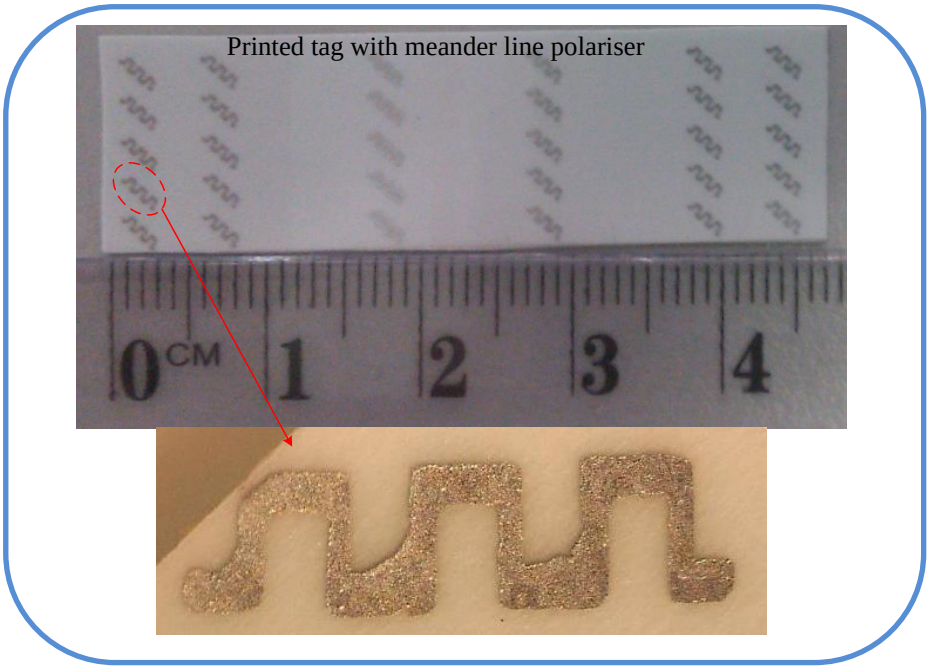

Figure 2-7 Printed tag with structural anomalies.

Moreover, the performance of the tag has also been tested for tagging of highly reflective items, for instance aluminium can. The bending effect of the tag was also considered in the proposed theory of the image-based system and reliable performance was experienced. The measurement set up for different scenarios is shown in Figure 2-8.

From the above attributes of the proposed chipless RFID tag, it is inferred that the EM-image based mm-wave tag not only mitigates many limitations of other reported chipless RFID tags but all surpassed many propagation issues of chipped RFID tags. Therefore, the proposed tag will become a potential identification technology for future industrial applications.

2.6 Potential advantages of the reader system

In chipless RFID systems, the reader is required to accomplish all the data processing tasks as the tag is a fully passive structure with no signal processing capabilities. This may increase the complexity, cost and realisation of the reader system beyond a practical point. In the proposed technique of the cross-polar image-based chipless RFID system, the reader is fairly simple considering its required sophisticated reading process. The main advantages of the proposed reader system can be summarised as:

i. Chirp waveform on a transmitter (Tx) module

In most EM-imaging systems, a pulse shaped chirp signal is used in the reader to illuminate the target [74, 80, 81]. The parameters of the chirp pulsed shape signal defines the range resolution of the processed EM-image. In the proposed technique of the cross-polar image-based system, the azimuth resolution through the SAR technique is used for data encoding purposes. Although, a fine range resolution may suggest a noticeable content capacity, it has not been used in this research due to the huge bandwidth requirements. Therefore, in the proposed technique, a chirp pulse signal with reasonable chirp rate is being utilised. The required spectrum of the chirp signal for the proposed application of EM-imaging in mm-wave band is technically practical and meets the regulatory requirements. The range resolution in the proposed application is a course resolution compared with azimuth resolution and obviously range resolution has no effect on the final data encoding capacity.

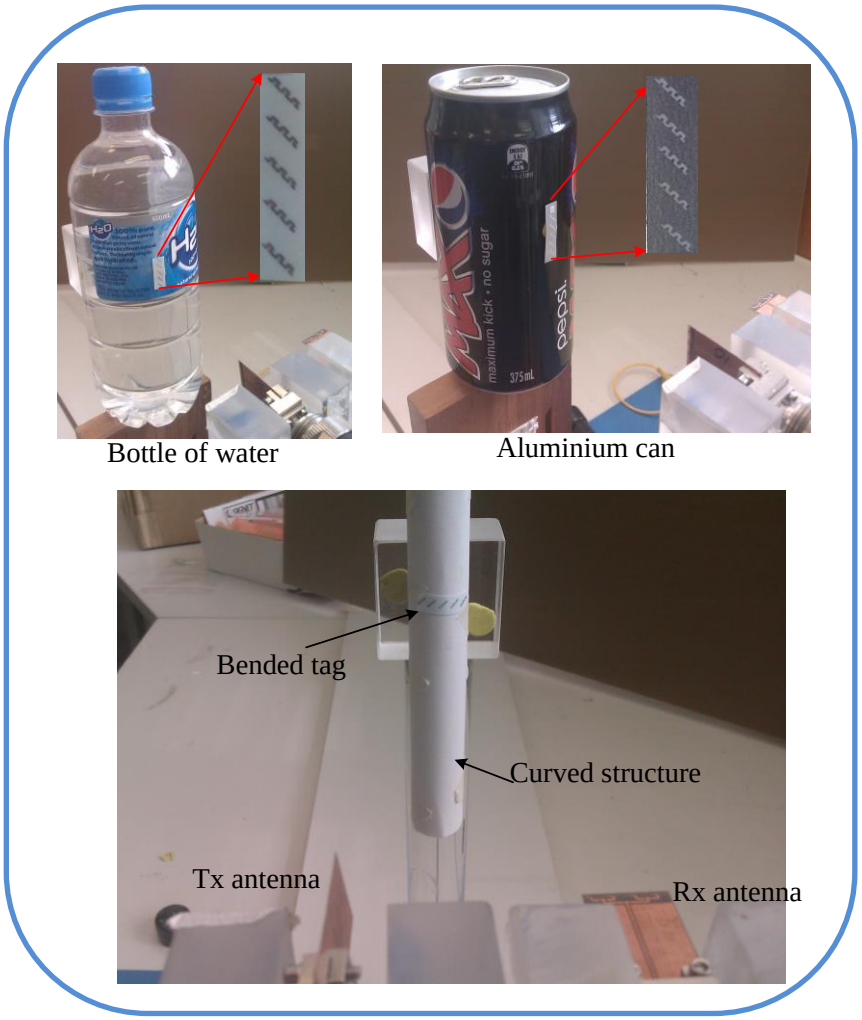

Figure 2-8 Various measurement scenarios for testing tag performance.

ii. Low profile, light weight and cheap antenna structure

The reader antennas for the reader side are fully planar structures that are printed on the Taconic TLX-8 substrate through the normal PCB fabrication process. Each antenna is an array of four double side printed dipoles (DSPD) on which the total size of the array is 1.5×2.5 cm^2 including its feedline. The antenna performance is suitably tailored for the proposed application, specifically its CPL and radiation patterns. The light weight and small size of the antenna structure is also very convenient for the physical movement of the array as required for creation of a synthetic aperture around the tag. However, appropriate suggestions are provided to eliminate the physical movement of the antenna and increase the reading time. Example includes the MIMO-based array antenna concept proposed at the end of this dissertation for fast imaging purpose [82].

iii. No requirement for calibration

In the proposed approach of the cross-polar image-based system, deletion of the background clutter is not required as those interferences are in a co-polar direction while the system is cross polar-based. Moreover, no reference tag is utilised for calibration of the reading process. These factors facilitate the reading process and simplify the reader system.

iv. High robustness toward interference

The system shows high robustness towards any interference coming from objects around the tag, which result in fewer constraints on the reader system. The reader's antennas are not required to create nulls in any direction for minimisation of interference, hence benefiting freedom on their radiation patterns. Moreover, no extra signal processing is necessary on the reader side to cancel the interferences.

From the above discussion on the proposed tag and reader architecture, it is evident that an EM-image based chipless RFID system is implementable in commercial domain. Although, it is perceived that 60 GHz transceiver modules, switching elements and antennas are too expensive for commercial applications, the advent of 60 GHz modules [83], switches [84], the developed antenna [85], and in-house developed signal processing algorithm proves the commercial potentials of the proposed system.

2.7 Conclusion

This chapter has identified the requirements of industry for main stream applications and reviewed the tag cost, content capacity and other specifications, showing that billions of yearly tag consumptions would only be financially feasible if the tag price should drop to below one cent. The chipped tag was considered from a cost perspective and shown to be too expensive due to the silicon chip requirement. Consequently a chipless tag was considered the only RFID product with potential to address the cost requirements of industry.

Time-domain based chipless RFID systems, e.g SAW tags, were identified as the most successful product available in the market to date. However, products with high encoding capacity using this technique are too expensive, and cheap solutions suffer from very low data encoding capacity within a reasonable and practical tag size. Frequency domain-based chipless RFID systems provide an enhancement of the data encoding capacity of the chipless RFID systems based on the laboratory condition. However, their performance significantly drops when a printed tag structure is tested. This is due to the low Q factor of the printed resonators through using conductive ink on paper. Moreover, printing inaccuracy results in a frequency shift that reduces the reliability of the reading process. Other hybrid systems were also briefly reviewed. Phase domain-based systems suffer from very complex reader architecture, while the system performance is very sensitive with respect to a minor change in the tag structure or surrounding area.

Due to the limitations of the current techniques in chipless RFID systems, a cross-polar image-based chipless RFID system was proposed. The tag fulfils the tag cost expectation of below one cent. The tag requires no maintenance as no active or sensitive part is included in the tag structure. The tag is also not vulnerable to mechanical damage due to its fully printable structure. The proposed approach also considers anomalies during the tag printing process, with the tag's response being very robust to the bending effect. It also has a reliable reading performance when attached to highly reflective items. The tag's content capacity is far beyond that of other techniques with high robustness towards multipath, clutter, and surrounding interferences, hence it is suitable for industrial environments.

The reader was also considered and its main modules were introduced. The low profile and light weight reader antennas make movement of the reader possible. The high CPL of the array structure provides interference robustness. The required chirp type signal suggests a

simple structure for the transmit module of the reader. No switching system or extreme narrow pulse shape generators were needed for the reader.

The potential of the proposed technique suggests a great potential of acceptance by the identification industries and huge potentials on the RFID chipless market. The next chapter presents the fundamentals of the EM-polarisers as the unit cell of the proposed chipless RFID tag.

Chapter 3 EM-imaging through reflective EM-polariser

3.1 Introduction

Discussions carried out already prove that fulfilment of industry expectations is addressed only if the RFID tag is chipless, fully printable, and has high data content capacity comparable to that for barcodes. Potential advantages and limitations of the current techniques in chipless RFID systems have been briefly introduced in Chapter 2. Technical specifications and practical factors influencing the time, frequency and phase–domain based chipless RFID systems have been reviewed and their actual data encoding capacity based on a printed tag structure was verified. It was concluded that the current techniques severely suffer from poor performance in providing enough data capacity for a small sized tag if the tag is printed on paper using conductive ink. Poor ink conductivity, lossy paper, and finally printing inaccuracy, significantly reduce the final content capacity of the tag to a level that is far beyond industry's expectation [86].

The idea of EM-imaging for data enhancement in chipless RFID systems was briefly introduced in Chapters 1 and 2. The EM-imaging technique differs from other reported techniques in chipless RFID system in one important aspect. In all proposed techniques to date, the tag surface is illuminated by the reader at one glance and its data is retrieved simultaneously. Conversely, in EM-imaging every small section of the tag surface is scanned separately through a reader and the tag's data is decoded independent of the other parts of the tag. Hence, the data capacity of the tag can noticeably increase compared with other approaches. In other words, the EM-imaging adds a spatial diversity to the current frequency, time or phase-domain based systems. The conventional data encoding schemes and the new EM-imaging approach are illustrated in Figure 3-1. In a normal RFID system, the whole tag surface is illuminated by the reader at one specific time and encoded data is retrieved from its response. However, in the image-based system every section of the tag is sequentially scanned with the reader antenna and the encoded data in each specific section is individually being read. It appears that the new idea of EM-imaging simply multiplies the content capacity of the tag. However, two main questions shall be addressed in this new scenario; *i)* how to precisely scan the tag surface and *ii)* how to encode data in a small section of the tag's

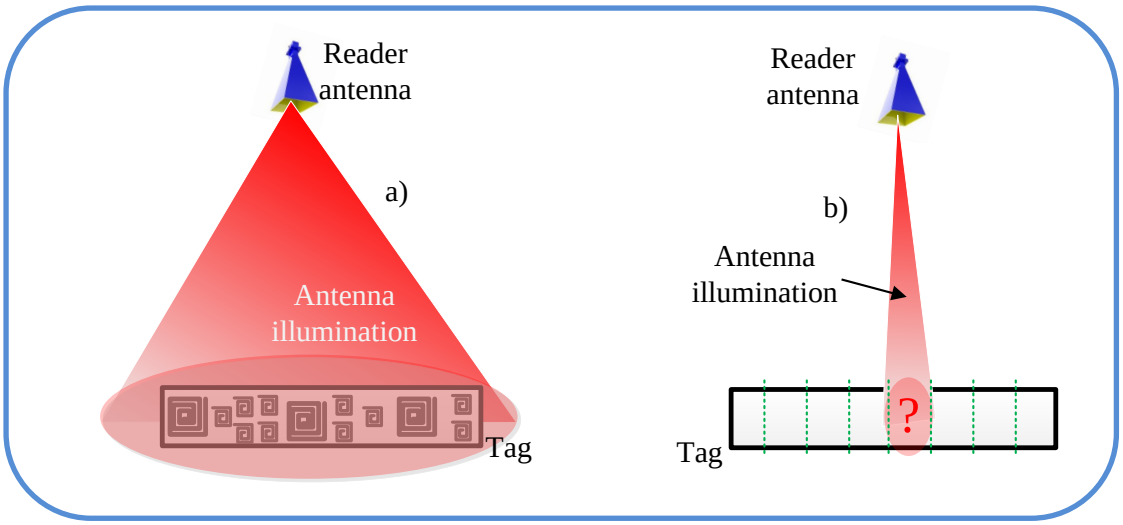

Figure 3-1 Reading schemes in a) conventional RFID system, and b) image-based system.

surface. Answering these two important questions develops the hypothesis of the PhD thesis. This hypothesis is presented in the following sections.

Figure 3-2 shows the structure of the current chapter to mature the idea of EM-imaging for the RFID applications. The earth imaging system, as the first and most important application of electromagnetic imaging, is firstly reviewed. This provides a basic understanding of the electromagnetic imaging principles. Then scanning of the tag's surface is technically considered based on the antenna theory and other perspectives including the frequency of operation and reading distance. The requirement for a synthetic aperture technique and the necessity of mm-wave frequencies are addressed in this part. It is concluded that in certain frequency ranges, scanning of the tag surface in millimetre order is technically possible. In the next step, the difference between earth imaging and chipless RFID tag imaging is highlighted. It is shown that the criteria of the reflected signal level as used in earth imaging is not suitable for RFID applications. The usage of polarisation of the reflected signal instead of signal power level is proposed in this regard. A strip line as an effective electromagnetic polariser is introduced and theoretically analysed. This builds a completely new approach which differentiates the RFID tag imaging from its ancestor, earth imaging. Meander line as a more effective EM-polariser than strip line polariser is then introduced. Finally, it is concluded that the EM-imaging technique is applicable for RFID applications through technically tailored parameters.

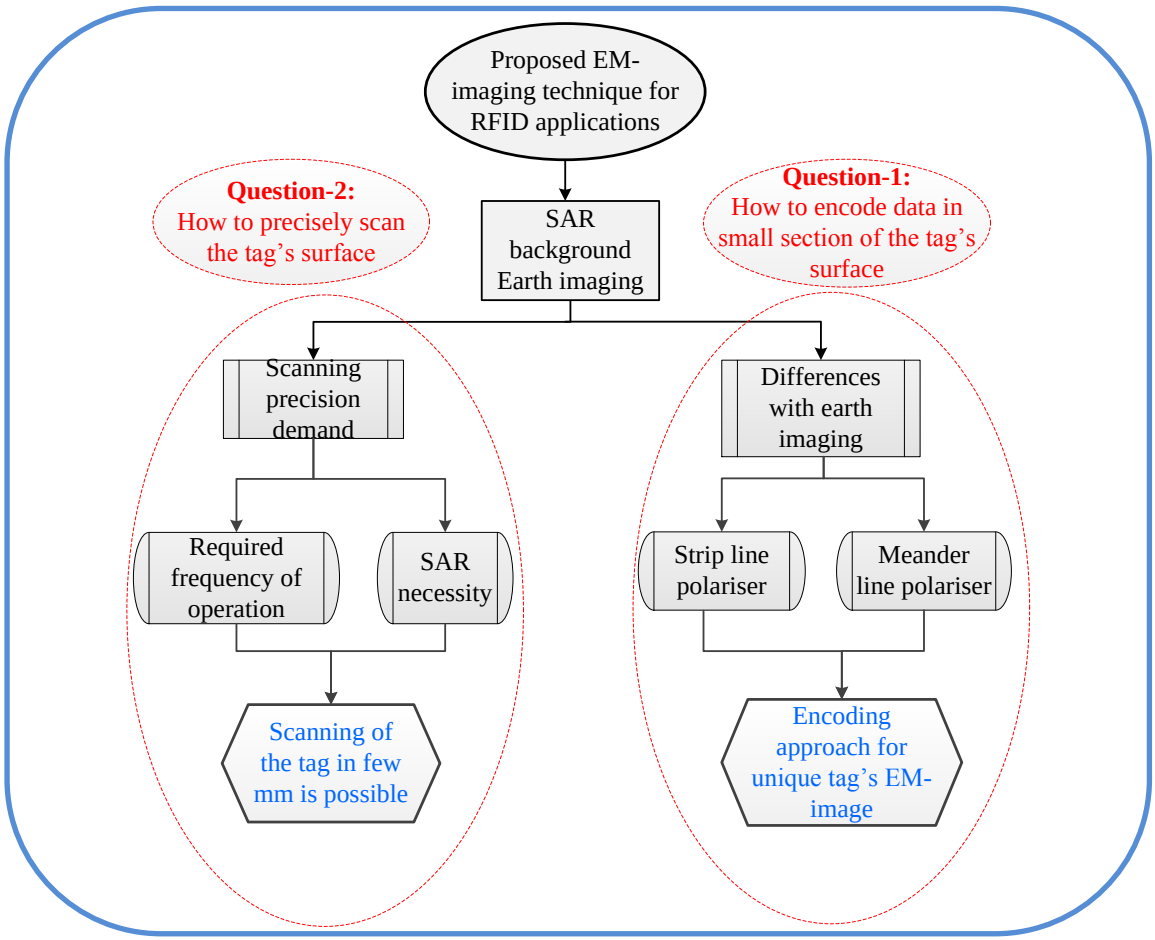

Figure 3-2 Flowchart of discussion in Chapter 3.

3.2 Triggered idea by Earth imaging

Earth imaging is the first and most important application of the SAR EM-imaging technique to date. In an earth imaging system, the Earth's surface is interrogated by a radar system which is normally mounted on an air/space-craft. A super narrow beam antenna is required at the craft station to precisely scan the earth surface. Based on the reflected signal from each section of the earth, the radar system forms the related EM-image. However, based on the antenna theory, this super narrow beamwidth radiation mandates a massive antenna with few kilometres size. Fabrication of the antenna in kilometre size is extremely difficult and handling it by an air/space-craft station would be impractical. Instead of utilising an impractical big antenna, Carl Wily [87] proposed to simply move a small antenna around the earth and constructively add the received signal at different positions of the radar system. This concept is called synthetic aperture radar (SAR) to signify that a signal synthesis accomplishes what would otherwise require a large antenna aperture. After SAR-based signal

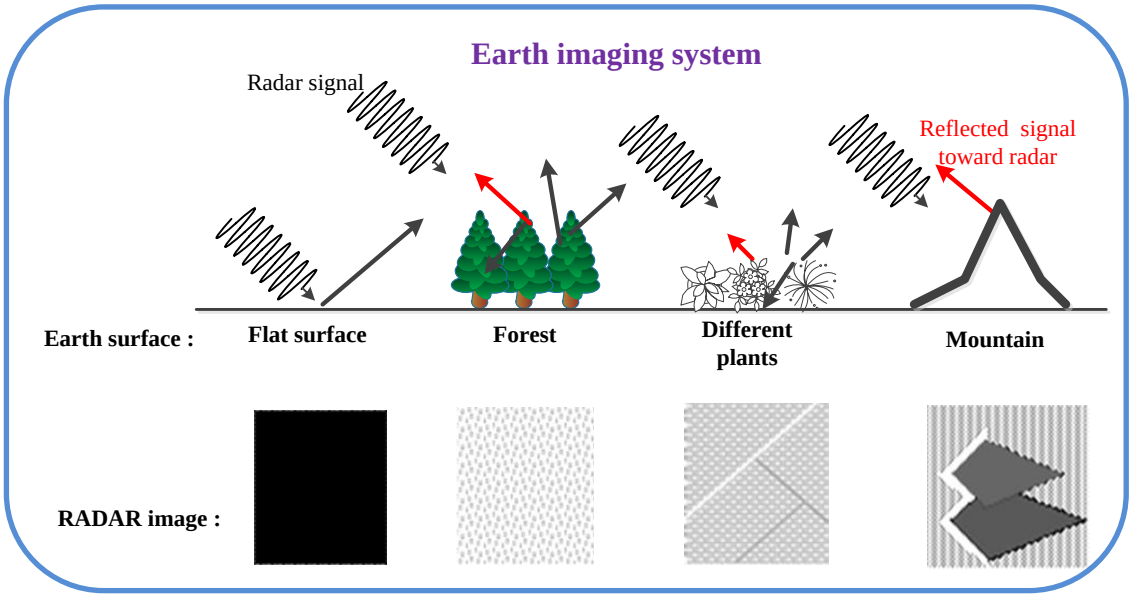

Figure 3-3 Reflection strength based on terrain roughness in earth imaging system [88].

processing, the strength of the reflected signal from each section of the Earth's surface is linked to its EM-image and shows the terrain of the Earth's surface. Rough surfaces result in higher reflection and therefore a brighter part in the EM-image; a building or mountain for example. An impinged signal on a flat surface is reflected in the opposite direction, by Snell's law, hence radar receives no energy and a black image is formed. Figure 3-3 shows the principle of image brightness in an earth imaging system. This working basis may initiate the idea of shaping the RFID tag surface in such a way to create a unique image when illuminated by a proper EM signal. This is discussed in more detail in the following sections.

3.3 Precise scanning of the tag surface

The accuracy of scanning in the proposed image-based system directly relates to the associated data encoding capacity. Therefore, to find out what is the minimum required scanning precession, one should know about the expected content capacity of the chipless RFID system. On the other hand, the size of the tag shall also be limited to certain values. For many RFID applications, the size of a credit card (85×55 mm^2) appears to be the maximum allowable size of the RFID tag [11, 47].

The expected content capacity of the chipless RFID systems is more difficult to standardise as every industry has its own requirements and expectations. However, many research entities

assume 50 bits data encoding capacity for a chipless tag structure as the ultimate capacity of these systems [16, 17, 89]. This may suggest one bit/cm ^{2} as the very satisfying data encoding capacity of a chipless RFID system.

$$Encoding\ capacity = \frac{50}{8.5 \times 5.4} \approx 1\ bit / cm^2 \qquad (3.1)$$

Therefore, the targeted scanning precession in the proposed image-based system should be around 10 mm. This means that the reflected signal from each one cm^2 of the tag surface shall be processed separately by the reader. The straight forward approach for analysing the effect of each small section of the tag is to utilise a reader antenna in which its radiation pattern illuminates every 10 mm of the tag surface separately. This illumination area is known as the *footprint* of the reader on the tag surface as shown in Figure 3-1. To interpret this footprint size with the 3-dB beamwidth of the reader antenna, the reading distance is required. The normal reading distance of the chipless RFID system is currently limited to 50 cm as the tag has no internal power source and the reader relies only on the backscattered power [90]. Figure 3-4 shows the reader footprint on the tag surface with two image resolutions. The range and cross-range resolutions are defined by ρ_r and ρ_σ respectively. These two resolutions with the reading distance (d) and 3-dB beamwidth of the antenna are also shown in Figure 3-4.

3.3.1 Frequency band selection

As discussed earlier, a rough estimate of 10 mm scan resolution requirement has already been gained through the maximum expected data encoding capacity of the chipless RFID system. To find the best suitable frequency range(s) for the proposed image-based system, it is necessary to relate the parameters of Figure 3-4 to each other. The image resolution, whether in range or cross-range, simply corresponds to d and 3-dB beamwidth ($\theta_{3\text{-}dB}$) of the antenna through:

$$\rho_i = d.\tan(\theta_{3-dB}) \ ; \ where \ \ i = r, cr \qquad (3.2)$$

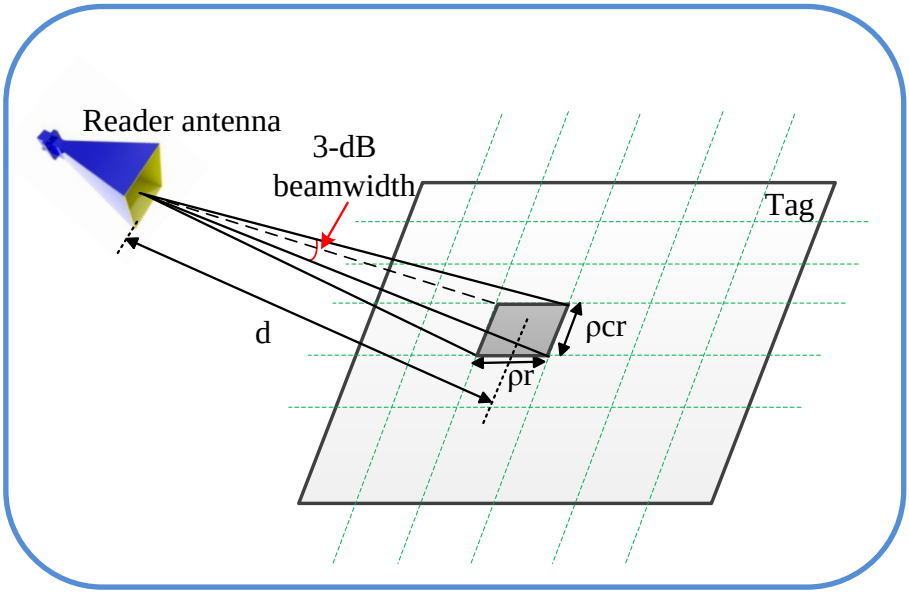

Figure 3-4 Reader footprint on tag structure.

This formula is figuratively shown in Figure 3-5. The expected beamwidth of the reader antenna is very narrow and normally varies between 1-6° as stated above. Creation of such a narrow beamwidth requires a very large antenna size as the antenna beamwidth inversely relates to the antenna physical size. The exact relation between the antenna's beamwidth and its physical size depends on the aperture illumination function, which controls the main beam and side lobes of the radiation pattern of the antenna. However, a practical rule-of-thumb for typical illumination functions expresses the beamwidth in terms of aperture size and the wavelength as follows:

$$\theta_{3dB} = \alpha \frac{\lambda}{D} \tag{3.3}$$

where θ is the 3-dB beamwidth of the antenna in radians, λ is the wavelength, D is the antenna physical size and α is a constant reflecting the main lob widening due to the weighting aperture. For a uniform aperture weighting, $\alpha \approx 0.89$ and hence (3.2) is changed to $\theta_{3dB} = 50\frac{\lambda}{D}$ when θ is measured in degrees. By assuming 1° beamwidth demand, the required aperture size is depicted in Figure 3-6 based on various frequency ranges. The actual required antenna size is also shown for three common ISM bands of 2.4, 24 and 60 GHz.

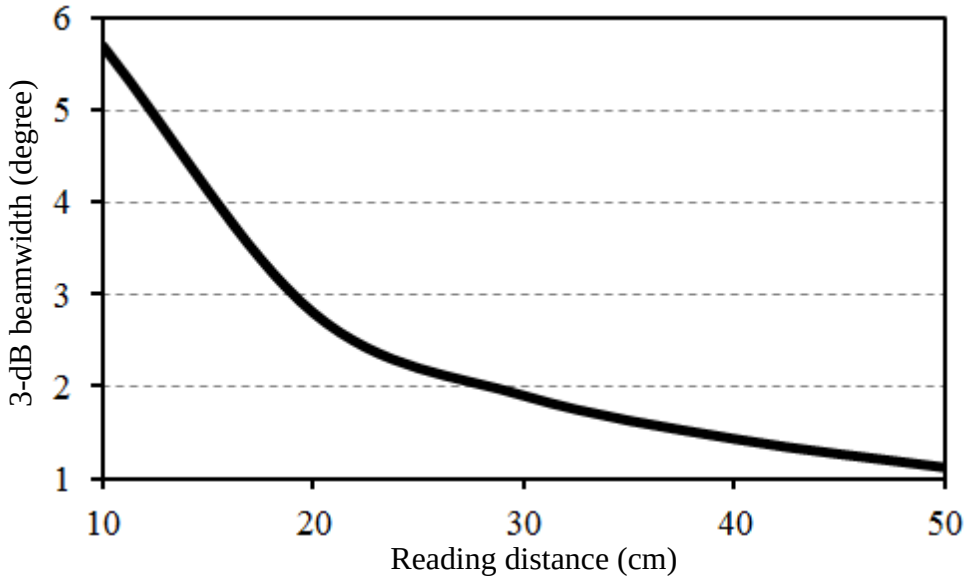

Figure 3-5 **R**equired 3-dB beamwidth of reader antenna versus reading distance.

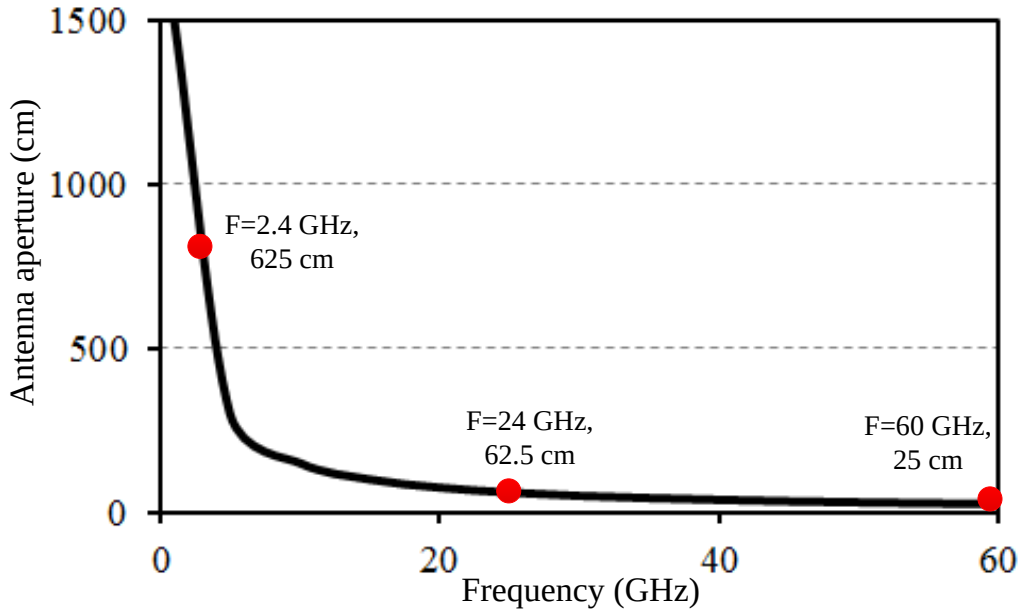

Figure 3-6 Required antenna aperture size for 1° beamwidth.

Among three available ISM bands, 2.4, 24 and 60 GHz, only the 60 GHz band offers an antenna size that may be practical for a reading distance of 10-50 cm. In frequencies below 60 GHz, the required aperture size of the antenna is much bigger than the reading distance, hence would be a non-practical scenario for the proposed technique. This is the main reason that the mm-wave band of 60 GHz is selected for the proposed image-based chipless RFID system. In the next sub section, the general aspect of the proposed 60 GHz band is reviewed to provide a broader range of information about its technical and regulatory requirements.

3.3.1.1 60 GHz frequency band

The 60 GHz frequency band experiences high free space attenuation, 128 dB/km based on Friis transmission equation. Furthermore, an extra attenuation is also involved in the 60 GHz band due to the high oxygen absorption in this particular band, 15-20 dB/km [91], see Figure 3-7. This high attenuation of signals at 60 GHz makes it unsuitable for long range communication services. However on the other hand, high attenuation provides a unique advantage for frequency re-use and interference-free conditions. Therefore, it is advantageous for certain applications as an ideal candidate frequency band. For instance, inter-satellite links at 60 GHz are well protected from any terrestrial interference by high atmospheric attenuation. It has also been an attractive frequency candidate for military and highly secure communications regarding its severe absorption by building materials, which could ensure that signals cannot travel far beyond their intended recipient. Fortunately, because of the rich legacy of these applications, a wide variety of components and subassemblies for 60 GHz products are available today [92]. The above-mentioned characteristics of the 60 GHz frequency band have stimulated the regulators of telecommunications to recognise this frequency band as an unlicensed option for short range indoor/outdoor applications [93]. According to the Radio Regulations (RR) prepared by the international telecommunication union (ITU), the bands 55.78-66 GHz are allocated to fixed and mobile services in all three ITU regions. Also, footnote 5.547 of the ITU Radio Regulations designates the bands 55.78-59 GHz and 64-66 GHz as suitable for high density applications in the fixed service [93]. Following the ITU allocation, most countries have recognised some specific portions of 55-66 GHz as ISM frequency bands [32, 94]. Table 3-1 shows samples of the regulators decisions. Moreover, the maximum transmitting power limitations for interference reduction or human exposure issues for this frequency range are less limited by telecommunication regulators. The maximum EIRP of 40 dBm and maximum power to the antenna of 10 dBm are normal values that cover the regulatory limitations in most countries. The minimum frequency bandwidth is also set to 100 MHz and therefore most commercial producers have selected it as their channel bandwidth [31-34]. Hence, it can be concluded that the technical and regulatory situation of the 60 GHz frequency band makes this frequency range an ideal candidate for imaging purposes in the RFID applications.

Table 3-1 Available spectrum on 60 GHz band

Country/Region	Frequency (GHz)
Australia	59.4-62.9
USA & Canada & Korea	57-64
Japan	59-66
Europe	57-66
China	59-64
$EIRP_{max}$	40dBm
P_{trans}	10dBm
$bandwidth_{min}$	100 MHz

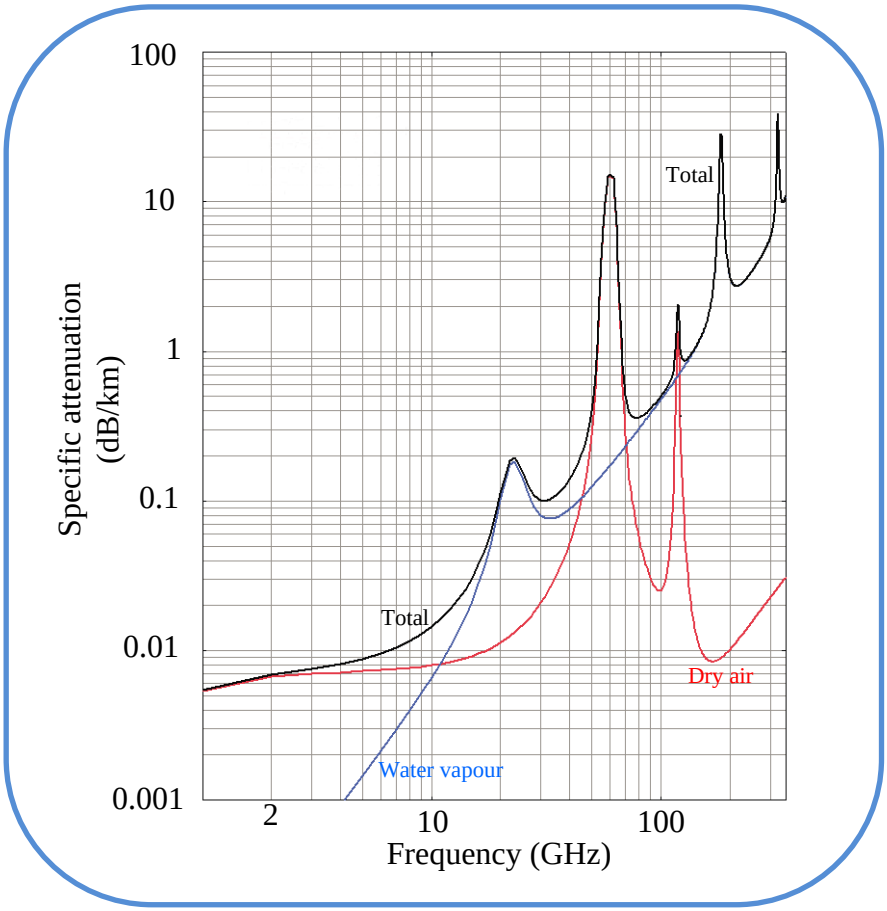

Figure 3-7 Specific attenuation due to atmospheric gases [91].

3.3.2 Lower printed tag cost at mm-wave

It is well known that optimal tag reflection corresponds to metallic tags that are at least as thick as the skin depth, or the electrical current depth necessary to completely reflect the EM wave due to the surface AC currents. The skin depth as a function of radio frequency and material conductivity is shown in Figure 3-8.

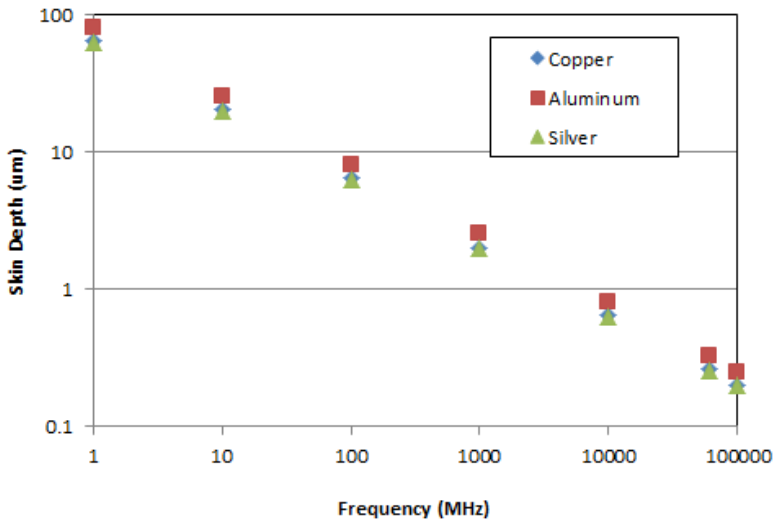

Figure 3-8 Tag frequency vs. skin depth in microns for various materials [95].

Therefore near-field-communications (NFC) tags at 13.6 MHz typically use >20 μm stamped aluminium and whereas UHF antennas (960 MHz) need only 5~10 μm stamped aluminium or plated copper. On mm-wave band 60 GHz, the required thickness reduces to below 1 μm. These processes also insures low AC skin losses due to smooth planar metal film surfaces vs. rough metal surface which can have higher losses [95].

Other methods for printing RFID tag include nano-silver ink printing with post flash cure to solidify metal pigments or thermal film metal transfer printing with post plating. However each of these processes requires additional steps to build up the required optimal metal thickness. This is true, for example, of the Kurz SECOBO® thermal transfer antennas shown in Figure 3-9.

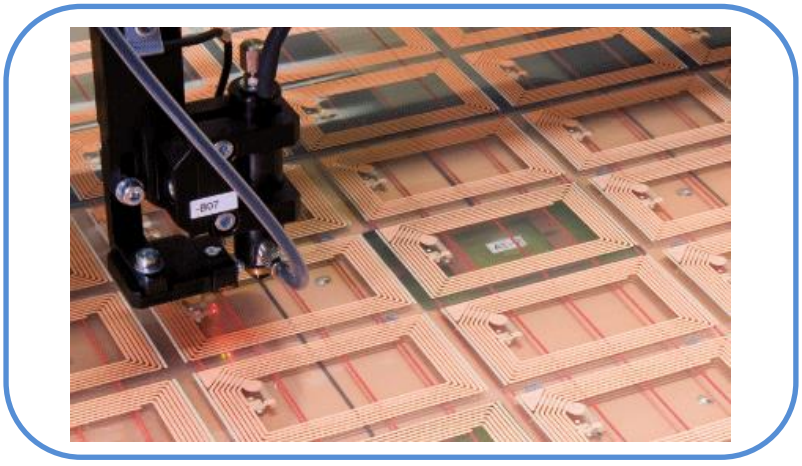

Figure 3-9 Kurz SECOBO® antennas [96].

However as the RFID frequency of operation continues to increase, the required skin depth thickness decreases. Thus from the perspective of the metal film thicknesses necessary for efficient interrogation signal reflection, there are tremendous advantages to utilizing a higher frequencies for chipless RFID operation. Thinner metal RFID antennas mean more viable lower cost tag fabrication techniques such as inkjet and metal foil transfer can be used with greater throughput and yield, though surface roughness also becomes more important at higher frequency owing to high current densities near the surface of the metal tags.

3.3.3 Synthetic aperture radar necessity

Recalling from Section 3.2, the SAR technique proposed for earth imaging applications, as carrying a kilometre sized antenna by an air/space-craft station is impractical. Although in the RFID application, the required antenna size for 1° beamwidth requirement is only 25 cm, Figure 3-6. Therefore, it appears that a single antenna would be sufficient for the required precision scanning of the tag. However, one should note that the calculated beamwidth by (3.3) is only valid for the far field region of the antenna. If the measurement point locates inside the near field, then it is unlikely to expect 1° beamwidth. The far field distance of the antenna with 25 cm aperture size at 60 GHz is 25 m that is far beyond the reading zone of the chipless RFID systems:

$$R_{far\ field} = \frac{2D^2}{\lambda} = \frac{2\times(0.25)^2}{5\times10^{-3}} = 25\,m \qquad (3.4)$$

SAR would provide a solution for this scenario. A small antenna at 60 GHz with short farfield distance is utilised at the reader side. This antenna generates a large beamwidth due to its small physical size and hence is not capable of providing the required scanning precision. However, if the antenna moves around the tag to create a synthetic aperture then the post signal processing results in a narrow beamwidth of 1~5° order depending on the synthetic aperture length.

Therefore it can be concluded that the practical limitation of carrying a kilometre sized antenna necessitates the SAR technique for earth imaging purpose, while the technical limitation of farfield distance mandates the SAR approach for RFID application. This would be similar to a body EM-imaging application. In human body imaging, the usage of a single large antenna with narrow beamwidth is feasible. However, maximum transmission power on

human body is limited due to the regulations. Therefore, a small antenna(s) with low transmission power on the SAR working basis is utilised to meet the regulation requirements and simultaneously provide the required high image resolution.

Finally as the conclusion to Section 3.3, it appears that the scanning of the tag surface in millimetre order at the reading distance of 10-50 cm is technically and practically feasible only at the ISM band 60 GHz and above; 95 GHz for example. However, due to the far field limitation, the synthetic aperture radar technique shall be utilised at the reader side. This means that the relative movement of the reader and tag is an integral part of the proposed theory. However as will be introduced in Chapter 8 of this dissertation, it is possible to combine the multiple input multiple output (MIMO)-based technique with the current proposal to eliminate the physical movement necessity and significantly improve the reading time of the proposed theory [82].

3.4 Tag shaping for unique EM-image purposes

It was discussed that the scanning of the tag surface is technically feasible at mm-wave bands. The next step of maturing the idea of imaging for the RFID application is to design a chipless tag in such a way that the tag obtains a unique EM-image. To shape the tag's surface for creation of a unique EM-image, no component other than paper and conductive ink shall be considered otherwise the tag cost would exceed industry expectations. The unique EM-image of the tag therefore shall be constructed by combining conductive and non-conductive sections on the tag's surface. As the dielectric part has a rougher surface, then the expectation is to have a brighter image than that of the conductive part, based on previous knowledge from the earth imaging application, Figure 3-3. Based on this information, one may suggest a structure similar to a barcode as shown in Figure 3-10. Conductive and non-conductive strips create different levels of reflection on the reader side, hence a unique EM-image would be created with different arrangement of the strips on the tag surface. To examine this idea, two separate conductive and dielectric strips are simulated through 3-D full wave CST software on the 57-64 GHz band as the frequency band of operation. The strips are illuminated by a linearly polarised plane wave and their levels of backscattered signals on the reader side are measured. The results are shown in Figure 3-11 in which the reading distance is 30 cm, the incident electric field is one V/m, and it is parallel to the main axis of the strip. The first interesting aspect of the result is that the reflection from the conductive strip is higher than

that of the dielectric strip which contradicts what was expected from the earth imaging system introduced in Section 3.2. This issue is considered shortly. The second feature of the simulation result is the very close signal level of the two strips type. The difference between two scenarios is less than 3 dBm. This is not a reliable field strength difference especially considering that it is a simulation result. It would be very difficult to separate reflections from conductive and dielectric strips in a real scenario, especially when the clutter and multipath effect of the surrounding objects are considered. Changing the polarisation of the incident E-field does not affect the ratio of the received signal from conductive and dielectric strips.

To find out why a conductive strip reflects more energy than that of the dielectric type, two reasons may be mentioned. First, the illumination angle, the angle between the reader antenna and the tag, is 90° in the current scenario. This means that all of the impinged energy to the conductive strip is reflected back toward the reader according to Snell's law of reflection.

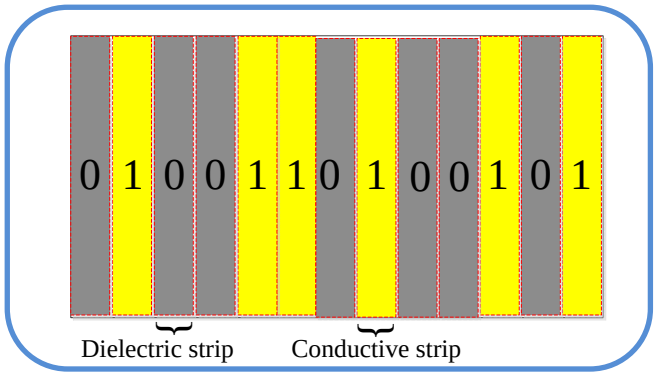

Figure 3-10 Initial proposed tag structure based on earth imaging concept.

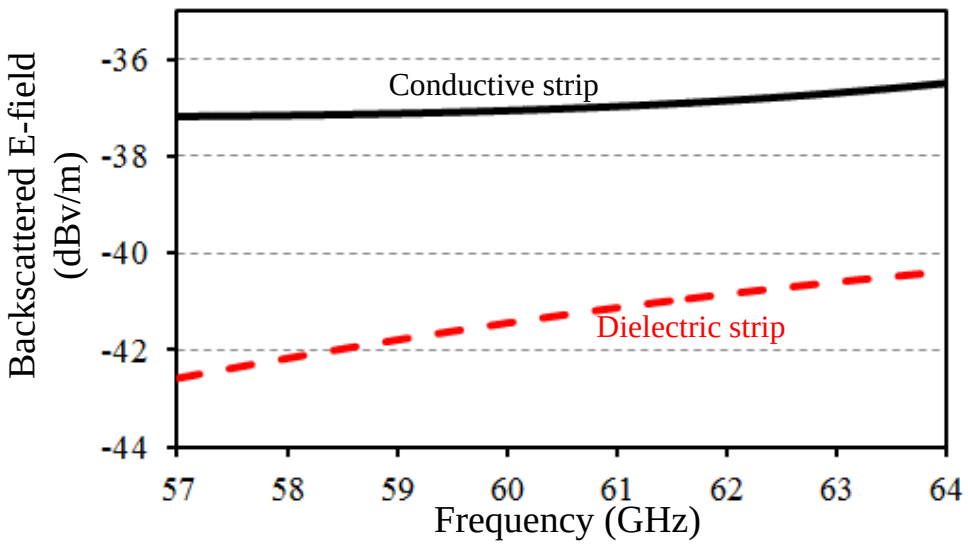

Figure 3-11 Backscattered signals from different types of strips; simulation result.

While for the dielectric surface, some of the incident energy is spread out due to its rougher surface. A squint angle other than 90°, like the earth imaging application, results in higher reflection towards the radar from the rougher surface.

Moreover, in the earth imaging application, the received signal is based on reflection energy only. While in the RFID application, as a short range communication service, the impinging signal induces a surface current on the conductive strip surface which acts as a second source of electromagnetic emission. This causes a higher signal from the conductive strip. These two effects are shown in Figure 3-12. The 90° reading scenario causes higher reflection from the conductive strip towards the reader, as the dielectric strip spreads out some of the energy towards other directions. An incident signal causes an induced current (red arrows) on the conductive strip surface, which act as a second source of energy.

As mentioned before, irrespective of the reason for a higher reflection from the conductive strip than that of the dielectric strip, the difference between the received signal strengths is not on a level that ensures a reliable reading process in a practical sense, due to the clutter and multipath interferences.

While it appears that the signal level approach similar to the earth imaging application is not able to provide a reliable way for imaging purposes, the unique behaviour of a conductive strip suggests an interesting algorithm for data encoding on the tag surface. This is discussed in the next section.

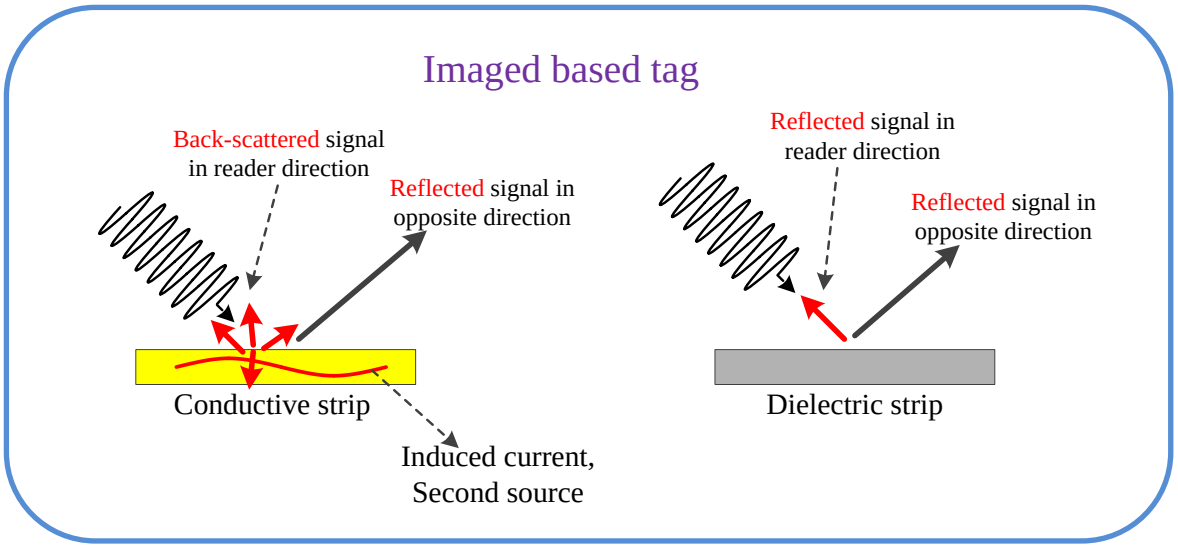

Figure 3-12 Reflection scenario in RFID tag.

3.4.1 Strip line as an EM-polariser

In the previous work described in Section 3.2, the main goal was to measure the received signal level based on various illumination angles and polarisation schemes from different strip types. Although working on the basis of a different received signal level did not provide a reliable approach for the data encoding algorithm on a chipless tag structure, a very interesting phenomenon was observed during the simulation. It was noticed that the backscattered signal from a narrow conductive strip shows elliptical polarisation behaviour while the strip is illuminated by a linearly polarised signal. This means that the conductive strip is capable of changing the polarisation of the incident signal. This issue has been considered more seriously aiming for possible application in the chipless RFID system. It was found that for a narrow conductive strip, the backscattered signal may include a polarisation component that is orthogonal to the polarisation of the incident signal, hence the conductive strip acts as an EM-polariser. The de-polarisation aspect of the conductive strip suggests working on a cross-polar basis instead of a co-polar basis, which most conventional techniques are. This provides significant superiority as a cross-polar working basis may eliminate or severely reduce noise, clutter and multipath effects on the system performance. Those factors are normally a significant concern in RFID systems and are considered the main limiting features. The theory behind this unusual behaviour of the conductive strip as an EM-polariser, is discussed here and the potential advantages and applications are considered in more detail in the next chapters.

3.4.1.1 Diffraction, Kobayashi potentials

Different phenomena are involved when a conductive strip is illuminated by an EM-signal, for instance, reflection, refraction and diffraction. As a strip has a finite surface with straight edges, it can behave differently based on the polarisation and frequency of the incident wave as well as strip size and its orientation. Reflection based on Snell's law is the normal behaviour that is expected for a wide strip, compared to the wavelength. However, when the strip is narrow enough, diffraction would be of more concern and act as the dominant phenomenon. In prior decades, many studies investigated diffraction from a metallic strip or a slot in a metal plane using various numerical and analytical techniques [97-104]. All research and studies on diffraction can be summarised as follows [105]:

- Geometric Optics (GO) [98]
- Physical Optic (PO) [99]
- Geometrical Theory of Diffraction (GTD) [100]
- Uniform Asymptotic Theory of Diffraction (UAD) [101]
- Uniform Theory of Diffraction (UTD) [100]
- Physical Theory of Diffraction (PTD) [102]
- Spectral Theory of Diffraction (STD) [103]
- Method of Equivalent Current (MEC) [104]
- Hybrid methods

Each method has its own advantages and limitations. Among them, geometrical optics (GO), physical optics (PO), and uniform theory of diffraction (UTD) are the most common approaches. The Kobayashi potential (KP) method is an analytico-numerical technique used as an alternative to previously mentioned techniques with more accurate results and less procedure complexity [106]. Diffraction by a conductive strip on a dielectric slab has been thoroughly studied as a title of PhD thesis by Imran [107]. He formulated the far field pattern and induced surface current on an infinite strip etched to a dielectric slab based on the polarisation of the incident plane wave. This sub-section is a snap shot of his work related to the current research.

Figure 3-13 shows the geometry of the diffraction phenomenon where a conductive strip with negligible thickness etched on a dielectric slab is illuminated with a plane wave. The plane wave incident angle is Φ_0. The strip width is $2a$ and it is infinite in z direction. The diffracted wave depends on the polarisation of the plane wave. Two separate polarisations are considered: *(i)* Parallel-polarisation, $E = E_0 a_z$, and *(ii)* Orthogonal-polarisation, $E = E_0 a_x$.

In the parallel polarisation, the incident E-field is parallel to the main axis of the strip, the backscattered signal may have components in x or z direction. The co-polar and cross-polar components are defined by (3.5) and (3.6) respectively [107]:

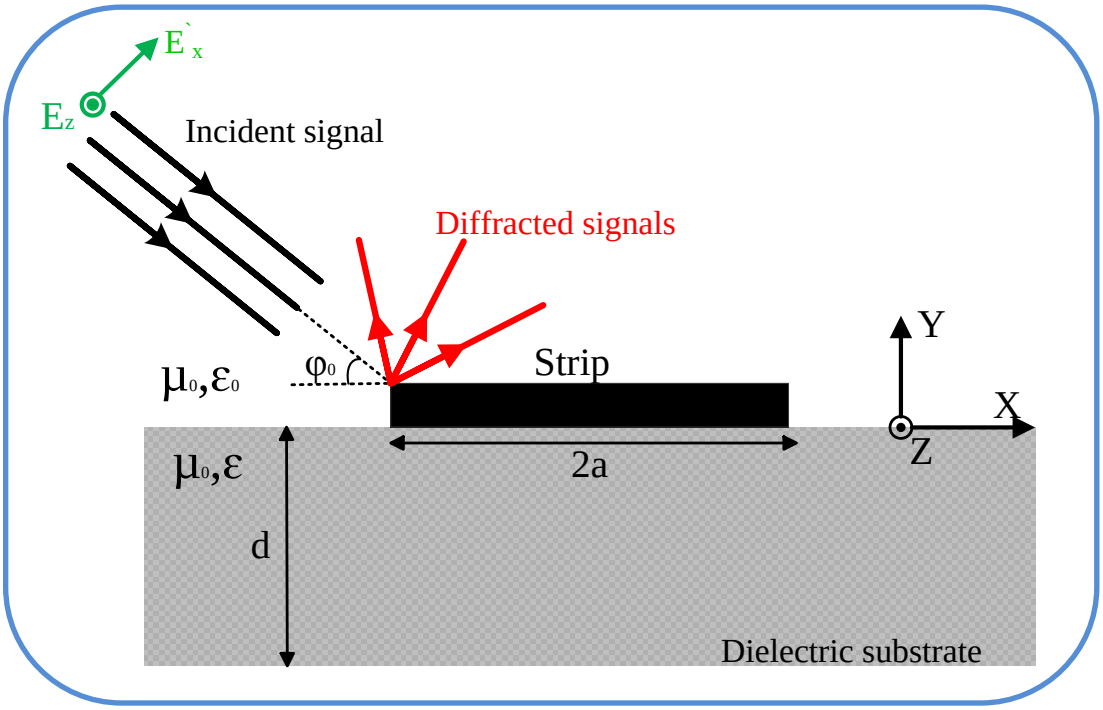

Figure 3-13 Geometry of diffraction by conductive strip on dielectric slab.

$$E_z^d \approx \sqrt{\frac{\pi}{2k_0\rho}} exp[-jk_0\rho - j\frac{\pi}{4}] \sum_{m=0}^{\infty} [A_m J_{2m}(k_0 cos\phi) + jB_m J_{2m+1}(k_0 cos\phi)] tan\phi \quad (3.5)$$

$$H_z^d \approx \sqrt{\frac{\pi}{2k_0\rho}} exp[-jk_0\rho - j\frac{\pi}{4}] \sum_{m=0}^{\infty} [C_m J_{2m}(k_0 cos\phi) + jD_m J_{2m+1}(k_0 cos\phi)] tan\phi \quad (3.6)$$

In the orthogonal polarisation, in which the incident E-field is orthogonal to the polarisation of the strip main axis, the co-polar and cross-polar components are found from (3.7) and (3.8) respectively:

$$H_z^d \approx \sqrt{\frac{\pi}{2k_0\rho}} exp[-jk_0\rho + j\frac{\pi}{4}] \sum_{m=0}^{\infty} [C_m J_{2m+1}(k_0 cos\phi) + jD_m J_{2m+2}(k_0 cos\phi)] tan\phi \quad (3.7)$$

$$E_z^d \approx \sqrt{\frac{\pi}{2k_0\rho}} exp[-jk_0\rho + j\frac{\pi}{4}] \sum_{m=0}^{\infty} [A_m J_{2m+1}(k_0 cos\phi) + jB_m J_{2m+2}(k_0 cos\phi)] tan\phi \quad (3.8)$$

In the above expressions, J_m is the Bessel function, (φ,ρ) is the coordinate of the observation point and $k_0 = a.\omega\sqrt{\mu_0.\varepsilon_0}$ is the normalised wave number. A_m, B_m, C_m and D_m are the expansion coefficients and should be found separately by numerical approaches and through the following expressions [107]:

$$\sum_{m=0}^{\infty}[G(2m,2n;k_0)][C_m + MA_m] = -M[J_{2n}(k_0\cos\phi_0)] \tag{3.9}$$

$$\sum_{m=0}^{\infty}[G(2m+1,2n+1;k_0)][D_m + MB_m] = -Mj[J_{2n+1}(k_0\cos\phi_0)] \tag{3.10}$$

$$\sum_{m=0}^{\infty}[H(2m,2n+1;k_0)][A_m - MC_mZ_0^2] = j\tan(\phi_0)[J_{2n+1}(k_0\cos\phi_0)] \tag{3.11}$$

$$\sum_{m=0}^{\infty}[H(2m+1,2n+2;k_0)][B_m - MD_mZ_0^2] = -\tan(\phi_0)[J_{2n+2}(k_0\cos\phi_0)] \tag{3.12}$$

where $n = 0, 1, 2, \ldots,$ M is the admittance parameter and

$$G(\alpha,\beta;k_0) = \int_0^{\infty}\frac{J_\alpha(\xi).J_\beta(\xi)}{\sqrt{\xi^2 - k_0^2}}d\xi$$
$$H(\alpha,\beta;k_0) = \int_0^{\infty}\frac{J_\alpha(\xi).J_\beta(\xi)}{\xi}d\xi \tag{3.13}$$

A comprehensive derivations of the above expressions based on the different values of the parameters has been provided in [107]. Among these results, the relation between the strip width and the cross-polar component is the concern of the current application. It is shown in [107] that the normalised wave number affects the strength of the cross-polar components of the diffracted signal. Moreover, the cross-polar component is also dependent on the angle of observation. For a certain value of the normalised wave number, that is relevant to the strip width, the maximum cross-polar component is achievable over a wide range of observation angles. The co-polar and cross-polar components of the diffracted signal are figuratively shown in Figure 3-14 that proves that a well-designed strip is capable of creating a cross-polar component while illuminated by a linear polarised incident signal.

This is a significant result of the diffraction effect. It simply means that for a certain strip with adequate dimensions, it is possible to expect cross-polar components in the backscattered signal with respect to the incident wave. Hence, the simple structure of a strip line acts as an effective EM-polariser. This interesting aspect of the diffraction is used on the current research for providing an effective data encoding algorithm in a chipless tag. Therefore, one may recall that diffraction was the main issue in the barcode system as it limits the barcodes data encoding capacity and its reading range. In contrary, the proposed approach of EM-imaging in chipless RFID system is fully based on the diffraction effect.

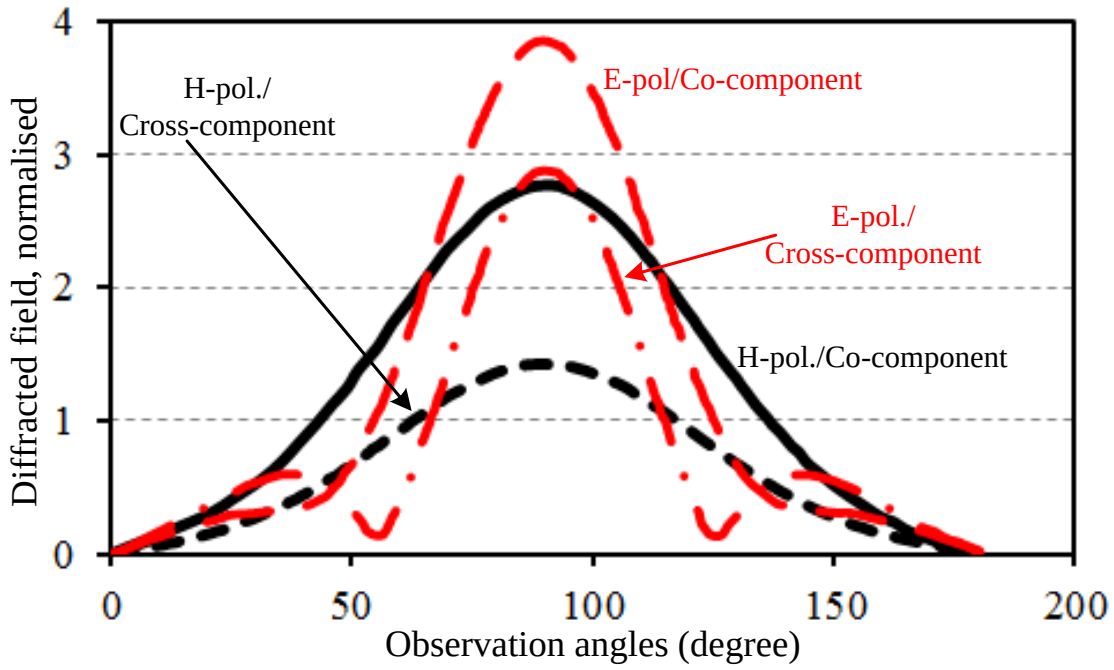

Figure 3-14 Co- and cross-polar components of diffracted signals, linear scale.

3.4.1.2 Cross-polarised resonance

In the previous section, the cross-component of the backscattered signal from a narrow strip with infinite length due to the diffraction effect has been discussed. This simply means that diffracted signal by the strip edge creates a cross-polar component. Moreover, due to the diffraction effect, it is also possible to maximise the backscattered cross-polar component by utilising the resonance behaviour of the strip structure. In a real scenario, the strip has a finite length, hence it is possible to design the length of the strip to resonate at a particular frequency. Maximising the backscattered cross-component, one may suggest orienting the strip at 45˚ angle with respect to the incident plane wave. This causes the induced current on the strip surface, as a secondary source of EM-wave, to emit signals in both co- and cross-polar directions as shown in Figure 3-15. It is important to note that in this scenario, the length of the strip plays the major role while in diffraction phenomenon, the strip width was the main concern.

The strip line shown in Figure 3-15 is simulated as an E-polariser through full wave EM solver CST microwave studio. The strip is illuminated with a linearly polarised plane wave while the incident E-field maintains a 45˚ angle with the strip axis. Two E-field probes are oriented at a certain distance, 30 cm for example, to measure the backscattered signal

components at co- and cross-polar directions. The results of the simulation for backscattered fields vs frequency are shown in Figure 3-16. The cross-polar component of the backscattered E-field shows peak and the co-polar component shows null at the resonant frequency. This is due to the fact that at co-polar direction, both the antenna (resonant) mode and the structural mode RCS are dominant and cancel each other [46]. Contrary to that in cross-polar direction, only the resonant mode is dominant hence cross-polar component shows a peak value. This cross-polar component is immune to co-polar structural mode, and ambient noises and interferences. This is the main advantage of the EM-imaging chipless RFID tag. As is clear from the figure, in a certain band depending on the strip length, the cross-polar component is significant and hence the strip line can be considered as an effective EM-polariser at a certain frequency band.

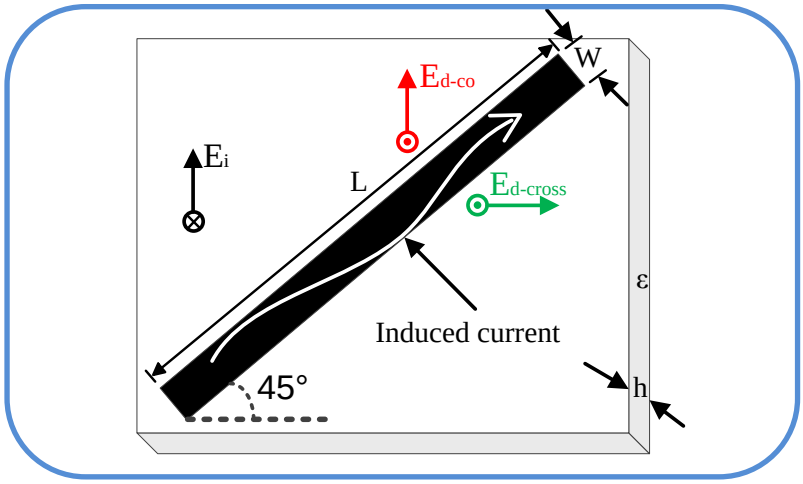

Figure 3-15 Strip orientation for creating cross-polar component, L= 1.45, w= 0.2, ε= 2.55, h=0.0127, all in mm.

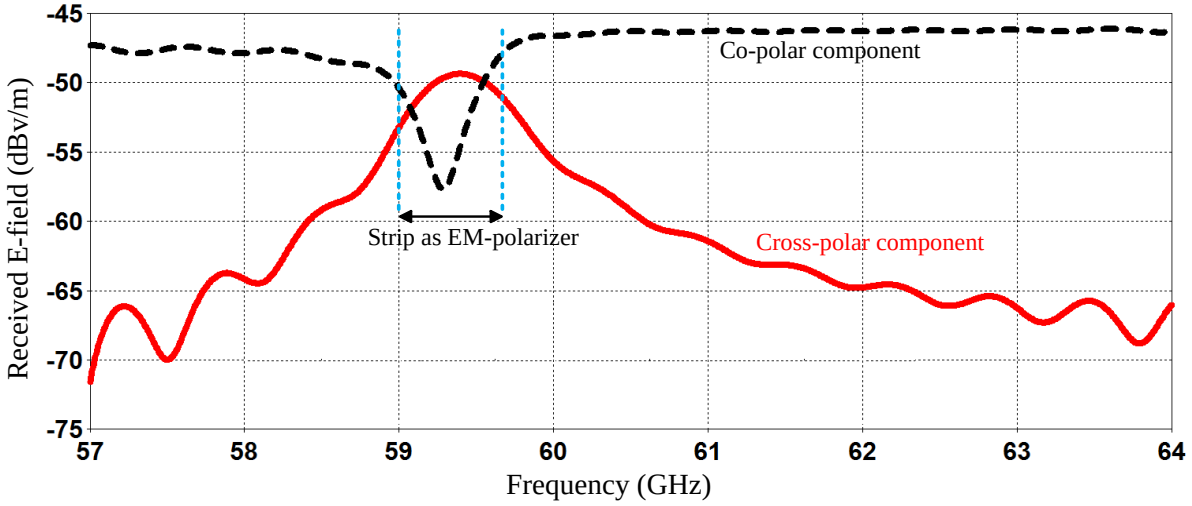

Figure 3-16 Simulated co/cross-polar components of backscattered signal, single stripline , L= 1.45, w= 0.2, ε= 2.55, h=0.0127, all in mm.

3.4.1.3 Multiple strips effect

It will be shown soon that to accommodate the required RCS power level at the receiver side, it is required to utilise more than one strip line or any other polariser on the tag surface. This is almost mandatory for satisfying the signal to noise ratio (SNR). Therefore, it is important to explore the effect of multiple strip lines on the backscattered signal.

A. Multiple strips with the same dimension

If an accurate and precise fabrication process is utilised for tag manufacturing, then it is reasonable to expect that all the strip lines have exactly the same dimensions. Obviously, if the strip lines are the same length and width, then a similar response to what is shown in Figure 3-16, with a higher received E-field level, is expected. To validate this expectation, five strip lines with the same dimension are placed near to each other (one mm distance). The simulated co- and cross-polar backscattered E-fields are shown in Figure 3-17. Comparing Figure 3-16 and Figure 3-17, one notices the followings phenomena:

i) Resonance frequency shifts from 59.5 GHz to 58.2 GHz, about 1.3 GHz.

ii) Resonance bandwidth spread from 0.7 to one GHz.

iii) Amplitude of the backscattered signal increases by approximately 6.5 dB from -49 dB/m to -42.5 dB/m. This is approximately five times ($10 \times \log 5 = 7$ dB) amplification as expected.

Both *i)* and *ii)* can be related to the coupling among strips as they were placed very close to each other (one mm). This means that Figure 3-17 is not simply a multiplication of Figure 3-16. However, the initial expectation on the received power level has been almost confirmed.

B. Multiple strips with slightly different lengths

In the previous section, the effect of multiple strips with the same dimension has been considered. It is very important to explore the behaviour of the received signal on co- and cross-polar directions if strips have slightly different dimensions; lengths for example. Shortly, the importance of this case is realised when the tag is printed by an ink-jet printer. The printed strip lines do not have exactly the same length because of printing inaccuracy.

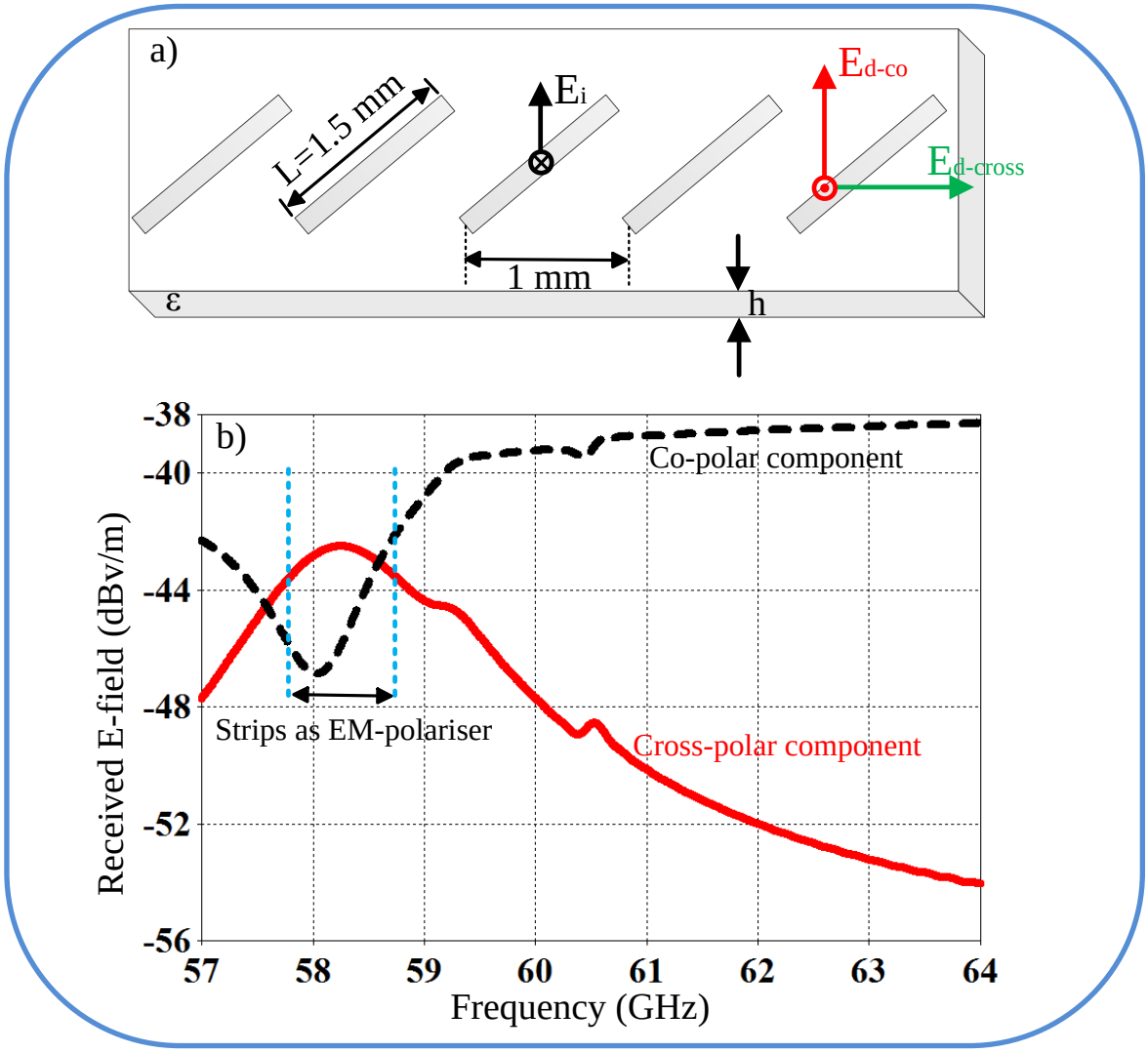

Figure 3-17 a) Five strip lines with same length, b) Simulated co/cross-polar backscattered signals**.**

To simulate this case, multiple strips with slightly different lengths are considered while they are again placed close (one mm) to each other. Five strip lines, whose lengths vary from 1.6 to 1.7 mm, are considered. Figure 3-18 shows the simulation results of the backscattered fields and for ease of comparison, the result of a single strip is also reproduced in this figure. It is clear from Figure 3-18 that the RCS response from multiple strips with different lengths does not show any resonance behaviour. There are some fluctuations on the received signal level, but detection of the resonances is very difficult if not impossible. The co-polar component of the E-field is 5-10 dB higher than that of the cross-polar component. Irrespective of higher co-polar level, the proposed system is a cross-polar system. The advantages of the cross-polar based technique are revealed during the measurement process.

In conclusion, one may notice that the strip line polariser, if designed and oriented properly with respect to the incident filed, can act as an effective EM-polariser on a certain frequency band. This simply means that the strip line is capable of rotating the polarisation of the incident linearly polarised wave to the orthogonal direction when the signal is backscattered by the strip. However, if multiple strips with slightly different dimensions are utilised, then no resonance behaviour can be detected in their backscattered signal, while they are still capable of creating a significant cross-polar component at the backscattered direction over a relatively wide frequency band of operation. Therefore, it can be concluded that proposed EM-image based chipless RFID tag is an RCS level based not a resonant frequency based device. The image of the tag is constructed from the cross-polar RCS level of the tag. The next section, presents the meander line polariser as an effective unit element of the proposed EM-image based chipless RFID tag.

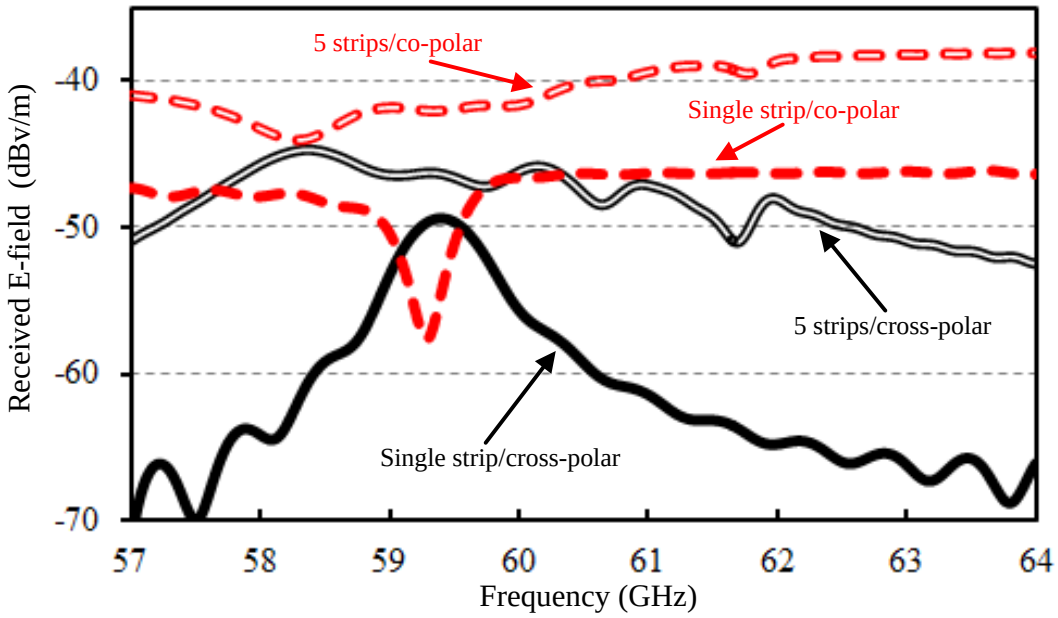

Figure 3-18 Simulated co/cross-polar components of backscattered signal.

3.4.2 Meander line: a new EM-polariser

A meander line polariser consists of at least one layer of meander line shaped conductors, usually printed on a circuit board [108]. A plane wave with 45° incident angle with respect to the principal axis of the meaner line, illuminates the structure as shown in Figure 3-19. The incident field can be decomposed into the vertical and horizontal components. Each component experiences different phase shifts in such a way that the phase shift difference

should be 90°, but their amplitude remains equal. As a result, the combined field in the transmitted signal is a circular polarised wave, and therefore the component is called transmission EM-polariser [108], see Figure 3-19.

Normally three to four layers of meander lines are required to create a complete circularly polarised transmission signal [108-110]. A transmission meander line polariser is also acts in the reverse direction and can convert a circular polarised wave (CP) to a linear type signal. This type meander line structure is widely used in satellite communications [111, 112].

Though, in the proposed application of the chipless RFID system, a reflection EM-polariser is required as the reader normally measures the backscattered signal of the tag. A possible solution for a reflection EM-polariser structure based on the meander line structure is shown in Figure 3-20. The structure utilises multi-layer meander lines with a ground reflector.

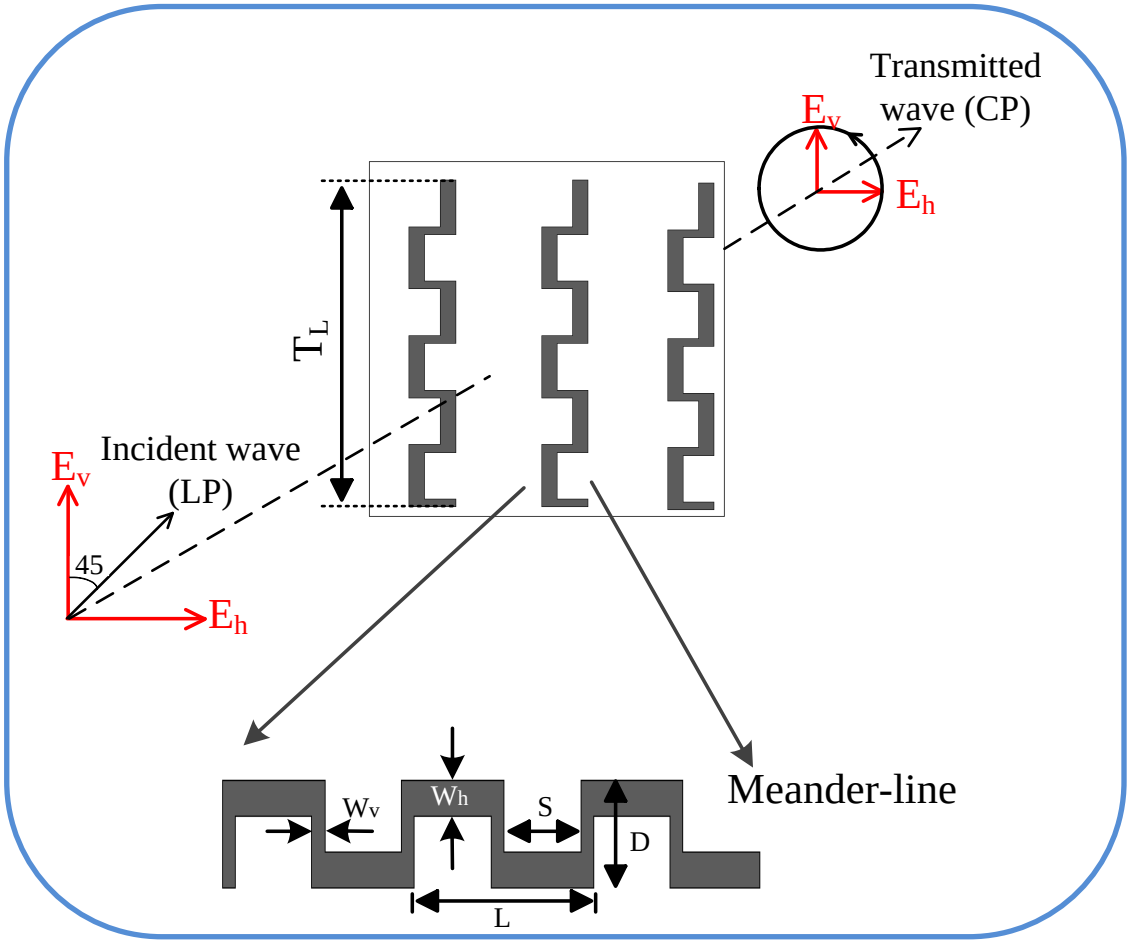

Figure 3-19 Meander line as transmission EM-polariser.

The linearly polarised incident wave (E_i) is converted to a circular polarisation wave while passing the multi-layer meander line structure. For the x-polarised incident signal shown in Figure 3-20, the passed signal from the meander line structure is a left hand circular polarised (LHCP) wave, for example. This wave is completely reflected back by the ground plane while its rotation direction will be reversed. Hence the new wave with right hand circular polarisation (RHCP) is inserted in the multi-layer meander line structure. This signal is converted to a linear polarised wave as the meander line changes the input circular polarised (CP) signal to a linearly polarised (LP) wave. However, the E-field of the final reflected wave (E_r) is orthogonal to the direction of the E-field of the original incident wave (E_i). Hence the goal of the meander line as a reflection EM-polariser is achieved.

While the proposed approach of the multi-layer meander line with a ground plane reflector is technically appropriate for the proposed application of the chipless RFID system, it would not be a suitable solution for RFID tag structure. The multi-layer structure of the tag contradicts the expected sub cent tag cost that is only addressed through a single layer printable tag structure. Therefore, to propose a single layer structure, the meander line dimensions have been re-designed based on a diffraction and resonance principles similar to those for strip line polariser as introduced in Section 3.4.1. Hence, only one layer meander line is utilised with no ground plane. This means that the parameters of the meander line structure as shown in Figure 3-19 are designed to maximize the cross-polar component of the backscattered signal. Similar to the case of the strip line, again both diffraction and resonance behavior of the meander line are utilised simultaneously for the maximum cross-polar component. The expectation is to achieve better performance from the meander line due to the increased design freedom. While the strip line has mainly two design parameters: strip width and length, in the meander line polariser there are more design parameters: W_h, W_v, D, S and L that provides more design flexibility, see Figure 3-19.

A single layer meander line is designed through parameter optimisation in CST aiming to provide the highest cross-polar component backscattered RCS. The structure is assumed to have the same length that for the strip line for comparison purposes. The simulation result is shown in Figure 3-21 while the parameter of the design for the strip line and meander line are as follows:

For the strip line: T_L = 1.6 , α =0.2

For the meander line: T_L = 1.6, W_h = 0.2, W_v = 0.1, D = 0.37, L = 0.5 (all values in mm), and ε_r = 2.55

It is clear from Figure 3-21 that the meander line cross-polar component acquires sharper resonance for the same polariser length (T_L=1.6 mm). Moreover, the cross-polar E-field component of the meander line is 2-3 dB higher than that of the strip line. This equals to five dB more received power level. The higher cross-polar component sets freedom on the reading distance and better signal to noise ratio (SNR) of the system.

The effect of the multiple meander lines structure is not considered as addressed for the strip lines. The reason is disclosed in the next chapter when the printed version of the meander line is being considered as the multi-bit chipless RFID tag. However, it can be generally said that a printed meander line experiences significant shape anomalies due to printing inaccuracy. This causes a lack of resonance behaviour in the RCS response, similar to what was shown for multiple strip lines in Figure 3-18.

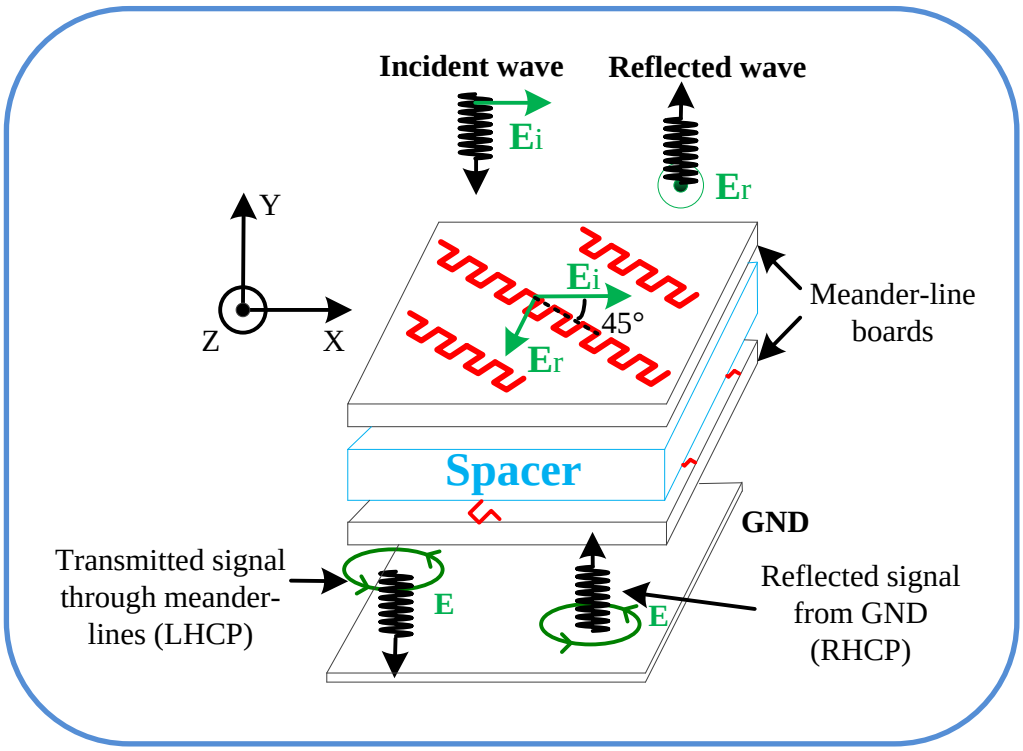

Figure 3-20 Multi-layer meander line structure for reflection EM-polariser.

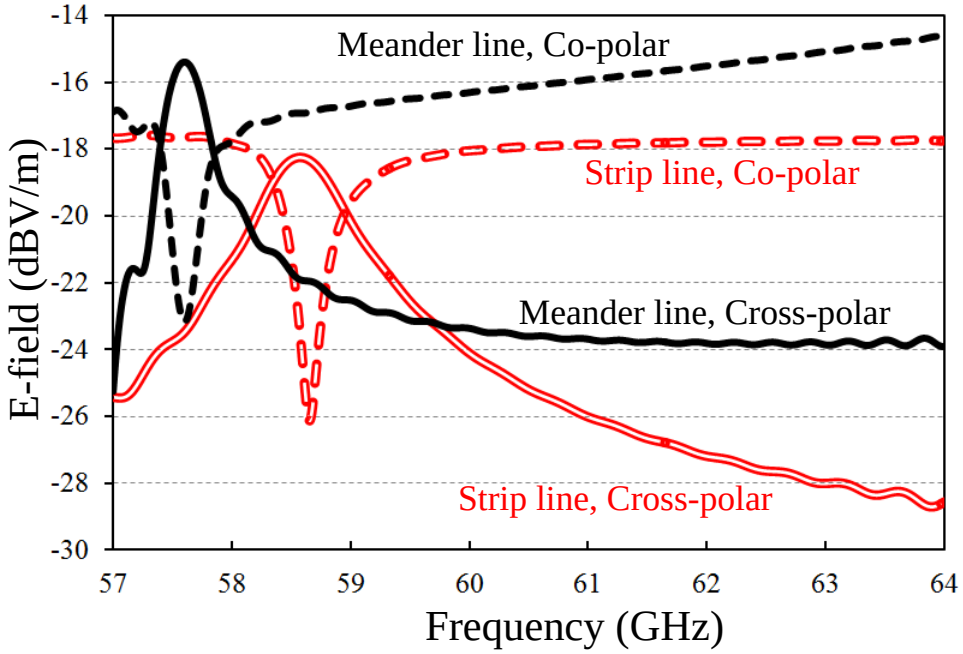

Figure 3-21 Simulated co/cross-polar component of single layer stripline and meander line structure.

3.5 Conclusion

In this chapter the EM-imaging has been proposed as an alternative technique to the current available data encoding approaches. In contrary to the conventional approaches which the tag's surface is interrogated once and the encoded data is then retrieved, it was proposed to utilise the EM-imaging technique to scan every small section of the tag surface sequentially. Then the effect of each section is used to reconstruct the tag's image which reveals its encoded data. Two questions related to this idea were how to precisely scan the tag surface and then how to encode data in a small section of the tag.

In the first part of the chapter, precisely scanning the tag in millimetre order was considered. It was shown that through wise selection of the frequency band, the precise scanning is possible at the normal reading distance of the chipless RFID system. The mm-wave band of 60 GHz and above was proposed for this purpose. The general situation of the unlicensed 60 GHz band has been reviewed from a technical and regulatory perspective. The low regulatory

restrictions on the EIRP of this band have been highlighted that makes the band very suitable for the proposed technique.

Earth imaging applications were considered in detail as the most important application of the EM-imaging. The similarities and differences between earth imaging and the RFID application have been considered. It was shown that the working basis of the reflected signal level that is used for earth imaging is not appropriate for the RFID application due to the low differences between reflection from conductive and non-conductive parts of the tag surface. Then the idea of polarisation rotation through a narrow conductive strip has been proposed that provides a new approach for EM-imaging of the tag. The strip line as an EM-polariser has been tested through simulation results. Moreover, the effect of multiple strips and strips with slightly different lengths were also considered. Those results are useful when the measurement result of the strip line is considered in the next chapter.

The meander line as a transmission EM-polariser was considered. The multi-layer structure of the meander lines was introduced and proposed as a reflective EM-polariser. The idea of the multi-layer structure was rejected as it contradicts with the targeted tag cost of below 1¢ in the proposed application of the RFID systems. Then the meander line was re-designed on a single layer structure without any ground plane. The meander line was simulated shows sharper and higher cross-polar components than those for the strip line. The strip line and meander line suggest a reliable approach to shape the tag' surface in a way that the tag's EM-image would be unique. Therefore, it can be concluded that this chapter proves that the EM-imaging of the tag is technically possible at 60 GHz mm-wave band and higher frequencies. Moreover, it reveals a new way for shaping the tag surface for a unique EM-image purpose through the printed EM-polarisers of the strip and meander lines.

Chapter 4 Practical data encoding EM-polariser

4.1 Introduction

In the preceding chapter, EM-imaging for chipless RFID tag has been introduced. It was shown that through EM-imaging techniques, scanning of the small section of the tag surface for data retrieving purpose is possible at the mm-wave frequency bands of 60 GHz and higher frequency bands. Synthetic aperture radar technique as a powerful imaging approach was suggested for RFID applications. The theories of EM-polarisers in the form of strip line and meander line as practical and effective unit cells of data encoding device have been presented. The working basis of these EM-polarisers has been presented in terms of their backscattered cross-polar components. The simulation results confirmed the behaviour of the strip line and meander line EM-polarisers as the basic structure for data encoding elements for the proposed image based chipless RFID tag.

This chapter considers the fabrication process of the introduced polarisers. The polariser-based tag is fabricated through an accurate photolithographic process on a dielectric structure. Then the same tag structure, strip line and meander line polarisers, are printed with a SATO inkjet printer that utilises conductive ink on a paper substrate. These two tag samples, through different fabrication processes are carefully investigated by an electronic microscope regarding their precise dimensions and shapes. It is shown that the printed sample suffers severely from shape anomalies and changes in dimensions due to the printing resolution of the SATO printer.

Then the fabricated tags, through a photolithographic process and printed tags with SATO printer, are measured with real antennas to explore the actual performance of the designed EM-polarisers. While the precisely fabricated tags show almost the same performance as expected through simulation in Chapter 3, the printed samples lost all their resonance behaviour. This is, however, in agreement with the simulation results of the multiple strip lines with slightly different dimensions in Chapter 3. Then the possible data encoding algorithm based on the measurement results for both tags prototype are discussed. Finally the appropriate data encoding approaches suitable for the commercial use of the proposed image-based technique, the printed tag, are considered. This step matures the proposed technique for real world applications and it provides the appropriate ground for further research and work in the rest of this thesis.

4.2 Tag fabrication

Two stripline and meander line EM-polarisers were designed in Chapter 3 and working on the frequency band 57-64 GHz. These two designs and the related parameters are shown in Figure 4-1. Designs are based on Taconic TLX-8 with ε_r =2.55 and thickness 0.127 mm. As can be seen, the design accuracy is 0.05 mm. The total length of each polariser is around 1.6 mm. It is possible to fabricate a single polariser, however, the expected received power shall be considered. As discussed in Section 3.3.1.1, the band 57-64 GHz is an ISM band with generous permitted radiated power compared with other lower ISM bands. The maximum EIRP at this frequency band is around 40 dBm in most the countries [31, 113] as presented earlier in Table 3-2.

By assuming 10 dB average gain of the reader antenna, the input power to the transmitter can be up to 30 dBm or equivalent to one watt. This provides noticeable reading range for short range radio communication services including chipless RFID systems. In the measurement process, the performance network analyser (PNA) Agilent E8361A is used due to the lack of individual transmit and receive module on 60 GHz band at the Monash Microwave, Antennas, RFID and Sensors (MMARS) laboratory. The maximum transmit power of the PNA is limited to -5 dBm at the 60 GHz band meaning the total EIRP of 5 dBm by assuming 10 dB antenna gain. To compensate this practical power limitation, more than one polariser is used to provide the minimum reading range of 10~15 cm. Therefore, in all of the measurement processes in this chapter onward, an array of five vertical polarisers are used to create enough RCS at the reader side as shown in Figure 4-2.

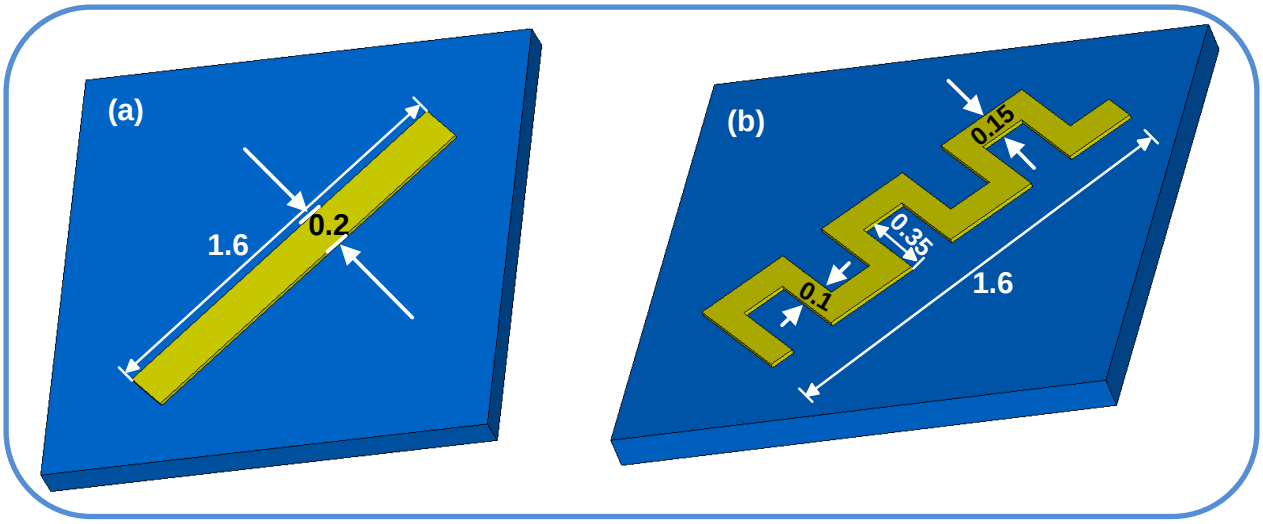

Figure 4-1 (a) Strip line polariser, (b) Meander line polariser; all values are in mm.

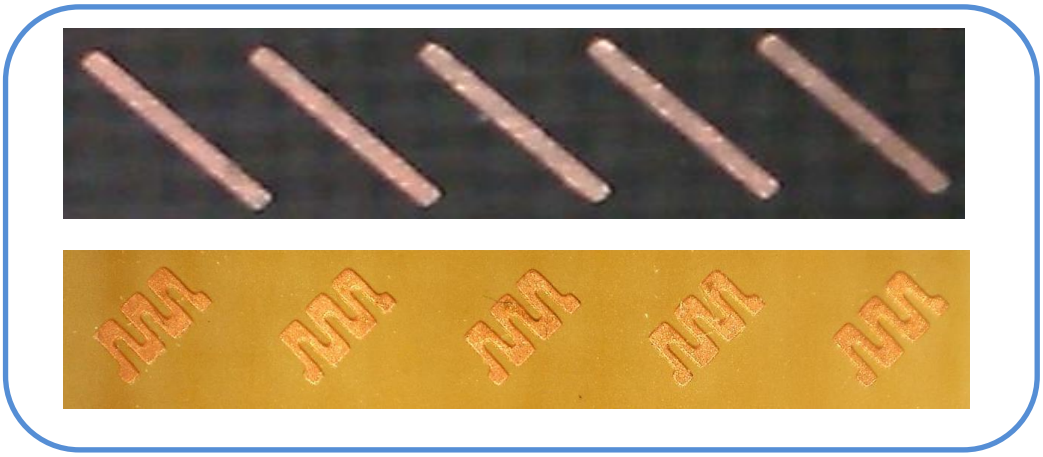

Figure 4-2 Fabricated EM-polarisers through photolithographic process.

4.2.1 Photolithographic fabrication process

The designed polarisers, strip line and meander line, are fabricated through a photolithographic process. The conductive part is the annealed copper and dielectric is the Taconic TLX-8 with ε_r = 2.55 and thickness 0.127 mm. The photographs of these two polarisers are shown in Figure 4-2.

4.2.2 Printing process

It was thoroughly discussed in previous chapters that any suggestion for chipless RFID systems shall be based on the printed tag structure. Otherwise, obtained results based on perfect materials and costly fabrication processes does not guarantee the successful performance of any proposed approach at the commercial stage. This is the most significant phase of the research field in the chipless RFID systems. Many techniques and ideas have been proposed in this area of research. Some show satisfactory achievement at early stage of the research. However, no further deployment of them has been seen in the market only due to a significant performance reduction based on the printed tag structure.

To evaluate performance of the proposed image-based approach for the chipless RFID applications, the polariser-based tag is printed by a SATO GL4e industrial thermal silver ink based printer with a 600 dpi resolution [114]. SATO uses aluminum-based ink as the conductor and normal paper is utilised as the substrate.

Figure 4-3 SATO printer used for tag printing purpose.

Figure 4-3 shows the printer itself and the photograph of the printed polarisers are shown in Figure 4-4. For the strip lines, the final lengths of the printed lines are measured with an electronic microscope and the values are shown in the figure. While the designed lines are exactly 1.6 mm in length, the actual lengths which were printed are different. A tag with comprises of multiple strip lines with slightly different lengths have been previously considered in the simulation step of Chapter 3. Now one may notice the reason for that simulation. Actually it was simulated the real situation of the strip line based tags when printed through a cheap SATO printer device. For the meander line case, the final dimensions are not measured due to the large number of design parameters for each meander line. Instead, the micrograph of a printed meander line is shown in Figure 4-4, which clearly shows the anomalies occurring during the printing process.

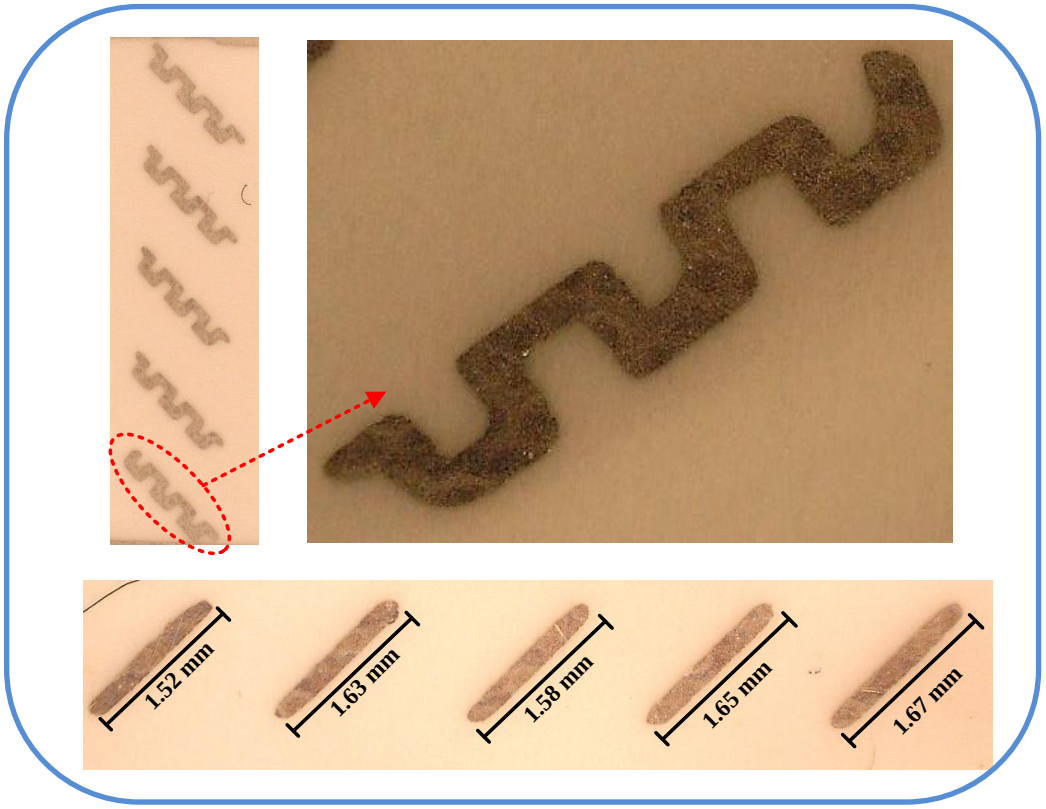

Figure 4-4 Printed meander line and strip line tags.

4.3 Measurement and results

This section shows the measurement results of two tags prototypes through different fabrication process. First, the experimental set-up is discussed. This set-up is almost fixed in all measurements of this thesis to provide a common base for ease of comparisons. Then, the performance of a precisely fabricated tag through PCB process is presented. Finally, a printed tag with SATO printer is tested.

4.3.1 Experimental set-up

The system set-up for the measurement process is shown in Figure 4-5. On the reader side, two antennas are used. Antennas are double side printed dipoles (DSPD) that have been designed to cover the whole frequency band 57-64 GHz. They are very small, which is suitable for the SAR application due to the requirement of physical movement. The main aspects of the antennas are their high axial ratios or equivalently low cross-polar level. This is vital for the cross-polar based system. Moreover, antennas have wide azimuth beamwidth that

is required to interrogate the tag surface from different angles. The design parameters and procedures of the antenna is discussed in Chapter 6 of this dissertation. For measurement purposes, antennas are oriented orthogonally and they are connected to the PNA. Considering the low cross-polar level of the designed antennas and their orthogonal orientation, a very low signal leakage between transmit (Tx) and receive (Rx) antenna is expected. The Tx antenna transmits a vertically polarised wave and the Rx antenna picks up the signal in horizontal polarisation. A plastic pole is installed in front of the antennas on which the tag is attached. The PNA's transmit power is -5 dBm that is its maximum power at the mm-band 60 GHz. Due to the limitation of the PNA transmit power, the reading distance is set to 10 cm. It will be shown in Chapter 6 that the average gain of the antenna is 5.5.-7 dB_i, hence the maximum EIRP used in this measurement set up is only +0.5~2 dB_m. Considering the maximum allowable EIRP of +40 dB_m based on the regulatory standards, hence the reading distance in the proposed technique would increase up to 50 cm if adequate transmitter is available. Also as mentioned before, 5 polarisers are assumed at the tag surface to create enough backscattered power at the receive (Rx) antenna. The PNA measures the S_{21} versus frequency of the system, hence cross-RCS of the tag in dB_m versus frequency is shown by the PNA.

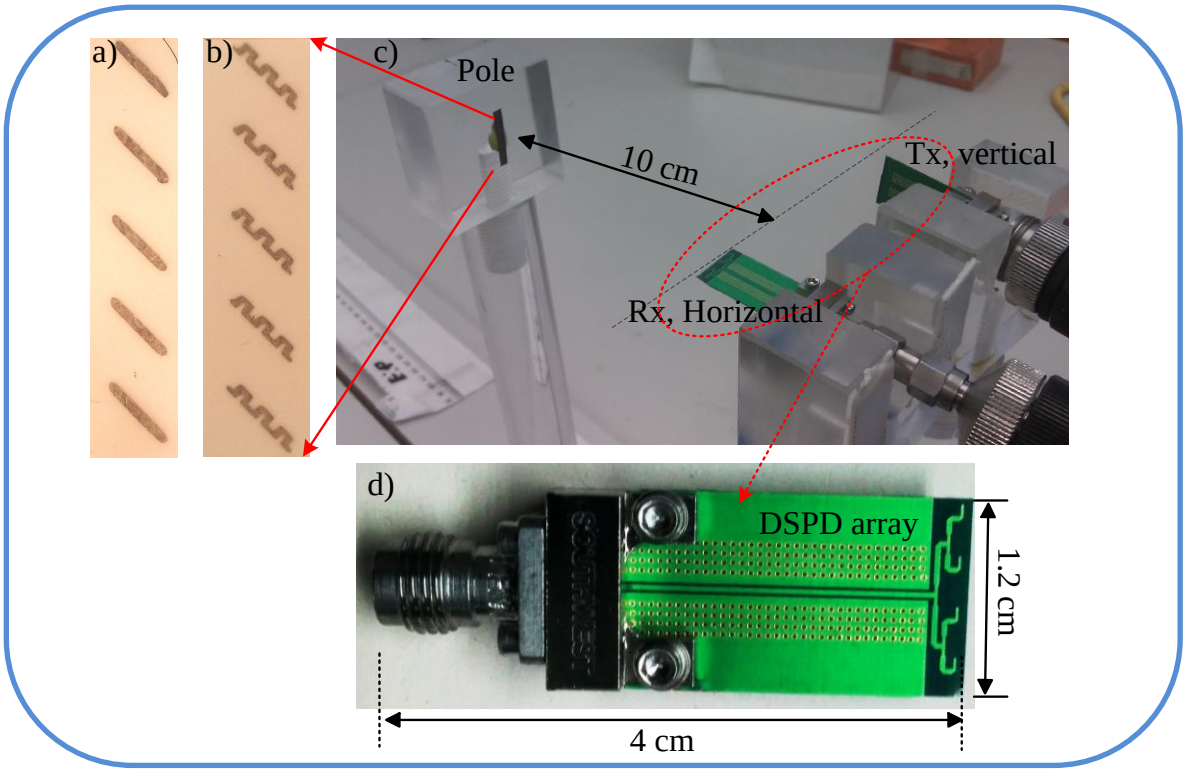

Figure 4-5 System measurement set up, a) printed strip lines, b) Printed meander lines, c) whole system, d) Reader antennas.

4.3.2 Precise tag results

The fabricated tags through the photolithographic process that have been introduced in Section 4.2.1 and shown in Figure 4-2, are attached to the pole for measurement purposes. The tag surface is interrogated by a vertically polarised antenna and the receiver at the reader measures the backscattered signals with a horizontal polarised antenna. The S_{21} in dB versus frequency is shown in Figure 4-6. The red dashed line in Figure 4-6 shows the S_{21} when no tag is attached to the pole in front of the reader antennas. The signal level is below -65 dBm. This presents the amount of signal leakage and mutual coupling between the two orthogonally polarised antennas as well as the effect of a plastic pole. The very low signal level is not unexpected as antennas are oriented orthogonally and each antenna has a low cross-polar level.

Attaching a tag comprises of five precisely fabricated strip lines through a photolithographic process significantly increases the received power level by at least 15 dB as shown in Figure 4-6. The signal level would be up to 30 dB higher at the resonance frequency 60.2 GHz. This result clearly verifies the strip line as an effective EM-polariser. Comparing the measured results with the simulation outcomes in Chapter 3 confirms that the resonance bandwidth of the tag has been increased in the real scenario. The broader resonance bandwidth is important as it challenges the resonance-based idea for data encoding. Even though the tag has been fabricated through an accurate and expensive process by utilising high quality copper and dielectric substrate, the actual Q factor of the element is lower than that of expected in simulation.

Interrogating five precisely fabricated meander lines by the vertical oriented antenna, creates a backscattered signal which includes a high orthogonal component. This cross-polar component is easily picked up by the receive antenna oriented horizontally. Similar to the strip lines case, the received signal level is almost 18 dB higher than that of the "*no tag*" case. At the resonance frequency 60.5 GHz, the signal level is 30 dB stronger. The meander lines show a higher Q factor than that of the strip lines. However, their resonance bandwidth is again increased with respect to the simulation results shown in Chapter 3.

In summary, it can be concluded that the strip line and meander line act as an effective EM-polariser at the designed band 57-64 GHz. They both suffer Q factor reduction due to the non-ideal behaviour of elements in a real scenario, specifically at the mm-band 60 GHz. While, their resonance behaviour are clearly noticeable and suggest an approach for the data

encoding algorithm, it is shown in next section that the resonances will disappeare if the same tag structure printed through an inexpensive fabrication process.

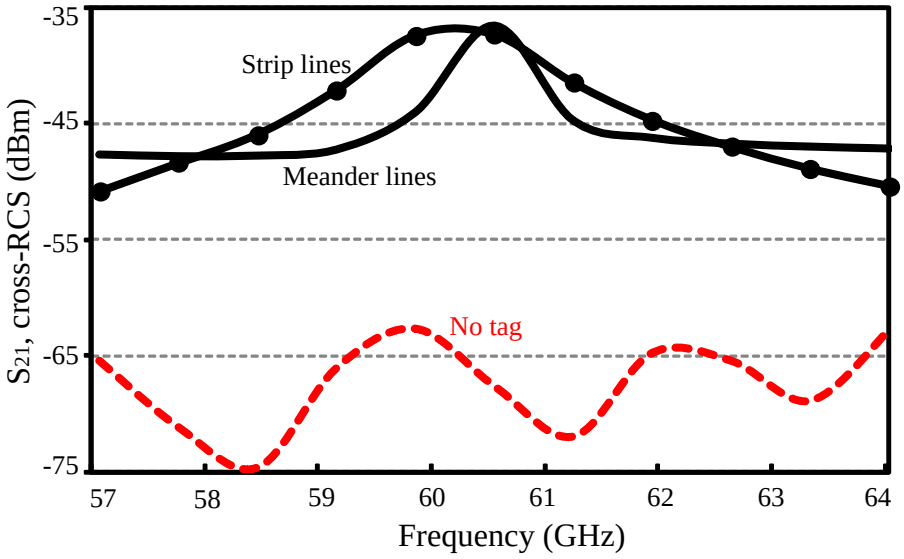

Figure 4-6 Measurement result for photolithographic fabricated tags.

4.3.3 Printed tags results

The printed tags using the SATO printer discussed in Section 4.2.2 and shown in Figure 4-4 are considered for measurement purposes. The conductive aluminum-based ink is utilised over paper for the printing process. It has already been shown that the strip lines are not the exact same length and meander lines suffer from structural anomalies occurring during the printing process. For measurement purposes, printed tags are interrogated by a vertical polarised antenna which is expected to collect a noticeable amount of signal with a horizontally oriented antenna due to the usage of EM-polarisers at the tag structure. The transmit power of the PNA and reading distance are set as for the case of the precisely fabricated tag discussed in Section 4.3.1. The measurement results are shown in Figure 4-7.

For comparison purposes, the "*no tag*" case result is shown again. If a tag that includes five printed strip lines is attached to the reading pole, the received power level increases by at least 18 dB over the entire frequency range of 57-64 GHz. This clearly accredits the strip lines as EM-polarisers even for the printed structure. However in this scenario, no resonance behaviour is seen in the response of the printed structure. Resonance(s) disappears due to the low conductivity of the utilised ink and lossy paper substrate which significantly reduces the

Q factor of the structure. Moreover, the printing inaccuracy results in multiple strip lines with slightly different dimensions as shown in Figure 4-4. As expected by the simulation results in Chapter 3, no resonance behavior shall be expected from their aggregate response.

Interrogating five printed meander lines by a vertical polarised antenna, a high cross-polar component is expected to be picked up by the horizontally oriented receive antenna. Similar to the strip lines case, the received signal level is 20~25 dB higher than that of the "*no tag*" case. Moreover as seen for the printed strip lines, no resonance is detectable at the whole frequency range of operation for the printed meander lines. Again the low Q factors of the structure and shape anomalies due to printing inaccuracy, as shown in Figure 4-4, are the reasons for almost uniform response on the 57-64 GHz band.

The results of measurement for the printed EM-polarisers are very important as they present the final shape of the tag in its commercial phase. Hence, any proposal for the encoding algorithm shall be based on the performance of the printed tag as discussed in this section and shown in Figure 4-7.

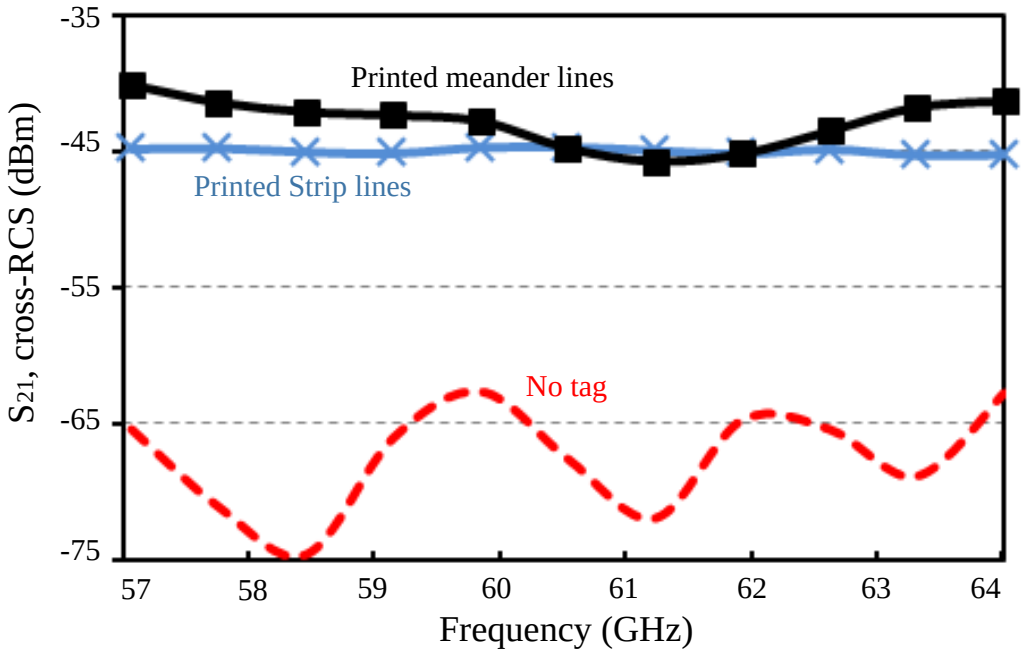

Figure 4-7 Measurement results for printed strip and meander line tags.

4.3.4 Cross-polar RCS

The results of measurement for the PCB and printed EM-polarisers shall be considered very carefully as they presents two critical aspects of the research. These two factors can be summarized as follow:

i) Proof of polariser performance. The results shown in Figure 4-6 and Figure 4-7 confirm the performance of the strip and meander lines as effective polarisers. All measurements were performed in the laboratory environment and not in an anechoic chamber. Moreover, no calibration or reference tag has been utilised. These considerations endorse the suggested stripline and meander line as suitable, low cost, compact and effective polarisers in the mm-band, which validates the data encoding method in the suggested image-based chipless RFID system.

ii) Rejection of resonance-based encoding approaches. Extensive system tunings have been considered to calibrate the SATO printer for a most accurate printing result. All the printed tag structures show almost the same results as shown in Figure 4-7. It appears that the low cost printing technology is not mature enough for the demanded accuracy in RFID applications. This suggests that any resonance-based approach for data encoding faces huge limitations at the commercial phase of the system implementation. High resolution printing methods in the order of 10-20 µm are too expensive and slow processes, laser printing for example.

Irrespective of lost resonant at the backscattered signal due to the printing inaccuracy and low quality of materials in the tag structure, the measured high cross-polar signal can be utilised for a cross-polar RCS based data encoding algorithm. This new basis is used in the proposed theory of the EM-image chipless RFID system. Therefore, in the proposed image-based technique, the system does not rely on resonance detection hence, is robust towards the printing inaccuracy and therefore the low cost printers are still viable methods.

4.4 Discussion on data encoding method

4.4.1 Pros of EM-polarisers

The measurement results based on the precise fabricated tag and the printed tag discussed in Section 4.3 have revealed the potential advantages and limitations of the proposed strip

line and meander line as EM-polarisers. The most advantages of the proposed polariser-based tag are:

i) **Small size**. The size of the polarisers is less than 0.5×2 mm^2 which makes them very suitable for data encoding in the RFID applications. The tiny size of the polariser, due to the simple structure of the component and the mm-wave band of operation, elevates the chance of high data encoding capacity in the proposed technique.

ii) **Cross-polar working basis**. The interrogation signal by the reader is converted to the orthogonal polarised backscattered signal due to the EM-polarisers on the tag surface. This working basis provides huge advantages for the proposed system with elimination of noises and the interferences from different sources. System robustness towards multipath interference and clutter and no requirement for system calibration are the unique advantages of this cross-polar working basis.

iii) **Adequate performance with the printed tag**. The proposed simple tag structure guarantees its adequate performance even on a fully printed tag as confirmed in the measurement step in Section 4.3. Suffering from shape anomalies and inaccurate dimensions, the polariser-based printed tag performs well for creation of a high cross-polar component at the backscattered direction. This assures the successful implementation of the proposed technique for real applications.

The only limitation of the proposed technique is the lack of resonances at the backscattered signal. The measurements showed that it would not be practical to expect multiple resonances from a printed tag structure. The printing inaccuracy negates the idea of recognising the tag by its frequency signature in co- or cross-polar responses. Although working on lower frequencies may reduce the effect of printing inaccuracy, the limited spectrum available on lower frequencies and the very low Q factor of the printed resonators, still affect the final encoding capacity of the system [79]. Although this limitation originated from immature printing technologies for low cost items, it is the duty of the proposed technique to suggest a suitable data encoding approach addressing the capacities of the current printing technologies. Otherwise, any solution based on the very accurate and costly tag fabrication process finds no place in the RFID market.

4.4.2 On/off image-based data encoding algorithm

The idea of EM-imaging has already been introduced in Chapter 3. It was stated that in the imaging technique, every small section of the tag surface is sequentially scanned by the reader and its related encoded data is retrieved, see Figure 3-1. Now, the way that data can be encoded in every small section of the tag surface is discussed. It has already been shown that a small size EM-polariser can create strong enough cross-polar components in the backscatter direction, which can be easily detected by the reader array antenna. One may suggest using these polarisers on the tag surface as the data encoding elements. In this approach, the tag surface comprises a matrix of $m \times n$ pixels as shown in Figure 4-8. Every pixel which is as small as 2×2 mm^2 may include one polariser. When the reader scans a particular pixel, the presence or absence of the polariser results in a completely different received signal level at the cross-polar direction that acts as a binary data; existence of the polariser as "1" and no polariser as "0", for example. Therefore, binary digit data encoding approach is implemented by the polarisers. No resonance is to be found from the backscattered signal for data encoding. Creation of such precise scanning on the tag surface in millimetre order in the real scenario is a matter of question though. In Chapter 7, the EM-imaging theory is reviewed in detail and it is shown that this scanning precession of the tag surface is possible at a suitable frequency range and with appropriate approaches. The final result shown in Chapter 7 with five millimetre scanning precision proves the validity of this suggestion.

At this stage, the general system structure for the first phase of the proposed image-based theory can be figuratively shown as in Figure 4-8. The system requires the reader's physical movement around the tag to create a synthetic aperture. The length of this aperture governs the horizontal resolution on the tag surface, known as cross-range or azimuth resolution. It is discussed in Chapter 7 that a 20~30 cm synthetic aperture size would be enough to create 2~5 mm cross-range resolution on the tag surface at the reading range of 10~20 cm. The ability of the system to provide precise vertical resolution, known as range resolution, depends on the type and frequency band of the transmit signal. At the aforementioned reading range, the range resolution of 2~10 mm is also feasible with a high rate chirp signal covering a significant bandwidth. This issue is also discussed in more detail in Chapter 7. The requirement of the physical movement of the reader can be replaced by a linear array of radiators on a MIMO working basis. This enhances the reading time and elevates the potentials of the proposed theory. The detail of this new MIMO-based reader is introduced in Chapter 8.

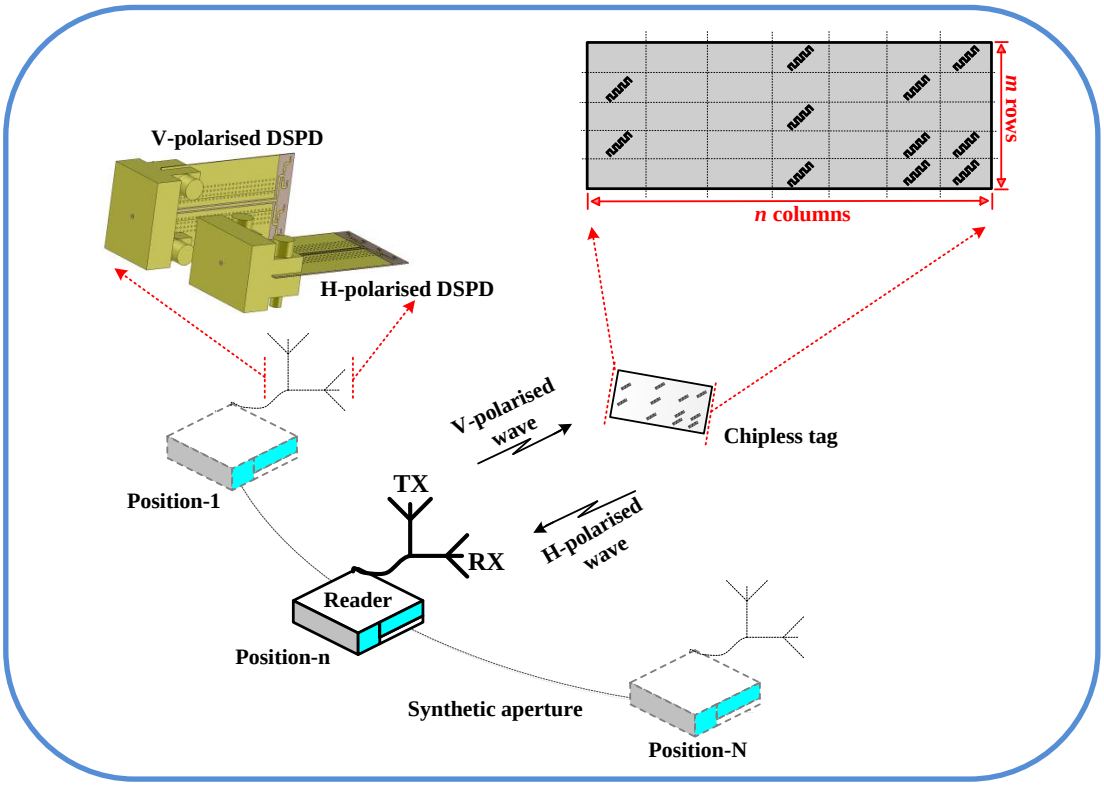

Figure 4-8 General system structure based on SAR theory.

By assuming the tag surface comprises $m \times n$ pixels and each pixel may have one polariser as its data encoding particle, then the total data encoding capacity of the tag is 2^{mn}. Recalling the size of the suggested pixel as 2×2 mm^2, the data encoding capacity in the proposed theory has the potential of more than 20 bits/cm^2. This suggests a huge content capacity. However, the system complexity to reach this maximum data encoding density is also noticeable. The data encoding capacity can be sacrificed for a simpler reader structure. The data capacity of 2 bits/cm^2 is measured in Chapter 7, based on a printed tag structure and with a fairly simple reader system in a real environment without any calibration. This suggests more than 90 bit content capacity for a credit card size tag of 5.5×8.5 cm^2. The measured result shown in Chapter 7 proves the above claimed data encoding capacity.

The next chapter presents the mathematical model of the proposed system and its superiority to mitigate noise, interference and adverse propagation issues such as reading tag on a metal object, liquids and bent surface.

4.5 Conclusion

This chapter has considered the fabrication process of the designed polarisers. The strip line and meander line-based tags were fabricated through two different technologies. First, the EM-polariser based tags were made through an accurate and costly photolithographic process. Each tag included five polarisers oriented vertically. Then the same designs were printed with a SATO printer. The SATO printer uses conductive aluminium ink for printing on normal paper. Two samples of the tags have been accurately examined with an electronic microscope. The printed meander lines showed considerable shape anomalies. Printed strip lines were also measured to find their final lengths. It was found that five strip lines had different lengths than the designed dimensions.

Both PCB and printed tags for each case of the strip line and meander line have been measured in a real scenario. Two sets of double sided printed dipole arrays were used at the reader side. They were oriented orthogonally as transmit and receive antennas. The array antennas were connected to the PNA and various types of tags were placed in front of the antennas. The measurement process was carried out in the laboratory environment. Precise fabricated PCB tags for both a strip line and meander line polarisers showed similar results, as expected by the simulation in Chapter 3. Their resonance bandwidths, however, were broadened due to the non-ideal behaviour of the copper and substrate and other environmental and propagation issues at the measurement process. On the other hand, printed tag structures did not exhibit any resonance in their backscattered signal. However, they were showing significant cross-polar components. Non-resonance behaviour was linked to their shape anomalies and also related to the very low Q factor of the printed polarisers.

The results of printed tags have been considered as the significant performance of the proposed EM-polarisers for real world application in RFID systems. Then the data encoding algorithm was proposed based on this minimum criterion. As the resonance frequency signature based approach for the printed tag was failed, an alternative on/off image-based technique was suggested for the data encoding algorithm. In this approach, the presence or absence of an individual polariser on each small pixel of the tag surface acts as binary data “1” or “0”. When the reader precisely scans the tag surface, it receives a completely different signal level based on the existence of polarisers. The maximum theoretical content capacity of the system based on this approach has been presented next. It has been addressed that to reduce the system complexity, the data encoding capacity is sacrificed for a simpler system

structure. Finally, the claimed data encoding capacity based on a fully printable tag structure and a simple reader system with low frequency bandwidth, is still much higher than that already shown by other competitors in the chipless RFID systems.

Chapter 5 Printed EM-polariser performance

5.1 Introduction

Electromagnetic (EM) polarisers have been introduced in Chapter 3. The edge diffraction of the polariser and the antenna mode RCS of the polariser result in significant cross-polar components in the backscattered direction. This is the basis for the cross-polar EM-image based chipless RFID system.

Next the proposed EM-polarisers were fabricated through a photolithographic process and printed with a SATO GL4e industrial thermal silver ink based printer with 600 dpi resolution. Both prototype tags were tested in the laboratory environment. Both tags through two different fabrication processes showed prominent de-polarisation behaviour. While the impinging signal was linearly polarised, the reflected signals showed high cross-polar components. However, for the printed tag structure, no resonances were detectable on the received signal, due to the printing errors of the SATO printing and low quality of the materials. Therefore, it has been established that SATO printed tag still provide adequate cross-polar RCS, while is useful for EM-image based binary data encoding. This result has been discussed in details in Chapter 4.

In this chapter, the robustness of the EM-polarisers toward unwanted reflections and multipath interferences is considered. This system robustness is one of the most important salient aspects of the proposed EM-polarisers. First, the equivalent system model is introduced to ease the network analysis of the proposed EM-polariser based system. The effectiveness of the system for unwanted reflections is proved mathematically. Then different measurement scenarios are considered to investigate the system robustness in various scenarios. It is shown through measurement that the EM-polarisers can effectively create cross-polar RCS components in the backscattered direction on which the receiver easily detects the presence of the EM-polarisers. The effect of reflections from other objects and multipath interferences are also considered in the measurement process and the system robustness is proved. This finding suggests huge advantages of the EM-polariser based system for industrial environments. Moreover, the polariser-based tag is shown to be very efficient for tagging of highly reflective items; water bottles or metallic cans for example. The bending effect of the tag conformal to various types of objects, on its cross-polar performance, is also considered in this chapter.

The robustness of the proposed tag for harsh industrial environments is presented at the end of this chapter. The cross-polar based system effectively decodes the tag's data with reasonable reader complexity. No complex system calibration process is needed for the proposed system structure. All the measurements and conclusions are based on the performance of a fully printed tag structure in a laboratory environment.

5.2 System analytical model

To explore the potential of the cross-polar based system, the equivalent system network is introduced. This enables the mathematical analysis of the tag response and realization of the system robustness towards reflection and multipath interferences. Moreover, in the theoretical evaluation of the proposed technique, the drawbacks and limitations of the co-polar based system as the working basis of many current techniques in the chipless RFID systems, is explored. It should be noted that the frequency, time and, most of hybrid domain based chipless RFID tags works on the co-polar backscattered signal hence susceptible to noise and interferences. To alleviate the situation, rigorous calibration is required to extract data.

As previously discussed, the tag is interrogated with a linearly polarised signal; vertical polarisation, for example. The backscattered response is picked up by the receiver in the orthogonal direction; horizontal polarisation for example. The RCS of the tag relates to many parameters including the frequency and polarisation of the impinged signal, the aspect angle of the tag and its physical size and structure [80]. For a certain frequency and aspect angle, the RCS behaviour depends on the interrogation signal's polarisation by [115]:

$$\sigma = \begin{bmatrix} \sigma_{vv} & \sigma_{vh} \\ \sigma_{hv} & \sigma_{hh} \end{bmatrix} \tag{7.0}$$

In (7.0), σ represents the tag's scattering behavior. Each matrix element, σ_{ij}, shows the tag response in a j polarisation scheme while interrogated by an i polarised signal. For simplicity, the vertical (v) and horizontal (h) polarisations are assumed in this work while (7.0) is valid for any orthogonal polarisations.

Evaluation of the proposed technique requires a circuit model. The suggested model shall include all the elements of the technique. One possible model for the chipless RFID system was introduced by [116]. This model includes the effect of Tx and Rx antennas, the response

of the chipless tag and the equivalent response of all interfering objects surrounding the tag as shown in Figure 5-1. Each block in the model shows a specific section of the communication link. As two vertical and horizontal polarisations were assumed in the model, then each box has a 2 × 2 S-parameters matrix which characterises its behavior in co- and cross-polar directions.

In Figure 5-1, the transceiver module on the reader side is denoted by block *M*. The source is assumed to send a pure V-polarised signal and the receiver is expected to collect the backscattered signal only in a H-polarisation direction. However, due to the non-ideal behaviour of the elements involved in the link, there is the possibility of errors in the tag detection process. The model is intended to find those errors and mathematically evaluates their weights in the final performance of the system. The Tx antenna and its connected cable and connectors are symbolised by block *T* or the transmit path. Likewise, the receiver antenna and cables are shown through box *R* or receive path. The coupling among Tx and Rx antennas always exist. To show the effect of coupling, block *D* is considered in the model. Existence of the tag in front of the antennas causes reflection of energy towards the reader's receive antenna. This is the intended reflection which carries the tag information. This link is shown by block *C* in Figure 5-1. Apart from direct coupling and reflection by the tag, there is the possibility of receiving the signal through the reflections by other objects around the tag. This includes everything located in the reader's reading zone. The item to which the tag is attached, such as the walls, floor and ceiling, are examples. Normally these reflections are undesirable phenomena and known as interference. Their effects significantly contribute to system performance, and therefore, shall be considered in the schematic block diagram. The box *I* represents the effect of all those interfering factors so it covers all unwanted reflections, multipath interferences, and clutter.

The S-parameter matrix of the reader, *M*, can be related to the S-matrix of other blocks by:

$$M = TDR + TCR + TIR \tag{7.1}$$

In the above equation, *TDR* shows the amount of coupling or direct leakage between transmit and receive antennas. This part is independent of the effect of the tag or other objects. Therefore, leakage, *L*, can be directly measured when there is nothing in front of the antennas.

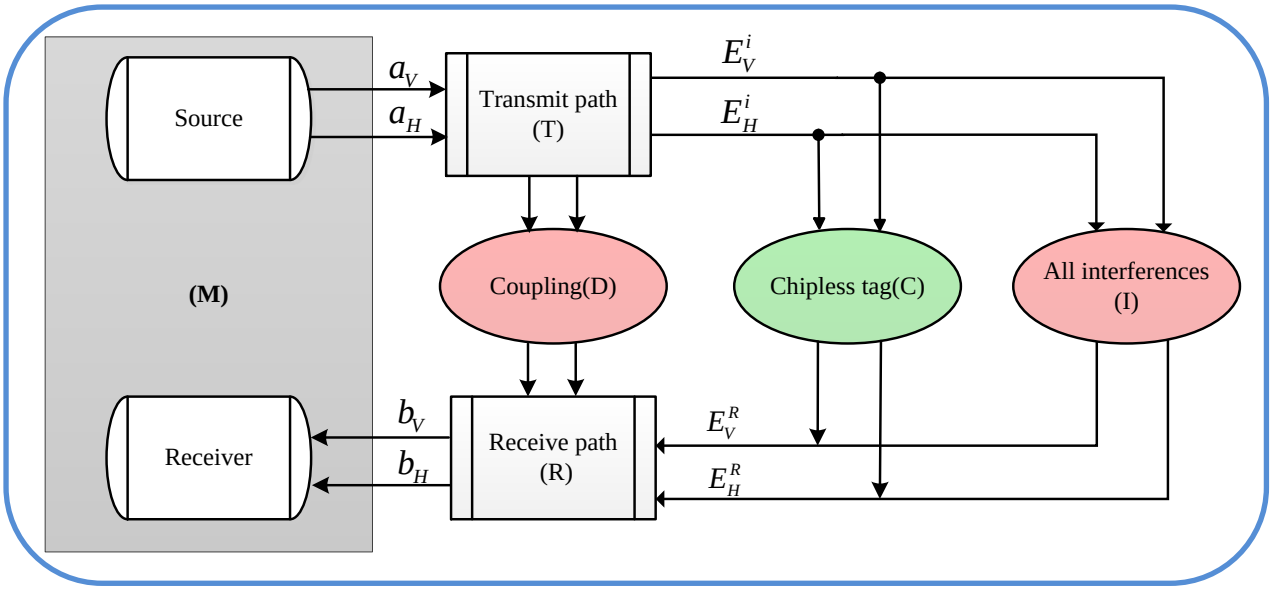

Figure 5-1 Schematic block diagram of the chipless RFID system.

$$L = TDR \tag{7.2}$$

Therefore, one can combine (7.1) and (7.2) to have:

$$\begin{bmatrix} M_{vv} & M_{vh} \\ M_{hv} & M_{hh} \end{bmatrix} = \begin{bmatrix} L_{vv} & L_{vh} \\ L_{hv} & L_{hh} \end{bmatrix} + \begin{bmatrix} T_{vv} & T_{vh} \\ T_{hv} & T_{hh} \end{bmatrix} \cdot \begin{bmatrix} C_{vv} & C_{vh} \\ C_{hv} & C_{hh} \end{bmatrix} \cdot \begin{bmatrix} R_{vv} & R_{vh} \\ R_{hv} & R_{hh} \end{bmatrix} + \begin{bmatrix} T_{vv} & T_{vh} \\ T_{hv} & T_{hh} \end{bmatrix} \cdot \begin{bmatrix} I_{vv} & I_{vh} \\ I_{hv} & I_{hh} \end{bmatrix} \cdot \begin{bmatrix} R_{vv} & R_{vh} \\ R_{hv} & R_{hh} \end{bmatrix} \tag{7.3}$$

As already assumed, the transmit signal is V-polarised and the receive signal is H-polarised. Therefore, M_{vh} is the interested *S*-parameter (forward transmission coefficient) for the proposed cross-polar system. M_{vv} is also important to compare the performance of the proposed system with other co-polar based systems. These two S-parameters are driven by:

$$\begin{aligned} M_{vv} = {} & L_{vv} + (T_{vv}C_{vv} + T_{vh}C_{hv})R_{vv} + (T_{vv}C_{vh} + T_{vh}C_{hh})R_{hv} + \\ & (T_{vv}I_{vv} + T_{vh}I_{hv})R_{vv} + (T_{vv}I_{vh} + T_{hv}I_{hh})R_{hv} \end{aligned} \tag{7.4}$$

$$\begin{aligned} M_{vh} = {} & L_{vh} + (T_{vv}C_{vv} + T_{vh}C_{hv})R_{vh} + (T_{vv}C_{vh} + T_{vh}C_{hh})R_{hh} + \\ & (T_{vv}I_{vv} + T_{vh}I_{hv})R_{vh} + (T_{vv}I_{vh} + T_{hv}I_{hh})R_{hh} \end{aligned} \tag{7.5}$$

(7.4) and (7.5) are related to the physical characteristics of the elements in the reading process. If they are carefully investigated, the complexity of (7.4) and (7.5) can be reduced. For example, the terms I_{vh} and I_{hv} represent the de-polarisation aspect of the unwanted reflection toward the reader. The usual expectation is that reflection through surrounding objects would be at the same polarisation. Specifically at mm-wave range, the objects are too

big to create a de-polarised signal due to the diffraction effect. Multipath interferences and clutter also show no de-polarisation behaviour, hence the I_{vh} and I_{hv} can be correctly assumed to be zero. T_{ij} and R_{ij} on which $i \neq j$, are related to the antenna polarisation or the antenna's CPL. As is shown in the next chapter, the designed array antenna for the proposed image-based chipless RFID system has a high CPL of more than 20 dB. Moreover, the PNA Agilent E8361A has a high quality cable and connectors with very high isolation in the order of 80 ~100 dB [117]. This means that the value of T_{ij} and R_{ij} are less than 0.01 and again can be correctly neglected.

By applying the aforementioned simplifications, (7.4) and (7.5) become:

$$M_{vv} = L_{vv} + T_{vv}R_{vv}(C_{vv} + I_{vv}) \tag{7.6}$$

$$M_{vh} = L_{vh} + T_{vv}C_{vh}R_{hh} \tag{7.7}$$

In the above formulas, L_{ij} refers to the leakage between Tx and Rx modules of the reader whether in co- or cross-polar directions. The following statements are related to the leakage:

- ✓ *Leakage measurement*. In an empty environment, leakage (L_{ij}) can be directly measured. The value of L_{ij} depends on the internal characteristics of the designed antenna and is also related to the physical distance between the Tx and Rx antennas. Once L_{ij} is measured, it does not change with varying the reading scene.

- ✓ *Significance of leakage*. The leakage for the co-polar case would be much higher than that of the cross-polar scenario $L_{vv} > L_{vh}$. If the co-polar leakage (L_{vv}) is not controlled well, it may significantly affect the final system performance.

- ✓ *Leakage control*. The leakage control for the co-polar, L_{vv}, is much more complex than that for the cross-polar, L_{vh}. This is because in the co-polar case, both transmit and receive antennas are on the same polarisation scheme and, hence, they are more likely to interfere to each other.

Therefore, it can be concluded that the leakage in the cross-polar case is much less than that of the co-polar and, hence, it has less effect on the reading process. Moreover, the leakage

control is also much easier in the cross-polar scenario. This is one of the most significant advantages of the cross-polar scenario over the co-polar working basis.

In (7.7) which relates to the cross-polar scenario, the term $T_{vv}C_{vh}R_{hh}$ refers to the mixed effects of the Tx, Rx and the tag. To accurately determine the coupling coefficient $T_{vv}.R_{hh}$ due to the filtering effect of the transmitter and receiver antennas, it is required to utilise a reference tag with known scattering behaviour. Therefore, the tag's scattering term (C_{vh}) can be easily found as:

$$T_{vv}R_{hh} = \frac{M_{vh}^{ref} - L_{vh}}{C_{vh}^{ref}} \tag{7.7}$$

$$C_{vh} = \frac{M_{vh} - L_{vh}}{M_{vh}^{ref} - L_{vh}} C_{vh}^{ref} \tag{7.8}$$

where L_{vh} is a fixed value based on the Tx and Rx antennas distance and M_{vh}^{ref} is the measured scattering parameter of a reference tag.

One may suggest performing the same approach for the co-polar scenario. However, as it is clear from (7.6) an extra term I_{vv} also exists for the co-polar case. The I_{vv} counts the effect of reflections from surrounding objects around the tag. As the tag size is very small compared to other surrounding objects, then the I_{vv} is much larger than the C_{vv} in (7.6). This means that it is not possible to extract the tag response without the information about its surrounding objects. Indeed, it is required to first calibrate the system based on a specific orientation of objects in the reading zone and then detect the response of the tag by subtracting two measurement results. Although with this calibration process, the tag reading would be possible in the co-polar scenario, the approach is very sensitive to any changes in the surrounding objects orientations or tag movement. This means that if the tag moves in the reading zone or if one object around the tag changes its place or aspect angle, then it is required to calibrate the system again. On the contrary, the cross-polar scenario is not dependent on the surrounding objects and no information is required. This is a very significant aspect of the cross-polar working basis, as the system is working well in an unknown reading zone only with a unique calibration set up. This aspect of the proposed cross-polar system is shown in a practical scenario in the following sections.

5.3 Effects of multipath interference and clutter

The strip line and meander line were measured in Chapter 4 with respect to their de-polarisation aspects. Both precisely fabricated PCB tags and the SATO printed tags were able to provide high cross-polar components in the backscattered direction, hence, acting effectively as EM-polarisers. Moreover, it was also mathematically shown in Section 5.2 that the proposed cross-polar technique suggests high robustness towards multipath interference as its dominant feature with respect to the co-polar working basis. This aspect of the proposed approach is verified through a real measurement process in this section.

The measurement set up is similar to what was explained in Chapter 4 and shown in Figure 4-5. The reading distance, transmit output power and all other parameters are the same for making the comparison possible. Exploring the effect of multipath and reflection interferences on the reading process, the measurement is accomplished in the lab environment and not in an anechoic chamber. Moreover, a harsh and severe multipath situation is implemented by using some randomly selected highly reflective objects. Three horn antennas are directed toward the reader antennas. A large printed circuit board with 35 × 45 cm^2 is also placed in front of the reader. This reading arrangement considers the most sever interference situation for the system reading process. The Tx and Rx antennas together with the highly reflective items are shown in Figure 5-2.

To simulate the high clutter situation, a big copper plate is attached to the reading pole. The size of the plate is very large compared with the reader antennas and the reading distance. It is 20 × 25 cm^2. This highly reflective barrier causes a challenging situation for many traditional chipless RFID systems. The reflection from this plate (I_{vv}) is much higher than that of the tag (C_{vv}) as discussed in the previous section. Therefore, the detection of the tag would be impossible unless the effect of high reflection is deleted through a calibration process. The calibration however, is sensitive to any changes in the orientation of the objects around the tag and the tag movement. This scenario is shown in Figure 5-3.

These two scenarios are considered in the measurement process and the results are shown in Figure 5-4. For comparison purposes, two results from a normal situation are also repeated in Figure 5-4. They are a "*no tag*" case and a printed meander line tag in a normal situation from Chapter 4, Figure 4-7. As the graphs in Figure 5-4 show, the effect of multipath interference and clutter on the received signal are almost negligible and very similar to the

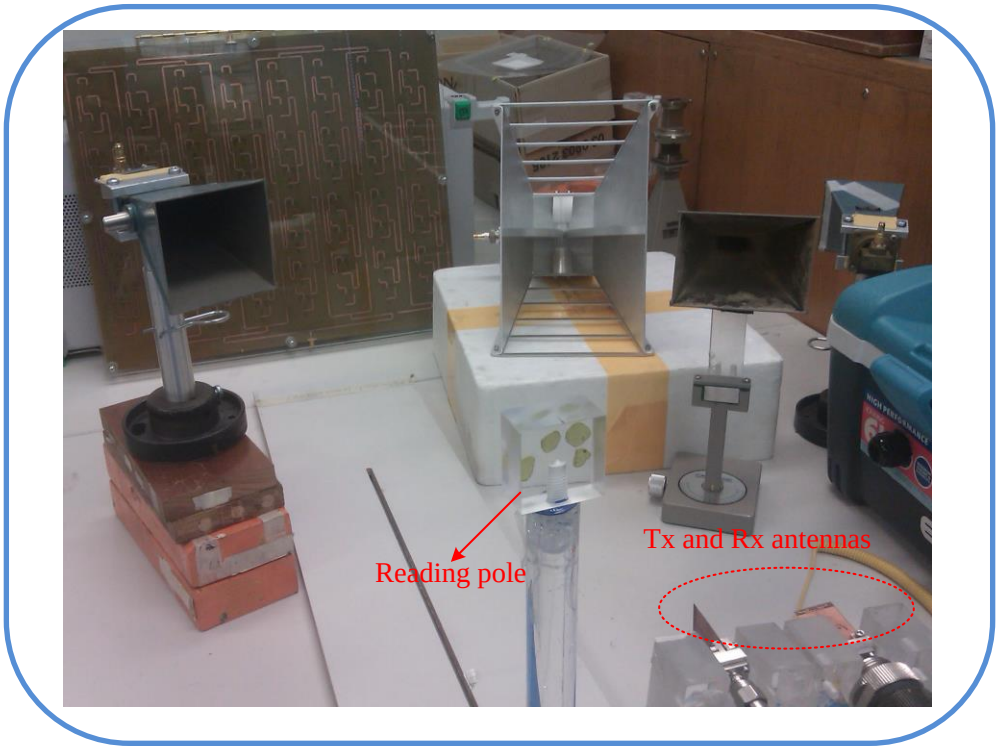

Figure 5-2 Severe multipath interference scenario.

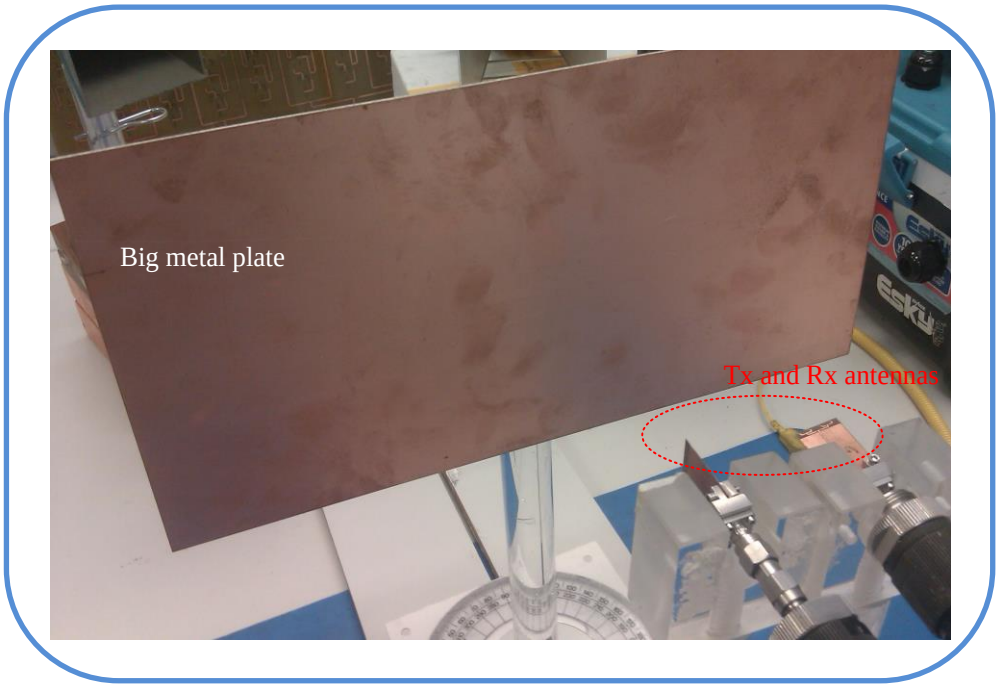

Figure 5-3 High clutter situation for the tag reading process.

case when no tag is attached to the pole. This clearly matches with the mathematical conclusion regarding the robustness of the proposed technique to the multipath and high clutter effects. Reflections from objects around the tag are mostly in a co-polar direction, while the receiver picks up cross-polar components only. This significant advantage of the proposed cross-polar based technique is very important for practical usage of the chipless system with respect to other co-polarised based systems [25, 26, 65]. In most cases, chipless RFID systems are vulnerable to multipath interferences and they require supplementary approaches; for example multi-steps calibration or reference tags [25, 26, 59, 90].

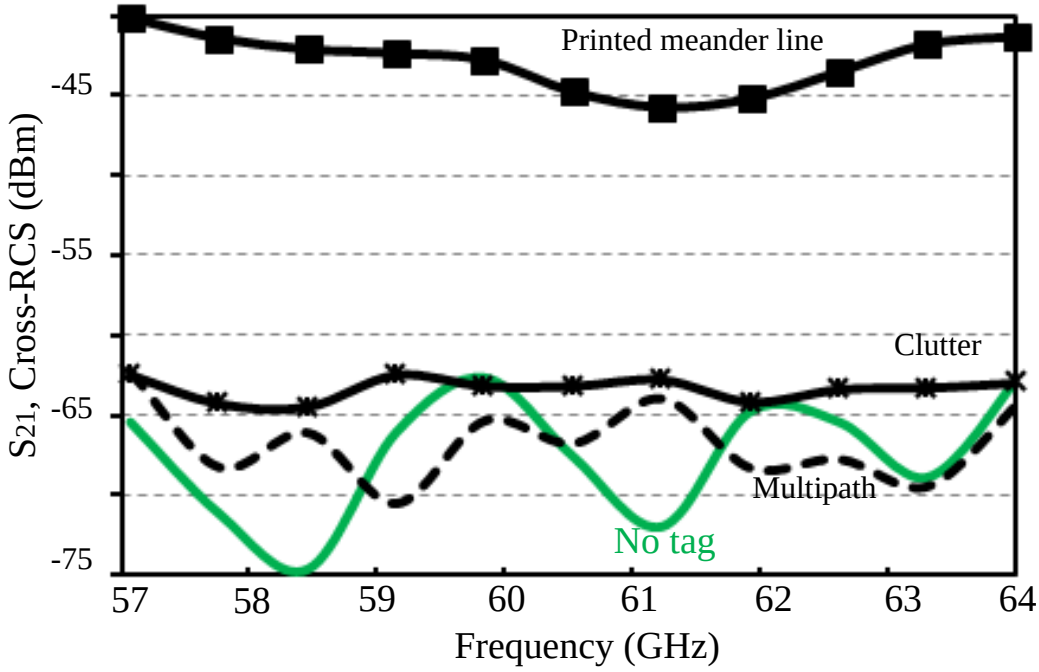

Figure 5-4 Measurement result for multipath and high clutter situations.

5.4 Effect of highly reflective items

In the previous section, the robustness of the proposed technique towards severe multipath interferences and high clutter situations has been verified. In this section, the intention is to authenticate the de-polarisation aspect of the printed EM-polarisers while they are attached to highly reflective items. This covers the ultimate practical scenarios of the chipless RFID systems. For this purpose, two highly reflective objects are considered. First, a plastic bottle containing water is measured. As the reflection from water is unpredictable so it may cause degradation of the reading process. Second, an aluminum can containing liquid is considered.

The high reflection from the conductive body of the container as well as the bending effect affects the measured results. These two scenarios are discussed in this section.

5.4.1 Liquid container

A normal plastic bottle of water is considered, to evaluate system performance. The tag is a single-layer structure consisting of printed polarisers on paper. The object and attached printed tag are shown in Figure 5-5. The tag consists of normal printed meander lines as highlighted in the picture. The reading distance is set from the tag surface to the reader's antennas.

The measurement results for the water bottle are shown in Figure 5-6. For comparison purposes, the measured results of the "*no tag*" case are also shown in Figure 5-6. As the graphs show, when no tag is placed in front of the antennas, the received signal level is below -65 dBm. Having a water bottle that is comparatively very large with no attached tag has a minor effect on the cross-polar component of the received signal. A maximum of 5 dB increase is experienced in this case. However, if the same water bottle includes a tiny printed tag as shown in Figure 5-5, then the received signal is significantly elevated. The received signal level from the tag attached to the water bottle has 12 dB more compared to that when the water bottle has no attached tag. This margin provides a reliable reading scenario of the liquid containers. Therefore, it can be concluded that the system has satisfactory performance when attaching to the liquid container. It is important to mention that no calibration process to cancel out the surrounding effect is required to obtain the graphs of Figure 5-6. If the calibration process mentioned in the mathematical step at Section 5.2 is utilised, then a much clearer signal level is expected to be seen on the graphs for the cross-polar components of the received signals from the tag.

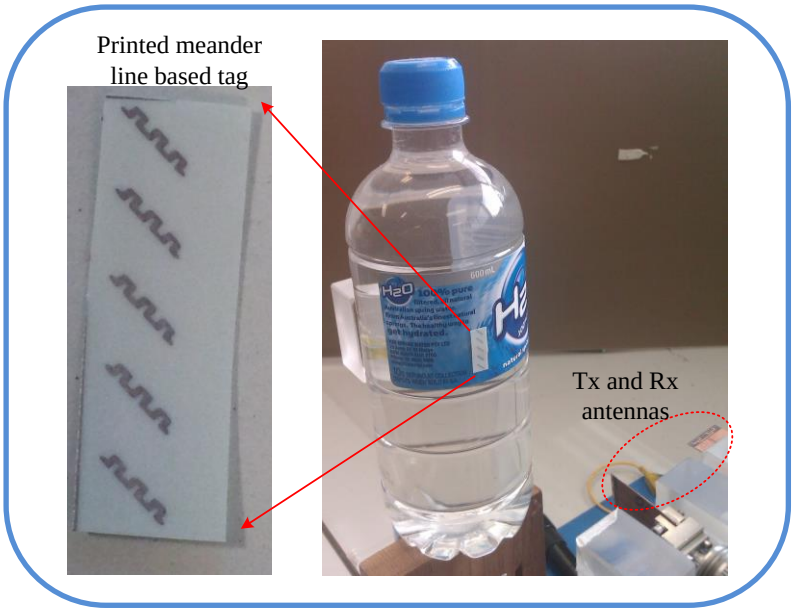

Figure 5-5 Printed meander lines tags attached to a plastic bottle of water.

5.4.2 Metallic objects

Tagging of metallic objects is always a challenging issue for RFID technologies due to the high reflection effect. An aluminum can is considered to evaluate system performance for this scenario. The tag is an etched out meander line of conductive surface on paper. This means that the base of the tag is conductive and the meander line shape is paper. Therefore, this tag is a negative image of the former tag used in the previous step for the water bottle. The measurement set up is shown in Figure 5-7 with the tag structure also highlighted.

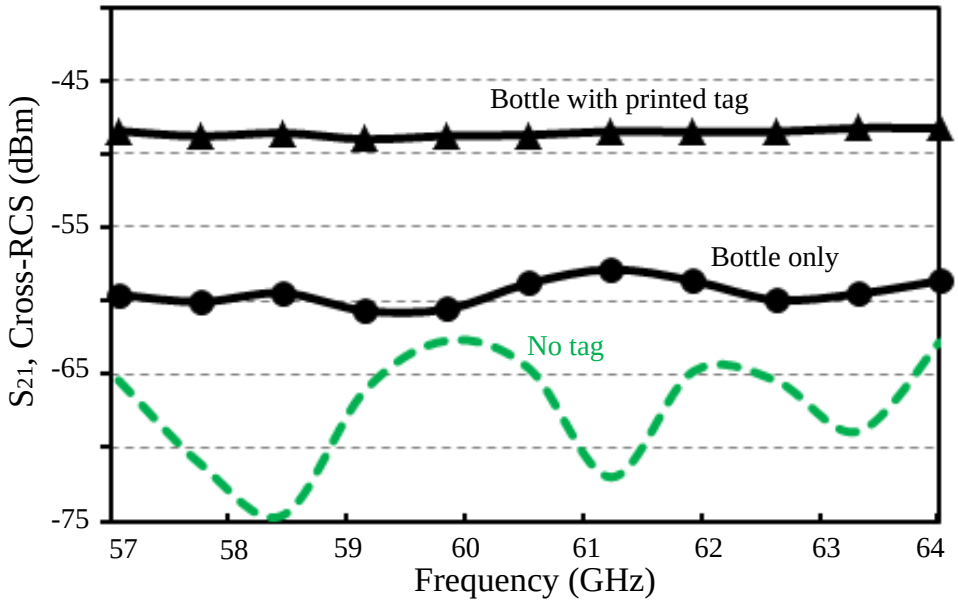

Figure 5-6 Measured received power level of a printed tag attached to a water bottle.

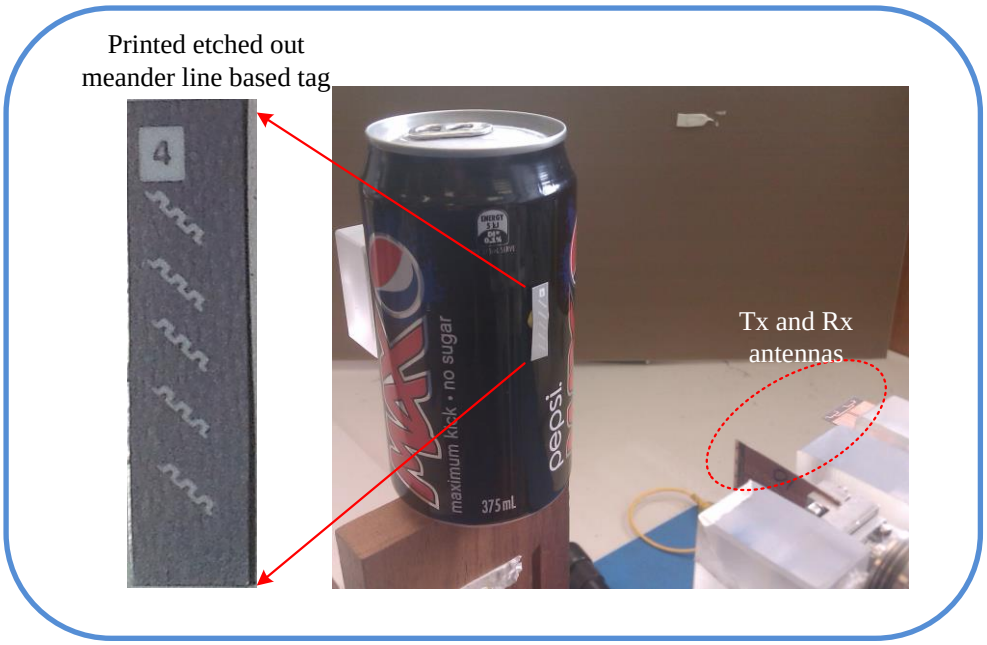

Figure 5-7 An etched out printed meander lines tag attached to an aluminium can.

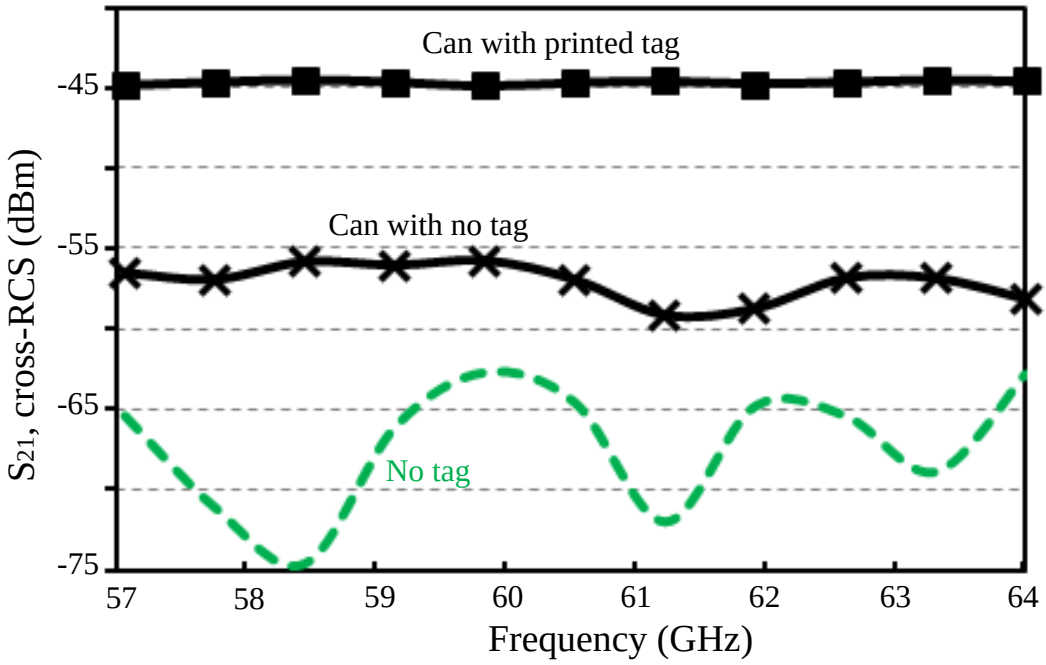

Figure 5-8 Measured received power level of single layer printed tag attached to a water bottle.

The measurement results are shown in Figure 5-8. The received signal level for the " *no tag"* case is also depicted in this figure. An aluminum can containing liquid without any attached tag, if placed in front of the reading pole, increases 5-7 dB of the receive signal in the cross-polar direction. If the same object is accompanied by a tiny printed tag, then it creates at least 13 dB higher cross-RCS on the reader side when compared with the "*can only*" case. It is again important to indicate that all the graphs in Figure 5-8 are the pure measured signal level without any calibration or cancelling out of interferences process. If the calibration step introduced in Section 5.2 is utilised, then a much easier reading process and decision making would be available for the reader. This measurement result clearly shows the potential of the proposed technique for tagging of metallic objects.

5.5 None optical LoS tag reading

The "line-of-sight" terminology in EM theory refers to propagation of EM-wave including optics in a straight line. Based on the frequency of operation, a radiocommunication link may be referred to as LoS or NLoS. Low frequency EM-wave does not need a LoS condition, HF broadcasting for examples. For higher bands, the transmitter shall see the receiver to be able to communicate effectively or a LoS condition is required, point-to-point communication in GHz bands for example. Based on this assumption, the proposed technique of imaging system is definitely a LoS system. Therefore, the reader requires LoS condition to detect and read the tag.

However, the LoS systems may be categorized further. The communication link in some LoS systems may require a clear/visible LoS between Tx and Rx without any obstacles. Very high frequency EM-wave and specifically optical communication systems are in this category. These systems are referred to as optical LoS systems. However, there are LoS systems that operate effectively even if some obstructions, in the form of EM-wave transparent materials, are in the reading zone. To categorize these two systems, the word optical LoS is referred to first systems. The second types of systems may be also referred to EM-LoS system. The optical based identification systems, barcodes and QR codes, are definitely optical LoS systems. Any barrier, even dirt may results in reading failure. This restricts the system flexibility and is seen as a main issue for many applications.

Considering the mm-wave band of operation, it is important to evaluate the system performance when the tag is read None optical LoS in an envelope or inside a box. This shows the system performance in None optical LoS conditions. For this purpose, multiple barriers are placed between the tag and reader. In this process, the tag is covered by the

medium. This is similar to the cases when the tag is attached to an item and covered by a medium as shown in Figure 5-9. The medium could be an envelope paper or a box made up from cardboard or plywood. Table 5-1 shows different types of media, their thickness and material compositions. This selection may cover a wide range of items.

Table 5-1 Multiple barrier

Barrier name	Thickness (mm)	Material
Foam	18	Polypropylene / Polyethylene (EPP/EPE)
Cardboard	2	Torn cardboard
Plywood	3	Wood veneer
Wood	20	Wood

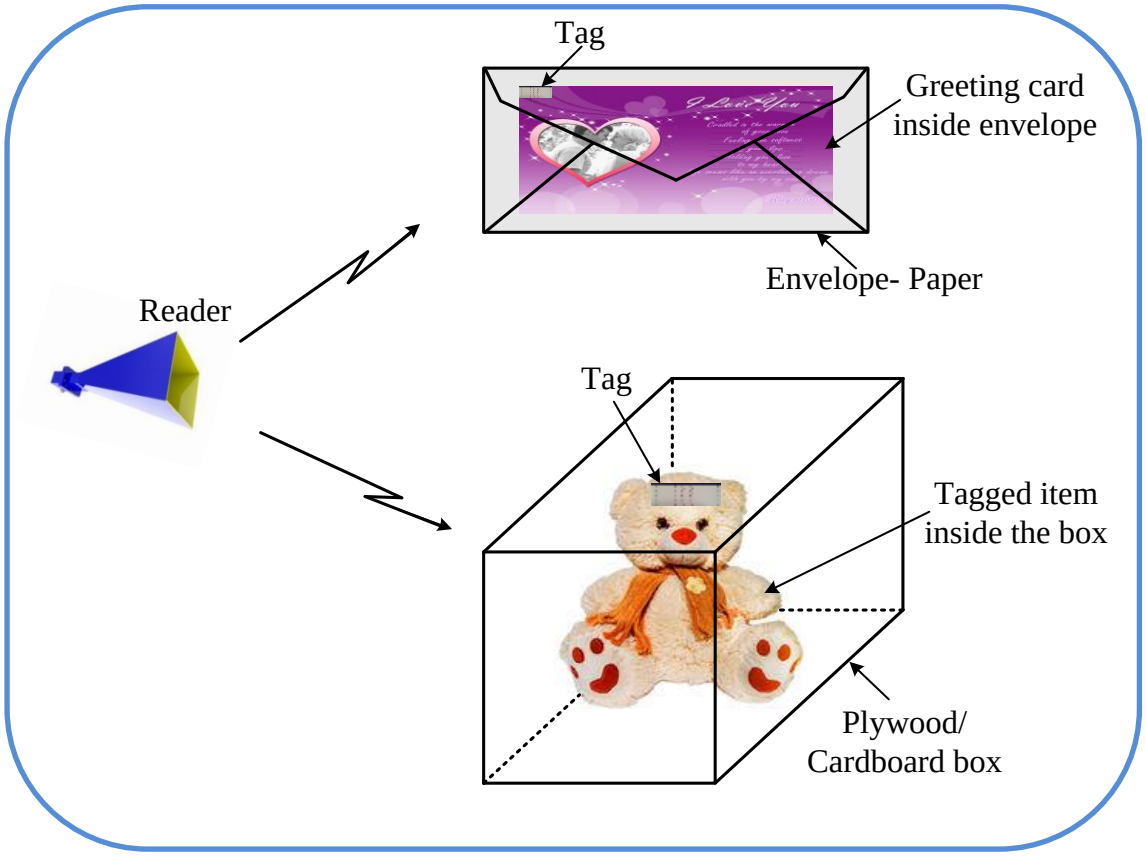

Figure 5-9 NLOS reading scenarios.

The measured result and the images of different types of media are shown in Figure 5-10. For all cases, except for a tick wood (2 cm thickness), the system is adequately capable of detecting the presence or absence of the tag from the different measured signal levels in the cross-polar RCS of the tag. This is a significant aspect of the system because it provides a None optical LoS secured identification of objects inside an envelope and in the boxes and

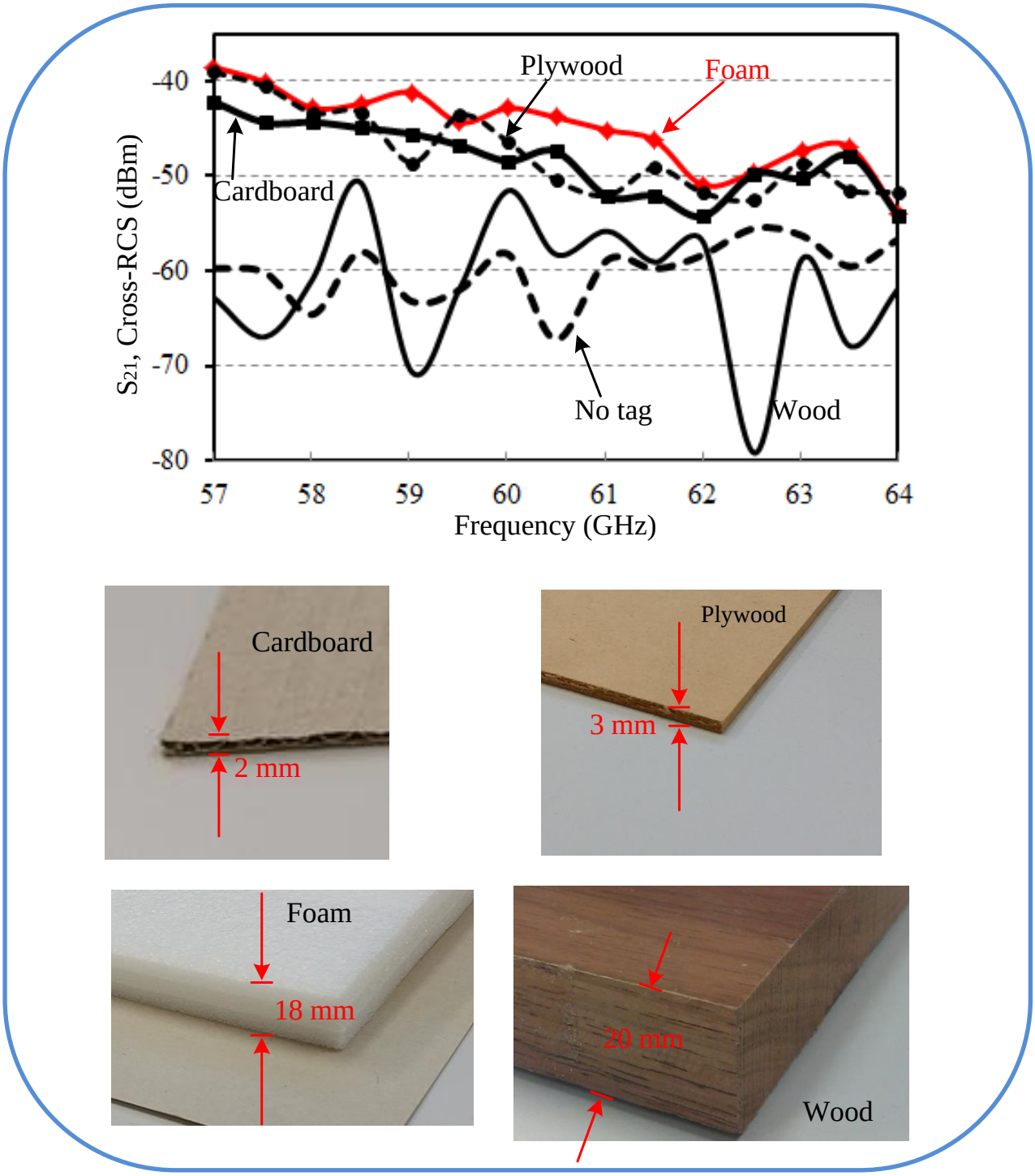

Figure 5-10 Effect of various barriers on reading process.

pallets without opening them. The mm-wave signals are very lossy in those media (plywood, cardboard, etc) and mainly require a clear line-of-sight reading condition. However, as the system is cross-polar basis, hence the receiver is capable of detecting even a weak signal due to the natural cancelation of background noise. This provides a substantial advantage for the reading process. This simply means that in practical scenarios, the tagged objects can be packaged without affecting the data decoding process. It is important to emphasize that the

results in Figure 5-10 are without any calibration process. Obviously, if the environmental effects are cancelled out with a predefined calibration process, then much cleaner signal level differences between the two cases is observed. This process may ease reading of the tag through 2 cm thick wood as well.

5.6 Bending effect on tag performance

In real identification and tracking applications, the attached tags, whether barcodes or RFID types, are vulnerable to bending circumstances. This means that when the tag is attached to an item for identification purposes, based on the shape of the item, the tag may not necessarily be in a flat configuration. This issue affects the performance of the tag in its decoding process. As the tag size increases, bending starts to be a serious issue as the attached tag on a wider range of items experiences the bending effect. There are very limited published works on the degradation of tag performance due to the bending of RFID tags or even barcodes [118]. The proposed tag structure in the current research is physically miniaturised one because of its mm-wave frequency band. Consequently the expectation is that bending would not be a serious issue for a wide range of products to which the proposed tag can be attached. Therefore, the system provides a fairly high robustness towards bending due to its miniaturised nature. However, it is important to explore how tag bending may affect the reading process, in a real scenario if the items are very small compared to the tag size.

It is important to clarify the idea of bending on the proposed tag performance. The final tag structure as is disclosed in Chapter 7 is a narrow strip with its width fixed at 1-1.5 cm and tag length varying from 5-10 cm depending on the demanded data capacity. Consequently, bending is expected to occur along the tag length and not on its width. Therefore, bending affects the total tag structure and not any individual printed polariser. This idea is figuratively shown in Figure 5-11.

As mentioned before, due to the very small size of the proposed tag structure, the attached tag may not experience the bending degradation effect for a wide variety of products and items. However for smaller items, the bending would be an issue in the overall system performance. To verify the performance of the proposed meander line polariser-based tag with respect to bending, small paper rolls of varying radii are prepared to which a tag can be attached. These paper tubes are denoted as S-i; i = 1, 2, 3, 4. Figure 5-12 shows the tubes along with their radius. For comparison purposes, a pencil is also included in Figure 5-12. To

better categorize the paper tubes, their radii along with the radii of some commonly used objects, such as a water bottle, an aluminum can and a pencil are summarized in Table 5-2. The second column of the table shows the curved radius of the objects to which the tag is attached. As can be seen, the radius of the biggest paper roll is smaller than that for a water bottle. The arc angle of the tag relates to the radius of the object to which the tag is attached. This arc angle also appears in Table 5-2.

Figure 5-13 figuratively shows how the object radius is related to the arc angle of the attached tag. As the length of the attached tag is fixed, the bigger objects create less of an arc angle of the attached tag.

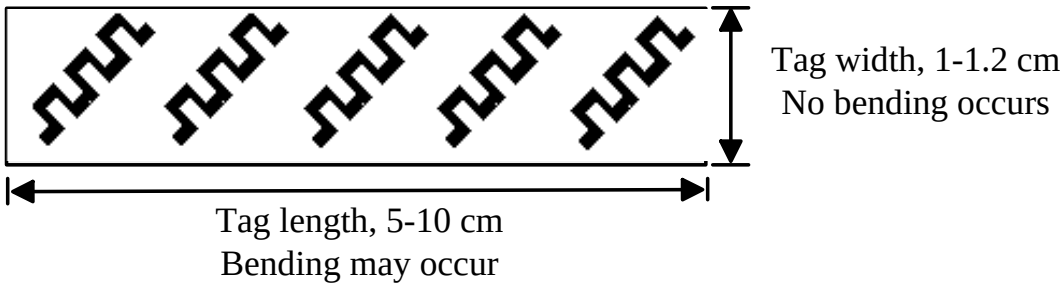

Figure 5-11 Expected bending on tag length.

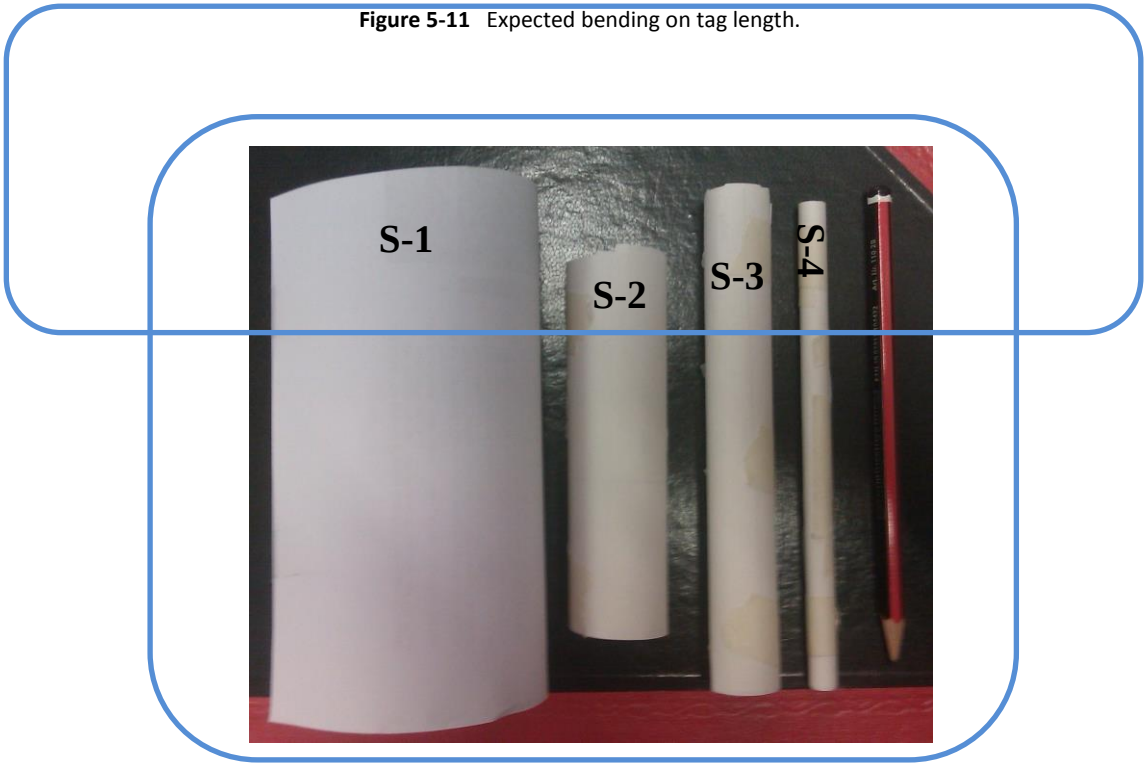

Figure 5-12 Different paper tubes with varying radii.

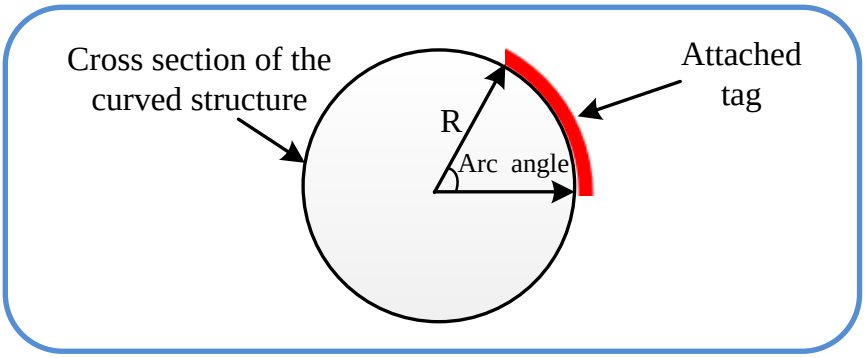

Figure 5-13 Relation between arc angle of attached tag and radius of objects.

Table 5-2 Dimensions of paper tubes and some well-known items.

Attached items	Curved radius, R (cm)	Arc angle (°)
Paper tubes S-1	2.5	34°
Paper tubes S-2	1.25	68°
Paper tubes S-3	0.85	101°
Paper tubes S-4	0.35	245°
Aluminium can	3.25	26°
Water bottle	2.75	31°
Pencil	0.4	214°

Figure 5-14 shows the measurement set up for the bending effect of the tag. Again two separate antennas are utilised as Tx and Rx which are located at 10 cm distance to the reading pole. Antennas are connected to the VNA and the transmit power of the VNA at 60 GHz is -5 dBm. The measured cross-polar components of the backscattered signal from various curvatures are depicted in Figure 5-15. For objects bigger than S-1(R = 2.5 cm), bending has a negligible effect on the received power level from the printed tag. Examples include a water bottle and aluminum can. This clearly confirms system robustness for a wide variety of objects. In other words, any object bigger than a water bottle experiences no bending effect on the proposed technique. For objects on which their radii are R< 2.5 cm, the received power level gradually decreases. However, the receiver still would be able to separate the signal of a bent tag from a "*no tag*" case. Only for items smaller than S-4 (0.35 cm radius), like a pencil, bending significantly degrades the system performance. For those items, the received signal level is only 5 dBm higher than that of "*no tag*" case, which may create

uncertainty in the reading process. From a result, it can be concluded that items with curvature radius of more than 1.25 cm have an acceptable performance when the tag is attached in the proposed technique.

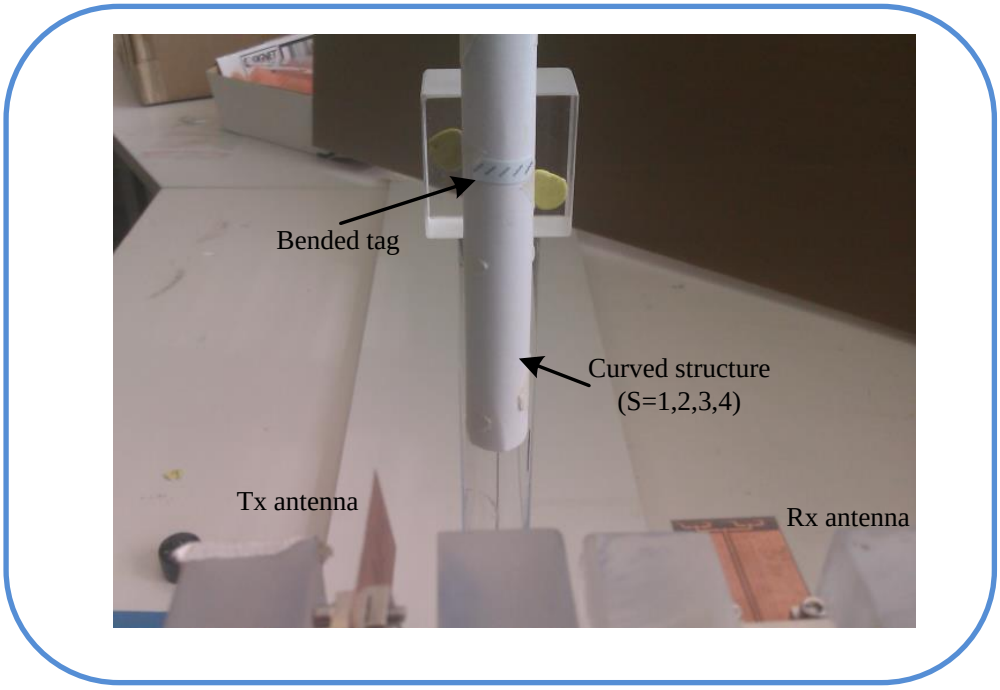

Figure 5-14 System structure for bending effect measurement.

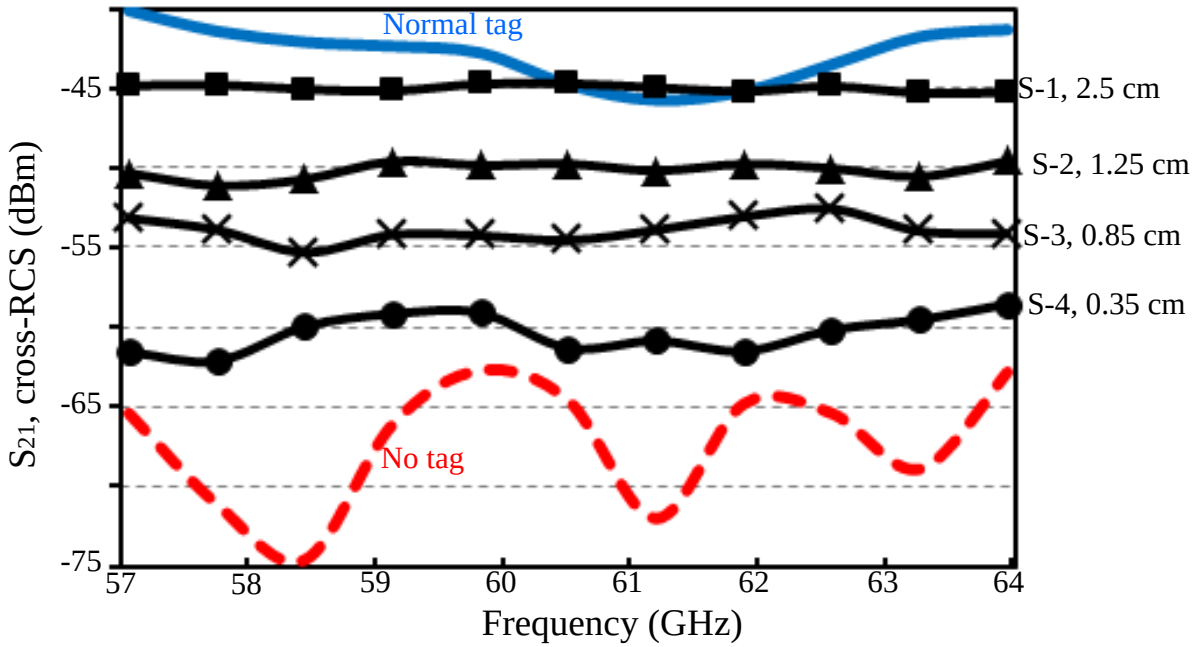

Figure 5-15 Measurement result based on different tag bending scenarios.

5.7 Conclusion

In this chapter, printed meander line polarisers were considered in more detail. As the tag is cross-polarised based, the performance of the meander line polarisers directly alleviate the whole system capacity and performance.

First an analytical model of the reading scenario was developed based on radar theory. In the proposed equivalent network of the system, the effects of Tx and Rx antennas, as well as the connecting cables and connectors were considered. Then the tag was considered in the communication channel between Tx and Rx antennas. Multipath and reflection from objects around the tag were also reflected in the analytical model. The system was analysed mathematically and it was shown that the system is very robust to multipath interferences.

Moreover, it was shown that co-polar based systems are very vulnerable to changes in the reading zone and they require frequent system calibration. In contrast, the proposed cross-polar system only involves one single calibration process and the tag movement or other changes in the reading environment do not affect system performance. This issue was nominated as a significant advantage of the proposed technique compared to other current approaches in RFID applications, which are normally co-polar based.

Different measurement scenarios were considered for confirmation of the analytical model of the system. First, a printed meander line-based tag was attached to a bottle of water. Then an etched out printed meander line-based tag was considered as the negative image of the normal printed meander lines for attaching to an aluminum can. In both cases, the tag reading process was successfully accomplished. While the effects of the water bottle and aluminum can without any attached tag were almost negligible in cross-polar direction, the presence or absence of an attached printed tag could be easily detected by the reader system in a real scenario. This step confirmed a noticeable potential of the proposed theory with respect to other techniques in the RFID applications. Most proposed approaches in a chipless RFID system normally face difficulty in reading the tag in the presence of highly reflective items.

Next, the system was tested for NLOS conditions. Different types of barriers were placed between the tag and reader and then the system performance was measured. It was shown that the reader easily detects the presence or absence of printed polarisers for a wide range of barriers including, plywood, cardboard and paper. This suggests huge potential for the

proposed system on reading the tagged objects with an envelope or inside the box without the requirement for opening them.

In the last part of this chapter, the effect of tag bending was considered. While tag bending restricts the performance of the most chipless RFID systems, and there are not many published works in this area, the proposed tag structure showed a very good performance for a bent tag. This was initiated by the mm-wave band of operation, which resulted in miniaturised tag size with very low bending vulnerability. Only for objects that are very small and narrow, a pencil for example, the bending may affect the reading process in the proposed chipless system.

The very successful performance of the proposed meander line as an effective EM-polariser in harsh environments suggests a very robust system. Considering that all the measurements were accomplished in a real laboratory environment using a poorly printed tag, it appears that the proposed system for chipless RFID systems is fully practical for industrial applications.

Chapter 6 Reader antenna

6.1 Introduction

The working basis of the proposed cross-polar image-based chipless RFID system has already been discussed in the last three chapters. Chapter 3 has shown that the linearly polarised interrogation signal is converted to an orthogonally polarised wave through EM-polarisers on the tag surface. The backscattered signal is picked up by the linearly polarised receive antenna that is orthogonally oriented in respect to the transmit antenna. It was also discussed in Chapter 3 that the proposed data encoding through EM-image of the tag requires a very fine scanning of the tag surface which is technically possible only at mm-wave band of 60 GHz and higher frequencies. There are some more technical and operational requirements for the reader that suggest a special antenna unit for the reader system. This chapter introduces a suitable in-house antenna development for the reader for the proposed technique of the cross-polar image-based system.

This chapter is organised as follow: it first reviews the technical and operational necessities of the reader antennas for the proposed technique. This part builds the basis of further activities in the rest of the chapter. Then the available or proposed antennas at the 60 GHz band are reviewed to confirm that "off-the-shelf" products are not suitable for the demanded requirements in the proposed approach.

When the actual demand for designing a new antenna set at 60 GHz is established, the process of antenna design is introduced. Material characterisation at the intended frequency band of 60 GHz, the proposed array of printed dipoles, the incorporated feeding network and finally the measurement results of the antenna characteristics are discussed respectively in detail. The developed antennas are used to read the proposed tag as introduced in the previous chapters.

6.2 Technical and operational requirements of the antenna

In this section, it is intended to derive all the technical and operational requirements of the reader antenna in the proposed technique. Based on these necessities, the antenna type and its characterisations are later constructed.

As the system is based on the separation of transmit and receive signals through an orthogonal polarisation scheme, the ability of the antenna to distinguish two polarisations is very important. This characteristic of the antenna is known as its cross-polar level (CPL). The CPL defines the quality of the signal polarisation. In other words, the ratio of the desired polarisation to the orthogonal/cross-component is known as the antenna CPL:

$$CPL = \frac{Desired\ \ field\ component}{Cross-polar\ \ field\ component} \quad 1 \le CPL \le \infty \ ; \ CPL(dB) = 20 \times \log(CPL) \quad \textbf{(6.1)}$$

In the proposed system, both transmit and receive antennas are close to each other and the transmit module doesn't require any switching mechanism. Therefore the high CPL, in order of 15-20 dB, is essential for the antennas. Otherwise, the direct signal leakage from transmitter to receiver due to the low isolation of the antennas may saturate the receiver and affect the tag reading process. The higher the CPL, the better is the receiver sensitivity with respect to the cross-polar tag response.

As was already shown in Chapter 3, a fine EM-image resolution on the tag surface is only accomplished through an advanced imaging technique, like SAR. In the SAR-based system, the reader moves around the tag to create a synthetic aperture. The received signals by the antennas at the designated positions are collected for further processing. This mandates a wide azimuth radiation pattern of the antenna to make it possible for illumination of the tag surface from different view angles. As is discussed in the next chapter, the length of the synthetic aperture depends on the tag size and the reading distance, however, the aperture size normally varies between 15-25 cm for a 10 cm reading distance.

Figure 6-1 shows the reading distance and the required half power beamwidth (HPBW) of the antenna in the azimuth direction. To consider the worst case, the synthetic aperture of 30 cm is considered in Figure 6-1 while the reading distance is 10 cm. The angle θ is therefore:

$$\theta = \tan^{-1}\left(\frac{10}{15}\right) = 33^{\circ} \quad \textbf{(6.2)}$$

And from (6.2), the HPBW would be:

$$HPBW = 2 \times (90^{\circ} - \theta) = 114^{\circ} \quad \textbf{(6.3)}$$

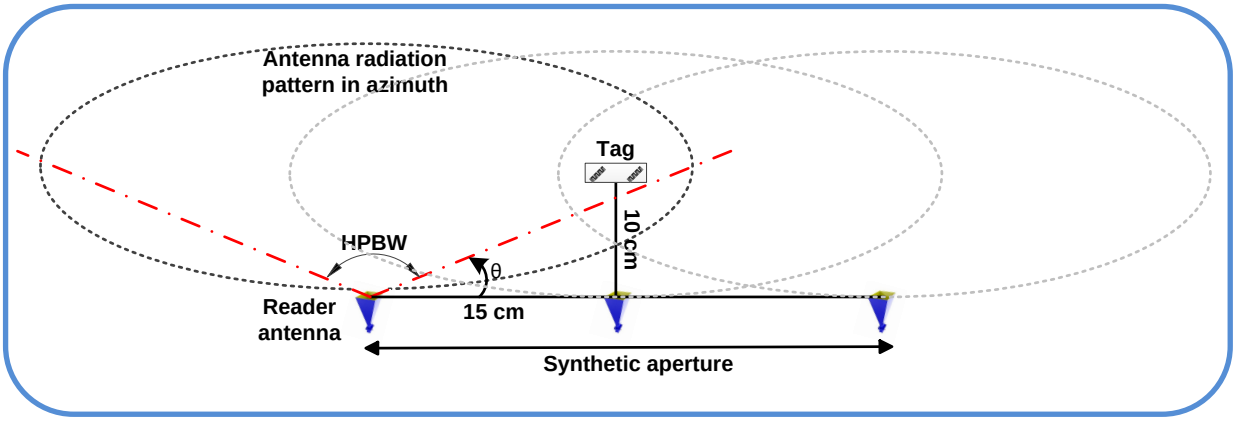

Figure 6-1 Required HPBW of the antenna.

It should be noted that the calculated HPBW is based on the linear trajectory of the reader around the tag. However, as shown in Figure 1-4 of Chapter 1, the actual path is a curve route which provides more flexibility for the antenna radiation pattern in the azimuth direction. The 115° is then selected as the worst case for the HPBW of the reader antennas.

The radiation pattern of the antenna in the elevation angle is not required to satisfy any specific limitations or requirements; however it is desirable if the antenna energy focuses only on the tag surface. This minimises the reflection from objects around the tag. It was already justified that the proposed system is very robust to multipath interferences, therefore no strict limitation is applied on the antenna's elevation radiation pattern. However, this tapered beam pattern limits the energy wasted in unwanted directions.

One of the requirements of the SAR technique is the relative movement of the reader and the tag. In the proposed technique, it is always assumed that the tag is fixed and the reader moves around the tag. Therefore, the size of the reader antenna shall be kept small and light weight for ease of movement for handheld applications.

In Section 3.3 the frequency band of operation has already been agreed to be 60 GHz. The exact required bandwidth of the antenna depends on the utilised technique for imaging purposes. As it will be discussed in the next chapter, large bandwidth of the system may be useful to provide a fine range resolution for the maximum data encoding capacity. Therefore, it is desirable that the antenna would be able to cover the whole ISM frequency band of 57-64 GHz. This implies around 12% bandwidth requirements for the antenna.

In conclusion, it appears that the followings are the intended requirements of the reader antenna(s) for the proposed cross-polar image-based chipless RFID system:

(i) Operating at frequency band 57-64 GHz.

(ii) High cross-polar level in boresight direction, CPL > 15dB.

(iii) Fan-shaped radiation pattern with wide azimuth beamwidth >115° azimuth and desirable elevation beamwidth <15°.

(iv) Light weight and small size for handheld applications of the reader.

In the following section, a review of the reported 60 GHz antennas is presented followed by the proposed double side printed dipole array (DSPD) antenna at 60 GHz.

6.3 Off-the-shelf products

It was discussed that the 60 GHz band has already been used for inter-satellite communication links or for highly secure terrestrial mobile communication. The recent release of 57-64 GHz as an ISM band accelerates many products on this band for public usage [32, 94, 113, 119].

However, the higher attenuation of signals related to the 60 GHz band suggests a high gain antenna for short range communications links, in the order of few kilometres. Few available antennas have been found on the market which work on the intended frequency band, however their radiation pattern and impedance bandwidth appear to be unsuitable for the purposed chipless RFID system. Nokia's radio link Metro Hopper [120] is a high data rate communication link but only covers 57.2-58.2 GHz and has a large antenna size that is not suitable for the proposed chipless RFID application. Proxim [121] suggests products at 60 GHz which utilise antennas for covering the whole band of 57-64 GHz. The gains of antennas range from 25-35 dB_i. There is no information about the radiation pattern but high antenna gain suggests a large aperture size and narrow radiation pattern, which do not satisfy the required specifications for the image-based chipless RFID application. Moreover, no information about the polarisation cross-polar level is disclosed. Normally the ISM band of 57-64 GHz has been taken by companies for providing high data rate communication in point-to-point links [92, 93].

Therefore, it is expected that the proposed antennas in those applications have high gain and a narrow radiation patterns. Moreover, the antenna size is not an issue in those applications. Therefore, it is unlikely to be able to find an off-the-shelf antenna, which satisfies the necessities of the reader antenna for the proposed chipless RFID application.

6.4 Proposed array of printed dipoles

The general specifications of the required antenna outlined in Section 6.2 govern the type of suitable solution for the proposed reader antenna. One may suggest that an array of printed dipole antenna is a suitable candidate to meet the specification requirements. The printed antenna adequately satisfies the requirements of low profile, light weight and low cost attributes of the chipless RFID system. Dipole antennas provide wide radiation patterns in the azimuth direction, while their HPBW in the elevation angle depends on the dipole length. Moreover, the array configuration also provides the opportunity for controlling the beamwidth in the desired direction. Dipoles are normally linearly polarised antennas and are able to provide adequate cross-polar level for many applications. The compact size of the dipoles is another positive aspect for the proposed system. A printed dipole enjoys a few advantages over a microstrip patch antenna. They provide wider bandwidth, lower loss and less parasitic radiation of feed lines [122-125]. The candidate antenna is a double side printed dipole (DSPD). When compared with a single side printed dipole, the DSPD yields broader bandwidth and higher gain [126, 127].

Nesic [122] reports a one-dimensional array of printed dipoles fed by a microstrip line at 5 GHz with 7% bandwidth. The antenna works on its third resonance so provides higher gain than that of its first resonance. However, the very low antenna bandwidth on its third resonance has been mitigated by penetrating the feed line between two slots. No information on the radiation pattern of the antenna was disclosed in the report. Scott [127] shows a microstrip-fed printed dipole array using a microstrip-to-coplanar stripline (CPS) balun. In [122] and [127], the balun were not easy to match the impedance, and the structures were too big and bulky, hence, it was complicated to build an array structure [128].

Brankovic patented a pentagonal dipole antenna on a 64-element array configuration yielding 25% bandwidth at 60 GHz [129]. The radiation pattern of this work is not wide in the azimuth direction, and also no information of the cross-polar level was declared. Considering the pentagonal radiator shape, the lower cross-polar level is expected than that of

a normal dipole. Suh and Chang [128] report a 30 GHz printed dipole that has microstrip-fed coplanar stripline Tee junctions and yields 3% bandwidth. Alhalabi [130] showed a high-efficiency array of printed dipoles designed at 22-26 GHz. Varying feed line lengths create prescribed phase shifts between array elements. The same author also proposed a 60 GHz single dipole antenna [131] suitable for laptops and portable communication devices. From the above reviews it can be concluded that none of the reported antennas at 60 GHz are suitable for the proposed RFID system, However, the approaches proposed in [130] is generally followed to build a suitable reader antenna for the proposed application. As discussed before, the reader antenna for the proposed application requires satisfying a set of specifications that are necessary for different reasons. An array of DSPD fulfils all of the requirements outlined previously and repeated in Table 6-1.

Table 6-1 Technical and operational requirements of the reader antenna

Centre Frequency	60.5 GHz
Bandwidth	12%
Radiation pattern	Maximum 15° on E-plane Minimum 115° on H-plane
Cross-polar level	>15 dB
Substrate	✓ Low thickness for high cross-polar level ✓ Stable electrical and mechanical performances on mm-wave region
Gain	Between 5-10 dBi
Dimension	As small as possible(centimetre order)

In the design process, the first step is to select an appropriate substrate for the printed dipole antennas. The suggested dielectric is the Taconic TLX-8 since the authors group has an extensive experience with its performance at 24-27 GHz [132]. However, as the constitutive parameters, such as dielectric constant ε_r and loss tangents $tan\delta$ of Taconic substrate TLX-8, are not known at 60 GHz, a special test jig is built to measure the substrate parameters at 60 GHz. The next step is to design the dipole as the array radiating element. The dipoles are equipped with an unbalanced feed line which then is converted to a microstrip line. A microstrip to coplanar waveguide (CPW) feedline transition facilitates a V-type input connector assembly to be added with the array antenna. The array structure is precisely optimised to cover the entire band of 57-64 GHz yielding 12% bandwidth at 60 GHz. The flowchart of the DSPD array antenna design that yields a wide bandwidth and high cross-polar level for the image-based chipless RFID reader is shown in Figure 6-2. Each section of the design process outlined in Figure 6-2 is presented separately, and then the fabricated array is tested proving its actual potential for the proposed application.

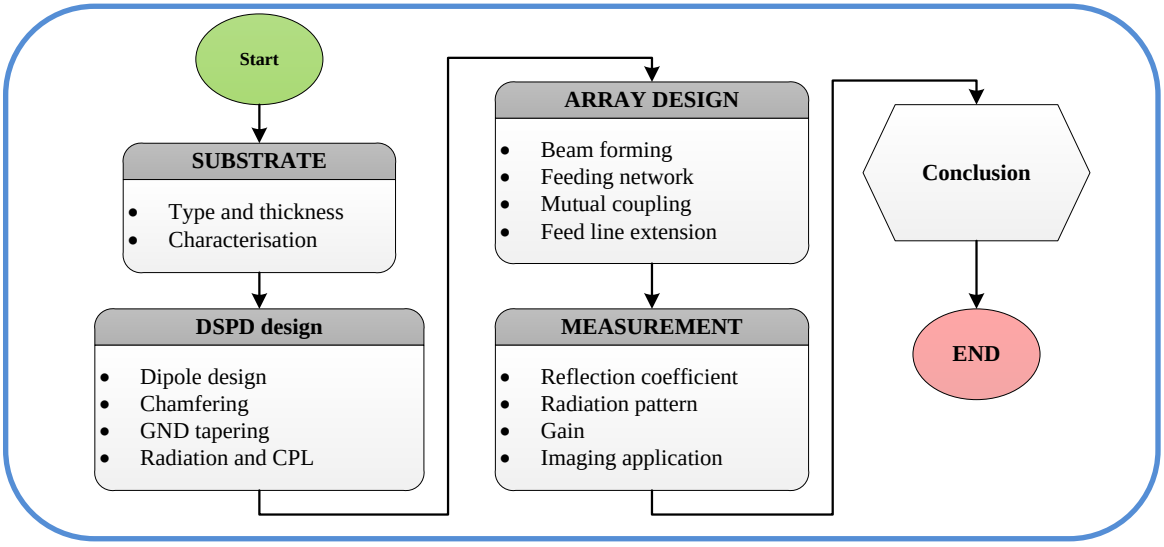

Figure 6-2 Design flowchart for array of DSPD's.

6.5 Substrate selection and characterisation

6.5.1 Substrate selection and thickness

The first step of antenna design is the selection of the substrate. The frequency of operation and required bandwidth govern the selection of the substrate. Substrate thickness, relative permittivity, loss tangent, copper thickness, and finally mechanical and thermal stabilities are the important factors of the substrate at 60 GHz. Precision in the design and substrate properties are critical for design success considering the 5 mm wavelength of the 60 GHz band.

As introduced previously, Taconic TLX-8 would be a suitable candidate as it satisfies many of the aforementioned factors [133, 134]. Its low dielectric constant enhances the antenna efficiency and bandwidth and its thin thickness is favourable for the high cross-polar level [18]. The substrate thickness is the first parameter to be selected. It is normally bonded by two contradictory factors. A thin substrate is required to minimize surface wave and hence for an efficient radiator while large required operational bandwidth of 12% suggests a thick substrate [135]. The substrate thickness should satisfy (6.4) to ensure the suppression of higher order radiation modes on the dielectric surface [136]. Based on (6.4), the substrate thickness must be less than 1 mm at 60 GHz.

$$\text{Thickness} < \frac{\lambda_0}{4\times\sqrt{\varepsilon_{reff}}-1} \approx 1.06 \text{ mm} \qquad (6.4)$$

In (6.4), the wavelength(λ_0) is between 4.68-5.26 mm for 57-64 GHz. ε_{reff} is the effective permittivity of the substrate. Considering the available commercial Taconic products, the Taconic TLX-8 with 0.127 mm thickness is selected. This thickness adequately satisfies (6.4) and ensures that only one surface wave, TM_0 with zero cut-off frequency exists in the substrate [137]. This thin substrate also enhances the cross-polar level of the antenna which is a critical aspect of the design [138].

6.5.2 Substrate characterisation

The knowledge of the actual constitutive parameters of the substrate is vital for accurate design, especially in the mm-band where dimensions based on the substrate characteristics, such as the relative permittivity and loss tangent, are tolerance-critical. Today, most substrate manufacturers specify the dielectric parameters of their materials at 10 GHz. Consequently, in the realised design at mm-band, frequency shifts attributed to permittivity deviation commonly occur [139]. Microwave measurement techniques to determine substrate permittivity and loss tangent at specific frequencies are [140, 141]: *(i)* transmission and reflection, and *(ii)* resonance techniques. Transmission and reflection techniques can be used to obtain the real part of the relative permittivity for a high or low loss specimen, but lack the resolution to measure low loss tangents. Resonant techniques are only suitable for low loss materials since the resonance curve broadens as the loss increases [142]. Usually, dielectric measurement using a resonance technique provides higher accuracy than that obtained from a transmission and reflection technique. It is, therefore, considered the most accurate method for dielectric constant and loss tangent measurement of planar structures. Considering the structural dimensions at the mm-band, the substrate integrated waveguide (SIW) resonators approach is proposed for substrate characterisation at the V and W-bands [140].

A Taconic [133] published data sheet of the TLX-8 at 10 GHz reveals the following information: $\varepsilon_r = 2.55$ and $tan\ \delta = 0.0019$. To measure the actual electrical parameters of the substrate at 60 GHz, the SIW cavity resonators are designed and fabricated at this band. Propagation and attenuation constants of a SIW resonator are related to the modal expansion theory of a rectangle waveguide [141]. Expression (6.5) shows the equivalent dimensions of the rectangle waveguide on which *a*, *b*, *d*, and *s* are defined in Figure 6-3. The number of via holes are 10 and 11 for *a* and *b* directions respectively as shown in the photograph of the sample SIW in Figure 6-4. The resonance frequency of the rectangle SIW resonator for TE_{mn0}

mode relates to the resonance frequency of the rectangle waveguide and can be calculated by (6.5) [143]:

$$f_{mn0} = \frac{c}{2\pi\sqrt{\varepsilon_r}}\sqrt{\left(\frac{m\pi}{a_{eff}}\right)^2 + \left(\frac{n\pi}{b_{eff}}\right)^2} \tag{6.5}$$

where a_{eff} and b_{eff} can be derived from (6.6), c is the light speed in free space, and ε_r is the effective dielectric constant.

$$x_{eff} = x - 1.08\frac{d^2}{s} + 0.1\frac{d^2}{x} \quad ; x = a, b \tag{6.6}$$

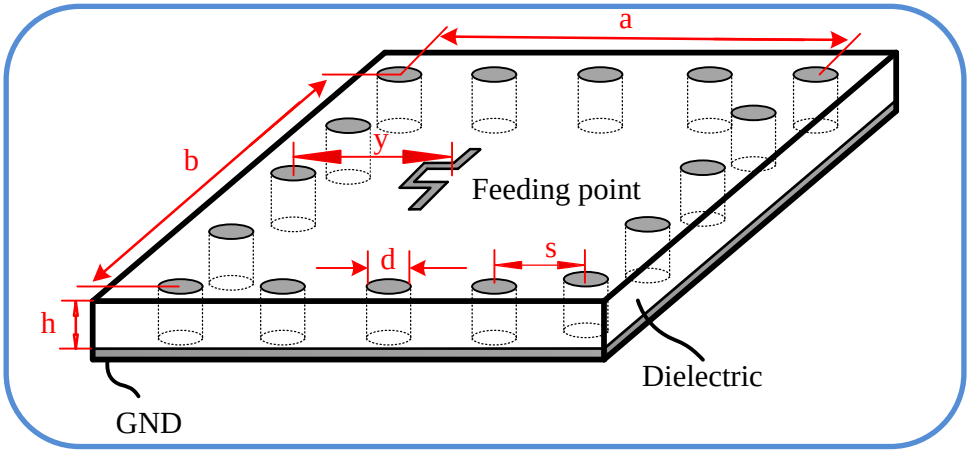

Figure 6-3 Layout of sample SIW resonator with via holes [24].

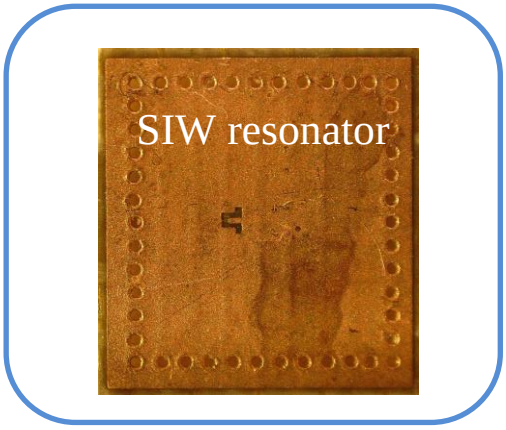

Figure 6-4 Photograph of SIW resonator for dielectric constant and loss tangent measurement of Taconic TLX-8 [140].

To find the effective dielectric constant, the proposed approach by Zelenchuk et al. [140] is followed. Six prototypes of SIW resonators are fabricated and tested to measure the substrate parameters at 60 GHz. The average dielectric constant of all six samples suggests the effective dielectric constant of the substrate, Taconic TLX-8, at 60 GHz. This average value for the six samples of SIW resonators is ε_r = 2.25. The average measured loss tangent is 0.0072 but there is a sample with a higher loss tangent. Therefore, the worst case is considered that is 0.01. These two values of the constitutive parametres of the substrate are substantially different from those for the published datasheet at 10 GHz. Table 6-2 summarises the results of the dielectric parameters at different frequencies. The new values of the substrate parameters of the substrate at 60 GHz are considered in the design process of the proposed DSPD array antenna.

Table 6-2 Dielectric parameters of Taconic TLX-8

60 GHz	ε_r = 2.25	$tan\delta$ = 0.01
10 GHz	ε_r = 2.55	$tan\delta$ = 0.0019

The measurement was performed with error correction calibration using an Agilent performance network analyser (PNA) E8361A. The accurate characterisation ensures the full wave EM solver CST Microwave Studio simulation results match with the measured data of the prototype array antenna.

6.6 Double side printed dipole

As discussed in Section 6.4, the proposed antenna is an array of double sided printed dipoles (DSPD). Hence, the first step of the design process is to design the appropriate array radiator element. The DSPD element with the design parameters is shown in Figure 6-5. The length of the dipole arm (L_a) mainly controls the resonance frequency of the dipole. It is also a function of the substrate thickness, h, and dielectric constant, ε_r. As the substrate does not cover the whole structure, the resonant length is not scaled with $1/\sqrt{\varepsilon_{reff}}$ as does an antenna in a homogeneous medium [20]. The initial value of the dipole length is related to the frequency of operation, f, and to the medium by (6.7) and (6.8) [26]:

$$Dipole\ length(2L_a) = 0.47\frac{v}{f} \quad ; v = \frac{c}{\sqrt{\varepsilon_{reff}}} \tag{6.7}$$

$$\varepsilon_{reff} = \frac{\varepsilon_r + 1}{2} + \frac{\varepsilon_r - 1}{2}\left[\sqrt{1 + \frac{12h}{w_a}} + 0.04\left(1 - \frac{w_a}{h}\right)^2\right] \quad (6.8)$$

In (6.7) and (6.8), v is the velocity of EM wave propagation inside the substrate, c is the speed of light in the free space and the rest of the parameters are defined in Figure 6-5. Based on (6.7) and (6.8), the required length of the dipole arm is 1.2 mm. This initial length is entered in full-wave EM solver CST Microwave Studio and the design is optimised to meet the specification requirements. After parameter sweeping in the CST, the simulated dipole arm length is 1 mm. The shorter length of the dipole through full wave simulation is due to the fact that the physical length of the dipole is always bigger than its electrical length. Hence the 1.2 mm dipole arm corresponds to the resonance at lower frequencies than that expected through (6.7).

The width of the dipole arm (W_a) is independently optimised to provide 50 Ω input impedance for the individual dipole. However, on the other hand, the parallel suspended feed line of the dipole arm is transformed to a microstrip line above the ground plane. The microstrip feedline is also expected to provide the 50 Ω input impedance for the beamforming network of the array antenna.

The width of the microstrip line, $W_{f,}$ is also designed independently. Two widths of W_a and W_f obviously are different as they are different types of transmission lines. Matching of these two transmission lines with different widths is manipulated by changing the chamfering depth, C_d. To enhance the bandwidth and performance of the array radiator, chamfering of the dipole element and tapered ground plane at the suspended parallel stripline to micro-strip line transition are used.

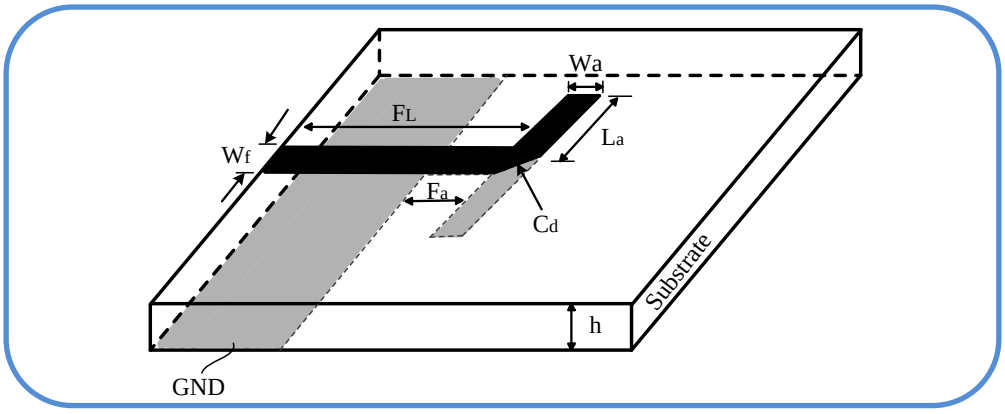

Figure 6-5 Single dipole, W_f = 0.37, F_L = 1.05, F_a = 0.55, W_a = 0.19, L_a = 1, C_d = 0.2 and h = 0.127, all in mm.

These techniques yield more than 12% bandwidth at 60 GHz while conventional design yields 7% bandwidth [20]. The following sections describe the matching techniques envisaged to enhance the radiator performance.

6.6.1 Dipole chamfering

Dipole antennas are inherently unbalanced circuits and create distortion in radiation patterns. Connecting a dipole to a feed line requires a balun network to match balanced and unbalanced circuits [143, 144]. There are many different types of balun networks based on the dipole antenna structure. Chen [145] suggests a double sided feed network on the substrate as the balun network for the planar dipole antennas. The bottom-tapered ground transition is designed to provide an impedance matching tuner with balanced output. The designed feeding network of the dipole antenna with the tapered balun transition is tuned by the angle of the tapered ground plane for impedance matching and balanced output. Almost the same balun structure is followed for the proposed array antenna. As shown in Figure 6-5, the double sided feed line provides a smooth transition between the unbalanced and balanced currents of the line that is connected to the ground plane and the dipole feed respectively. This configuration also simplifies the balun network. The proposed balun network does not require the bottom-tapered transition as suggested by Chen [145]. It is discussed in the next section why an abrupt bottom transition is selected instead of a tapered one.

As discussed earlier, chamfering of the dipole edge is required to match two different widths of the feedline (w_f) and dipole arm (w_a). Moreover, the right angle of the microstrip line creates an extra capacitance and also changes the electrical length of the line [146]. These two factors affect the impedance matching of the printed dipole structure and create signal reflection from the dipole and the feedline. Chamfering of the dipole edge where the dipole arm is connected to the feedline and the ground plane compensates those two effects. For symmetry, both dipole arms at their right angle transitions are supposed to be chamfered. However, from investigation in full-wave CST Microwave Studio simulation, it was found that only top arm chamfering provides best results. Figure 6-6 shows the input impedance return loss (S_{11} in dB) versus frequency for three cases: top arm, both arms and no chamfering at all. Considering the effect of different chamfering scenarios on the input impedance, the maximum RL of 27 dB is obtained with top arm chamfering. As the bottom arm is directly connected to the ground via the bottom feedline structure, it has a minor effect

on the impedance matching. In conclusion, only the top arm chamfering provides the optimum impedance matching.

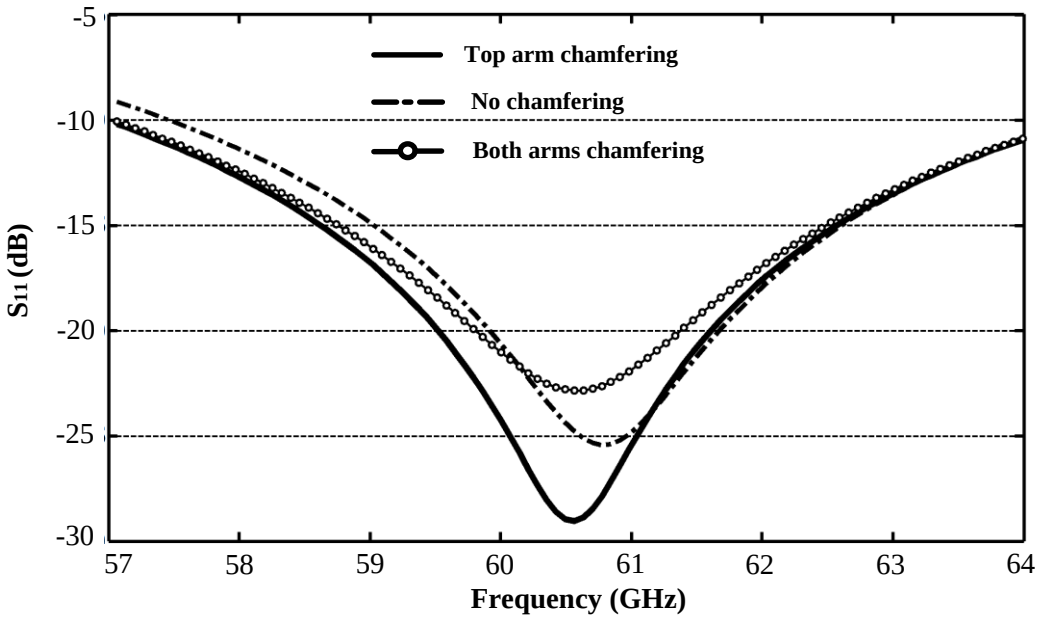

Figure 6-6 Chamfering effect of dipole arms on impedance matching.

6.6.2 Ground connection tapering

As stated above, to improve the performance of the dipole through a balun network, a tapered ground connection for the bottom feedline of the balanced feed network of the DSPD antenna was suggested by Chen [145]. The ground plane acts as a reflector for the printed dipole hence significantly influences both the radiation pattern and the input impedance. Therefore, the shape and distance of the ground plane from the dipole element determines the input impedance bandwidth, the beamwidth, gain and cross-polar level of the dipole element. The effect of the ground plane on the monopole and dipole elements' performance have been investigated in [13, 147]. Two types of ground planes, conventional (also called abrupt) and tapered ground planes, have been investigated. The effect of the tapered ground connection depends on its tapering angle. The tapering angle (α) is shown in Figure 6-7. The angle α in Figure 6-7 is changed to find the best performance of the dipole through parameter sweeping in CST. After the final result is achieved, it is compared with the conventional (abrupt) ground transition. However, the tapered connection causes a resonance frequency shift in the return loss. To accurately compare two scenarios, a few parameters of the top arm are re-tuned to have the same frequency resonances. Figure 6-8 shows the input impedance return loss versus frequency for both abrupt and tapered connections. It confirms that the abrupt

connection offers better impedance matching at the resonance frequency. This is what is normally expected for an abrupt connection. In fact, the logical expectation is to have lower bandwidth through abrupt connection than the tapered type ground connection. However, as shown in Figure 6-8, the abrupt and tapered connections successfully cover the whole frequency band of interest 57-64 GHz. Therefore, the abrupt type ground connection is selected for the proposed DSPD array antenna structure. This effect was also experienced by Alhalabi [13] over the lower frequency range of 20-26 GHz.

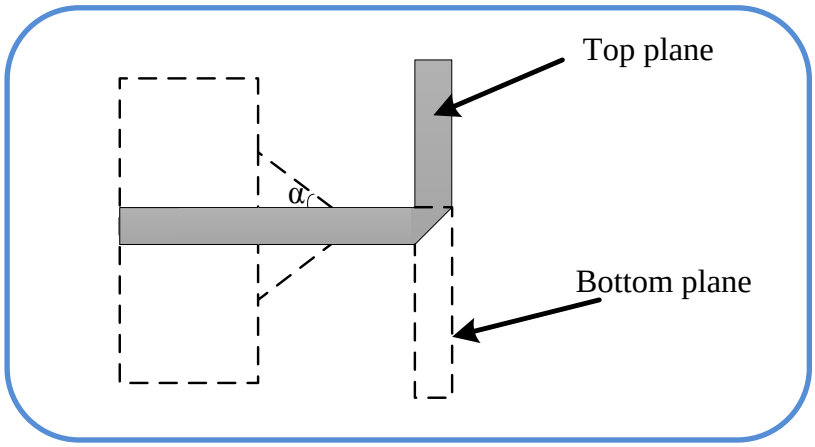

Figure 6-7 Embedded DSPD antenna with tapered ground connection.

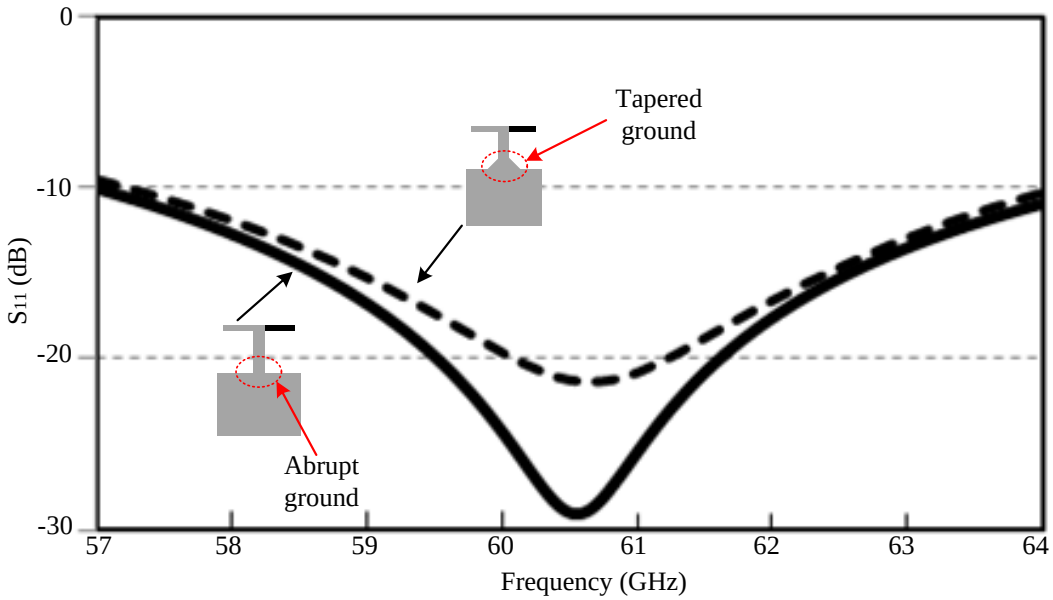

Figure 6-8 Ground connection's effect on matching of dipole.

6.6.3 Dipole radiation pattern and cross-polar level

The radiation pattern of a single DSPD is simulated with full wave EM solver CST Microwave Studio and the result is shown in Figure 6-9. The provided 3-D pattern can be presented on the E-plane and H-plane separately for better understanding. Based on the orientation of the single DSPD, the related E- and H-planes are shown in Figure 6-10. The xy plane that is the green circle in Figure 6-10 shows the E-plane, and the xz plane that is the red circle in Figure 6-10 is the H-plane of the single DSPD. The 2-D radiation patterns of a DSPD is depicted for three sample frequencies—58, 60 and 63 GHz in Figure 6-11.

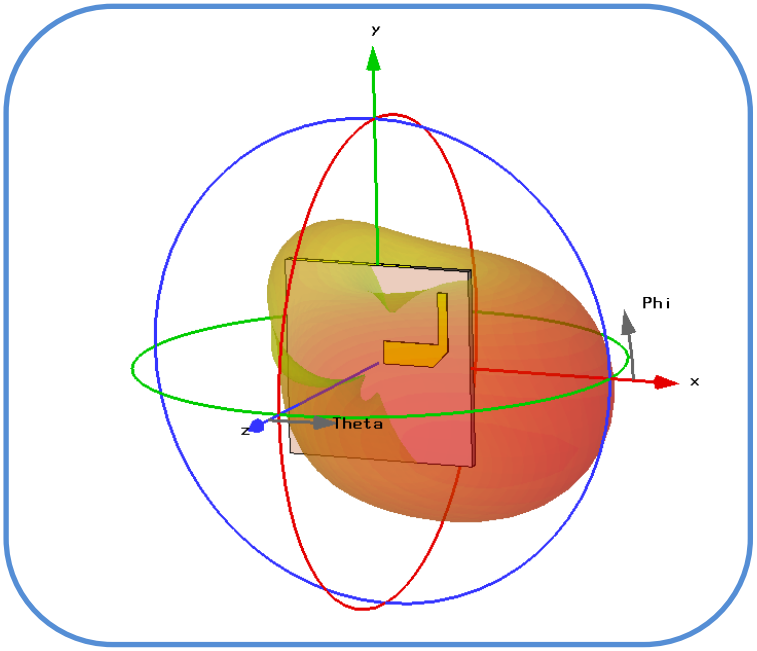

Figure 6-9 CST generated 3-D radiation pattern of double side printed dipole (DSPD) antenna.

As is shown later, the final array configuration is a linear array of dipoles which are oriented in Y-direction at Figure 6-10. Through general knowledge of array theory, one can conclude that the H-plane of the final array structure is similar to the single DSPD, while its E-plane would be different from that of a single DSPD. Therefore at this step, the H-plane radiation pattern of the single DSPD is of more interest as it shows the final H-plane of the array. The 3-dB beamwidth of the single DSPD on its H-plane, for three sample frequencies, is shown in Table 6-3.

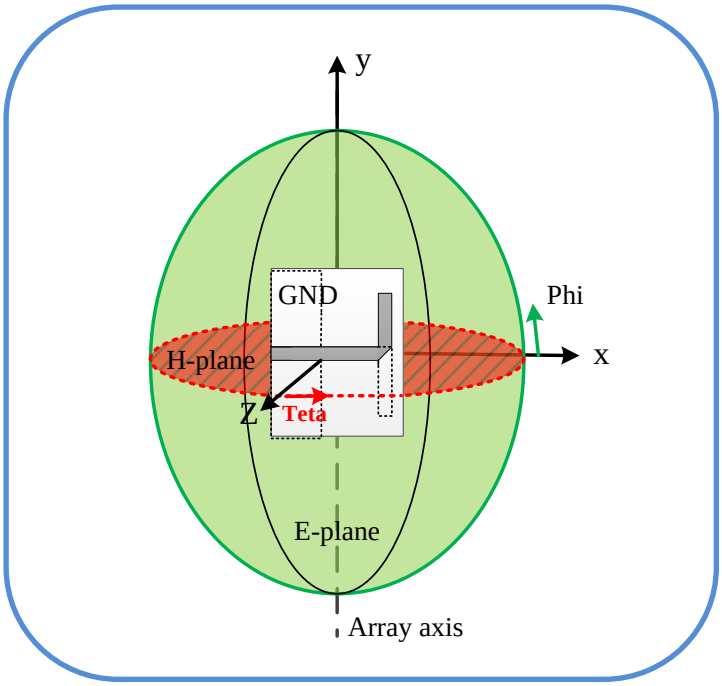

Figure 6-10 The DSPD schematic and related E- and H-planes.

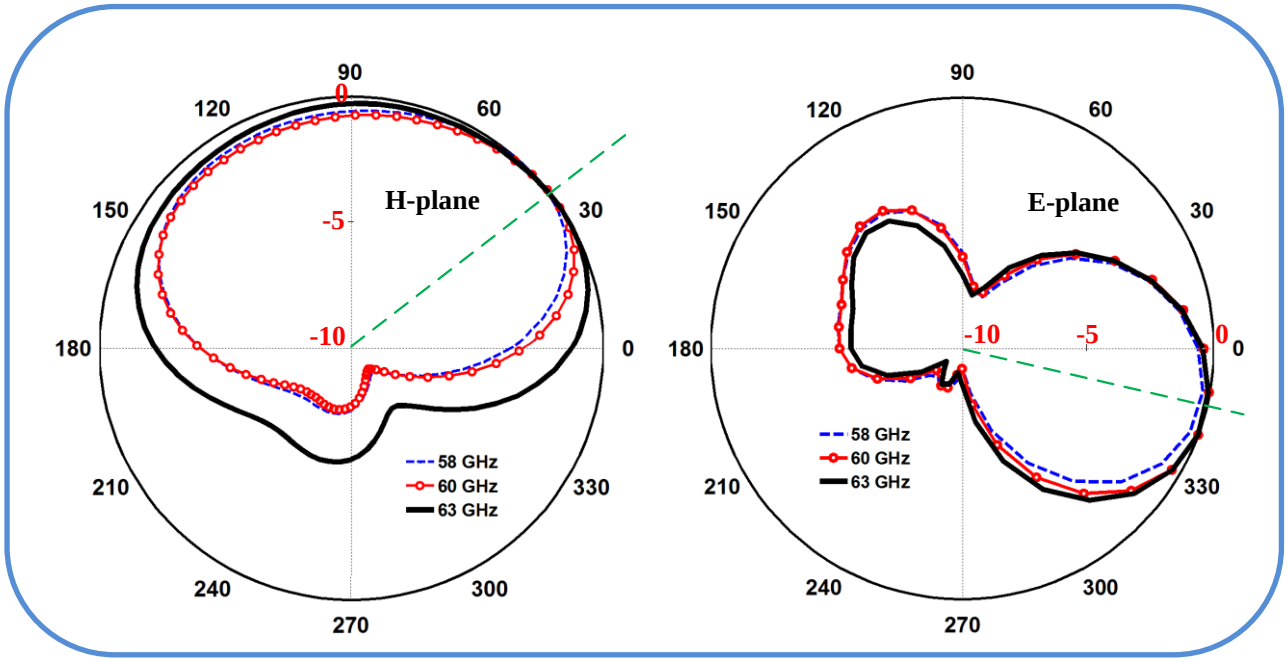

Figure 6-11 Simulated radiation pattern (E- and H-planes) of DSPD.

The values of the 3-dB beamwidth adequately satisfy the wide radiation pattern requirements of the final array as discussed in Table 6-1 of Section 6.2. This wide radiation pattern ensures that in the synthetic aperture approach, the tag's surface receives enough energy from the reader at different view angles. As is evident from the H-plane radiation pattern shown in Figure 6-11, the maximum radiation does not occur on the broadside

direction (φ=0) as expected. Instead, the pattern of a single DSPD is shifted to the left direction. This is because one side of the substrate includes the ground plan which pushes the radiation in the opposite direction. The direction of maximum radiation depends on the frequency and is approximately shown by the green-dashed line in Figure 6-11, however; it varies from -345° to -350°. This is because one arm is connected to the feed line while the other arm is joined to the ground plane via s strip.

Table 6-3 3-dB beamwidth of a single DSPD in H-plane

Frequency (GHz)	3-dB beamwidth (°)
58	194.8
60	197.1
63	201

Table 6-4 3-dB beamwidth of a single DSPD in an E-plane

Frequency (GHz)	3-dB beamwidth (°)
58	79.8
60	82.2
63	85

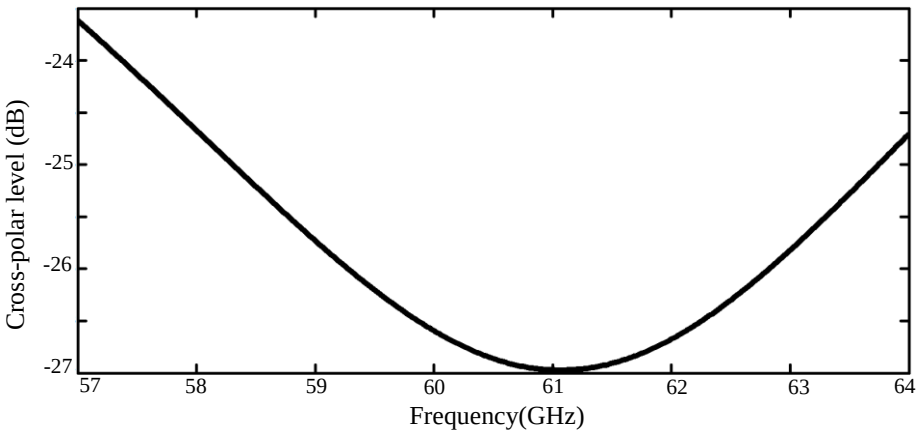

Figure 6-12 Simulated Cross-polar level of single dipole (DSPD).

Although, the 3-dB beamwidth of the E-plane radiation pattern of the final structure would be different from that of the single DSPD, for completion, the sample values of the 3-dB beamwidth are shown in Table 6-4.

As discussed in Section 6.2, the quality of the antenna polarisation known as its cross-polar level is a critical parameter in the proposed application. For the designed single DSPD, the cross-polar level is simulated by having co- and cross-polar probes in CST Microwave studio and measuring the S_{21} of the link. The simulated cross-polar level for a single DSPD is depicted in Figure 6-12. Over the entire frequency range of operation, this ratio for a single dipole is less than -23 dB. There is the opportunity of decreasing the cross-polar level by simply using the defected ground structure (DGS) [29]. However the provided -23 dB cross-polar level through the DSPD adequately satisfies the requirements of the proposed application, as is shown in the next chapter where the final signal processing results are revealed.

6.7 Array design

6.7.1 Required beamforming array

The antenna specifications discussed in Section 6.2 governs the array structure. From the beamforming aspect, as a fan shaped radiation pattern, wide azimuth and narrow elevation is required, then a linear array type would satisfy this specification. Multiple vertically aligned dipoles narrow the radiation pattern in the elevation angle. For the suggested 15° beamwidth in the elevation angle, see Table 6-1, an array of four elements would be satisfactory. The wide H-plane radiation pattern of a single DSPD as shown in Figure 6-11 fulfils the 115° required azimuth beamwidth. To select a proper feed network, the overall system structure for the image-based chipless RFID application shall be considered. In the proposed application, the antenna moves around the tag and illuminates the tag through different angles. The relative position of the tag and antenna is considered in the SAR-based signal processing to reveal the EM-image of the tag. Therefore, it is mandatory that the antenna has a unique and fixed radiation pattern shape in all positions during capturing of the backscattered signals from the tag. This is the reason why a phased array antenna wouldn't be a suitable candidate for this application as a phased array antenna creates various beam shapes on different angles [148]. From array theory, it is clear that the uniform excitation of the array's elements creates the maximum radiation intensity and the minimum 3-dB beamwidth in the boresight direction

[144]. Therefore, the requirement for a fixed fan shaped radiation pattern with the minimum beamwidth suggests a linear array of dipoles with uniform array excitation. A 4-elements array of DSPD's provides the required performance as calculated in Table 6-1.

6.7.2 Corporate feeding network

The requirement for a uniform excitation of the array elements and also having two separate Tx and Rx antennas at the reader side ease the power divider arrangement. A T-junction corporate feed power divider is one of the simplest type of power dividers and is used for the proposed application [149]. It is fully printable and low cost without any lumped element in the structure. These advantageous features make the T-junction power divider a very suitable candidate for feeding the DSPDs on the array structure. However, the T-junction power divider suffers from two major limitations. First, it utilises quarter wavelength transformer in its structure that restricts the operation bandwidth of the element. Second, it provides low isolation among output ports. The low isolation would be a major limitation for mono-static systems on which the same antenna is used for transmit and receive purposes. While in the proposed bi-static configuration, two separate antennas are utilised, therefore, the low isolation of the output is not an issue. The low bandwidth of the power divider, due to the quarter wavelength transformer, can be compensated by minor changes in the component design. Figure 6-13 shows a conventional two-way T-junction power divider and its dimensions. The length of the quarter wavelength transformer is fixed and it is intended to transform 50 Ω impedance to the 100 Ω. The length of the 50 Ω arm on each side of the

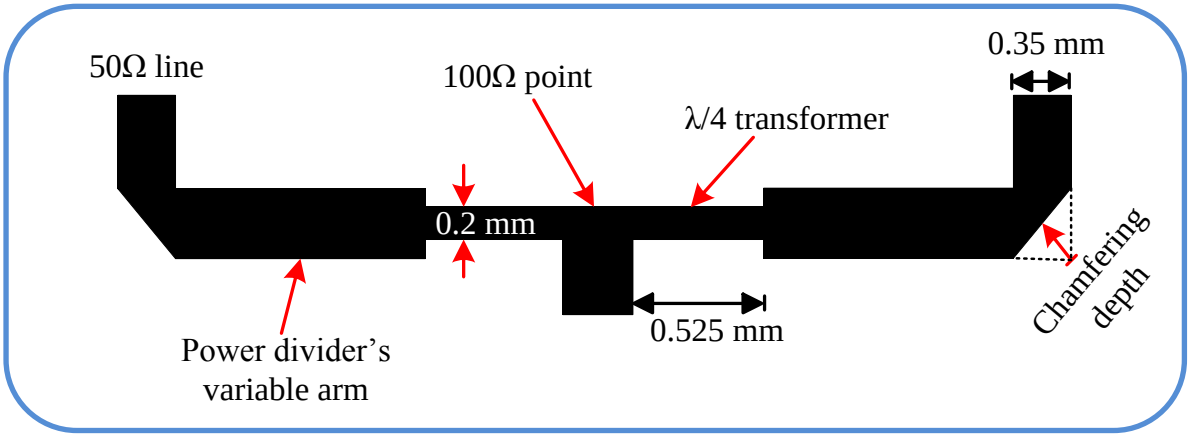

Figure 6-13 T-junction power divider.

power divider depends on the required physical distance between two connected dipoles. The chamfering depth is optimised through parameter sweep in the CST simulation tools.

The T-junction power divider, shown in Figure 6-13, normally acts properly in a narrow band operation. However, to enhance the power divider bandwidth, it is normally suggested to have a small V-notch in the dividing point of the T-junction structure, 100 Ω point in Figure 6-13. This gap is shown in Figure 6-14(a). In the current work however, it was found that a reactive stub acts better and can enhance the power divider bandwidth. The T-junction power divider with a reactive stub is also shown in Figure 6-14(b). The dimensions of the reactive stub are optimised through parameter sweeping of CST.

The corporate feed network of the proposed array antenna includes three two-way T-junction power dividers. This complete feed network is shown in Figure 6-15. As one can see, the length of the quarter wavelength transformer is the same for all three T-junctions. The lengths of the power dividers' arms vary based on the required physical distance between the radiators in the array configuration. The S-parameter of the corporate feed network is depicted in Figure 6-16. Figure 6-16 shows that S_{11} in dB versus frequency is adequately below -15 dB over the whole frequency range of operation. The minimum value of the reflection coefficient is -20.5 dB at 61.5 GHz. This is a noticeable result considering the narrowband aspect of the quarter wavelength sections in the power divider structure. Normally, four transmission coefficient curves are expected in Figure 6-16. However, as the transmission coefficients of each port (S_{j1} where j = 1, 2, 3, 4) are similar, only two of them are depicted as an example.

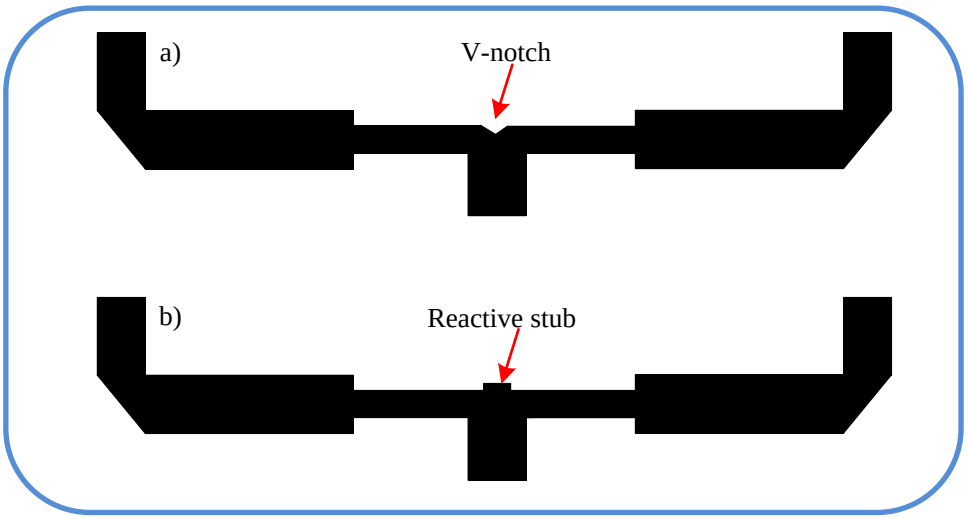

Figure 6-14 T-Junction power divider with a) V-notch b) reactive stub.

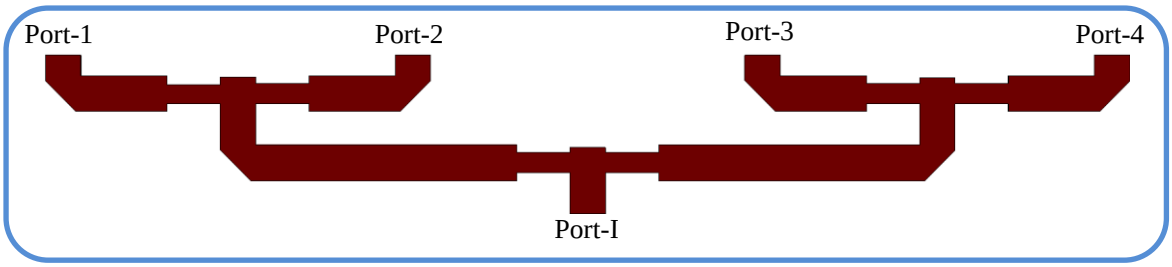

Figure 6-15 Complete corporate feeding network of array.

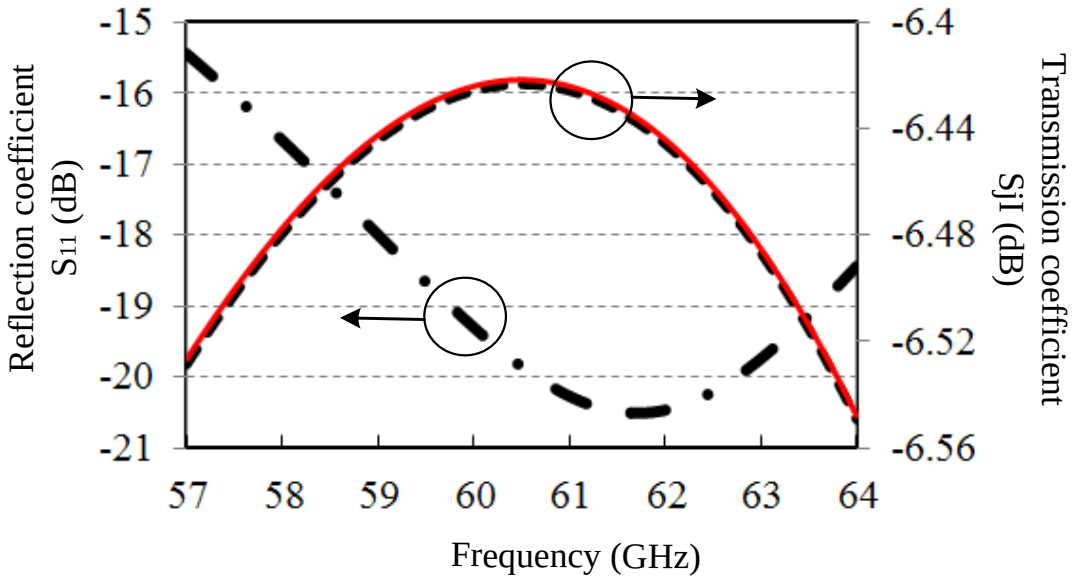

Figure 6-16 The S-parameter of the corporate feeding network of array.

The values of the transmission coefficient vary between 6.4 to 6.55 dB over the band. While the reflection is adequately low, almost a quarter of the input power is delivered to each port. Therefore, the array elements are uniformly excited.

Figure 6-17 shows the changes of the transmission coefficient phase on four different output ports. The phase of ports 1 and 2 are the exactly equal. The same is also valid for the phase ports 3 and 4 in Figure 6-15. There is a small difference between the phase of port 1&2, and 3&4. These differences are shown in Figure 6-17. As the difference is very small, 2-3 degree, hence it is not a serious issue in the total radiated power.

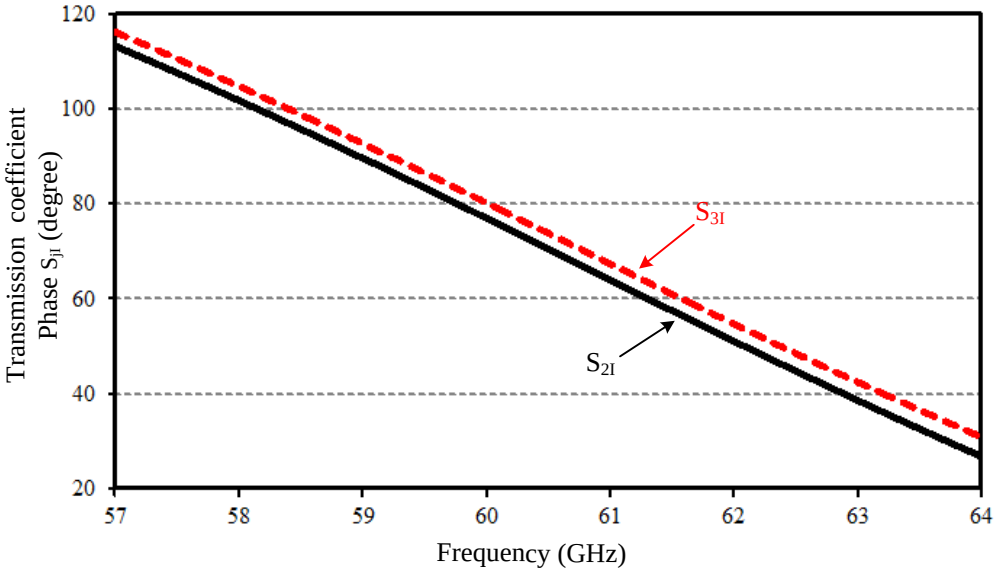

Figure 6-17 Transmission phase of different output ports (S_{21} and S_{31}) versus frequency for input port I.

6.7.3 Mutual coupling

Mutual coupling between the array's elements is a critical factor in the array design that can negatively affect the total performance of the array. Increasing the inter-element distance reduces the mutual coupling, however, a large distance between dipoles results in grating lobes in the radiation pattern if inner-element distance exceeds wavelength, λ.

While the half wavelength distance is normally selected as the inner-element space, larger distances ($\lambda/2 < d < \lambda$) are also feasible if narrower half power beamwidth (HPBW) is desirable. In the proposed application, as introduced in Section 6.2, smaller HPBW on the elevation angle is desired as it focuses more energy on the tag surface and minimises the reflections from surrounding objects. Therefore, the power divider's arm is tuned to provide 3.45 mm inner-element spacing equivalent to 0.65-0.73 λ over the band, (Figure 6-18). This large distance between elements reduces the HPBW, as well as minimising the mutual coupling among elements.

To simulate the isolation between two adjacent dipoles over the frequency band, two ports are connected to the dipoles and the transmission coefficient, S_{21}, is simulated in CST. Figure 6-19 shows the simulated result. The mutual coupling between two adjacent dipoles is adequately below -22 dB. It is important to consider the effect of the feed line on the transmission coefficient measurement. If the feedline causes a noticeable amount of loss on the transmitted signal, then S_{21} is shown very low on the simulation result while it doesn't necessarily mean low mutual coupling. Hence, loss occurring on the feedline can be seen as

an error on the transmission coefficient measurement. This feedline, which may degrade the S_{21} result, is highlighted in Figure 6-18. As is clear from the figure, the feedline length is only 0.8 mm (0.16 λ). The loss occurring on this section of the structure is very minor. By using the CST and/or advanced design system (ADS) facilities, it can easily be seen that the feedline loss only contributes 0.17-0.23 dB excess loss to the result, S_{21} of Figure 6-19. This means that the isolation between adjacent elements is below -22 dB over the whole frequency band of operation.

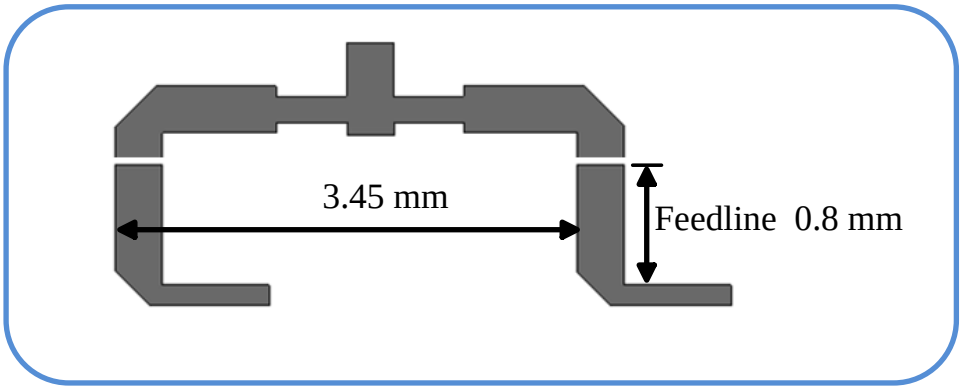

Figure 6-18 Two adjacent dipoles for mutual coupling measurement.

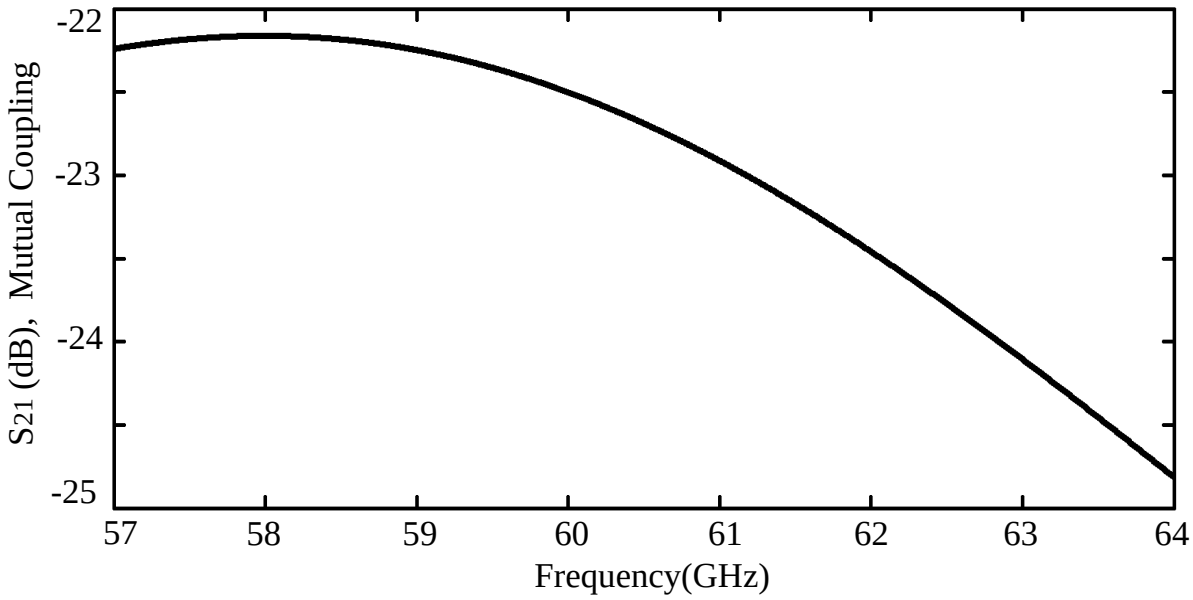

Figure 6-19 Simulated mutual coupling between adjacent dipoles.

6.7.4 Extended feedline

The designed corporate feeding network for an array of 4-elements shows an acceptable electrical performance over the frequency range of operation. It appears that the only remaining task is to connect the described array radiator in Section 6.6 to the feeding network and evaluate its final performance. The final structure of the array and its dimensions is shown in Figure 6-20. As one can see, the antenna width is only 3 mm and the length is 14 mm. The problem arises when the antenna structure is intended to be connected to its appropriate connector. A V-type connector that is suitable for the frequency range of operation has a much larger size than its antenna. Therefore, the structure shown in Figure 6-20 is not physically suitable for the V-type connector. Both objects are comparable regarding their physical sizes in Figure 6-21. To address this issue, the array's feed line shall be extended to provide enough space for connector installation. There are, however, two issues that shall be considered for the extension of the feedline, *(i)* the required length of the extension and *(ii)* the type of feedline for the extended part.

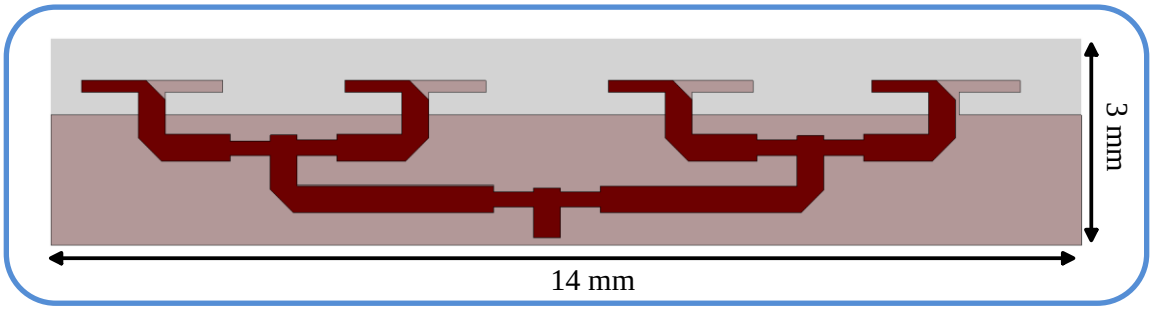

Figure 6-20 An array of 4 DSPD with corporate feeding network.

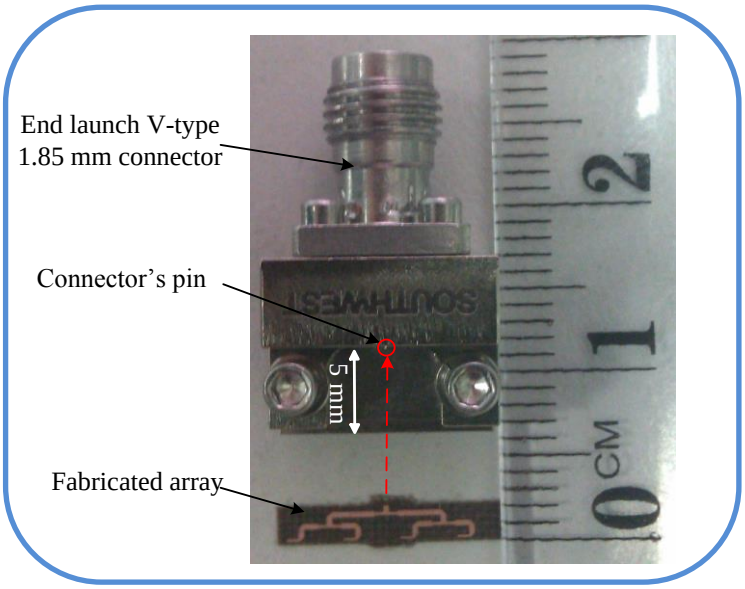

Figure 6-21 Comparing physical sizes of array antenna and V-type connector.

The feedline length is bound by two contradictory factors. First, the shorter line is preferred to minimise the loss occurring on the line and avoid unwanted radiation from the feedline. This implies that a 5 to 7 mm extension is enough as shown in Figure 6-21. On the other hand, however, the radiation pattern of the array shall be considered. As shown in Figure 6-11, the dipoles have a noticeable back-lobe due to their configuration. If the array antenna is placed very close to the connector, its back-lobe energy is reflected back to the broadside direction by the connector structure. This may disturb the radiation pattern of the array antenna. However, the major issue would be related to the increased level of the array cross-polar level due to reflection of the V-type connector. As discussed earlier, the cross-polar level is a critical parameter of the proposed antenna structure for the image-based application. To minimise this effect, the length of the feedline is extended beyond what was mandated by the physical requirements for connection purposes. As a trade-off selection for the feedline length, 20 mm extension is selected equal to almost 4λ. This provides enough distance between the connector and the array for minimum disturbance of the radiation pattern and degradation of the cross-polar level. However, the loss occurring on the line shall also be considered.

It is possible to simply extend the microstrip line, however, induced surface wave results in higher loss. To reduce the effect of a long feedline on the antenna performance, the coplanar waveguide (CPW) extension is used instead of a microstrip line. The grounded CPW line is immune to surface wave and it also provides better robustness to the cooper roughness than the normal microstrip line [150]. The prototype array is fabricated on Taconic, TLX-8 using a photolithographic fabrication process. The photograph of the assembled array antenna with extended CPW feedline and the V-type connector [151] assembly is shown in Figure 6-22. Due to the very tiny dimension of the connector's central pin, soldering would be very difficult and may cause distortion in the element performance. Therefore, the central pin only touches the feedline without any soldering.

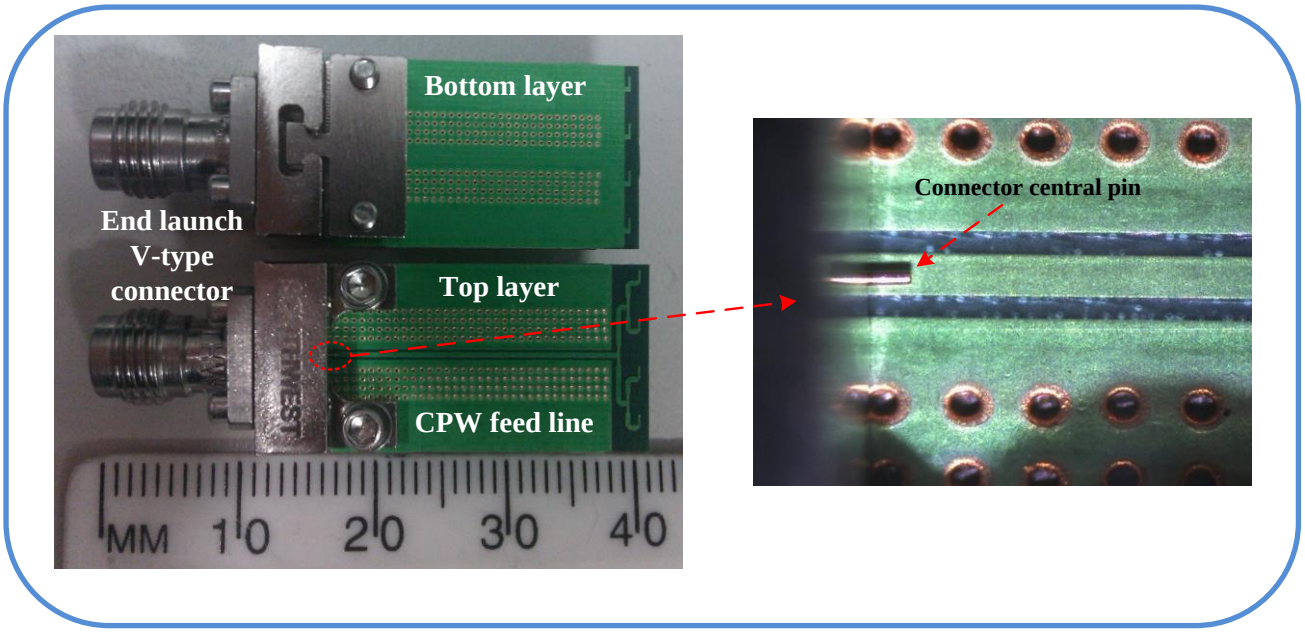

Figure 6-22 Extended CPW feedline and final array structure.

6.8 Measurement results

The prototype 4-element dipole array antenna shown in Figure 6-22 is firstly characterised for its input impedance return loss. This evaluates the general performance of the structure as an effective antenna at the desired frequency band of 57-64 GHz. Then the radiation patterns of the array in both E- and H-planes are measured. This verifies that the radiation pattern of the array is appropriately matched with what is required for the SAR signal processing purposes. The cross-polar level of the radiation pattern in both E- and H-planes are also considered and calculated to ensure that the array is adequately capable of picking up the intended polarisation while cancelling the orthogonal polarisation component. Finally, the average gain of the antenna is measured over the entire frequency band.

In all measurements steps, full two port error correction calibration and confidence check of the Agilent performance network analyser (PNA) E8361A are performed to ensure accurate results. In the following sections the results and discussion are presented.

6.8.1 Reflection coefficient measurement

The designed array of four DSPD's is simulated using CST Microwave Studio. However, as discussed before, the V-type connector may have significant effect on the final performance of the structure due to its large size at mm-wave range of 60 GHz. Therefore, the connector is also included in the simulation process to provide a more accurate result. The final structure, which is considered in CST is shown in Figure 6-23. Therefore, the effect of the microstrip to CPW transition, the 20 mm long feedline and V-type connector assembly are included in the simulations. The dimensions of the V-type connector are derived from its data sheet [152], however, the material of the connector was unknown. Aluminium (lossy metal) is assumed for the connector body and silver for its central pin. The fabricated antenna through the photolithographic process shown in Figure 6-22 is connected to the Agilent PNA for its return loss measurement after proper calibration of the system.

The simulated and the measured S_{11} in dB versus frequency are presented in Figure 6-24. It is important to again emphasise that the simulated and measured return loss reflects the effects of the array antenna, its long feedline, microstrip to CPW transition and the V-type connector assembly. Three main aspects of the graphs in Figure 6-24 can be categorised as follow:

i) Satisfactory return loss. As shown in Figure 6-24, both simulation and measured results yield more than 10 dB return loss over the frequency band of operation with maximum RL of more than 30 dB at 63 GHz. This ensures the satisfactory performance of the fabricated array on the band 57-64 GHz. It also confirms that the effect of a long feedline and the connector as well as the transition between microstrip to CPW, have been appropriately taken into account.

ii) Minor simulation and measurement mismatch. The graphs in Figure 6-24 are not fully matched to each other. Regarding the high frequency range of operation and also the fabrication technique used, some minor mismatching would be normal. To have a better understanding of the problem, the fabricated array is investigated thoroughly with a digital microscope. The dimensions of the array in different sections are measured and compared with the original values. The percentage of errors in various parts of the array is shown in Figure 6-25. As one can see from Figure 6-25, errors in different parts of the structure have significantly different values. While the width of the design is more vulnerable to errors, the lengths of the various parts are more immune to fabrication errors. For example, while some

widths are experiencing 11% error, the maximum error in array lengths was found to be only 0.4%. Inaccuracy in the line width significantly affects the impedance matching as it changes the line impedance. The effect of errors in line lengths are considered in the next part (iii) when the dielectric characterisation is being considered.

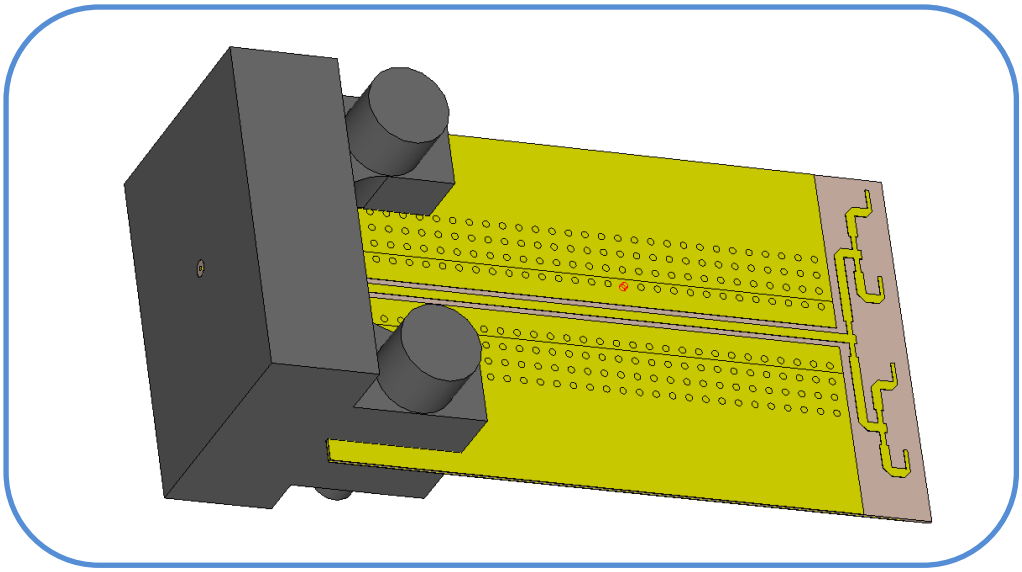

Figure 6-23 Array and V-type connector considered at simulation step.

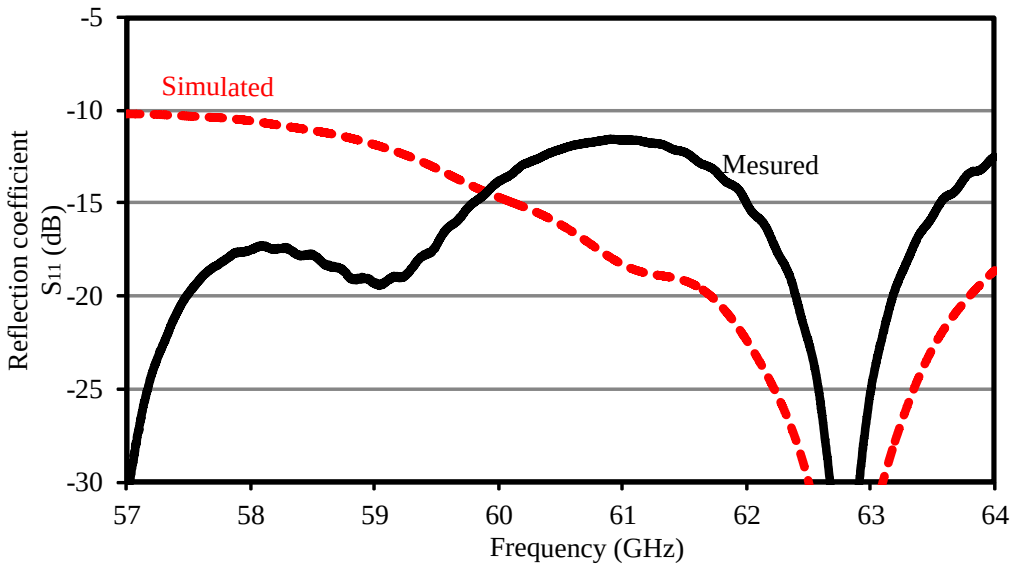

Figure 6-24 Reflection coefficient of fabricated array.

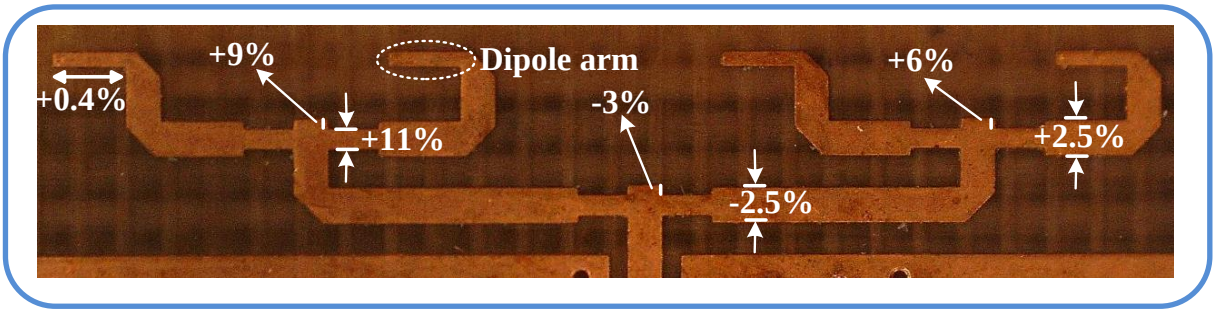

Figure 6-25 Percentage of errors in fabrication process.

Moreover to the errors occurring in the line widths, which result in impedance mismatch, one may suspect that residual surface waves, in the extended via grounded CPW line, and V-type connector assembly, cause impedance mismatch between the simulation and measured results. However, more than 10 dB return loss over the frequency band ensures no significant mismatch in the antenna and meets the specifications as discussed earlier.

iii) Accurate dielectric characterisation. The resonance frequency of the array is mainly controlled by the length of the dipole arm and the dielectric constant. As shown in Figure 6-24, the simulated resonance frequency and the measured resonance are both concentrated around 63 GHz. This means that the simulation and measured results are adequately matched from the resonance frequency perspective. As was already explored in *ii)* that the lengths of the dipole's arms are not significantly affected by the fabrication tolerance. Therefore, having the same simulated and measured resonance frequency confirms the accuracy of the dielectric characterisation method as described in Section 6.5.2. In other words, the calculated mean value of the measured ε_r for the Taconic TLX-8 at 60 GHz provides a good prediction of the used substrate performance at the 60 GHz frequency band.

6.8.2 Antenna fabrication error

At 60 GHz, the design would be very sensitive to any error during fabrication process. The effect of fabrication error was shown in previous section where inaccurate widths in the array feed network and dipole arms resulted in mismatch between the measured and simulated reflection coefficient. For the proposed image based chipless RFID system, at least two array antennas are required. However, the proposed technique may require more than 50 sets of array as will be discussed in Chapter 8 for the fast imaging purpose. It is therefore important to consider the design robustness to dimensional tolerances as process variation in

photolithographic etching always exists. Therefore, coordination with PCB manufacturing vendors before finalizing the design is crucial. Based on the accuracy of the fabrication process, it is normally required to re-tune certain parts of the design for better design reliability. It was discussed earlier that the T-junction power divider provides higher bandwidth when a reactive stub is utilised compared to a conventional V-notch in its structure. Moreover, it was found that the reactive stub significantly influences the design robustness to process errors while it also helps to broaden the element bandwidth.

Based on this finding, 5 samples of fabricated array antennas as shown in Figure 6-26 are measured by a digital microscope. The sample photograph of the feed network is also shown in Figure 6-26. The values of errors in different sections of the array structure is summarised in Table 6-5. As it is clear from Table 6-5, the width of lines in the printed circuit is more vulnerable to process error than the line length as discussed earlier.

Table 6-5 Fabrication variation

Parameter	P_w	D_a	P_t	I_g
Error(%)	[-1.5, 3]	[-0.2, 0.4]	[-7, 11]	[-3, 9]

The measured input impedance, return loss (S_{11} in dB) vs frequency through PNA for five fabricated array samples and the simulated S_{11} based on the accurate design values are shown in Figure 6-27. While the measured return losses are not completely matched with the simulation result due to the fabrication error, all five samples have acceptable performance (S_{11}>10 dB) in the frequency range 57-64 GHz. Moreover, one may notice all of the fabricated samples acquire almost the same resonance frequency as suggested through simulation, around 62.8-63.2 GHz. As all five samples have almost an accurate length of dipole's arms, see Table 6-5, therefore, the electrical parameters of the substrate was well predicted through SIW approach as discussed in Section 6.5.2. It can also be concluded that irrespective of fabrication error through conventional photolithographic PCB fabrication technique, appropriate antenna design at 60 GHz mm-band is feasible.

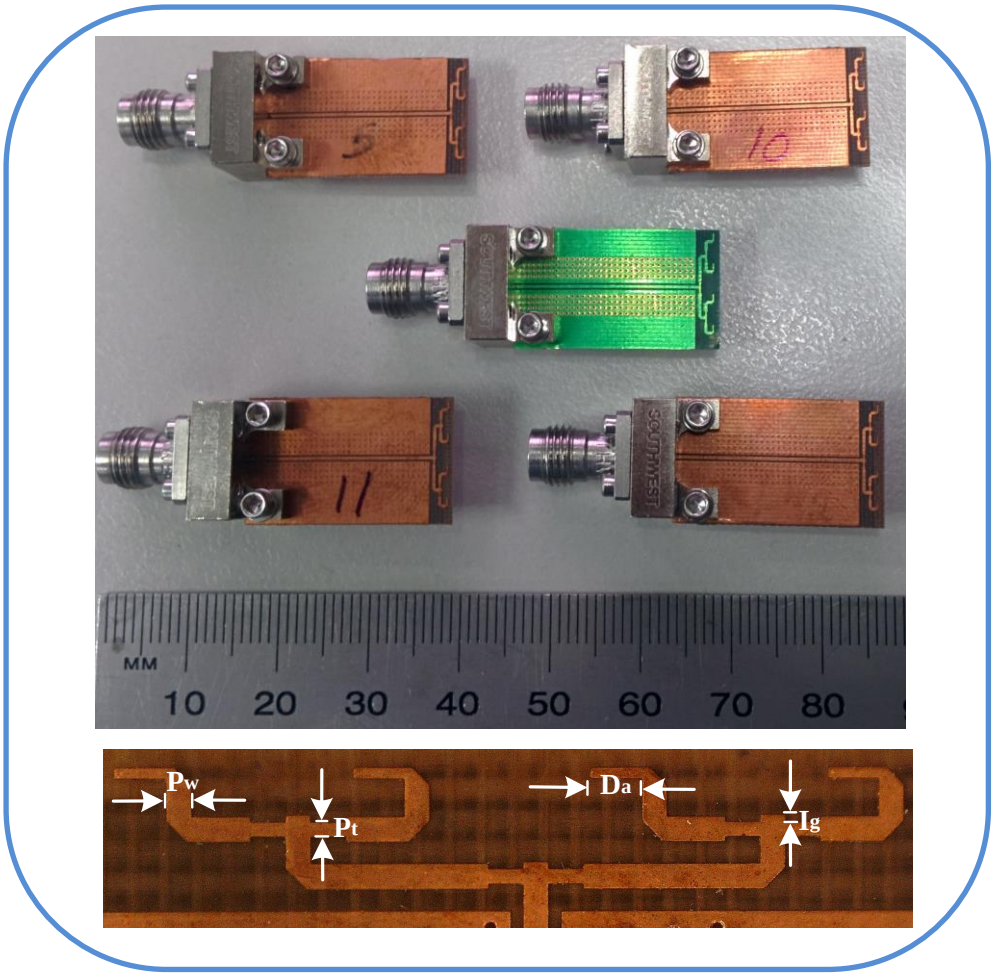

Figure 6-26 Five DSPD arrays and highlighted parametrized sections of array.

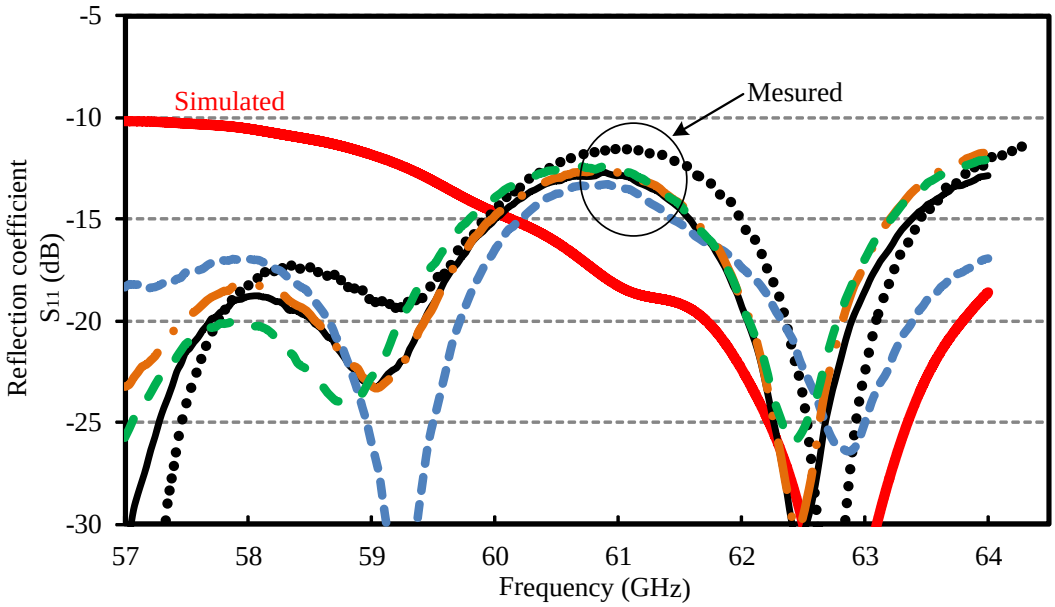

Figure 6-27 Simulated S_{11} and five measured return losses of sample arrays.

6.8.3 Radiation pattern measurement

After being satisfied with the performance of the array of DSPDs through input impedance return loss measurement, the radiation patterns of the fabricated array are measured.

Figure 6-28 shows a photograph of the system measurement set up with the standard gain horn antenna mounted on a fixed Perspex pole and the array antenna under test (AUT) mounted on a turntable. The AUT is tested as a receive antenna and a horn antenna [153], manufactured by Ainfoinc Inc., is used as a standard gain transmitting antenna. Agilent PNA E8361A in its receiver mode is used. The distance between two antennas is sufficiently higher than the farfield distances of the AUT and the horn antenna.

The radiation pattern is measured at every 10° step for a full 360° for both E- and H-plane cuts. As the automatic measurement facilities were not available on the MMARS laboratory, all measurements were completed manually. Some conical absorbers are placed around the antennas to reduce surrounding interferences. Figure 6-29 shows the measured and simulated co-polar and cross-polar radiation patterns at 58, 60 and 63 GHz for the E-plane. As one can notice, the main beam of the pattern is well-focused. This is required to minimise reflections from other objects around the tag and concentrate the radiated power on the tag surface. The measured radiation patterns are congruent with the simulation results with minor shifts in sidelobe levels. This can be seen as a good result considering the mm-wave range of operation and the manual measurement process of the pattern.

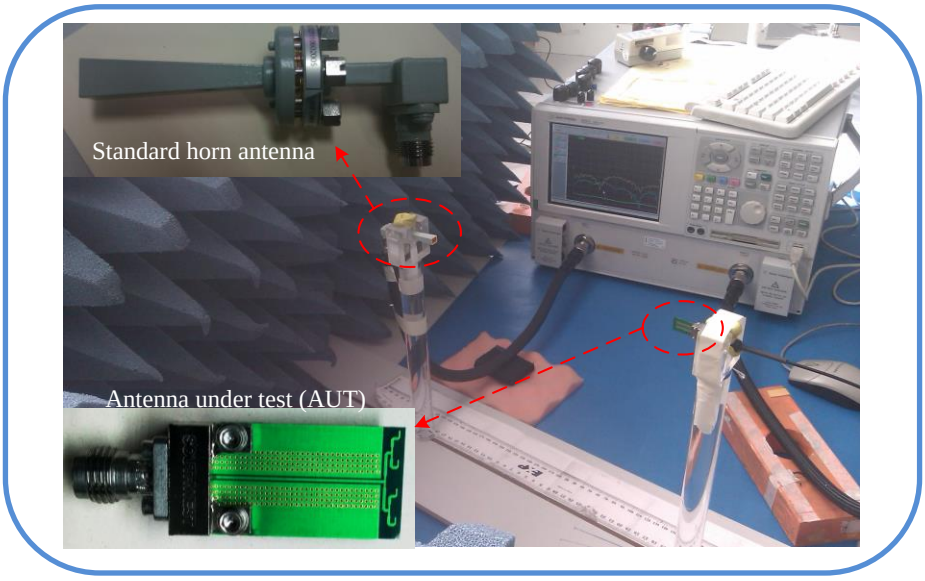

Figure 6-28 System set up for radiation pattern measurement.

Only the measured cross-polar result is shown in Figure 6-29 as the value of the CPL is more important rather the cross-polar pattern. As is clear from Figure 6-29, the CPL is adequately below -20 dB. This is a very satisfactory result considering the effects of the long feedline and the reflection from the big V-type connector. The measured and simulated H-plane radiation patterns of the designed array are shown in Figure 6-30. The shape of H-plane radiation of the array, including its V-type connector, is very similar to the H-plane of the single dipole shown in Figure 6-11. This is because the array's elements are oriented vertically, and hence, array configuration is not affecting the H-plane radiation pattern of a single element. Again, the measured and simulated co- and cross-polar radiations are very close to each other as was seen for the E-plane.

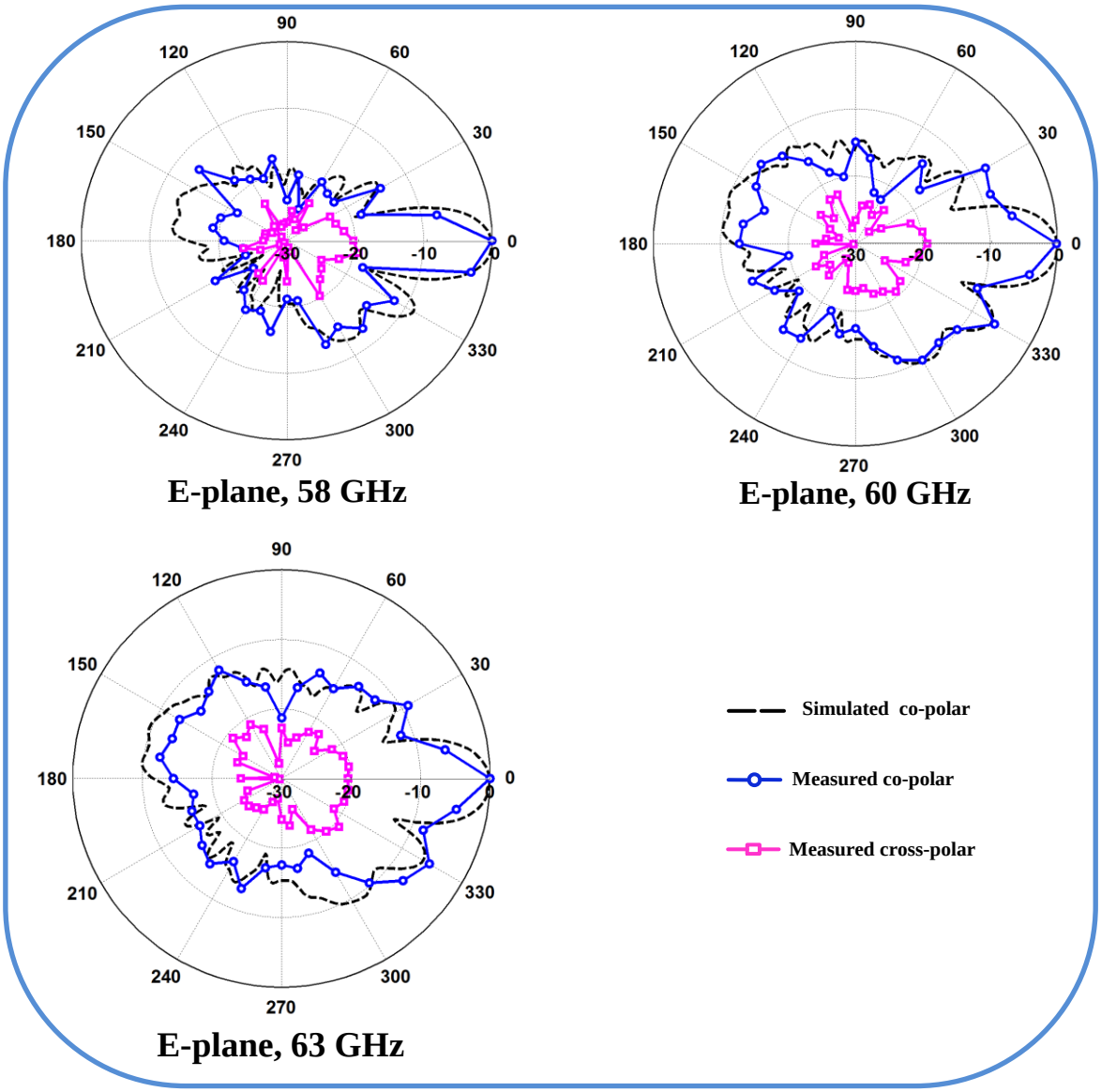

Figure 6-29 Measured and simulated E-plane radiation pattern, Co- and Cross-polar radiation.

Very minor difference between the two results specifically for angles above 30° is due to the focused radiation of the standard horn antenna. This means that when the AUT is turned around, it is slightly off the full illumination zone of the horn antenna and hence a little drop in the measured signal strength has occurred. The wide radiation of the whole structure including its connector, is essential for the appropriate usage of the designed array for synthetic aperture signal processing. As discussed earlier, the array shall illuminate the tag surface from different view angles, up to $\pm 60°$, hence a constant radiation over a wide angle is mandatory. Hopefully, the measurement result confirms that the fabricated array is capable of providing such a wide radiation pattern over the azimuth direction. The measured H-plane cross-polar radiation is also depicted in Figure 6-30. The value of the cross-polar level is below -20 dB for the broadside direction. However, for some angles, it may increase to -18 dB. This can be noticed on the graphs of Figure 6-30 for angles 10° and 330° for cases 58 and 63 GHz. As is discussed in the next chapter, this doesn't create any difficulty for separation of the cross-polar component of the tag response from its co-polar reflections. Again it should be mentioned that -20 dB cross-polar level on the H-plane is very well accepted for the designed array considering the effects of the long feedline and reflection from the big V-type connector.

Half power beamwidth (HPBW) of the array in its E- and H-plane quantitatively describes the radiation pattern. Regarding the wide azimuth radiation pattern, the measured HPBW for the H-plane would be acceptable in 10° measurement steps. However, for the E-plane radiation pattern, the suggested 10° measurement setup does not provide the required accuracy. For this purpose, it is therefore mandatory to measure the radiated power in more accurate angles, 1° for example. The 1° step measurement for HPBW of the array in the E-plane is shown in Figure 6-31. The re-measurement process for the E-plane is only repeated for the $\pm 10°$ of the boresight direction. This would be enough to provide a more accurate value of HPBW for the E-plane.

By considering the manual rotation of the AUT at every 1°, small errors are expected. To minimise this error, the measurement is repeated three times and the average value is considered. Figure 6-32 shows the co-polar radiation pattern in $\pm 10°$ of the boresight direction of the array antenna at 58 GHz. It shows that the measured HPBW is smaller when compared with the simulated HPBW. This process is repeated for the other two sample frequencies: 60 and 63 GHz. Table 6-6 summarises the HPBW of the array for both E- and

H-plane. It is important to notice that for the E-plane, the measurement accuracy is within 1° while for the H-plane it is 10°. For all cases, the measured HPBW is smaller than the simulation result.

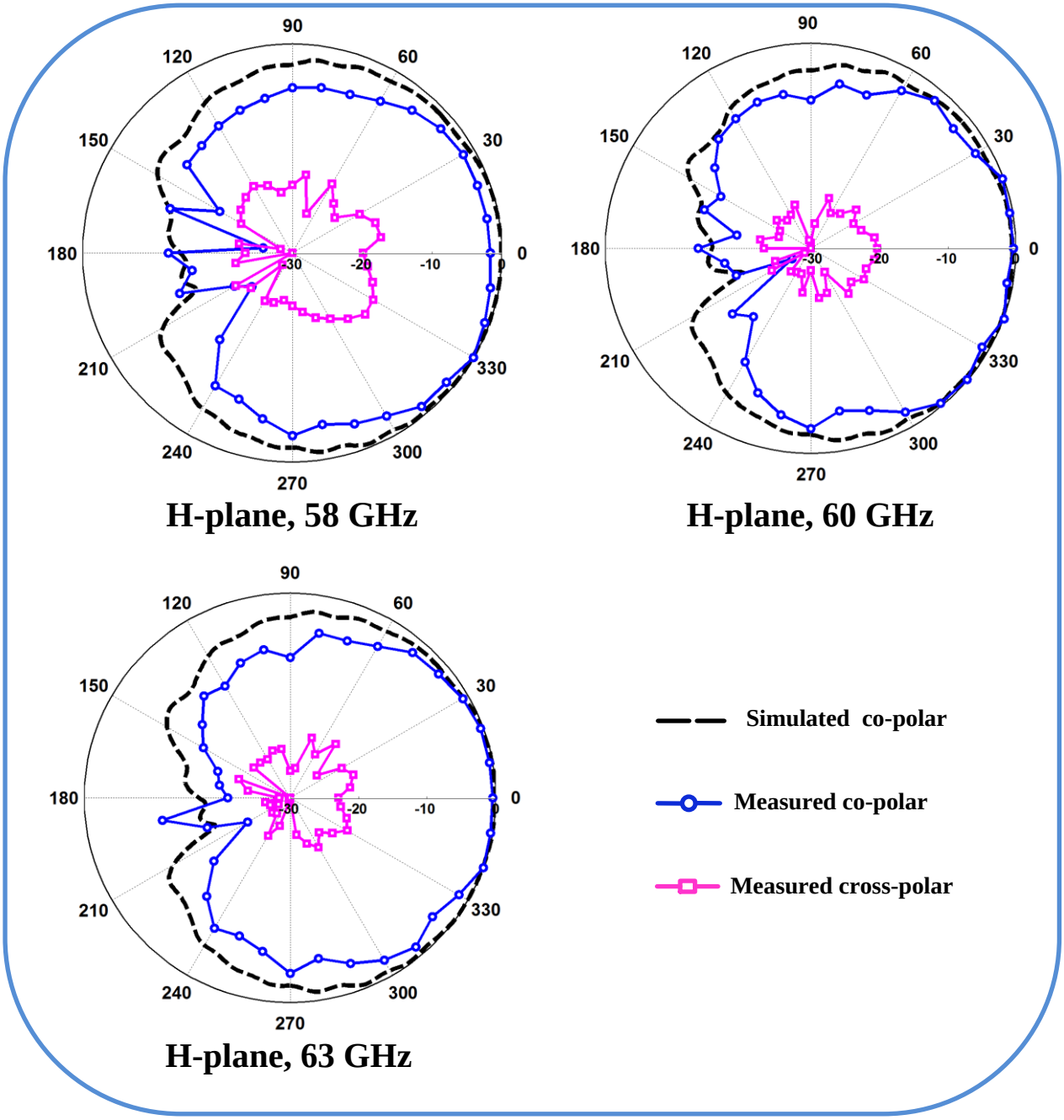

Figure 6-30 Measured and simulated H-plane radiation pattern, Co- and Cross-polar radiation.

Figure 6-31 HPBW measurement setup for 1° accuracy.

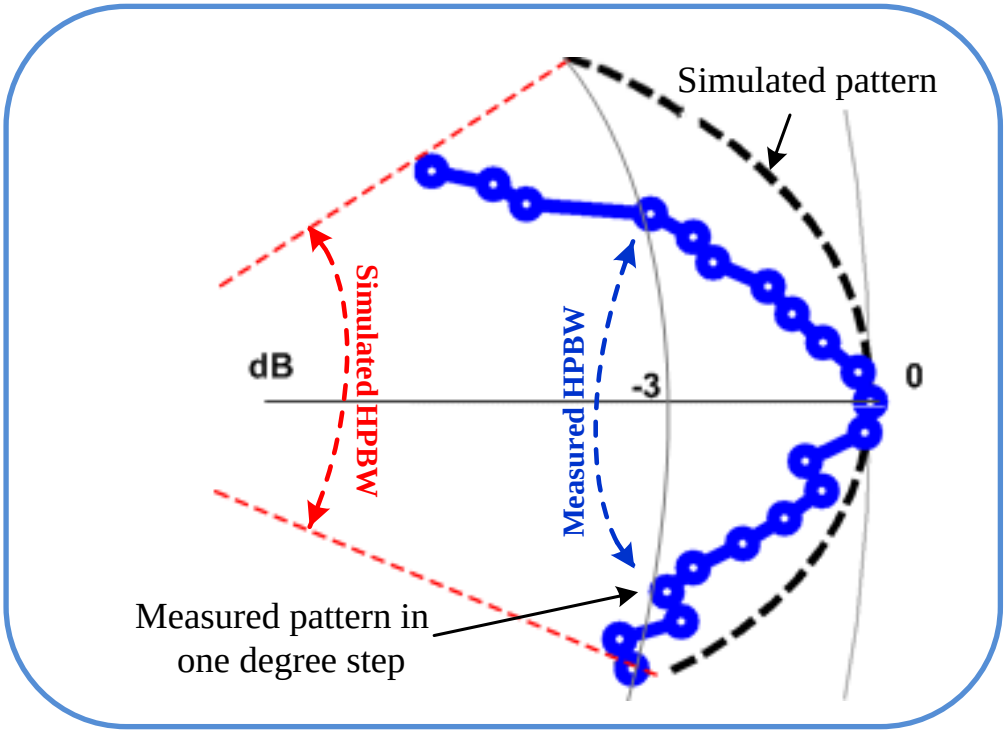

Figure 6-32 Measured and simulated HPBW of E-plane in 1° step.

Table 6-6 Simulated and measured HPBW in E-plane

Frequency (GHz)	E-plane		H-plane	
	Simulated	Measured	Simulated	Measured
58	21°	15°	182°	135°
60	18°	15°	185°	135°
63	17°	13°	190°	150°

The measured values of the HPBW reflected in Table 6-6 for both the E-and H-plane pattern adequately satisfy the required beamwidth of the array for the image-based chipless RFID application as previously summarised in Table 6-1. However, there is a difference between the measured value and the simulated HPBW for the H-plane. As mentioned before, the measured signal level, for angles higher than $\pm 30°$ of boresight, experiences a drop as the AUT is located a little off the illumination zone of the standard horn antenna. It is possible to increase the reading range to avoid this error, however, the limited transmission power of the PNA at a 60 GHz frequency range causes errors in the received signal level if the reading range exceeds 25 cm. The current measured HPBW of the H-plane is still wide enough (> 115°) for the proposed application. Therefore, no further action was taken regarding this measurement error.

6.8.4 Gain measurement

The final step of the array evaluation process is its gain measurement. It assures that the antenna is capable of providing enough energy in the desired direction. To measure the gain, a mixture of measurement, simulation and calculation is required and results shall be combined to provide the gain of the array. Again the standard horn antenna is used as the transmit antenna and the array, as the AUT receives the signal, while the Agilent PNA measures the S_{21} of the transmission link. The gain of the array relates to other parameters of the transmission link by:

$$S_{21} = P_{Tx} - P_{Rx} = G_{Tx} + G_{AUT} - L_{cable} - L_{FS} - L_{Feedline} \quad \text{all in dB} \qquad (6.9)$$

where G_{Tx} is the gain of the horn antenna,10.6 dB_i [153]. L_{cable} is the PNA cable loss and shall be measured directly by using full two port error correction calibration in the Agilent PNA E8361A. In this process, the loss of connectors and adaptors are also considered. Free space path loss, L_{FS}, is calculated using the Friss transmission formula [144]. The required inputs for the Friss formula are the distance and frequency. The feedline loss is required to be separately considered as the CPW feed extension is 4λ long and contributes significantly to the gain result. This loss has been separately simulated in CST and shown in Figure 6-33.

The 1.85 mm V-type Southwest microwave connector has VSWR of 1.25 [151]. This means that the impedance mismatch of the connector should not have a big effect on the gain

measurement. Therefore the connector's performance is not excluded from the gain measurement. By considering (6.9) and by combining the measured data with the calculated L_{FS} and simulated $L_{feedline}$, the final value of the gain versus frequency is shown in Figure 6-34.

As can be seen from the figure, the feedline loss and the antenna gain are congruent to each other over the whole frequency band. There is about 1.5 dB gain drop from 7 dBi due to 1.5 dB insertion loss variation of the feedline, 60-61 GHz. The absolute gain of the array antenna varies from 5.5 - 7 dB_i over the frequency band of operation as shown in Figure 6-34.

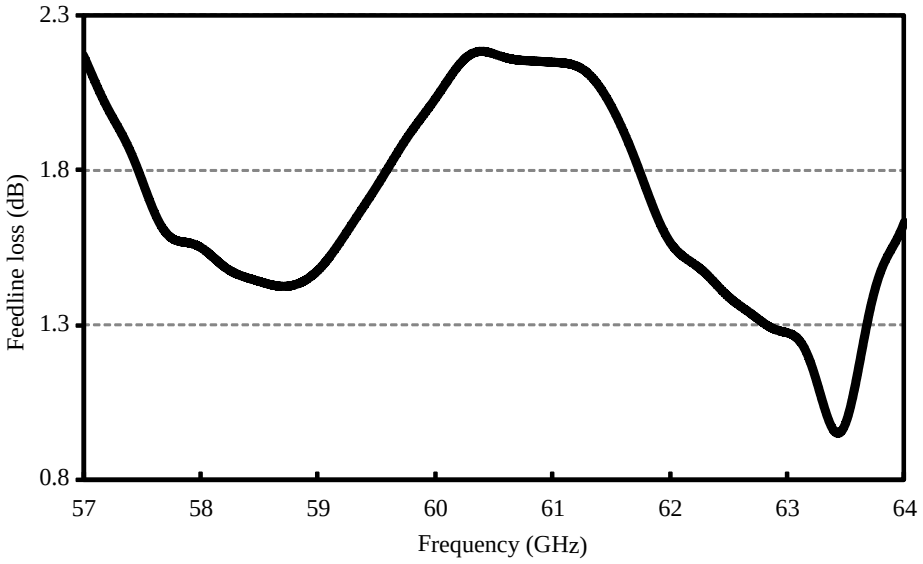

Figure 6-33 Simulated feedline loss of array.

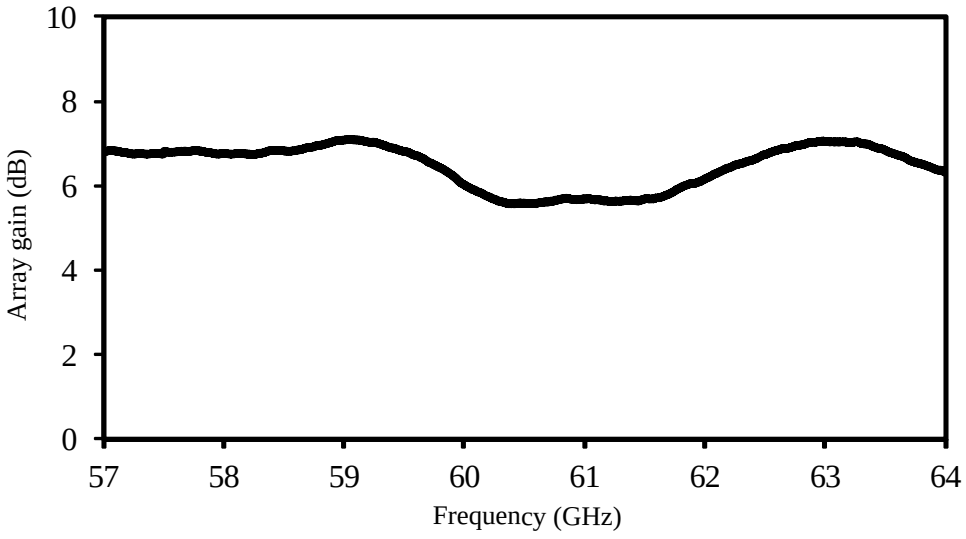

Figure 6-34 Measured gain of array.

6.9 Conclusion

This chapter first has reviewed the technical and operational necessities of the reader antennas for the proposed technique of the image-based chipless RFID system. Based on the proposed application, the technical specifications of the reader antenna were stablished first. A survey on the available open source products was conducted and their technical specifications were reviewed, aiming to fulfil the required parameters. It was found that "off-the-shelf" products on the mm-wave range of 60 GHz are not suitable for the demanded specifications in the proposed technique.

When the actual demand for designing a new antenna set at 60 GHz was stablished, the process of the antenna design was introduced. An array of double side printed dipoles (DSPD) antennas was proposed to satisfy the demanded technical specifications. This part built the basis of the further activities discussed in the rest of this chapter. A DSPD array antenna was designed and thoroughly investigated at 60 GHz for the image-based chipless RFID tags. The prototype antenna was design and fabricated on Taconic TLX-8.

First, the substrate was characterised using a SIW resonant technique. The measured constitutive parameters of the Taconic TLX-8 at 60 GHz significantly differed from that of published data at 10 GHz. The extract constitutive parametre data at 60 GHz was used for designing a 4-element DSPD array antenna. In the process of the design, the following advanced design techniques were used: *(i)* a broad band matching technique using dipole arms chamfering and abrupt ground plane for the dipole element, *(ii)* element array analysis and mitigating mutual coupling between elements, *(iii)* beam forming network with matching stub at the T-junction, *(iv)* microstrip to CPW transition and SIW based CPW extensions and finally, *(v)* a V-type connector assembly. The array of four DSPD elements covers the whole frequency range of 57-64 GHz yielding 12% bandwidth. The array and its feeding network were tuned to enhance the antenna performance. While the array dimension is very small and the standard printed circuit board technology was used for the antenna fabrication, the measurement results were well-matched with the simulation predictions. The antenna provided a uniform radiation pattern in the azimuth direction with a limited pattern on the elevation angle. The wide azimuth radiation pattern, H-plane, is suitable for the proposed cross-polar RCS-based chipless RFID application due to its requirement for SAR signal processing. The limited radiation in elevation angle, E-plane, also focuses the energy on the tag surface and minimises the unwanted radiation. The measured CPL was below -20 dB.

This low CPL was required for proper operation of the image-based chipless RFID applications. The measured gain of the array was 5.5-7 dBi over the entire frequency range of operation. The size of the array was 22×14 mm^2. The compact and simple structure of the array also made it suitable for many applications in the mm-wave region for low range wireless communication systems.

Chapter 7 EM-imaging

7.1 Introduction

EM-imaging fundamentals for data decoding of the chipless RFID system has already been presented in Chapter 3. The EM-imaging is only feasible at mm-wave bands of 60 GHz and higher frequencies, for the appropriate reading range, tag size, and expected data encoding capacity. A single antenna at the 60 GHz band does not provide the required millimetre order azimuth resolution, known as the foot print of antenna, at the normal reading distance of chipless RFID systems due to the far field restriction. The SAR technique is proposed as a solution for this purpose.

This chapter presents the SAR-based signal processing for the proposed chipless RFID EM-imaging. First, the basics of EM-imaging are reviewed and the necessity for using the SAR technique in different applications is discussed. It is shown that there are various applications where the SAR approach has both practical and technical advantages over other imaging techniques. The chipless RFID system is one of the applications for which the SAR is necessary for the technical reasons.

Then the main modes of operation for the SAR technique are introduced. The spotlight mode is highlighted due to its attributes for the proposed application in chipless RFID systems. The technical details of the SAR technique are reviewed to establish a fundamental basis for further steps in this chapter. The technical requirements for the transmit signal and the system general structure are defined in this section.

The technically achievable range and cross-range (azimuth) resolutions using the SAR technique are related to the technical parameters of the system in the next section. These parameters are the frequency of operation, available bandwidth, and synthetic aperture size. These parameters are then considered for the proposed chipless RFID application. The practical range and azimuth resolutions are defined. The ultimate data encoding capacity of the system is calculated based on the achievable resolution.

The appropriate data encoding algorithm is then discussed and a sample tag with only four bits data capacity is considered for the proof of concept. It is shown that changing only one bit of the tag data significantly changes the pattern of the received signal. Then the written codes based on the simplified spotlight mode reveals the final EM-image of the tag's encoded data. This step confirms the applicability of the proposed technique at its last stage. The

effect of synthetic aperture size on the achievable EM-image is also studied and it is shown that a minimum aperture size of 22 cm is required to decode the four bits tag at 10 cm reading distance.

In the last section of this chapter, the ultimate encoding capacity of the proposed technique is considered based on the maximum allowable tag surface. A tag that is 5.5 times smaller than a credit card encodes 17 bits of data while it is fully printed by a SATO printer. This suggests more than 93 bits on credit card size tag is possible. This is a revolutionary step forward achieving EPC global standard from a mm-wave chipless RFID system.

7.2 SAR, an effective imaging algorithm

In this section, the SAR technique is briefly introduced and its main advantage on providing a fine cross-range (azimuth) resolution is presented. Different modes of operation for the SAR technique are defined and the appropriate mode for the chipless RFID system is proposed.

7.2.1 SAR versus conventional systems

Radar is an acronym of "radio detection and ranging" [80] and it normally refers to the use of EM-waves by the system. It is an important technology for military and civil applications. The resolution of the radar system shows the ability of the system to separate multiple scatterers in close proximity, known as the radar resolution. A 2-D resolution is normally enough for the radar system [154], however, there are some advanced techniques for providing 3-D information [80, 155, 156]. The two basic resolutions of the radar system are the range and track-range resolutions. The range resolution is proportional to the utilised bandwidth of the transmit signal. The track-range resolution is sometimes referred to as the cross-range or azimuth resolution. In the rest of this dissertation, the azimuth resolution is used. Azimuth resolution depends on the beamwidth of the radar antenna. A fine azimuth resolution requires a larger radar antenna to provide a narrow beamwidth.

In many applications, the size of the radar antenna is restricted due to the various reasons, hence, radar has a limited azimuth resolution. Carl A. Wiley introduced a new technique for enhancing the azimuth resolution of the radar system through a small antenna with the expense of complex signal processing [87, 154]. He proposed the use of a small antenna with fairly wide beamwidth. The antenna moves around the target and illuminates it through different angles. All the received signals are restored based on different radar positions. Then the signal processing of the stored signals results in a very fine azimuth resolution which normally requires a much larger antenna aperture than that of the actual utilised antenna.

Figure 7-1 shows the transition from a conventional radar system to a SAR-based system. Figure 7-1(a) presents a conventional radar antenna with large aperture size. This antenna can be replaced by an array antenna with large number of elements. The higher the number of elements, the more similar two antennas in Figure 7-1 (a) and (b) are. Based on the size of the antenna in Figure 7-1(a) and the frequency of operation, thousands of elements may be required in Figure 7-1(b). Instead of utilising a large number of elements, SAR technique suggests to use only one element and sequentially move it to different positions in the array configuration. By restoring the received signal in each individual position, the effect of array antenna with thousands of elements, Figure 7-1(b), or equivalently the effect of the real antenna in Figure 7-1(a) can be successfully constructed.

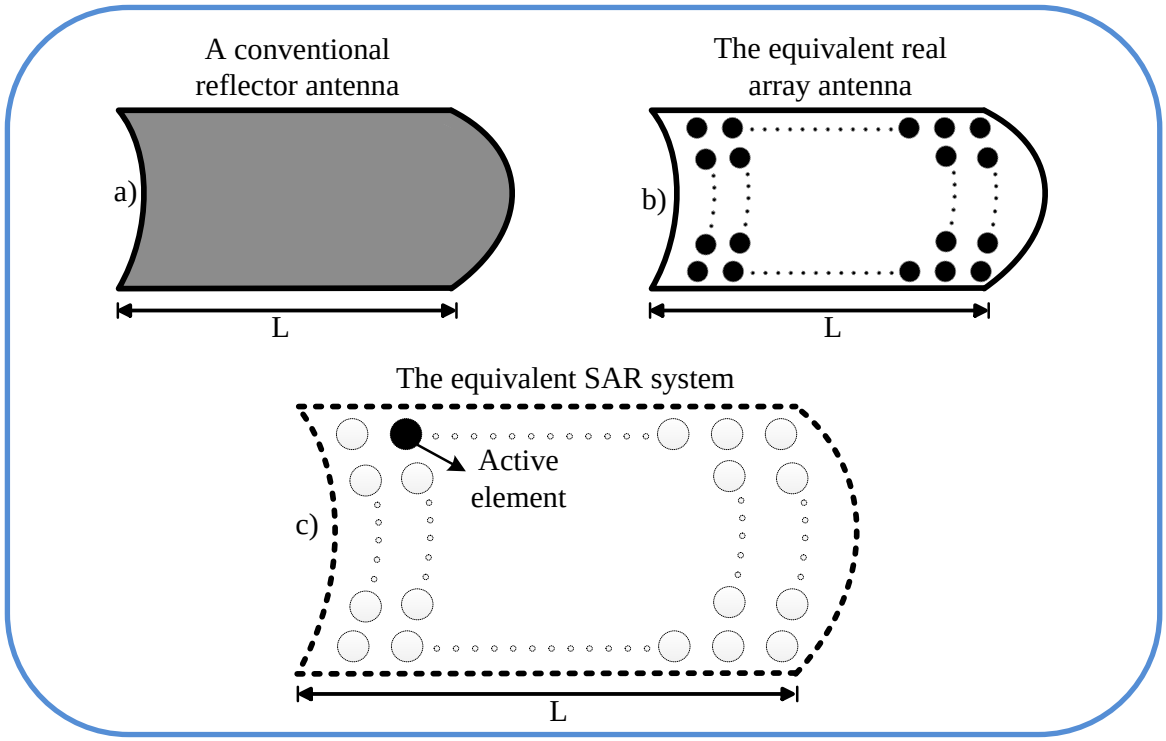

Figure 7-1 Evolution of conventional radar toward SAR system through array antenna concept.

7.2.2 SAR modes of operation

SAR-based systems may work in different modes of operation which depends on the system flexibilities and the application requirements. Three main modes of operations are: *i)* spotlight, *ii)* strip map and *iii)* scan mode [154]. In the spotlight mode, the radar system steers its antenna towards a certain area in which the target is located. The spotlight mode is normally used when the target area is small and a fine image resolution of the target is required. In the strip map mode, the radar antenna is fixed with respect to the system and the moving route. These two modes of operation are shown in Figure 7-2. The strip map mode is useful for providing a coarse-image resolution of a large area of interest, earth imaging for example. If these two modes are combined, then the SAR system works on the scan mode. The azimuth resolution provided by any mode of the SAR system directly depends on the length of the synthetic aperture size. In the strip map mode, the synthetic aperture length is fixed as the radar antenna has a fixed angle with the airplane. On the other hand, the spot light mode does not experience any limitations on its synthetic aperture length as the system has the ability to steer the beam of the physical antenna and illuminate the scene for a longer period.

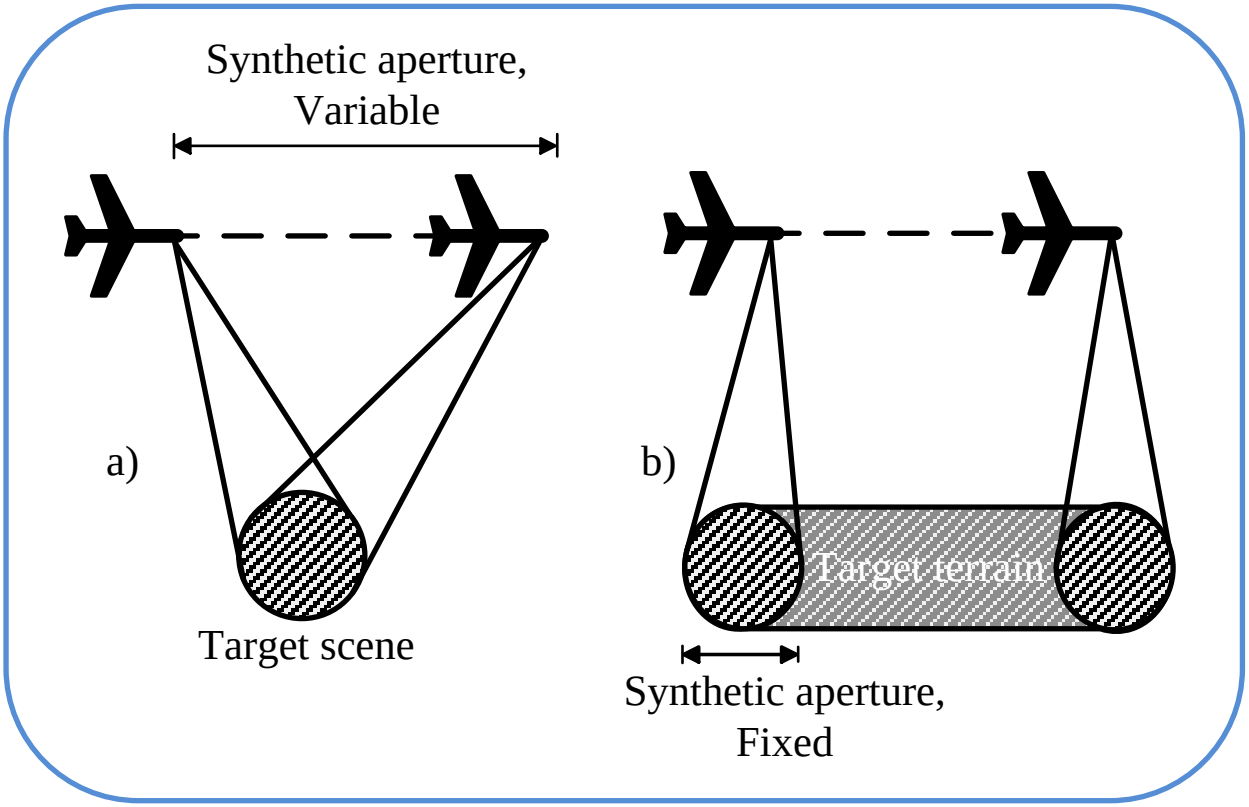

Figure 7-2 SAR modes of operation: a) Spotlight mode, b) Stripmap mode.

For the proposed mm-wave chipless RFID tag, the maximum area the tag occupies is less than a credit card size (85 × 55 mm^2). On the other hand, the maximum azimuth resolution is desirable as it defines the tag's data encoding capacity. Therefore, the spotlight mode of SAR seems to be an appropriate mode of operation for the RFID tag imaging. Through the curvature nature of the reader route around the tag, it is possible to focus the radiation pattern of the reader antenna on the tag surface and illuminate the tag through different view angles. Moreover, flexibility on the length of the synthetic aperture size at the spotlight mode results in finer azimuth resolution at the expense of a larger synthetic aperture length. This trade-off between the aperture size and the image resolution is discussed in Section 7.6.2 with measurement results. Figure 7-3 shows the system set up of the tag imaging process that is very similar to the spotlight mode in Figure 7-2.

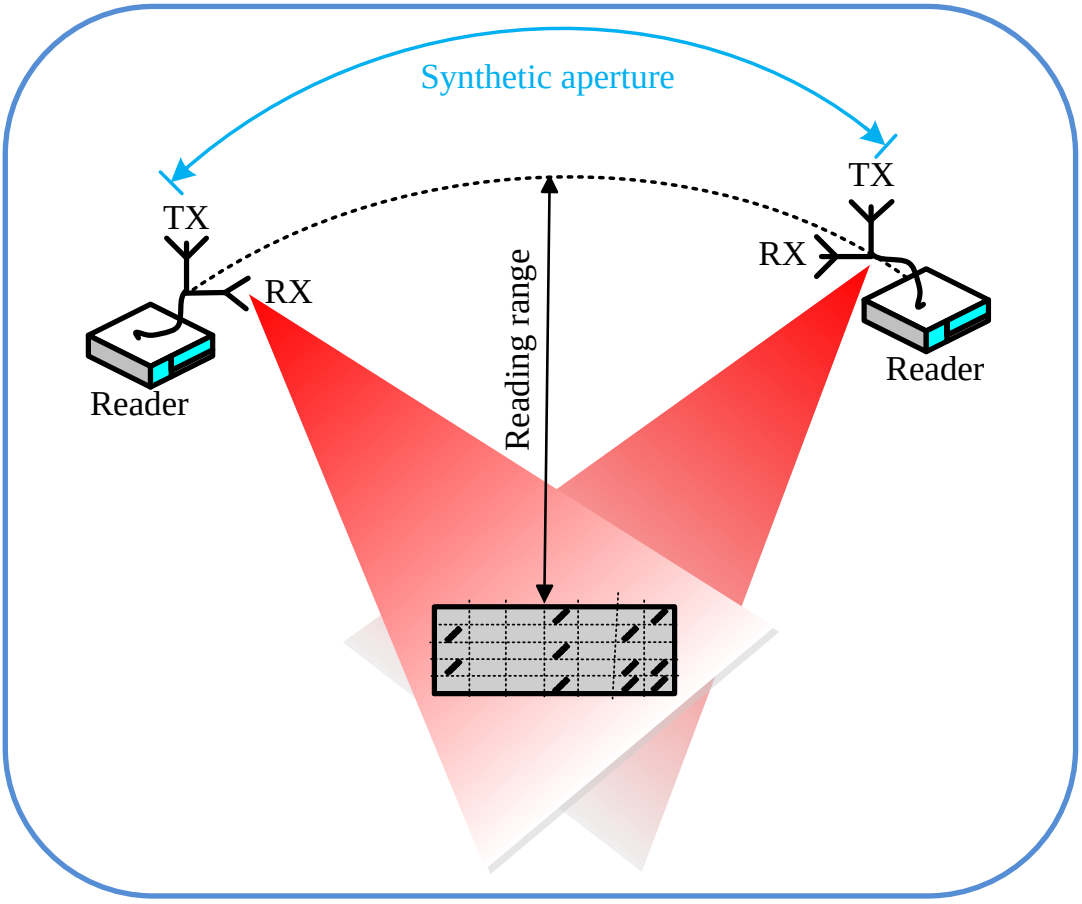

Figure 7-3 Spotlight mode of operation for finer azimuth resolution of chipless RFID tag.

7.3 SAR for chipless RFID

This section reviews the fundamentals of the SAR system and introduces basic expression describing the spotlight mode as the appropriate mode of operation for the proposed RFID application. Based on the expression derived in this section, the technical specification of the proposed RFID system is defined. Finally, the system capabilities on range and azimuth resolutions are determined.

7.3.1 SAR block diagram

The block diagram of a typical SAR-based system is shown in Figure 7-4. The radar antenna provides real time data of the scene. In many cases, the information about the movement of the radar system is collected during the operation of the system. These two sets of data provide the scene data as well as the complementary data of the radar motion. The *image formation processor* uses these two data sets to provide the SAR imagery to the *image processor* and subsequently to the *image exploitation segment* [154]. For many applications, including the earth imaging, the movement of the radar system is almost a fixed path, however due to unexpected factors like wind and the terrain of the earth, small variations of the radar route often happen. Therefore, the motion sensor is an unavoidable part of the system. For the RFID application, however, the movement is completely predictable as the radar moves on a rail. Therefore, this section can be ignored, while the information of the route would be easily considered in the subsequent modules mathematically. The detailed description of the modules in Figure 7-4 are described in [154].

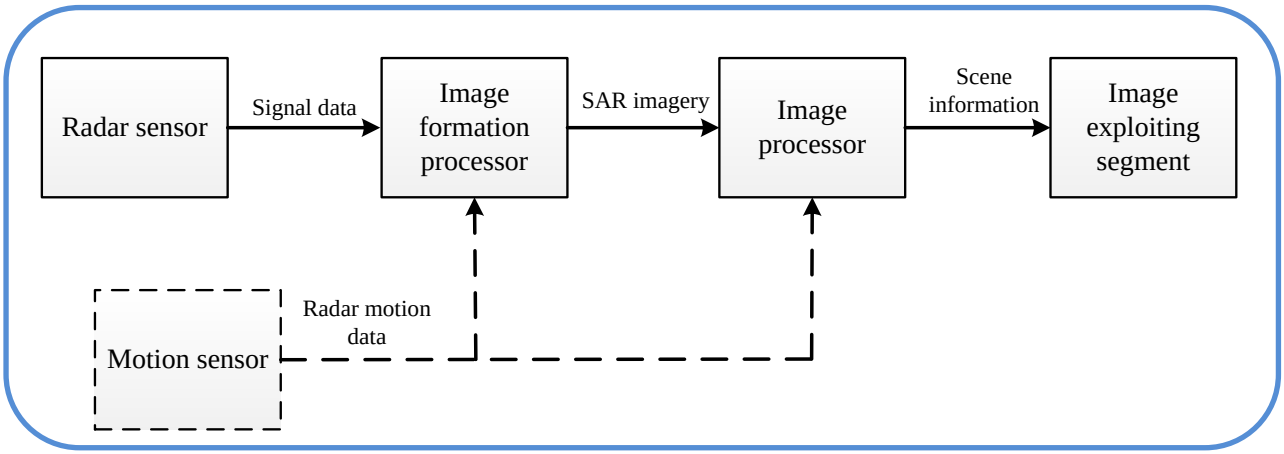

Figure 7-4 General block diagram of typical SAR-based system [154].

7.3.2 Range resolution

The synthetic aperture concept improves the azimuth resolution of the system only. The achievable azimuth resolution through the SAR technique is normally much better than that possible with a single antenna. Therefore the SAR concept is very commonly used when the size of the single antenna is limited due to technical reasons. However, accessing the same range and azimuth resolutions is normally required in many applications. Therefore, the fine azimuth resolution due to the SAR technique provides an incentive for utilising higher bandwidth signals for fine range resolution as well.

The radar's ability to separate two targets in range is known as *range resolution*. Based on the signal type used in the transmit section of the radar, the range resolution may vary. For a single short pulse, the radar can distinguish two adjacent targets in range, if the separation time between their echoes is more than the pulse width. The range resolution, ρ_r, is the minimum distance between two adjacent targets separated by the radar and is defined by:

$$\rho_r = cT_p / 2 \tag{7.1}$$

where c is the speed of light and T_p is the pulse width. Figure 7-5 illustrates the range resolution. Expression (7.1) is only valid if the targets and the radar system are in line as shown in Figure 7-5.

With a fine range resolution, shorter pulses are needed. However, to maintain a satisfactory average power level, high power pulses are required. There high power narrow pulses are difficult to generate. This means that narrower pulses, that are required for finer range resolution, contradict the requirement of a higher average transmitted signal for maintaining the minimum signal to noise ratio (SNR) for a fixed reading range. To satisfy both requirements, it is possible to have long, phase-coded pulses, which can be compressed with a signal processing operation after reception. In this scenario, a linear FM signal, known as the chirp signal, is transmitted during a long enough time as a pulse signal to satisfy the minimum transmission power requirement. However, signal processing after reception provides a fine resolution corresponding to a very narrow pulse shape.

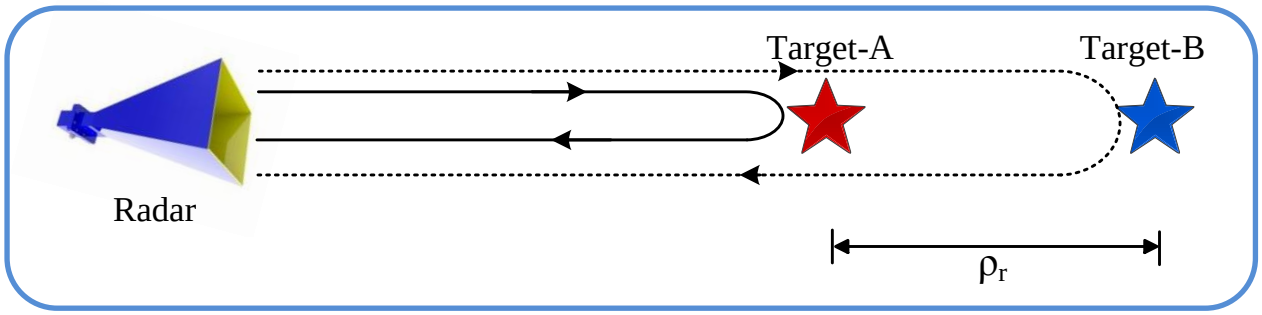

Figure 7-5 Range resolution concept.

This chirp signal is a common choice for a transmitted signal by many modern radar systems. In the chirp signal approach, the linear frequency modulated (FM) waveform exists over a pulse length of T_p that is adequately long for the minimum transmission power requirement. In this time frame, the frequency of the transmit signal which varies with time is a function of chirp rate, γ. The instantaneous frequency is then:

$$f_c + \gamma(t - nT) \tag{7.2}$$

where f_c is the centre frequency and $t = nT$ signifies the centre of the pulse. The related bandwidth B of this signal is γT_p. From the signal theory, a pulse with bandwidth B corresponds to the time duration of $1/B$. Hence from the above expression, the new range resolution of the chirp-based radar would be:

$$\rho_r = \frac{c}{2B} \tag{7.3}$$

This means that the range resolution of the system is enhanced by factor B after signal processing. This range resolution is much better than the initial range resolution corresponding to the physical length of the transmitted pulse, T_p.

The range compression factor is the ratio of the pulse's length before time compression (T_P) to its length after compression ($1/B$). The normal value of pulse compression ratio (PCR) is in order of $1e^5$. As an advantage of the linear FM signal, the analog bandwidth of the received signal is decreased, hence the required speed of an analog-to-digital convertor (A/D) unit is also slowed:

$$PCR = T_p B = \gamma T_p^2 \tag{7.4}$$

The assumption of having the radar system and the targets in one line is not always practically valid. In fact, in many applications, the radar has a slant view angle to the target, Earth imaging, for example. In this case, (7.3) and (7.4) are equivalently not showing the final range resolution of the system. Instead, the final range resolution known as the ground range resolution could be easily found from its equivalent slant range resolution through:

$$\rho_{gr} = \frac{\rho_r}{Sin\,\theta} \tag{7.5}$$

Where, ρ_{gr} is the ground range resolution that is the final resolution of the radar system on the target scene and ρ_r is the slant range resolution derived from (7.3) and (7.4).

Figure 7-6 clearly shows these two range resolutions. For the RFID application, the same scenario is valid. The reader antenna is at 90° towards the tag's surface. Meander lines are located at close proximity of each other, 1 mm for example. The reading range is in the 10~50 cm range based on the maximum transmitted power of the reader. The required signal bandwidth for these parameters based on (7.4) and (7.5) is in hundreds of GHz that is technically impractical to achieve.

Figure 7-7 shows the slant and ground range resolutions for the chipless RFID application. The front and side views of the tag are shown in Figure 7-7 along with the nominal parameters of the reading scenario. Therefore, it can be concluded that providing the fine range resolution of few millimetres on the tag surface is not possible due to the limited available frequency band of operation. Hence the range resolution has no benefit for data encoding purposes on the chipless RFID tag.

7.3.3 Azimuth resolution

The signal processing technique that SAR-based systems use to achieve a fine azimuth resolution is the feature that distinguishes the SAR-based systems from other imaging techniques [154, 157]. Synthetic aperture processing in azimuth exploits the linear FM modulation that the quadratic variation in range to a target introduces as the radar passes. The processor is able to compress this modulated azimuth signal to generate the resolution associated with a narrow beamwidth from a wide beamwidth antenna [154]. In a radar system, the radiation pattern of the radar antenna illuminates a cell and the presence or

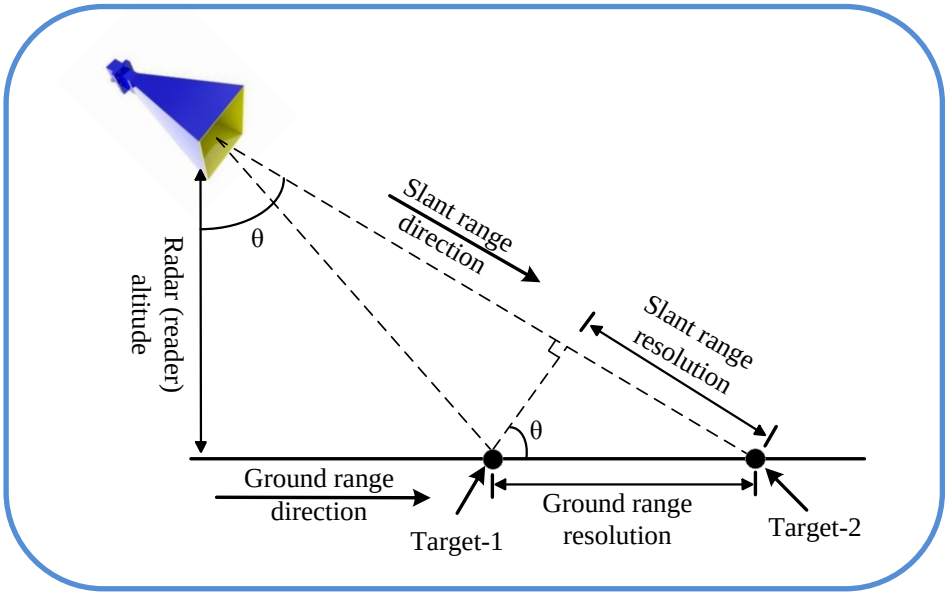

Figure 7-6 Slant and ground range resolutions.

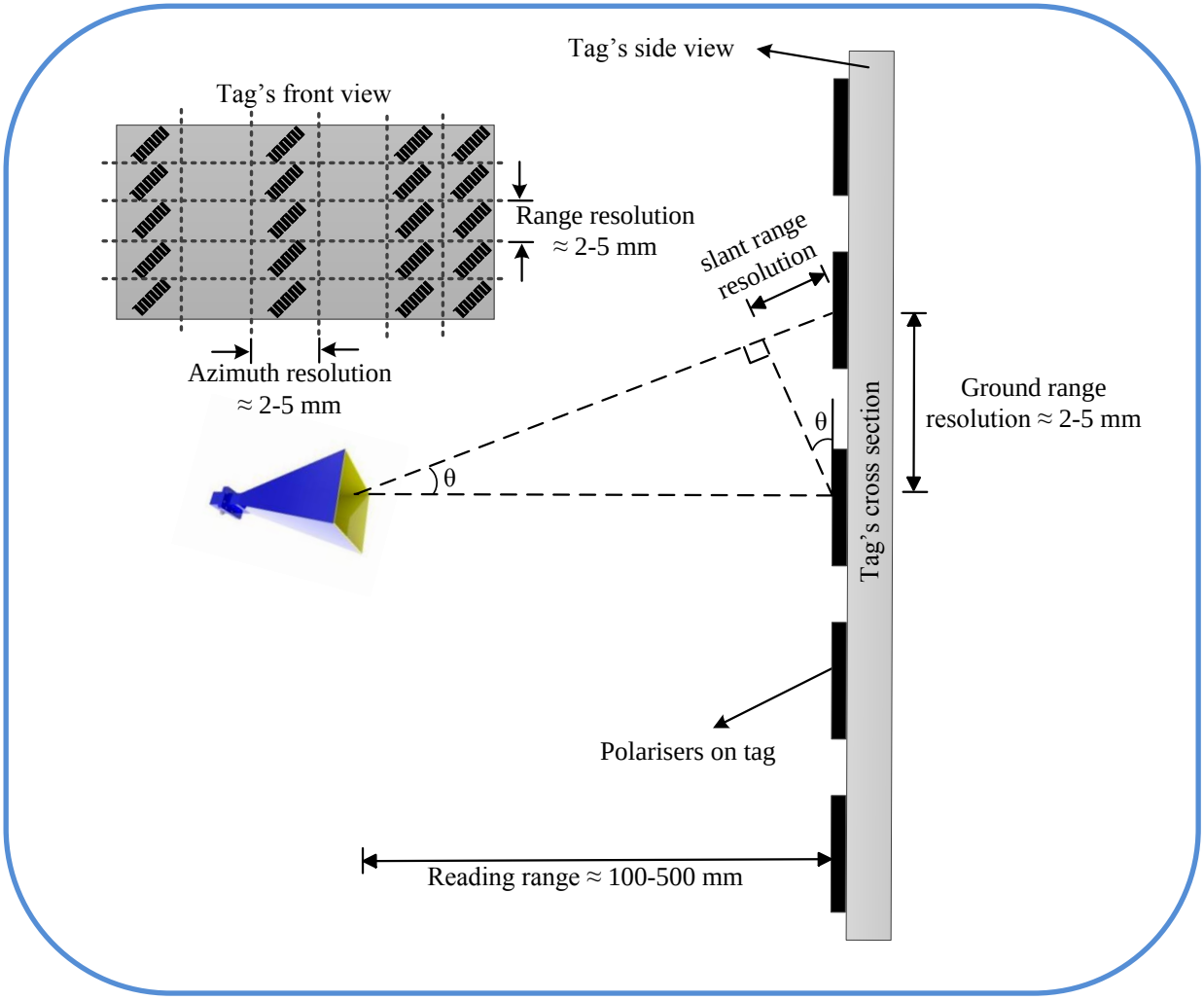

Figure 7-7 Ground and slant range resolutions of mm-wave chipless tag.

absence of any target(s) is discovered by the backscattered signal. Two targets can be distinguished if their angular separation is greater than the radar beamwidth. This means that radar is not able to resolve targets which are closer to each other than the radar beamwidth. The 3-dB beamwidth of an un-weighted antenna relates to its physical size (D) and frequency of operation (λ) by [144]:

$$\beta_a \approx 0.89\frac{\lambda}{D} \tag{7.6}$$

If the target is located at distance R, then the azimuth resolution of the radar is:

$$\rho_a \approx 0.89\frac{\lambda.R}{D} \tag{7.7}$$

For many applications the long distance of a target to the radar system (R) results in very coarse azimuth resolution. Increasing the azimuth resolution is restricted by the maximum allowable size of the antenna, D, in Earth imaging for example. In a SAR system, a small antenna, D, moves over a large path known as synthetic aperture antenna length, L, and illuminates the target scene with its wide beamwidth. The received signal at each individual position of the real antenna is added coherently with the proper phase adjustment to maintain the large synthetic aperture which yields a narrow beamwidth after proper signal processing. This means that physically scanning the target scene through a small antenna with a wide radiation pattern is equivalent to scanning the target scene with a much narrower radiation pattern in the processor.

For the chipless RFID application, the relation between the required synthetic aperture length and achievable azimuth resolution based on various reading ranges, R, is shown in Figure 7-8. As one can easily see, the necessary length of the synthetic aperture is completely practical to achieve the azimuth resolution of few millimeters. For example, in 15 cm reading distance, a 20 cm synthetic aperture is enough to provide less than 4 mm azimuth resolution on the tag surface. A 25 cm synthetic aperture length is normally enough to provide the azimuth resolution of less than 5 mm for a reading range up to 25 cm. As can be seen later in this chapter, the implementation of the system and the achieved image resolution confirms the values of the graphs in Figure 7-8. This means that although the range resolution of few millimetres requires huge spectrum bandwidth; the azimuth resolution is quite practical, and proposes a new method for data encoding on a chipless tag with noticeable data capacity. The implementation of the synthetic aperture radar theory for the chipless RFID is shown in this chapter.

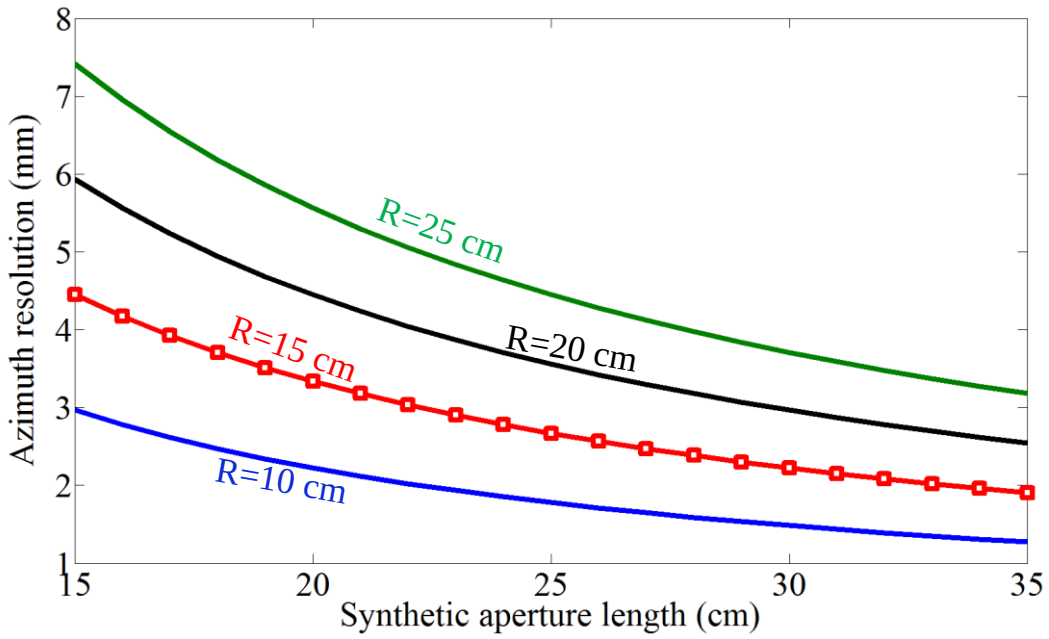

Figure 7-8 Azimuth resolution and required synthetic aperture length.

7.4 Tag structure for practical data encoding approach

As was already discussed the presence or absence of EM-polarisers on the tag surface, meander lines for example, conveys the encoded data to the reader. To detect the existence of the polarisers on the tag surface, the SAR EM-imaging is utilised. The provided image resolution using the EM-imaging technique reveals the final data encoding capacity of the system. If the tag surface is divided into a number of pixels, then each pixel may contain one EM-polariser as the data encoding unit. The presence and absence of polariser represents the "1" or "0" data respectively and hence carries one binary data bit. The size of the pixel on the tag surface governs the final data encoding capacity of the tag. The finer the pixel, the higher the data encoding capacity is. Figure 7-9 shows the pixelated tag surface. The width of the tag has m pixels and its length is divided into n pixels. Without losing generality, it is assumed that the pixels are square. This means that the tag surface comprises a matrix of $m \times n$ pixels. As each pixel carries one bit of data, hence the total data encoding capacity is 2^{mn}. It was already shown in Figure 7-8 that the resolution of the EM-imaging is in millimetre order, 3 mm for instance. Therefore, the theoretical data encoding capacity of the proposed technique can be one bit in every 9 mm^2 or equivalently more than 10 $bits/cm^2$. This would be a revolutionary data encoding capacity for a chipless RFID tag [158].

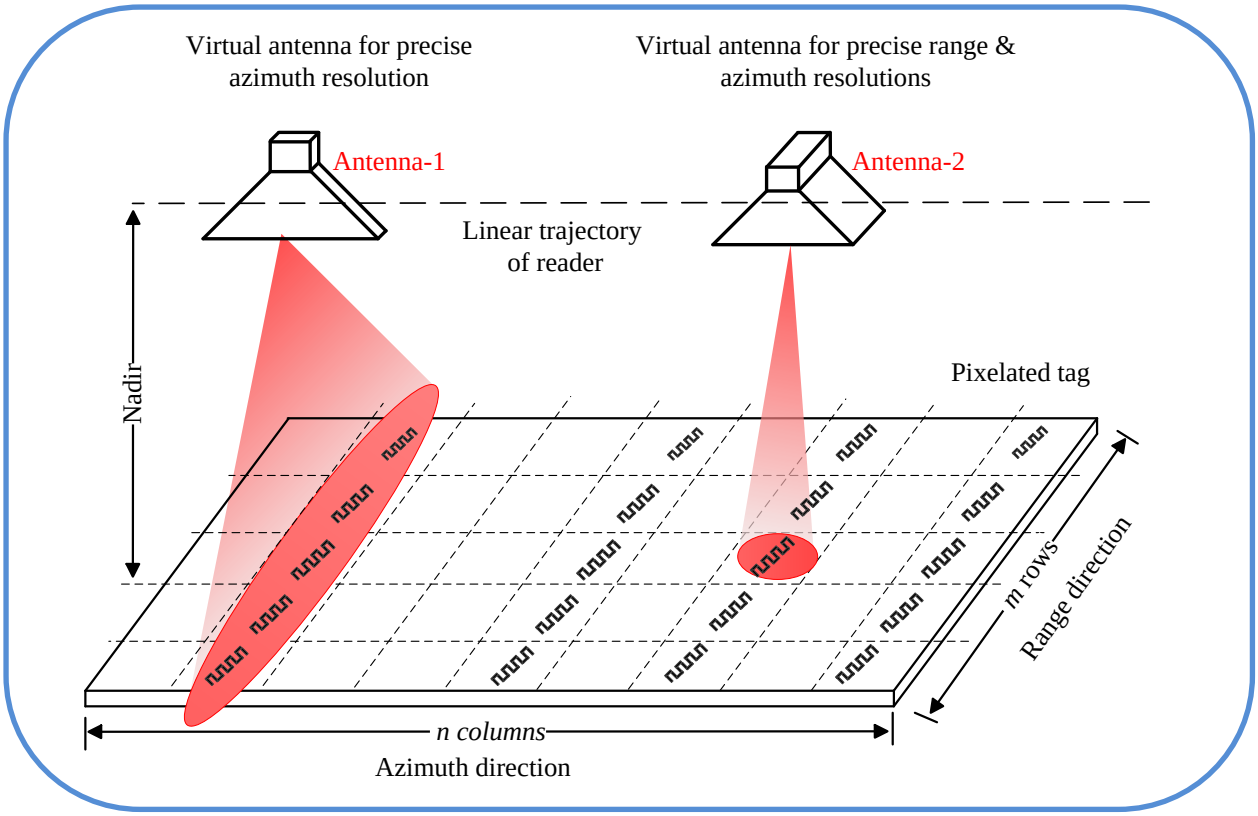

Figure 7-9 Tag structure and two different reading scenarios.

It was already shown that while few millimetres image resolution in the azimuth direction is completely practical through SAR technique, the same resolution in the range direction requires huge spectrum bandwidth, and hence results in an impractical approach. There is a claim that the range resolution can be improved significantly without using enormous bandwidth [159]. As no technical details of the referred work yet have been revealed, therefore at this stage, it can be concluded that providing the millimetre range resolution is not feasible for the proposed application with a reasonable amount of bandwidth.

Ignoring the fine range resolution means that the detectable pixels are rectangles rather squares. Each pixel having a millimetre width in the azimuth direction and a length of centimetre order in the range direction. This means that the presence or absence of a group of polarisers on each strip of the tag represents 1/0 encoded data. Hence the content capacity of the tag drops to 2^n. Based on this assumption, m has no effect on the encoding capacity. Normally five polarisers on each column of the tag surface are assumed to provide a higher backscattered signal level as also supported by CST simulation. The assumption of five polarisers on each strip is considered for all signal processing steps and is in line with all

measurements that have been completed and shown in previous chapters. Therefore in this new scenario, the tag's width that corresponds to *m* is fixed. As every column of the polarisers on the tag surface represents one bit of data, then the content capacity is proportional to the tag length. When the moving reader finishes a full synthetic aperture scanning, the effect of each strip of the tag is separately analysed after SAR-based signal processing. Based on the presence or absence of the polarisers, the reader then receives significantly different cross-polar power levels that can be used in the decoding algorithm.

In Figure 7-9 two virtual antennas are shown for two different scenarios. It is important to note that these two antennas are just for representation purposes and there is not any physically large antenna on the reader. Antenna-2 in Figure 7-9 represents the case when a SAR-based reader moves around the tag and simultaneously utilises a very short pulse signal with significant bandwidth. The reader is capable of providing a very fine image resolution in both range and azimuth directions. The equivalent antenna would be a large horn antenna that requires massive aperture in both sides. Antenna-1 in Figure 7-9 shows the equivalent horn antenna for a reader system that only utilises the benefits of the SAR technique with a limited bandwidth of the transmitted signal. This system is only capable of providing a fine azimuth resolution. The provided range resolution for antenna-1 is very coarse in comparison to its azimuth resolution. Therefore, the equivalent virtual horn antenna has an extended aperture in the azimuth direction and limited size in the range direction. As discussed earlier, this is the practical scenario for the current situation of the research. It is possible to propose a planar movement of the reader in both direction and hence provide fine image resolution in both directions. However at this stage, only the fine azimuth resolution through the movement of the reader antenna in one direction is considered.

The data encoding capacity of the system with only azimuth resolution is accommodated to the new rectangle shape of the pixels on the tag surface. Each pixel is 5×10 mm^2 with one bit of data encoding capacity. Hence, the equivalent data capacity is 2 bits/cm^2. This data encoding capacity is still very attractive for a fully printable chipless RFID tag with high system robustness towards multipath interferences.

7.5 SAR-based signal processing

In this section, the EM-image of the tag is derived through the described SAR technique. The tag is comprised of five meander lines as EM-polarisers in each column for data encoding purposes. As discussed in the previous section, a fine azimuth resolution is only targeted through the SAR technique. No attempt is made on range resolution because of the limited available frequency spectrum. Presence of five EM-polarisers on each column of the tag surface represents a binary data of "1" and no polariser means "0". The measured cross-RCS of each strip reveals the presence or absence of meander lines as the data encoding algorithm.

The signal processing fundamentals are based on the SAR technique for azimuth resolution and the range migration algorithm (RMA) for range resolution as described in [154]. Moreover, Charvat [81] simplified the proposed approaches in [154] for low range radar systems. He has suggested a practical and low cost radar system with image resolution of decimetre order. The current work follows the Carrara [154] and Charvat [81] approaches and techniques with appropriate modifications for the proposed application of the chipless RFID systems in mm-wave band.

7.5.1 System structure for data collection

The structure of the tag for EM-imaging is shown in Figure 7-9. The described antenna in Chapter 6, which covers the frequency band 57-64 GHz moves on a straight line around the tag. The straight line is assumed for simplicity of the signal processing. However, for the final stage, the curved trajectory as shown in Figure 7-3 shall be considered. The curved path provides better azimuth resolution as it uses the benefits of the spotlight mode of SAR operation. The reading range, the nadir in Figure 7-9, may vary from 10-25 cm. However, all the result shown in this chapter is based on 10 cm reading distance. This reading range is in line with all measurements carried out so far and shown in previous chapters. The reading step of the reader antenna is 2 mm that is equivalent to almost 0.4λ. This means that the reader illuminates the tag surface in every 2 mm and collects its backscattered signal, and then moves to the next position. The synthetic aperture size may vary from 20-35 cm. However for 10 cm reading distance, the length of 20 cm is normally assumed for the synthetic aperture size to achieve 5 mm azimuth resolution.

Considering the above mentioned parametres, the reading process of the tag requires a high number of separate transmissions and receptions of the signal for data collection purposes; 125 steps for a 25 cm aperture size, for example:

$$Number\ of\ reading = \frac{Aperture\ size}{reading\ step} = \frac{250\,mm}{2\,mm} = 125 \tag{7.8}$$

This seems to be very slow as the reader has many stops for data measurement. This limitation can be easily compensated through continuous movement of the reader through a servo motor. In this case, the Doppler frequency shift due to the continuous measurement process shall be also considered. There is software available, which considers the effect of the Doppler frequency shift in signal processing [160-162]. The second approach for compensation of the long reading process is introduced in the next chapter. In that approach, no reader movement is required, hence the reading process can significantly speed up.

For the range resolution, a normal chirp signal with FM modulation is assumed. The chirp rate of 400 GHz/sec, that is a nominal value for a chirp signal generator, is considered. At the mm-wave band, the start frequency of 58.2 GHz and stop frequency of 62.2 GHz are assumed. The pulse duration is 10 milliseconds hence the occupied frequency band of the chirp is 4 GHz. Considering (7.4), one may expect a very coarse range resolution in multi centimetre order. This is a much rough resolution when compared with azimuth resolution. This means that the effect of all five meander line polarisers on each strip of the tag surface are combined and cannot be separated by the reader.

7.5.2 Signal processing steps

As mentioned earlier, the RMA algorithm defined in [154] is followed for the SAR-based coding. The captured data based on various positions of the reader antenna, known as the raw signal, is processed by the RMA SAR-based algorithm. The RMA normally is divided into the following separate steps:

- Data collection,
- Azimuth Fourier transform,
- Matched filter,
- Stolt interpolation,

- Inverse Fourier transform, and
- Reflectivity image

When the reader moves around the tag, in each specific position, a 2-D data matrix is produced which contains the range profile data. Hence, the collected data has the formation:

$$S\left(x_i, w(t)\right) \tag{7.9}$$

where x_i contains the information of the reader position and the $w(t)$ is the instantaneous of the chirp signal and defines by (7.10) while the c_r is the chirp rate, f_c is the centre frequency of the signal and BW is the signal bandwidth:

$$w(t) = 2\pi\left(c_r t + f_c - \frac{BW}{2}\right) \tag{7.10}$$

The matrix format of (7.9) is considered as the raw signal by the codes for SAR-based signal processing. In the RMA approach, the azimuth Fourier transformation is applied to this raw signal. This is the first difference between the RMA and other conventional approaches in SAR-based signal processing, polar formation algorithm for example. The Fourier transformation changes the time-domain signal, $S(x_i,w(t))$, to its equivalent wave number domain, $S(k_x, k_r)$.

The next phase of the RMA is application of a 2-D phase compensation to the azimuth-transformed signal [154]. This operation perfectly corrects the range curvature of all scatterers at the same range as the scene centre. The matched filter is defined through the following expression on which the R_s shows the distance between to the target centre [81, 154]:

$$S_{mf}(k_x, k_r) = e^{jR_s}\sqrt{k_r^2 - k_x^2} \tag{7.11}$$

Following the matched filter step, Stolt interpolation is applied in the RMA algorithm. It simultaneously compensates the range curvature of all scatterers by an appropriate wrapping of the SAR signal data. This means that the 2-D SAR data from the wave number domain (k_r) to the spatial wave number domain k_y through the following expression [154]:

$$k_y = \sqrt{k_r^2 - k_x^2} \tag{7.12}$$

A 1-D interpolation must be conducted across all the azimuth wave number k_r to map them onto k_y thus resulting Stolt interpolated matrix S_{st} (k_x, k_y) [81].

At this point in the RMA, the processed signals from all scatterers are 2-D linear phase gratings. A 2-D inverse Fourier transform is computed to fully compress the scatterers in range and azimuth [154]. The above mentioned process as illustrated in the Figure 7-10.

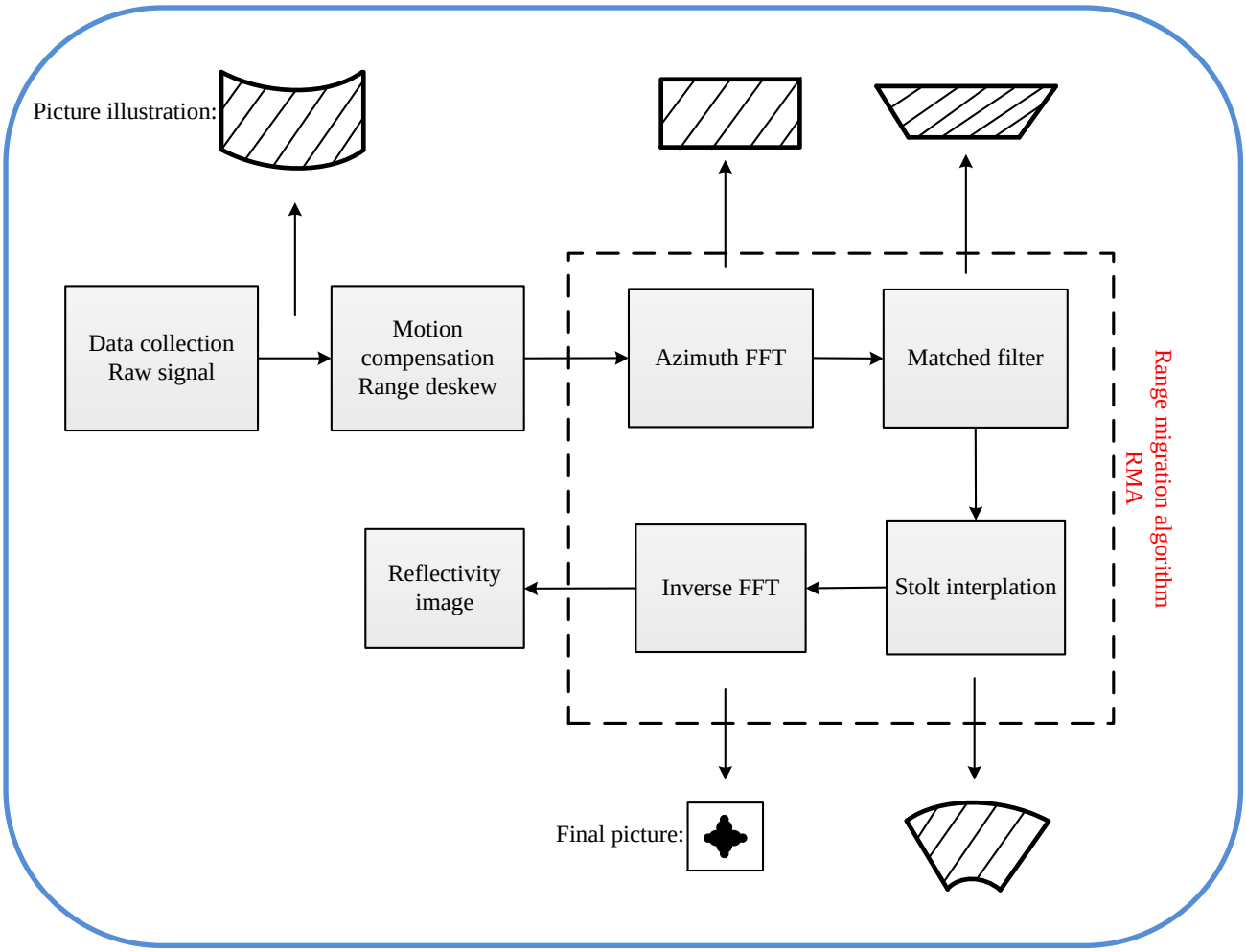

Figure 7-10 Image formation processing using RMA [154]

7.6 Results

The measurement set up is similar to what explained in Chapter 4. Two sets of the designed array of DSPDs antennas introduced in Chapter 6 are used as Tx and Rx antennas. They are connected to the VNA while oriented orthogonally. The printed tag with a SATO printer is located at 10 cm distance of the antennas. The reading distance of 10 cm is considered in all of the measurements in this section because of restricted output power of VNA. At the frequency band 57-64 GHz, the maximum levelled power of VNA is -5 dBm. Considering the maximum gain of array antenna, 7.5 $dB_{i,}$ the EIRP of the system is only 2.5 dBm. However, it has been mentioned in Chapter 3 that the maximum EIRP of 40 dBm is allowed in this band [31, 32]. Therefore, the reading distance may increase to at least 50 cm in commercial phase of the proposed EM-image chipless RFID system if a higher power signal source is available at 60 GHz.

7.6.1 Proof of concept

Considering the proposed system structure and its related technical parameters, two tags with different encoded data are considered. To prove the concept of the data decoding through EM-imaging, the tags only include four bits of data, “1001” and “1011”. The tags are 2 cm long while their width is fixed to almost one cm comprising five meander line in each column. A sample tag with four-bits of data is shown in Figure 7-11.

These two tags are interrogated through the reader at different angles while the reader moves on a straight line of 22 cm. It is important to note that the length of synthetic aperture is 20 cm; however to scan the total tag’s surface it is required to add the length of the tag to the initial synthetic aperture length. As mentioned in the previous section, the reader utilises 4 GHz bandwidth. The received signal before SAR-based signal processing, the raw signal, is shown in Figure 7-12 and Figure 7-13. Based on the position of the reader, various power levels are detected that depend on the frequency of operation. The power levels shown in Figure 7-12 and Figure 7-13 are the normalised power for two tags “1001” and “1011”, respectively. The raw signals shown in Figure 7-12 and Figure 7-13 convey no information at this moment, hence the steps mentioned in Section 7.5.2 shall be taken to extract the tag information. However, comparing the two figures reveals that only changing one bit of the tag’s data completely changes the pattern of the received signal.

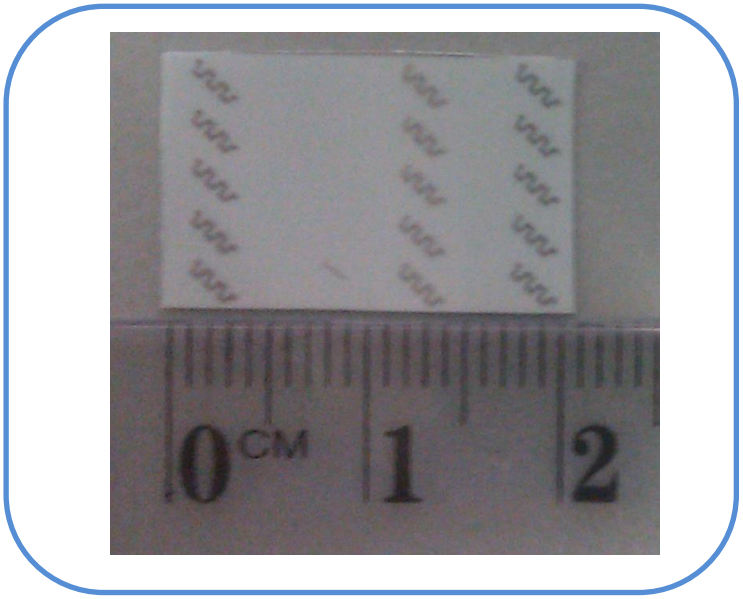

Figure 7-11 Photograph of 4-bit printed tag.

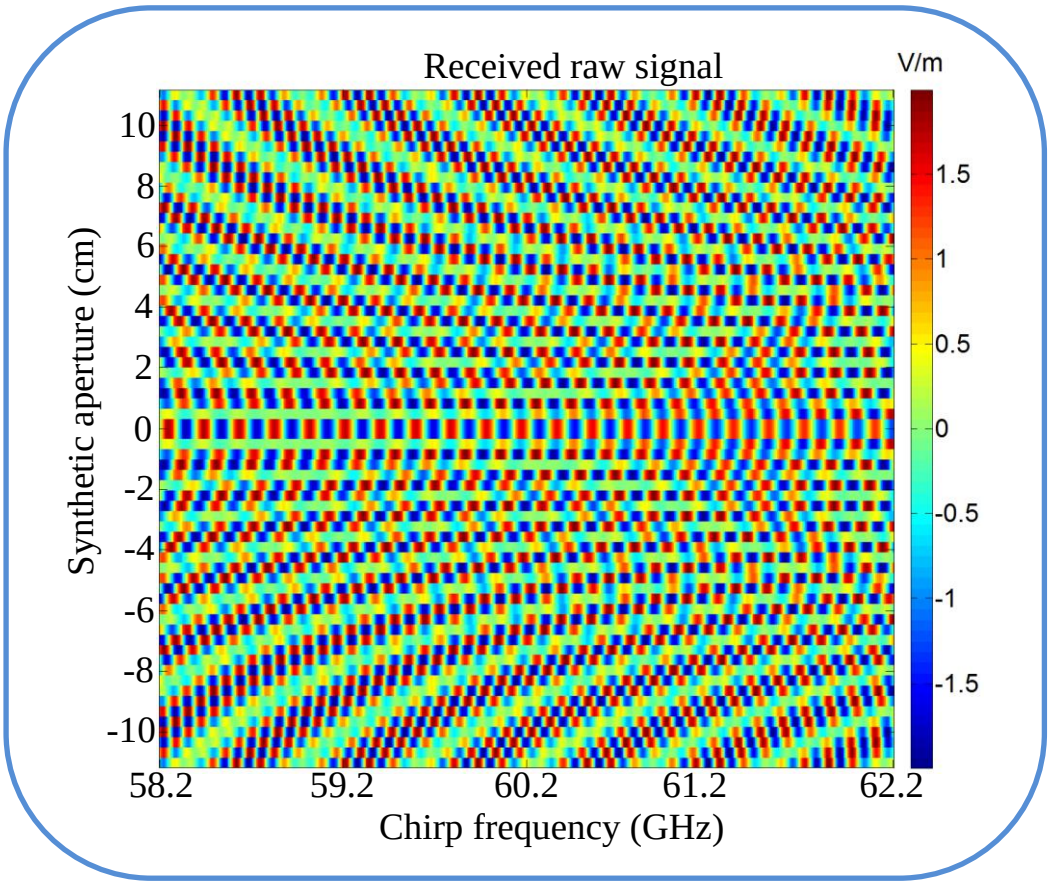

Figure 7-12 Raw SAR signal for tag with data "*1001*".

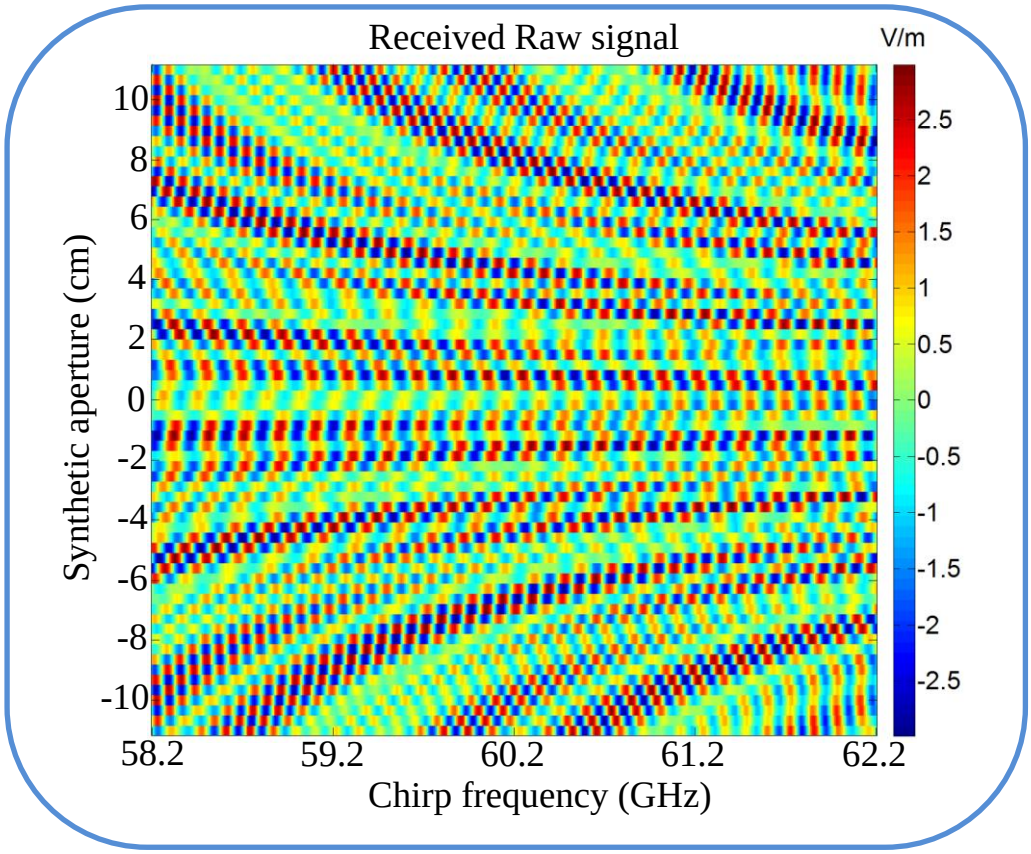

Figure 7-13 Raw SAR signal for tag with data "*1011*".

After appropriate signal processing for azimuth resolution based on the SAR theory and the RMA-based technique for range resolution, the EM-image of the tag is captured. The related EM-images of the tags with "1001" and "1011" data are shown in Figure 7-14 and Figure 7-15, respectively. The images shown are like the image of a single point scatterer. However, it is important to note that the effect of five meander lines in each column (strip) of the tag surface is combined together through coarse range resolution and their aggregate received power is considered and shown in these figures. This is why the image has a single bright point for each column of five polarisers.

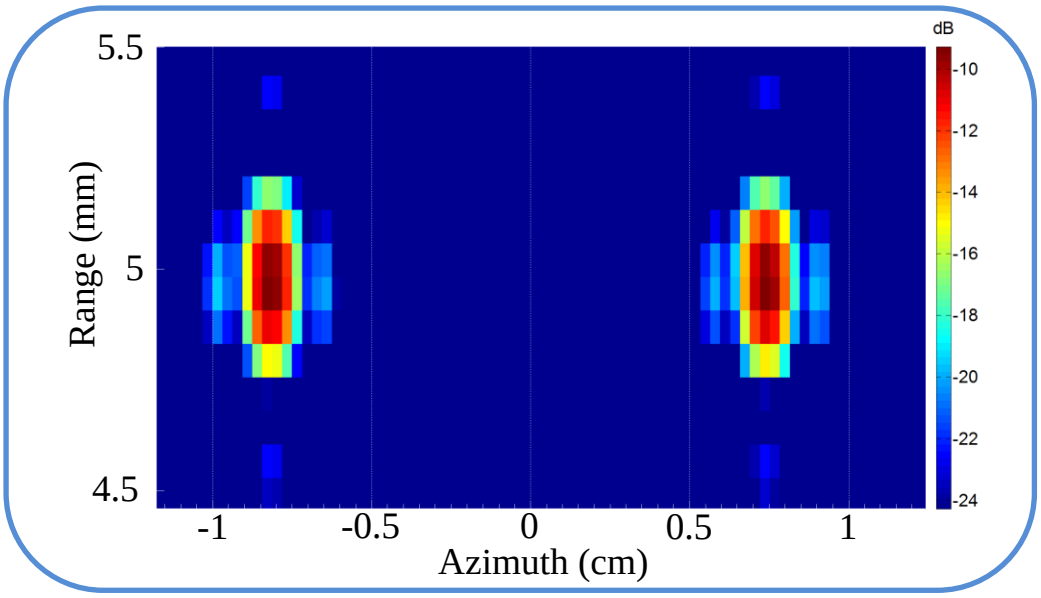

Figure 7-14 EM-image of *"1001"* tag with 22 cm aperture size, reading range 10 cm.

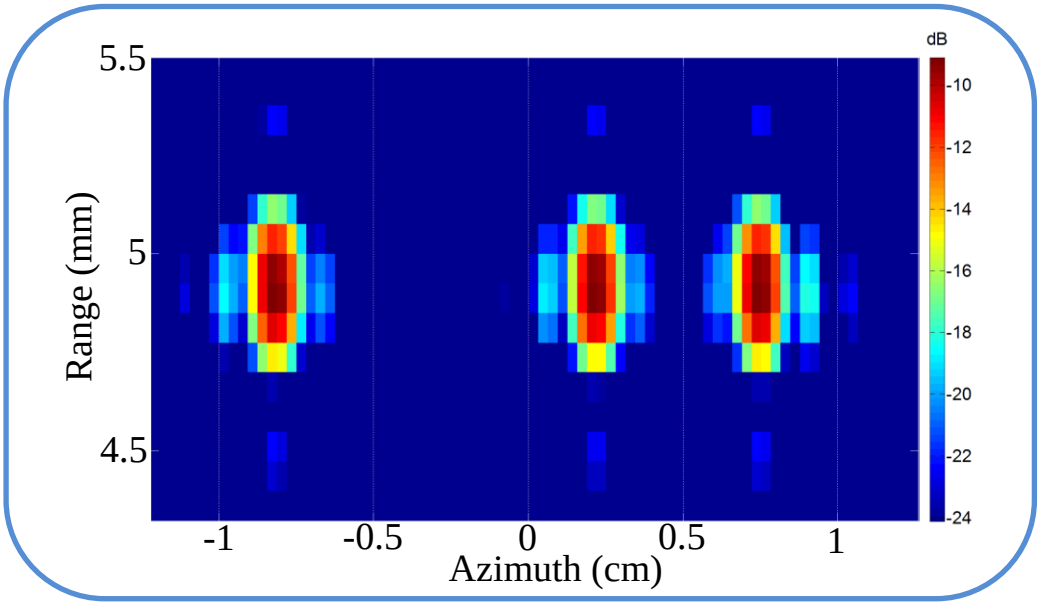

Figure 7-15 EM-image of *"1011"* tag with 22 cm aperture size, reading range 10 cm.

The vertical axis which relates to the range and is in millimetre order **is not the real range** resolution of the processed EM-image. It is actually assumed that all the five polarisers are located on the centre point of the strip. For coding purpose only a length of 1 mm is considered for the strip. Hence the vertical axis includes the total length of around 1 mm. It is possible to assume that these five polarisers are distributed over the total column length. This results in another value for the vertical axis, 10 mm for example. However, the actual range resolution is much higher than the values shown in Figure 7-14 and Figure 7-15.

The values on the colour bar show the difference between the signal level, in the cross-polar direction, from a strip with five EM-polarisers, and the reflection from parts of the tag without any polariser. These values are matched with what was experienced in the measurement process in Chapter 4. One may recall that five printed meander lines created a 15 dB higher cross-polar component when compared with the no tag situation, Figure 4-7. As the colour bars in Figure 7-14 and **Figure 7-15** show, the maximum received power level of five printed meander lines are 14 dB higher than the response of other parts of the tag without meander line polarisers.

From Figure 7-14 and Figure 7-15, it is clear that the EM-image of the tag is effectively capable of revealing the encoded data on the tag surface with printed meander lines. The reflections by meander lines as EM-polarisers are noticeably higher than that of the tag's surface and other surrounding objects around the tag. This suggests a very robust and reliable approach for data encoding. The data encoding capacity of the tag relates to the resolution of the EM-image. Based on Figure 7-14 and Figure 7-15, the azimuth resolution is 5 mm and it is clearly shown in the processed images of the tags. This is the actual and real azimuth resolutions so far obtained by the utilised technique in the signal processing step. Considering the width of the tag which includes five meander line polarisers, the data encoding capacity can be easily calculated. Each detectable column of polarisers on the tag surface has therefore the width 5 mm that is the actual azimuth resolution. The length of the strip is equal to the width of the tag. For five meander lines on each column, the maximum width of the tag or the length of the column is one cm. Hence, the total area that each column occupies is 0.5 cm^2. As each column may represent "1" or "0" or one binary bit, therefore it can be concluded that the total data encoding capacity is 2 bits/cm^2 or equivalently four different states on each square cm. This is the data encoding capacity that has been achieved so far. However, the author does believe that with more advanced signal processing techniques, the achievable data encoding capacity can be doubled. The total data capacity of the tag directly depends on its length. Each 0.5 cm of the tag length encodes one bit of data and for increasing the encoded data, the length of the tag needs to increase.

7.6.2 Image resolution versus aperture length

The tags discussed in the previous section encode four bits of data and have been read at 10 cm distance. The aperture size of the synthetic antenna was assumed to be 22 cm. Moreover,

the reader moved on a linear route around the tag. The graphs in Figure 7-8, however suggest smaller aperture size for the 5 mm image resolution in the reading distance of 10 cm. Testing this suggestion, aperture sizes less than 22 cm are considered. Two lengths of 12 and 17 cm are assumed for the synthetic aperture length. The EM-images of the same tag as for Figure 7-15, "1011", are shown in Figure 7-16 and Figure 7-17 for the aperture lengths 12 and 17 cm, respectively.

As is clear from Figure 7-16, the provided image by 12 cm aperture size does not decodes the tag's data of "1011". The effect of each column of polarisers has spread over the other segments of the image that is not matched with the initial size of the tag. The image in Figure 7-16 has almost five cm length while the initial tag is only two cm long. Hence, the image resolution of 5 mm is no longer existed for the case of 12 cm aperture size.

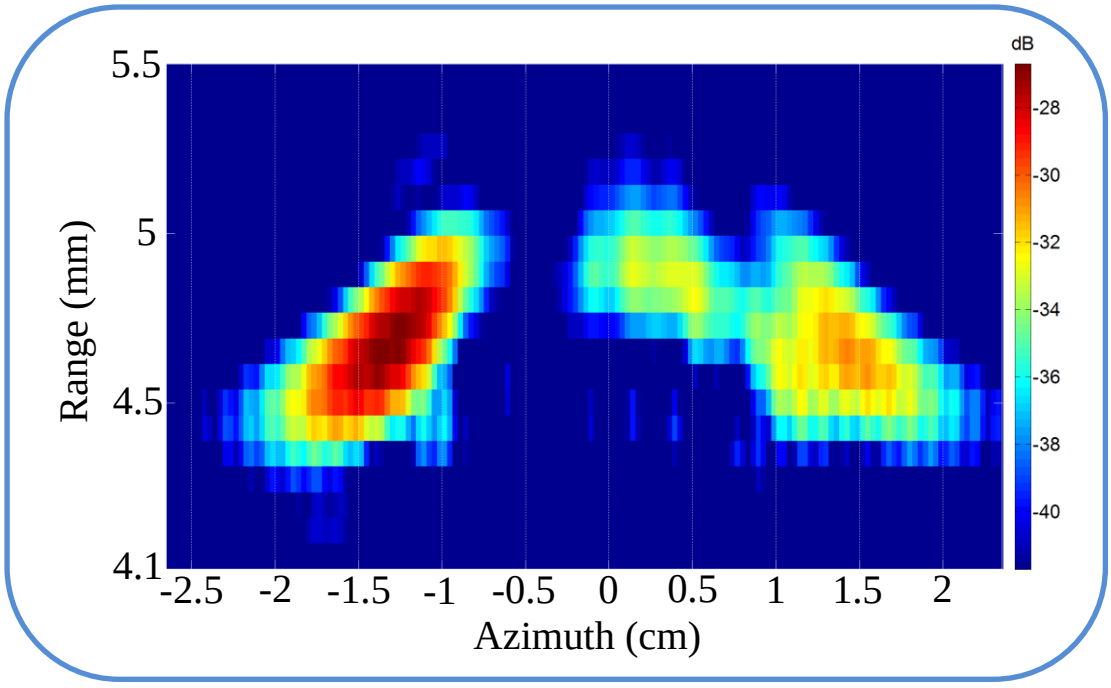

Figure 7-16 EM-image of the tag "*1011*" with 12 cm aperture size.

Increasing the aperture size to 17 cm elevates the final image resolution. In this case, the effects of three columns of polarisers are detectable on the tag's image. However, the final azimuth resolution is less than what is already shown in Figure 7-15. Again, the image of the tag spreads to three cm while the initial tag is two cm. Moreover, the vertical position of the column of polarisers in Figure 7-15 is very clear and matches the actual position of the meander lines on the tag surface. While in Figure 7-17, the image shows inclined rows of

polarisers, which makes it difficult to separate the effect of the adjacent columns of polarisers. Therefore, for the aperture size of 17 cm, the data encoding is very difficult if not impractical.

Three reasons can be suggested for the difference between the predictable image resolution as calculated and shown in Figure 7-8 and the actual image resolution after signal processing. First, the graphs in Figure 7-8 are based on (7.7) that relates to a reflector antenna type [144]. While the system structure of the tags in Figure 7-14 and Figure 7-15, the reader travels on a straight line instead of a curved line. Moreover, (7.7) is related to a physical antenna, while in the signal processing a finite number of sample points are existed to simulate an array antenna structure. The differences between these two ideas are qualitatively shown in Figure 7-1. Finally, the utilised signal processing algorithm is the standard SAR-signal processing approach. There are advanced SAR-based signal processing techniques which enhance the final image resolution.

It is important to differentiate between the required aperture length for a certain azimuth resolution and the final aperture length for imaging the whole tag. The theoretical length of the synthetic aperture was shown in Figure 7-8 for a certain azimuth resolution based on various reading distance. Moreover, it was discussed in this section that in real scenario, larger synthetic aperture is required than that of expected in Figure 7-8.

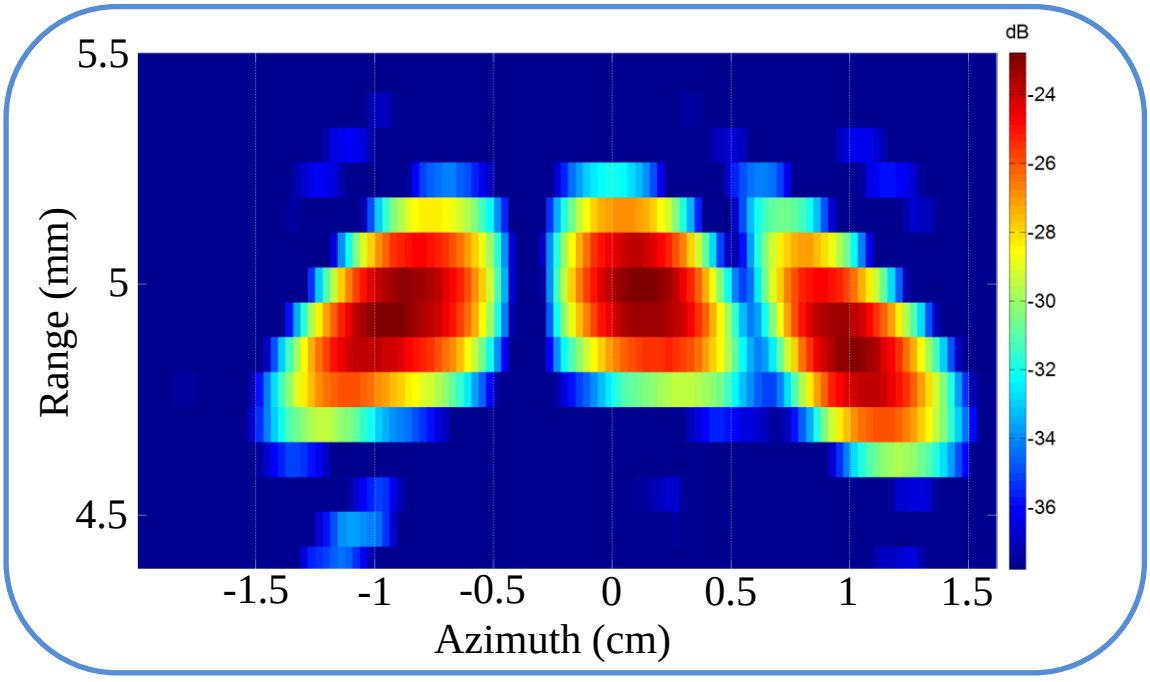

Figure 7-17 EM-image of tag with "*1011*" data with 17 cm aperture size.

It is crucial to emphasize that this length is the minimum length, known as fundamental aperture length (D_f) that is required to provide the expected resolution. However, for covering the whole tag, the reader shall move more than this fundamental aperture length. This operation is shown in **Figure 7-18**. The reader is required to move around the tag for D_f length to be able to provide a certain azimuth resolution. For example, 20 cm synthetic aperture is required for 5 mm resolution as shown in Figure 7-14 and Figure 7-15. However, as the tag is 4 bits and has 2 cm length, hence the final synthetic aperture size would be 22 cm to cover the whole tag for data decoding purpose. The results are shown in Table 7-1. As one may notice the fundamental aperture length of less than 20 cm is not large enough for targeted 5 mm image resolution.

Table 7-1 Synthetic aperture size and image resolution

Minimum final Aperture length (cm)	Fundamental aperture length (D_f) (cm)	Image resolution (mm)	Tag length (cm)	Tag data capacity	Reading process
12	10	> 5	2	4	Not successful
17	15	> 5	2	4	Not successful
22	20	5	2	4	successful
24	20	5	4	8	successful
25.5	20	5	5.5	11	successful
28.5	20	5	8.5	17	successful

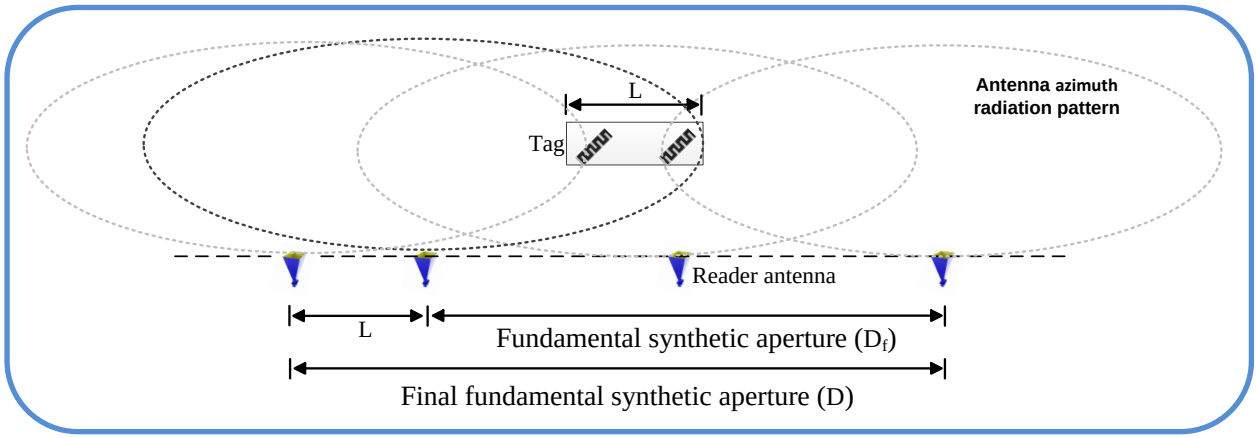

Figure 7-18 Final and fundamental aperture length.

Therefore, the length of 12 and 17 cm were not able to decode a tag with 4 bits data encoding capacity and 2 cm tag length. If the fundamental aperture length 20 cm is addressed, then based on the length of the tag, the final aperture length is determined. The values of Table 7-1 are considered for the measurement of higher bits tag at the rest of this chapter.

7.6.3 High data content tags

In Section 7.6.2, the concept of EM-imaging for data encoding purposes was presented and its applicability is aproved. It was shown that a four bits tag can be read at 10 cm distance through a moving reader and after post signal processing, the EM-image of the tag at a cross-polar direction successfully reveals the encoded data on the tag surface.

In this section, the final data encoding capacity of the proposed approach is shown. It is important to mention that similar to any other approaches in the chipless RFID system, the final data encoding capacity of the tag directly depends on its physical size. Obviously, more data can be encoded on a larger tag surface. Normally the credit card size of 55 × 85 mm^2 is considered as the maximum allowable size of a chipless RFID tag. The maximum data encoding capacity of any proposed technique is considered based on this maximum allowable physical size.

Multiple tag structures with different encoded data are considered to show the performance of the proposed theory and its final data encoding capacity. The printed tag structure, its received raw signal, and finally, its EM-image is shown in **Figure 7-19** for a tag with eight bits of data. As suggested, the tag length is four cm and its width almost one cm. The expectation is to encode one binary code in each 5 mm of the tag length. The final image of the tag clearly shows the position of each column of 5 polarisers on the tag surface. There is no overlay between adjacent columns. The SAR aperture size is (20+4) cm. 20 cm is required for 5 mm azimuth resolution and 4 cm shall be added due to the total length of tag. Figure 7-19 shows the tag image based on 24 cm total aperture. This length is shown in the raw signal graph of Figure 7-19.

Figure 7-20 and Figure 7-21 show two tags with 11 and 17 data bits, respectively, along with their final EM-image. The raw signals are not shown for these two cases. Again the aperture size for each case is approximately the initial aperture length 20 cm plus the length

of tag. As is clear from the related EM-images, the processed image successfully reveals the presence or absence of polarisers on each column of the tag surface, hence data decoding is performed successfully. These results confirm the validity of the proposed theory at its maximum performance capability. As discussed before, the acquired cross-range resolution is again 5 mm and the width of the tag is around 10 mm with five polarisers on each column.

Therefore, the detectable data encoding capacity of the printed tag is 2 bits/cm^2. For a chipless tag of 8.5×1 cm^2, 17 bits can be encoded as shown in Figure 7-21. This tag is 5.5 times smaller than a credit card (8.5×5.5 cm^2). Hence it can be concluded that in an area equivalent to a credit card, 93 bits encoding capacity is feasible. This encoding capacity for a chipless RFID system is very attractive. However, when other aspects of the proposed technique have been recalled, the significant advantages of the proposed technique are very attractive for industries. The acquired data encoding capacity is based on a fully printed tag structure. The printed tag is fabricated on a paper substrate with the minimum conductive ink usage. There are many structural anomalies on the printed tag. Irrespective of these printing issues, it performs adequately for data encoding purposes. The robustness of the proposed tag structure with respect to multipath and clutter interferences has been already shown through measurements. The chipless tag is also applicable for tagging of metallic and high reflective items. The tag provides a reasonable performance when bent around on the products' surface. Considering all of these aspects of the tag, specifically its data encoding capacity, it can be concluded that a very successful and innovative approach has been proposed for the chipless RFID systems.

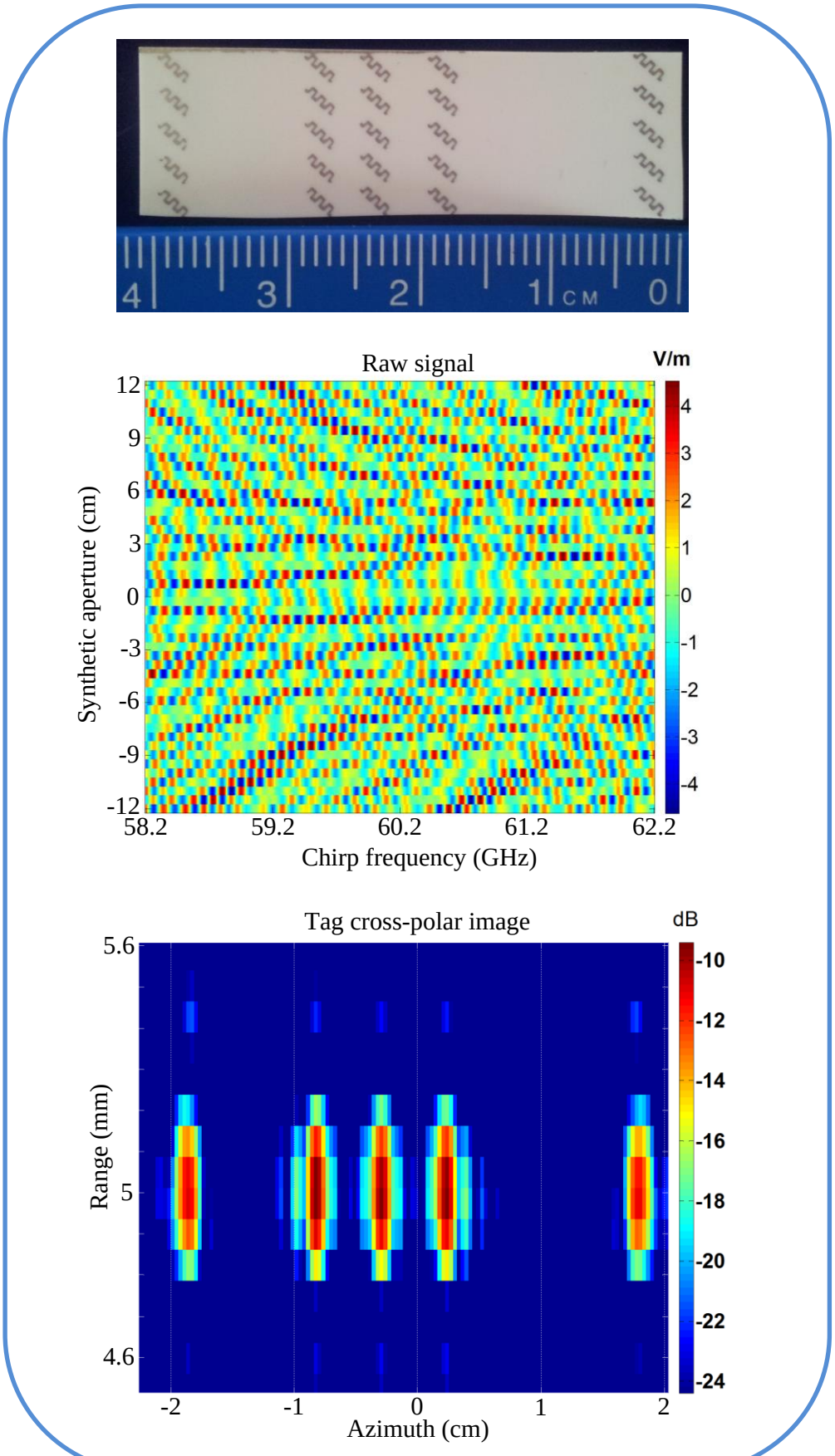

Figure 7-19 Raw SAR signal and final EM-image of printed tag with 8 bits of data, aperture size 24 cm.

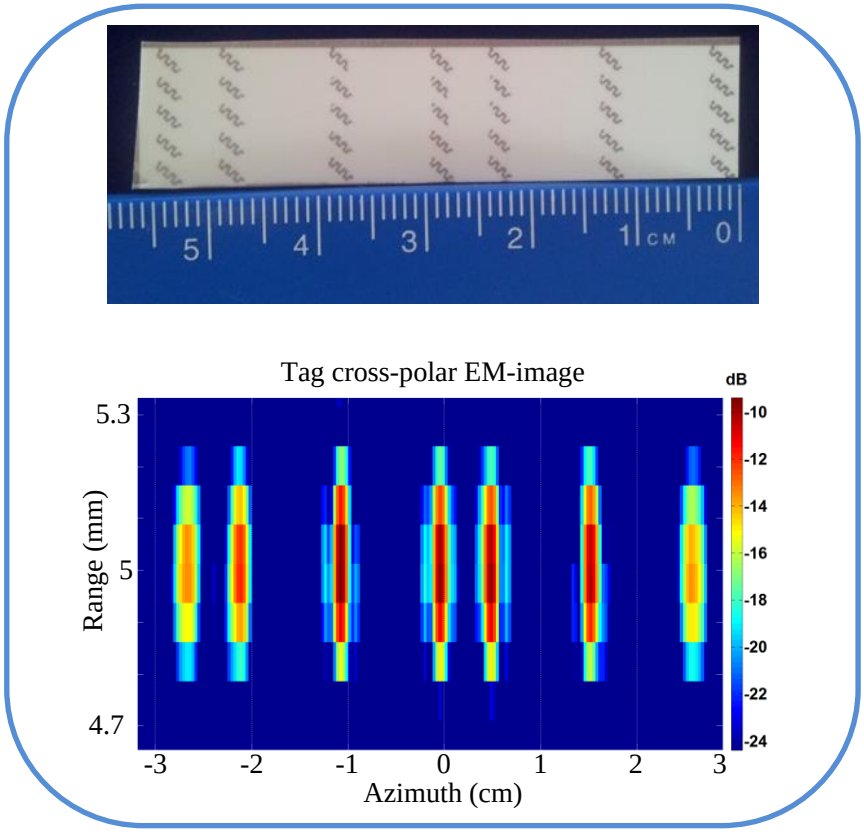

Figure 7-20 Cross-polar EM-image of tag with 11 bits of data, aperture size 27.5 cm.

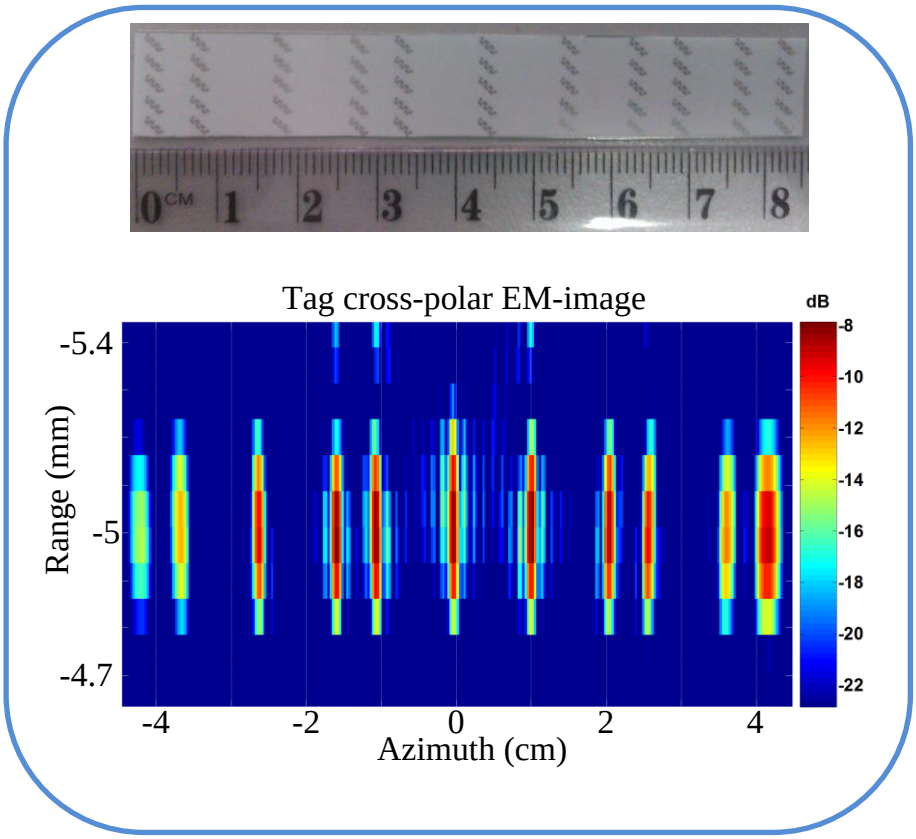

Figure 7-21 Cross-polar EM-image of tag with 17 bits of data, aperture size 30 cm.

7.7 Conclusion

The synthetic aperture radar theory has been briefly reviewed in this chapter. It was shown that tag imaging requires the implementation of the synthetic aperture theory with regard to some technical requirements. Then three modes of operation of the SAR theory along with their attributes and limitations were discussed. Although the strip map mode is applicable for the proposed application, the spotlight mode is able to provide better azimuth resolution due to the increased length of the synthetic aperture size. Hence, the spotlight mode of operation was proposed as the image resolution with the highest priority in the proposed application.

Then the image resolution in range and azimuth direction was associated with the system parameters such as frequency of operation, available bandwidth, reading range, and synthetic aperture size. Based on the features of the chipless tag, it was found that fine range resolution is not achievable considering the limited available frequency band. Hence in the proposed theory of EM-imaging, only azimuth resolution can be used for data decoding purposes. Based on this, the final tag structure and data encoding algorithm were proposed. The theoretical data encoding capacity of the system was also introduced and provides a very high data encoding capacity. The required aperture size, reading distance and other parameters were also included in the calculations and assumptions.

In the final stage of this chapter, the electromagnetic images of some sample tags with different data encoding capacity have been shown. First simple tags with only four bits of data were reviewed. Their final EM-image successfully decoded the tags' data that revealed the applicability of the proposed theory of imaging for chipless RFID application. The effect of aperture size was also considered at this stage. It was found that the actual required aperture size was almost compatible with what was expected through theoretical calculation. The final achieved image resolution is 5 mm in azimuth direction based on the straight trajectory of the reader, in the strip map mode. However, if the final curvature movement of the reader is inserted in the signal processing process, in the spotlight mode, the better azimuth resolution of 2 mm can easily be expected. Then based on the satisfactory results gained from the 4 bits tags, larger tags with higher content capacity were considered. The maximum length of the RFID tag, 8.5 cm, was utilised to encode 17 bits of data while the tag width is only 1cm, 5.5 times narrower than a credit card size. This step revealed the ultimate data encoding capacity of the proposed technique beyond 90 bits/credit card or 2 bits/cm^2. This suggested a very attractive content capacity for a chipless RFID system, based on results

that have come from a fully printable tag structure measured in a lab environment with high multipath interference and clutter robustness, as discussed previously.

Considering the final result achieved through signal processing in this chapter, it can be concluded that the EM-imaging is an applicable technique for chipless RFID system. This is the first time that all details of EM-imaging chipless RFID system has been publicly disclosed which may open a new area of research for the chipless RFID systems and other applications. It was discussed earlier that other approaches normally rely on the frequency domain and time domain responses of the tag. However, the proposed approach of cross-polar EM-imaging suggests an alternative methodology for data encoding on the tag surface, that is fully robust to printing inaccuracy and low Q factor of the printed circuit on the tag. While EM-imaging can be considered as an independent technique for chipless RFID systems, it may combined with other conventional approaches in chipless RFID systems for enhancement of their capabilities. The few limitations of the proposed technique are discussed in the next chapter along with some practical solutions for addressing them.

Chapter 8 MIMO-based array antenna for fast imaging

8.1 Introduction

EM-imaging as a data encoding approach for the chipless tag has been introduced earlier. It is confirmed that EM-imaging is an effective approach to high data capacity chipless RFID systems. The measurement results have revealed the salient attributes of the SAR imaging technique regarding its: *i)* superior data encoding capacity, *ii)* robustness detection against multipath and clutter interferences, and *iii)* reliable performance to printing inaccuracy. However, there are two limitations associated with the proposed EM-imaging technique that may deter its full potentials in mass deployment of the chipless RFID systems in the market. The main issue which is associated with the proposed EM-imaging technique is the requirement for relative movement of the reader and tag. This chapter considers this limitation and proposes a fairly simple solution for accelerating the tag imaging process. The second limitation that is the tag orientation sensitivity, is addressed in Chapter 9.

This chapter is organised as follow: *i)* requirement of the relative movement of the reader and tag in the proposed EM-imaging technique is first introduced. *ii)* the phased array antennas with agile beamforming capability are considered as a solution for reader movement and its system complexity is discussed. *iii)* the new idea of MIMO-based array antenna is presented. *iv)* a MIMO-based array antenna is designed for fast imaging of the tag and the result of simulation is presented. Finally, *v)* the approach for optimization of the MIMO-based system is introduced as the next phase of this research. The stream of discussion in this Chapter is shown in Figure 8-1.

8.2 Reader physical movement

EM-imaging of the tag's surface through SAR requires relative movement of the reader antenna with respect to the tag. As the tag is normally fixed or its movement trajectory is not predictable, hence a fixed tag and a moving reader antenna are assumed to be the most practical system configuration. Therefore, a moving reader antenna on a defined trajectory around the tag, is the general case of the proposed system configuration. As discussed in Chapter 7, illumination of the tag and gathering its backscattered signal from different view angles normally requires large number of individual transmit and receive scans, for example

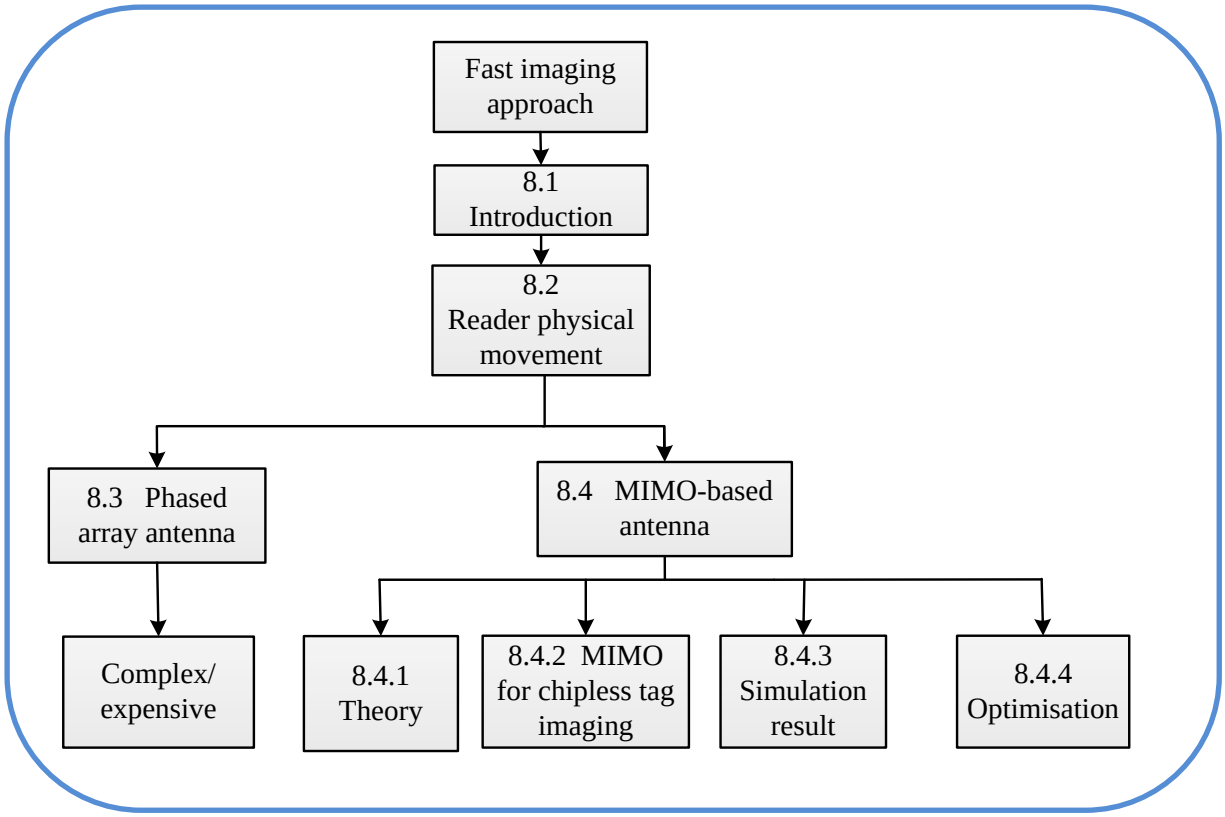

Figure 8-1 Stream of discussion in Chapter 8.

125 times. This severely affects the system's reading speed which may be seen as a main drawback of the proposed approach. The movement of the reader around the tag for the SAR processing shall not be based on the operator's hand movement. Obviously, the speed, aperture length and other factors cannot be maintained accurately for SAR signal processing through manual movement. Instead, the moving reader antenna will be encompassed in a jig and the antenna moves over a rail of maximum 30 cm length while controlled by a stepper motor as shown in Figure 8-2. Therefore, the moving reader antenna collects the backscattered signals while continuously moves around the tag, similar to earth imaging approach. In this scenario, a Doppler frequency shift due to continuous movement of the reader antenna is expected. Although this stepper motor based moving reader antenna provides a much faster reading time, 300-500 millisecond, the reading time is still not considered very fast in the current demand. Moreover, mechanically movement of the antenna is not compatible with other innovative approaches as proposed in the EM-imaging technique. To mitigate this issue, a phased array antenna and a MIMO-based array antenna are considered as the substitutes of the mechanically steered antenna. The potential advantages and limitations of these two proposed approaches are briefly discussed in the following sections.

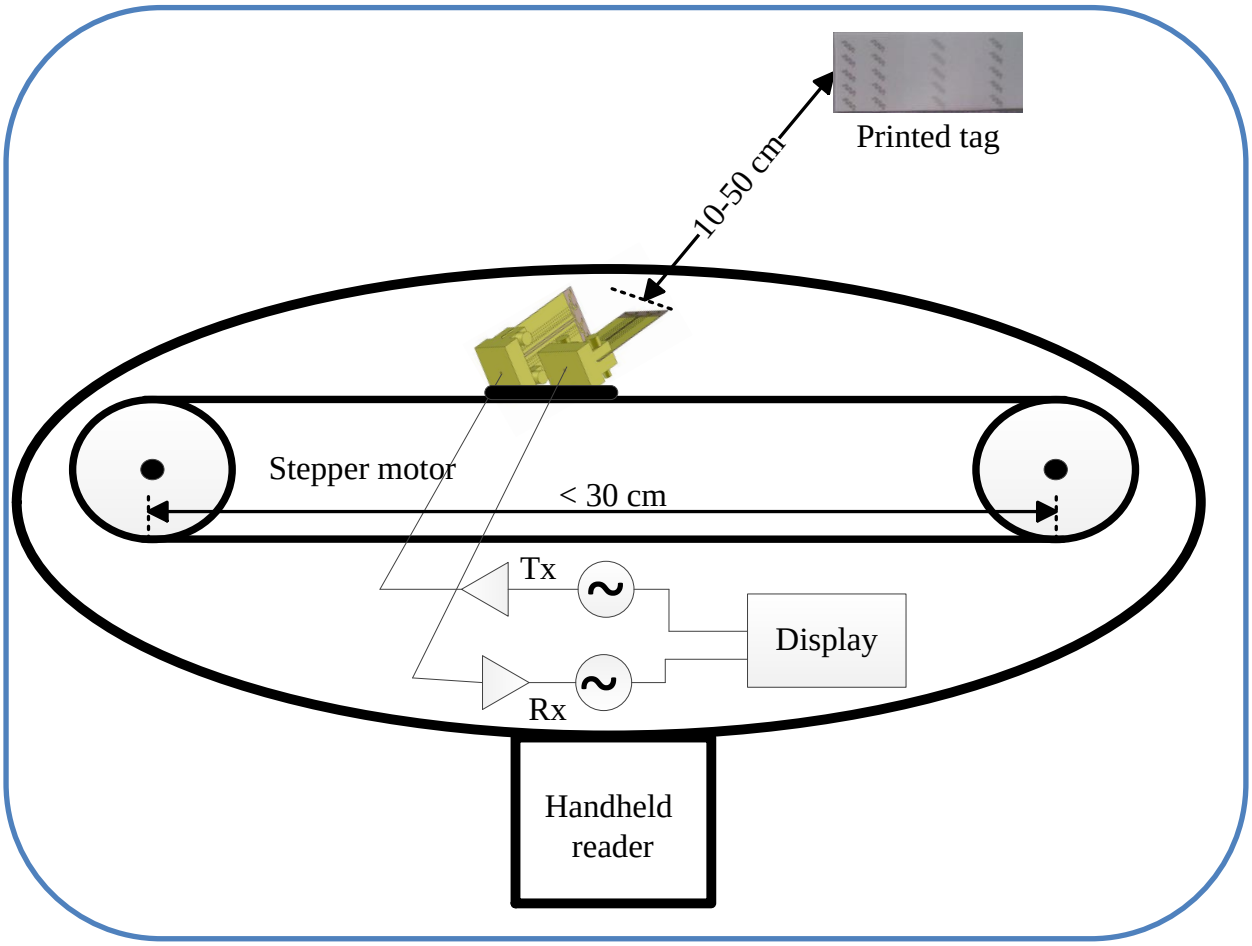

Figure 8-2 Handheld reader with mechanically moving antennas.

8.3 Conventional phased array antenna

Phased array antennas have emerged as the most advanced technology in the modern day radar systems. It provides huge enhancement in performances that are of interests in radar systems, modern wireless communications and many commercial applications. In a phased array antenna, antenna elements are precisely controlled in relative excitation of phase and amplitude to generate directional beams and nulls in desired direction [144].

Figure 8-3 shows the block diagram of a phased array antenna. As is shown in the figure, the signal first arrives (or departs) to the right element. The second element of the array receives the signal with Δt delay. The next element receives the signal with a delay of $2\times \Delta t$ and so on. If proper phase adjustment is utilized at the feeding point of each array element, then the signal from a desired direction, θ for instance, could be constructively added to each other. This simply means that the whole array performs as a unique antenna and effectively receives signals from the direction θ.

Appropriate relative phase adjustments of the array elements in the time domain is known as the time domain beamforming. This happens by creating precise time delays in the received signals of each array element. Time domain beamforming provides an accurate result for a wideband signal, however, the precision of the delays are restricted to the capabilities of devices for precise time delay control.

It is also possible to use the fast Fourier transform (FFT) and transfer the required adjustment of the array elements in the frequency domain instead of time domain through the following equations:

$$F\{x(t)\} = X(j\omega)$$
$$F\{x(t-\Delta t)\} = X(j\omega)e^{-j\omega\Delta t} \quad ; \quad \omega.\Delta t = \frac{2\pi fd\cos(\theta)}{c} = \Delta\phi \tag{8.1}$$

where $x(t)$ is the receive (transmit) radar signal in time domain and $X(j\omega)$ is its Fourier transform, d is the inter-element distance f is the frequency of operation, Δt is the relative time delay between each adjacent elements, ω is the equivalent frequency domain of the signal and $\Delta\varphi$ is the equivalent phase shift in each adjacent elements.

This means that through specific phase shift in the feeding route of each array element, the array can steer on a specific direction. Solid state digital phase shifters and voltage variable controlled attenuators are widely developed nowadays on which precise adjustment of each antenna element is possible based on the required "weight vectors". The frequency domain is a more common technique in the phased array systems than the time delay approach as it can provide much more accurate beamforming results.

Applying the phased array antenna theory to the proposed image-based chipless RFID system, two difficulties shall be considered. First, in the phased array structure, phase shifters or their equivalent time delay modules are needed. To precisely scan the tag surface in the order of a few millimetres, the phase shifters' granularity shall be very fine [163, 164]. Utilizing accurate phase shifters in the 60 GHz frequency band significantly increases the system cost. Moreover, when the phased array antenna scans the tag, the beam shape distorted with the view angle. This may not be a serious issue in many applications, however in the proposed EM-imaging theory, the fixed shape of the radiation pattern is vital otherwise the tag's image is distorted [74].

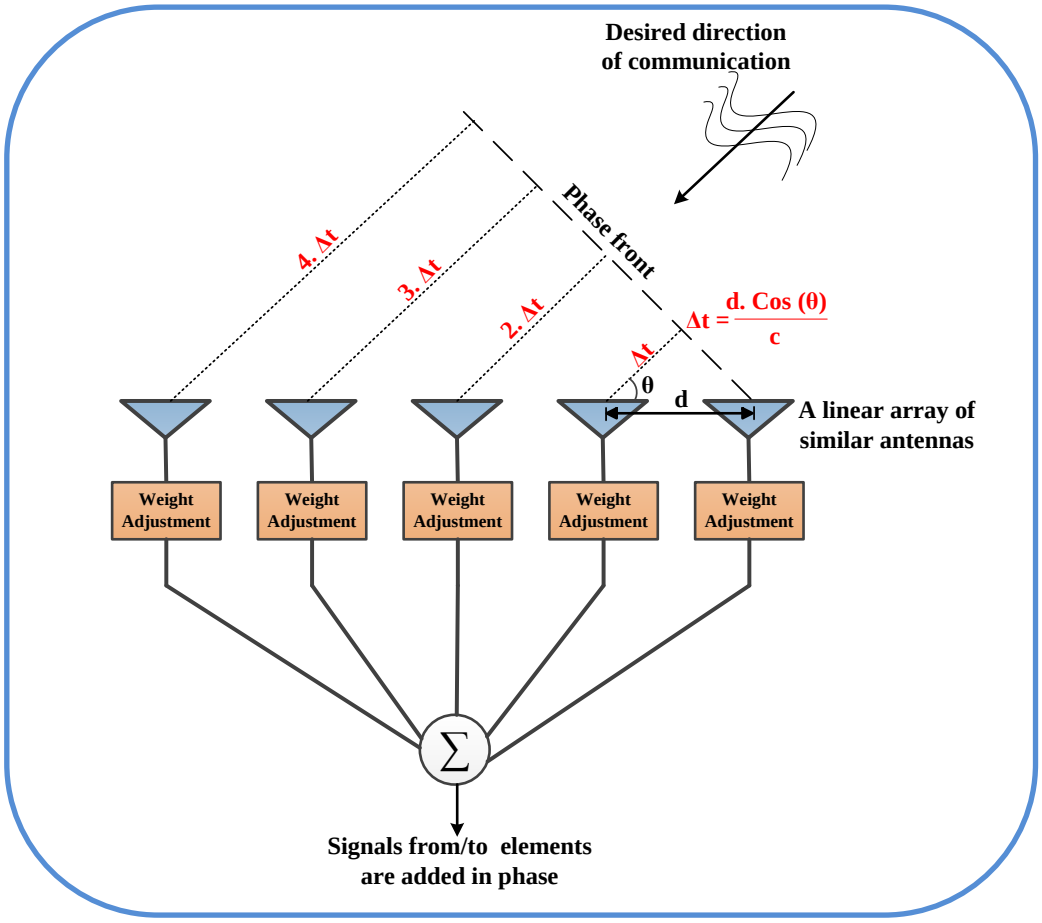

Figure 8-3 General block diagram of phase array antenna.

To minimise the variation of the agile radiation pattern at different view angles, it is possible to use very accurate feeding algorithm that provides the required amplitudes and phase shifts to individual elements [163]. In this approach, more accurate amplitude tapering modules and precise phase shifters are required that significantly increase the system's cost and complexity [163]. Therefore, phased array antennas with fixed beam shape are normally restricted to very high technology military applications. The proposed low-cost EM-imaging chipless RFID system cannot tolerate such an expensive and complex antenna system.

With the aforementioned limitations, it can be concluded that the usage of a conventional phased array antenna for replacement of the moving reader is not practically feasible for the RFID application. Therefore, an alternative to the conventional phased array antenna─a MIMO-based array antenna with reduced complexity─ is considered next.

8.4 MIMO-based phased array antenna

Considering the potential advantages on providing flexibilities and freedom due to the usage of multiple channels, the MIMO-based systems are of interests to researchers [165]. MIMO technique has recently provided noticeable simplifications on radar systems [166-168]. MIMO-SAR that employs multiple antennas to transmit orthogonal waveforms and multiple antennas to receive radar echoes. MIMO-SAR is recently proposed in remote sensing concept [169]. It is shown that the MIMO-SAR can be used to improve the remote sensing system performance. One of the main advantages of the MIMO-SAR is the greatly increased degrees of freedom by the concept of virtual antenna array [166]. In the conventional phased array radars, the transmitted signals through array elements are inherently dependants and only vary by some time delays or its equivalent phase shifts. However, in the MIMO-based system, each antenna transmits a unique waveform that is orthogonal to the waveforms transmitted by other antennas. This means that the return signals to each receive antenna element will carry independent information about the target, hence increasing the system freedom and flexibility. The phase difference caused by different transmitting antennas along with the phase differences caused by different receiving antennas can form a new virtual antenna array steering vector [166]. With optimally designed array elements' positions, a very long array steering vector with a small number of antennas can be created. This provides high flexibility and reconfigurability in antenna configuration [166, 170].

The idea of the MIMO-based array antenna is applied on the chipless RFID system. It is found that the new technique of MIMO-based array has huge potential for increasing the tag imaging time on a fairly low cost and simple reader configuration. This idea is introduced and developed further at the rest of this chapter for the chipless RFID imaging.

8.4.1 MIMO-based array theory

An 8-element MIMO-based antenna and its equivalent sparse arrays are shown in Figure 8-4. It shows the relation between the MIMO system and the traditional array antenna. In this simple example, four Tx and four Rx planar MIMO antennas are connected to each other [171]. It is envisioned to show the transition between the MIMO theory and its equivalent virtual array antenna without being deeply involved with the mathematical calculations.

In Figure 8-4, 8-element MIMO-based system is comprised of four Tx antennas and four Rx antennas. Each Tx antenna can independently transmit its signal and all the Rx receive antennas collect the backscattered signal. The normalised separation distance between Rx and Tx antennas are 6 and 9 respectively as shown in Figure 8-4. Dimension is not important but centimetre can be assumed as example. Receive and transmit antennas can be considered as an sparse array antenna with constant separation of 3 cm. This means that the Rx array is a sparse array of seven elements with separation distance 3 cm while the active and passive elements are distributed in the sparse array as:

1 0 1 0 1 0 1

The same assumption is valid for the Tx array with the following topology for the active and passive elements:

1 0 0 1 0 0 1 0 0 1

Based on the array theory, it can be shown that the array factor of each array antenna is equivalent to a polynomial of N-1 order on which N is the number of array elements [143, 172]. Therefore, the related polynomials of the receive and transmit arrays are respectively as follow:

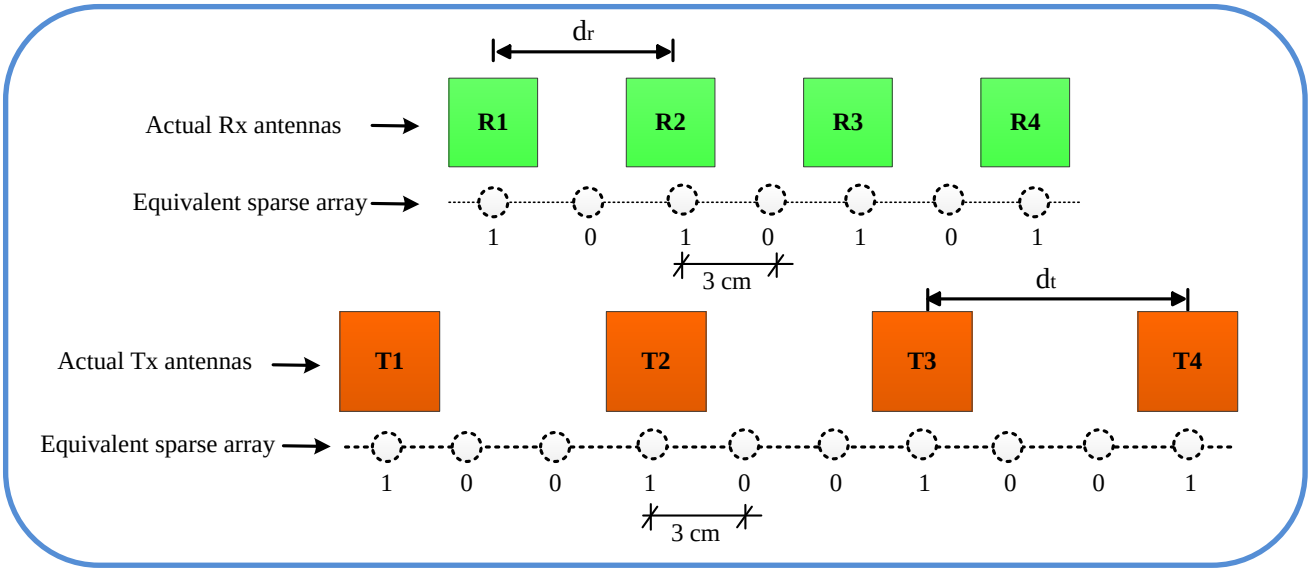

Figure 8-4 MIMO-based antenna system and the equivalent sparse array antennas.

$$P_r = 1.z^6 + 0.z^5 + 1.z^4 + 0.z^3 + 1.z^2 + 0.z + 1 = z^6 + z^4 + z^2 + 1 \quad ;\text{for Rx array}$$
$$P_t = 1.z^9 + 0.z^8 + 0.z^7 + 1.z^6 + 0.z^5 + 0.z^4 + 1.z^3 + 0.z^2 + 0.z + 1 = z^9 + z^6 + z^3 + 1 \;;\text{for Tx array} \quad (8.2)$$

It can be mathematically proven that the two sets of Tx and Rx antennas on MIMO-based configuration is equivalent to a virtual array antenna. This means that instead of analysing the MIMO-based antenna, one may consider the equivalent virtual array and almost expect the same radiation characteristics as the MIMO-based antenna. The details of expressions for relation between the MIMO-based system and the virtual array are not discussed here. It has been shown that the convolution of the Tx and Rx arrays defines their equivalent virtual array antennas and subsequently specifies the position of the active elements in the virtual array configuration [166, 171]. Therefore, two sets of the Tx and Rx antennas that have been considered as sparse arrays are mathematically linked to their virtual array antenna. Based on this assumption, the convolution of the Tx and Rx antennas in the time domain is equivalent to multiplication in the frequency domain. Hence, one may simply find the equivalent virtual array's polynomial through the following relation [166]:

$$P_v = P_r . P_t = z^{15} + z^{13} + z^{12} + z^{11} + z^{10} + 2z^9 + z^8 + z^7 + 2z^6 + z^5 + z^4 + z^3 + z^2 + 1 \quad (8.3)$$

where P_v is the polynomial of the virtual array. This polynomial which is in order of 15 relates to a 16-element linear array with the following active/passive topology:

1 0 1 1 1 1 **1** 1 1 **1** 1 1 1 1 0 1

In the above configuration, "0" means that position has no antenna and "1" represents an active antenna. The red positions with "1" also show duplicate element position. With this procedure, the MIMO-based structure of 4+4 physical elements is related to a virtual array of 4×4 elements. This idea is shown in Figure 8-5 which the physical MIMO based system and its equivalent virtual array antenna are presented simultaneously.

To have a more physical sense of evolution from MIMO-based system to the array antenna concept, one can track the signal route when it is transmitted by a specific transmit antenna (T_i) and received by all receive antennas. Let consider d_r and d_t as the separation distance between the Rx and TX antennas respectively. The relative position of each Tx antenna to the centre point of the transmit array antenna is denoted by d_{tn} and the relative position of each Rx antenna to the centre point of receive array is shown by d_{rm}, where m, n = [1, 4].

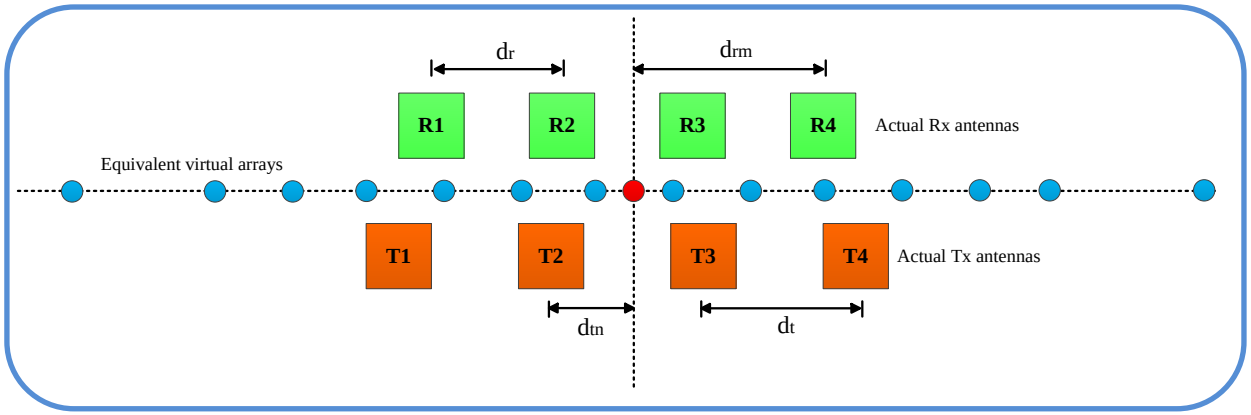

Figure 8-5 MIMO-based antenna and its equivalent virtual array antenna.

When one of the transmit antenna is active then the received signals to all receive antennas can be weighted by:

$$w_{m,n}(\theta_0) = e^{j(\frac{2\pi f}{c})(d_{tn}+d_{rm}).\cos(\theta_0)} \tag{8.4}$$

This clearly shows that the relative positions of each set of transmit and receive antenna and the relative phase shift in its equivalent virtual array. To establish a unique phase centre for all communication links between the transmit and receive antennas, one can shift the position of transmitters to a fixed point, the centre of transmit array for instance, and then find the phase shift occurring in the all receive array elements. This is shown for the two cases of T_1 and T_2 in Figure 8-6. While T_1 antenna is d_{t1} shifted to the right, all its related Rx antennas are equivalently shifted to the left side for the same amount. The same happens for case T_2. However, the amount of movement is now d_{t2}. If the shifted Rx antennas for these two cases are mapped to each other, they fill the gaps among physical elements. This is shown in Figure 8-6 by the dashed arrows and circles among active antennas. If the same procedure continues for T_3 and T_4, then the virtual array element is completed and would be similar to the declared virtual array polynomial and the position of the antenna in the virtual array as:

1 0 1 1 1 1 **1** 1 1 **1** 1 1 1 1 0 1

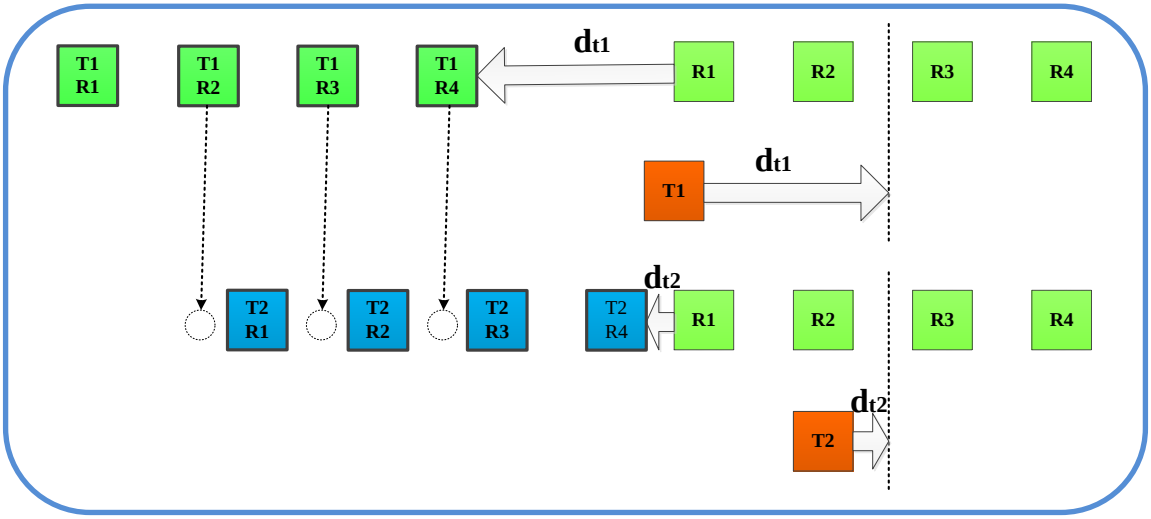

Figure 8-6 Relative phase shift between one particular Tx antenna and all Rx antennas.

8.4.2 MIMO-based array for chipless RFID imaging

To design the MIMO-based phased array antenna for the proposed chipless RFID system, the process described in [81] is followed. In the proposed configuration, every two Rx antennas are linked with five Tx antennas. Then the structure is cascaded to provide the larger required equivalent array antenna. The details of this proposed approach is discussed here and the simulation result is based on this configuration. However, the author believes that the proposed configuration of two Rx and five Tx antennas are not the best and optimum solution for large arrays. This issue will be discussed at the end of this chapter.

In Figure 8-7, the structure of the MIMO-based antenna is presented. It is important to find the separation distance between the Rx and Tx antennas on their array configuration. The angles θ_1 and θ_2 can be linked to other parameters as follow:

$$tan\theta_1 = \frac{2y_0}{X_{r0}} \quad ; \quad tan\theta_2 = \frac{2y_0}{X_{r0} + \Delta X_r} \tag{8.5}$$

where the parameters of (8.5) are defined in Figure 8-7. To find the position of the points *a* and *b*, one can write the following expressions:

$$\begin{aligned} x_a &= X_{r0} - \frac{y_0}{tan\theta_1} = X_{r0} - \frac{y_0(X_{r0})}{2y_0} = \frac{1}{2}X_{r0} \\ y_b &= X_{r0} + \Delta X_r - \frac{y_0}{tan\theta_2} = X_{r0} + \Delta X_r - \frac{y_0}{2y_0}(X_{r0} + \Delta X_r) = \frac{1}{2}(X_{r0} + \Delta X_r) \end{aligned} \tag{8.6}$$

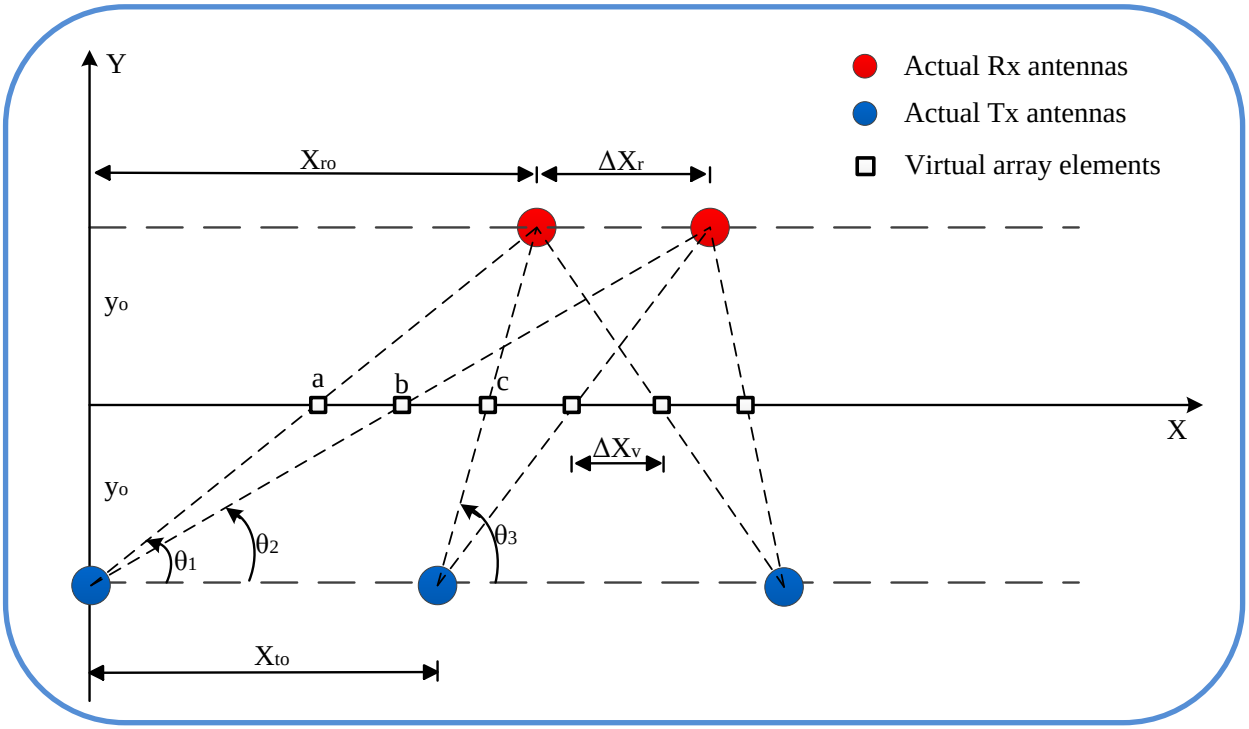

Figure 8-7 MIMO-based antenna and its equivalent virtual array.

Therefore, the separation distance of Rx antennas can be easily linked to the separation point of the virtual array elements, ΔX_v, through:

$$x_b - x_a = \Delta X_v = \frac{1}{2}\Delta X_r \tag{8.7}$$

If the same approach is followed for θ_3 and the distance between points *b* and *c* is found, one can easily reach to the following relation:

$$X_{t0} = 2\Delta X_r = 4\Delta X_v \tag{8.8}$$

We have already shown in Chapter 7 that the reader antenna has to illuminate the tag in the SAR technique every 2 mm. Therefore, the inner-space of virtual array element shall be 2 mm and equivalently, the physical Rx antennas have to be 4 mm and Tx antennas 8 mm apart from each other.

The total number of sampling points also governs the total number of required physical antennas. We have already discussed that "$m+n$" elements in Rx and Tx configuration may provide a virtual array of "$m \times n$" elements. It is important to mention this is a theoretical

criterion and shows the minimum number of required actual Tx and Rx antennas. For example, 8 and 13 physical antennas are utilized in [81] for only 44 virtual array elements. Based on the above mentioned theoretical relation, less number of antennas is expected for 44 elements virtual array. For the case of RFID application, it was shown earlier that the reader shall stop in around 125 individual points and illuminates the tag and capture the backscattered signal. Thus, the number of demanded virtual array elements is 125 points. It is possible to have slightly higher or even less number of array elements. Therefore, 125 points can be seen as a rough estimate. The proposed MIMO-based system topology for the Rx antenna in [81] includes two active antennas and then four passive elements in the sparse array configuration, for the 11000011 array polynomial. The Tx antennas having one active and one passive element scheme, 101010 for instance. Based on this assumption, the antenna distribution scheme is as follow:

For Tx array antenna: 1100001100001100011

For Rx array antenna: 10101010101010101010101

Based on the antenna distribution in Tx and Rx arrays, the following polynomials can be related to the Rx and Tx antennas respectively for the 44 elements requirements:

$$P_r = Z^{19} + Z^{18} + Z^{13} + Z^{12} + Z^7 + Z^6 + Z + 1$$
$$P_t = Z^{24} + Z^{22} + Z^{20} + \ldots + Z^4 + Z^2 + 1 \quad \textbf{(8.9)}$$

Obviously the convolution of the above polynomials results in a virtual array of degree 43. Similarly, for the case of 125 array elements, one may suggest the following polynomial for the Rx array antennas. This array includes 24 active antennas.

$$P_r = z^{67} + z^{66} + z^{61} + z^{60} + z^{55} + z^{54} + z^{49} + z^{48} + z^{43} + z^{42} + z^{37} + z^{36} + z^{31} + z^{30} + z^{25} + z^{24} + z^{19} + z^{18} + z^{13} + z^{12} + z^7 + z^6 + z + 1 \quad \textbf{(8.10)}$$

Based on the above assumption for the Rx configuration, the related Tx antennas can be defined through the following polynomials with 31 physical Tx antennas:

$$P_t = Z^{60} + Z^{58} + ... + Z^4 + Z^2 + 1 = \sum_{k=0}^{30} Z^{2k} \quad (8.11)$$

One may examine that the convolution of (8.10) and (8.11) which results in a polynomials of degree 127 which includes all the required elements.

$$P_{total} = \sum_{i=0}^{127} a_i . Z^i \quad (8.12)$$

In (8.12), coefficients a_i may be different than "1". In this case, it is not required to consider all relevant combinations between an individual Tx and Rx antennas. Therefore, through (31+24) physical antenna, it is possible to implement a virtual array with 127 elements. Through this configuration, the total number of array elements drops from 127×2 = 254 to only 31+24 = 55 elements. Moreover, the reading time in the proposed technique of EM-imaging would significantly increase while no complex system structure is utilised.

The summary of the MIMO-based system can be compared with a physical array and the conventional SAR technique as mentioned in Table 8-1. The conventional SAR technique has the minimum system complexity due to the usage of only one antenna. However, it provides a very slow imaging speed in conventional approach or slow imaging speed if a stepper motor is utilised. It is possible to develop an array antenna for fast imaging process while it requires huge number of elements which results in significant system cost. Instead, one may use the MIMO-based system with much lower number of elements and the requirement for a switching network.

Table 8-1 The MIMO-based advantages

	Number of elements	System complexity	Imaging time
MIMO-based antenna	M+N(min)	Switching network	Fast
Array antenna	M×N	Phase shifter/amplitude tapering	Fast
Conventional SAR	1	Physical antenna movement	Very slow/Slow(stepper motor)

8.4.3 Simulation result

Figure 8-8 shows the proposed structure of the MIMO-based system. 24 Rx antennas with 4 mm separation distance are linked with 31 Tx antennas with separation distance 8 mm. Hence, the total aperture size is less than 25 cm (31 × 0.8 = 24.8 cm) that is completely matched with the aperture sizes introduced in Chapter 7. The virtual array antenna with 127 elements is located between the Rx and Tx antennas. No phase shifter or amplitude tapering network is required. Only a switching network is utilized to connect one Tx and one Rx antennas at a time.

To test the validity of the proposed technique of a MIMO-based reader, a 6-bits tag is selected as example. The tag's image is simulated through MIMO-based reader system and then compared with the image through normal SAR technique. The result of signal processing is shown in Figure 8-9. In the SAR technique which includes 125 individual send and receive process, the EM-image is adequately shows the encoded data. If the same tag is processed through a MIMO-based system which utilises 55 physical antennas, then the image is depicted in Figure 8-9(c). The EM-image seems to be somehow noisier than that for the conventional SAR. Moreover, the imaged column of meander lines shows a minor inclined nature so slightly degrades the azimuth resolution. However, much faster imaging time of MIMO-based system, in few milliseconds, compensates the noisier tag's image. Moreover, it is possible to use higher number of physical antennas on MIMO-based system and improve the image quality. Alternatively, by optimisation of the antennas distribution on the MIMO-basis system one may expect a higher quality of the imaged tag. The optimisation process of the antennas distribution in the MIMO-based system is introduced in next section.

It should be noted that the usage of 24 Rx and 31 Tx antennas is based on the suggested topology of 2 Rx- 5 Tx antennas [81] and then cascading them for the required large aperture. This scenario is also based on linear sparse array theory assumption. Obviously, the number of utilised antennas is significant and may put restriction on the practicality of the proposed MIMO-based approach. This issue is discussed in next section. Moreover, the 6 bits tag was also used to show the difference between normal SAR approach and MIMO-based technique. The MIMO-based technique is capable of encoding 17 bits tag that is shown before in Chapter-7.

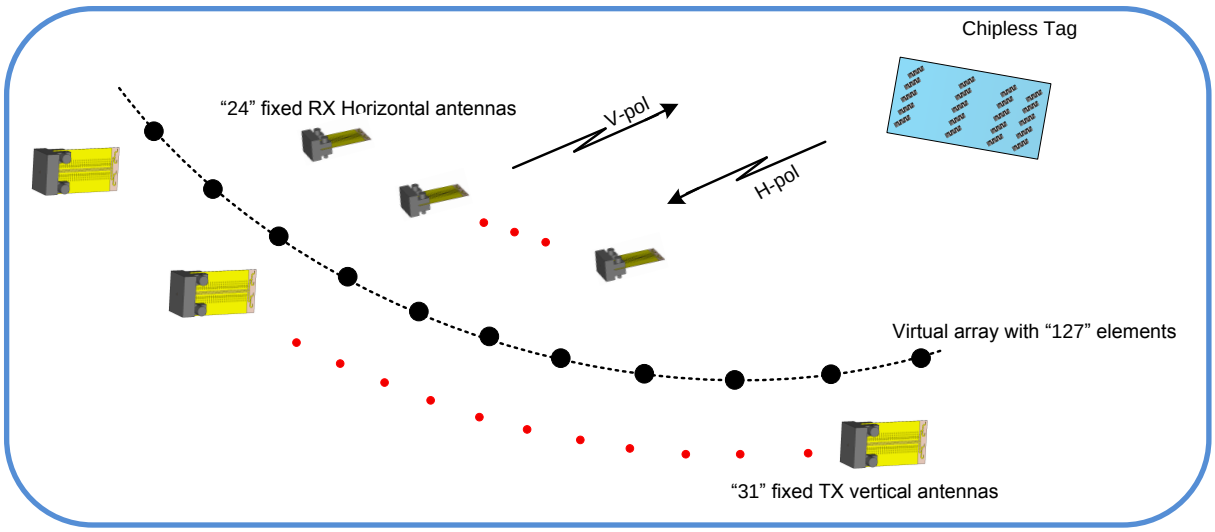

Figure 8-8 MIMO-based antenna for EM-image based chipless RFID system.

8.4.4 System optimisation of MIMO-based antenna

As discussed earlier, (24+31) separate antennas are utilised for the implementation of 127 virtual array antenna. The number of required Tx and Rx antennas are derived through the procedure introduced in [81]. However, the expectation is to have a virtual array of 127 elements with lower number of physical Tx and Rx antennas. This simply means the proposed topology in [81] is not optimum and it is possible to reduce the number of actual antennas and still expect the same virtual array. To optimise the MIMO-based system for the minimum number of physical antennas, two approaches can be considered, analytical approach and numerical optimisation approach. First, it is suggested to follow the analytical approach and try to find the optimum number of antennas. The following criteria shall be considered in optimisation process:

$$
\begin{aligned}
&P_r.P_t = 1 + Z + Z^2 + Z^3 + ... + Z^n \quad : \text{The targeted polynomial} \\
&\deg(P_r) = m \;\rightarrow \deg(P_t) = n - m; \\
&NoE(P_r) = k; \;\; Number\ of\ Rx\ element \\
&NoE(P_t) = t \;\; Number\ of\ Tx\ element \\
&c_1 \le \frac{k}{t} \le c_2 \\
&Min(k + t)
\end{aligned}
\tag{8.13}
$$

In the above set of expressions, the product of $P_r \times P_t$ shall produce a complete polynomial of order "*n*". The number of active elements in the Rx and Tx series is shown by "*k*" and "*t*",

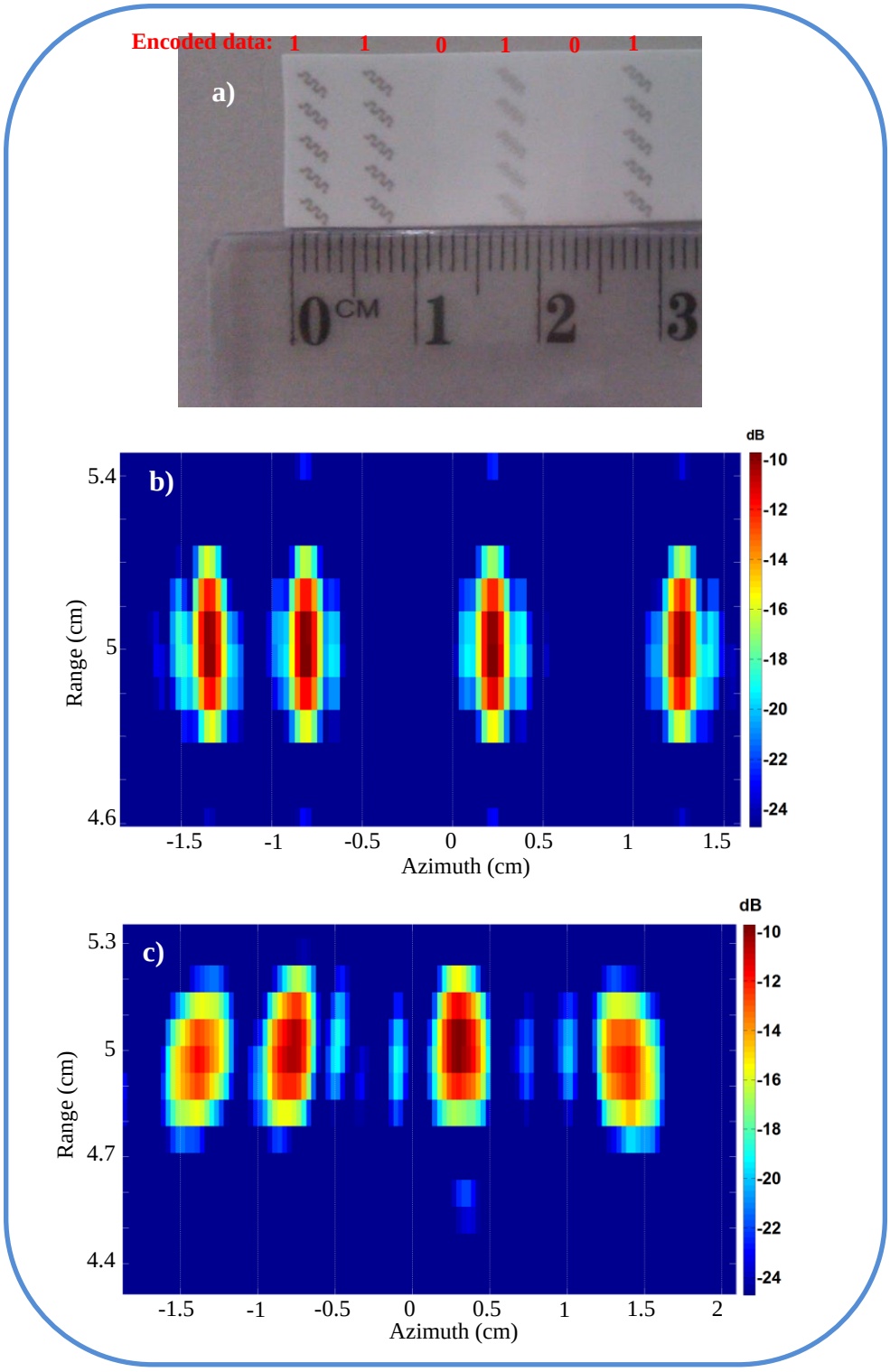

Figure 8-9 Photograph of a) printed 6-bit tag, b) tag image through normal SAR, c) tag image through MIMO-based technique.

respectively. There are some other limitations that shall be considered in the optimisation process. First, it should be noted that the relation between any two Tx and Rx antennas with their equivalent virtual elements is an approximate relation.

This relation is more accurate if the distance between the Tx and Rx antennas is negligible with respect to the distance of the target in front of the antennas. This implies an additional limitation in the above sets of formula in (8.13). Every Rx antenna shall be connected to its neighbour Tx elements and not to the Tx antennas that are physically located far from the intended Rx antenna. Otherwise, the results of analytical optimisation may be mathematically accurate but results in an impractical system configuration. Second, the goal is to minimise the $k+t$ while it is also desirable to have the minimum physical space occupied by the MIMO-based system. The other parameters of the system shall also be considered in the above sets of formula. The author has started solve this mathematical problem through analytical approaches and shall be introduced in future publications.

The second approach is the global optimisation process. If the analytical approach is not able to find the best configuration of the Tx and Rx antennas for the minimum number of physical antennas, then the global optimisation theories definitely help. In this case, the uniform distribution of the Rx and Tx antennas on their sets may not be met. The global optimisation process considers all available cases, which may exceed billions of possible cases, and then try to find the best (optimum) configuration. The genetic algorithm would be very suitable for this case as no real time solution is required [163, 173].

These two suggested approaches can be seen as the future direction of this research. There are a very few published works on MIMO-based phase array antennas. In most of them, when a large array structure is considered, the number and orientation set up of the Tx and Rx antennas do not follow any regular/classical approach [167-169]. In all of the cases, the utilised number of physical antennas is more than what expected through theoretical limitations. The suggestion is that not enough investigation has been carried out on this issue and the author believes that it is a very new and useful field of research. Any analytical and or numerical approach for minimising the number of utilised antennas for the MIMO-based phase array antenna significantly impacts on the current research and minimises the fabrication cost and system complexity.

8.5 Conclusion

The requirement for relative movement of the reader and tag has been considered as the main drawback of the proposed theory of EM-imaging for the chipless RFID systems. It was discussed that although mechanical movement of the reader is practically possible, it may not result in a time efficient process for tag imaging.

The possible solution of the phase array antenna was considered to provide a fast approach for tag imaging. Considering the requirement of the image-based chipless RFID system to a fixed radiation pattern in different scanning angle, it was addressed that the phase array antenna requires a complicated feeding algorithm and very accurate phase shifters at 60 GHz. This significantly increases the system cost that will not be accepted by industry. Hence, the conventional phase array antennas found to be impractical for the proposed EM-imaging chipless RFID system.

The new idea of MIMO-based array antenna was introduced. The theoretical basis of the MIMO-based array antenna has been briefly explained. The relation between the MIMO-based antenna and their equivalent virtual array was mathematically shown. Then based on the available techniques in the MIMO-based array antenna, a system was designed for fast imaging of a chipless RFID tag. The proposed MIMO-based system utilised 55 physical antennas that was equivalent to a virtual array with 254 elements. This system was utilised for chipless RFID tag imaging. Although the tag image through new MIMO-based reader antenna showed minor degradation when compared with the result of normal SAR-based system, the system performance was quite acceptable considering its much faster imaging process.

Two approaches of analytical and global optimisations were proposed to optimise the number of real antennas on the MIMO-based system for system cost and complexity reduction. These two approaches are under investigation by the author and his colleagues and shall be seen as an ongoing activity.

Chapter 9 Conclusion and future works

9.1 Review of the research

The main goal of this research was to introduce a new approach for data encoding on a chipless RFID tag structure considering all practical limitations for the commercial phase of the chipless RFID tags. This research was motivated by investigating the noticeable number of previous works on chipless RFID systems with almost no real product on the market. First, a comprehensive literature review on available techniques was accomplished to explore the real challenges of the chipless RFID tags for the market acceptance. It was found that regardless of many successful laboratory results, most of the proposed approaches were faced significant challenges when their prototypes were tested based on the real market expectation. Low quality materials used in a commercial tag structure along with fabrication inaccuracy happened during inexpensive tag production process substantially reduce the performance of the chipless tag in various techniques. It appeared that the researchers didn't consider the final commercial tag requirements in their investigations. This issue motivated the author to suggest an approach which includes these practical limitations of the chipless RFID tags.

Inspired by the Earth imaging application, the idea of EM-imaging was initiated as a possible solution for data encoding on a chipless RFID tag. This idea was completely different than other techniques suggested so far for the chipless RFID tag. In all of other conventional approaches, the tag surface is illuminated once by the reader, while in the proposed approach of EM-imaging the tag surface shall be sequentially scanned in few millimetres. Therefore, two questions arised. First, how to scan the tag surface with few millimetre precision and second how to encode data in a very small area. It was found that the ISM band 60 GHz has the potential providing such a precise tag scanning. Moreover, the SAR technique found to be mandatory due to some technical limitations. The strip line and meander line as EM-polarisers were also found to be suitable for data encoding considering their miniaturised size due to the mm-wave band.

The idea of polariser-based tag has been investigated through extensive measurement process. A printed tag was inspected regarding its performance on severe multipath and clutter interferences. Moreover, the tag was used on highly reflective items like liquid containers and metallic objects. The bent tag response was also investigated. The effect of barriers was considered to explore the potential of the proposed tag for secure item

identification. The result of all those measurements disclosed the salient attributes of the proposed tag. While many of the earlier proposed chipless RFID tags had difficulties in the aforementioned scenarios, the satisfactory results of the proposed cross-polar based tag suggested it as a suitable candidate for the real industrial applications.

In the next step, the printed tag was considered with appropriate SAR-based signal processing algorithm for its EM-image. The tag was shaped based on a reasonable frequency band for a course range resolution and through a practical synthetic aperture size for a fine azimuth resolution of 5 mm. This provided the data encoding capacity of 2 bits/cm^2 that would be a revolutionary data encoding capacity for a printed tag structure. Multiple tags with different data capacity have been investigated and their final EM-image successfully decoded the tags' contents. This proved the applicability of the EM-imaging technique through proposed approach for data encoding purpose in a printable chipless RFID tag. The utilised data encoding algorithm scenario effectively revealed information of a 17-bits tag while the tag was 5.5 times smaller than a credit card. The potential advantages of the EM-imaging technique would be very attractive for the identification industries as it suggests a low cost identifications means with high data encoding capacity.

Finally, addressing the slow reading time of the proposed technique, the idea of MIMO-based system was suggested for a fast EM-imaging. This idea showed satisfactory result while it is required to continue the research for better performance and minimum number of antennas.

The research and scholarship have been supported by the ARC Discovery Project Grant: DP110105606: Electronically Controlled Phased Array Antenna for Universal UHF RFID Applications. This research started on July 2011 and finished in February 2015.

9.2 Addressing the research objective

The new approach of mm-wave image-based chipless RFID system has provided a practical solution for a low cost, fully printable tag with high content capacity in a reasonable tag size. The proposed technique successfully showed its potential advantages for a chipless and printable tag in the industrial environments with high multipath interferences. The proved data encoding capacity was also much higher than that suggested for a printable chipless tag to date.

The outcomes of the research which fulfils the research objectives are as: *1)* proposing a new idea in chipless RFID systems completely different than other conventional techniques, *2)* introducing the strip line and meander line as effective EM-polarisers, *3)* a cross-polar working basis with many advantageous potentials for industrial environments, *4)* new on/off data encoding algorithm based on the performance of the printed tag structure, *5)* tailoring the SAR signal processing algorithm based on the requirements of the chipless RFID system, *6)* proposing the new approach of MIMO-based array antenna to tag fast imaging process.

The salient attributes of the proposed technique suggest it as a reliable new approach for putting the chipless RFID system on track especially for main stream applications with billions of yearly tag requirements. The stream of information on this dissertation can be summarised as follow:

Chapter 1 outlines the overall work on mm-wave image-based chipless RFID system. First, a brief overview of the industries with identification and tracking requirements was provided to readers. These industries were categorized into various classes based on their tag requirements. It was found that secure identification, anti-theft capability, cheap identification solution, tagging of highly reflective products, high data capacity, tracking along identification, identification through long reading range, and many more are examples of important factors for industries. Irrespective of different priorities in product identification, there are two main factors which matter in all applications: the data encoding capacity and the system cost. For applications with millions of items for tagging, high data capacity of the identification system is a must. However, for applications with a limited number of objects, high data encoding capacity may be utilised for secure and higher reading reliability by sacrificing some of the available data bits. Moreover, cost reduction is the main initiative for the usage of the identification systems in industry. Obviously, the cost of the identification system and its tagging price must be low and competitive enough to initiate the request for the system. Barcode system as a well-stablished identification technique has been then reviewed regarding its ultimate potentials for addressing the current demands of industries. It was shown that the limitations of the barcodes on providing enough content capacity and also their high labour cost are not compatible with the needs of industries in the modern international trading market. The new idea of EM-imaging for data encoding purposes was suggested and introduced briefly. The salient potentials of this new technique were disclosed, which suggested a revolutionary enhancement of the system performance based on a fully

printable tag. Finally, this chapter summarised the aims and success of this research, introduced the original contribution and provided the thesis outlines.

The literature review related to the proposed technique of mm-wave image-based chipless RFID systems was provided in **Chapter 2**. The technical superiorities of RFID systems as a modern and capable identification system were briefly presented. High data capacity, long reading range, secure identification, no line-of-sight requirement and no/minimum human intervention were highlighted for RFID's. However, it was shown that the main stream industries with billions of yearly tag requirements are not capable of replacing their old barcode-based systems due to the much higher cost of RFID systems. Reduction of the RFID system's cost through decreasing the expense of the microchip in each RFID tag didn't happen due to the some basic limitations. A chipless tag, an RFID tag without any microchip, appeared as the only solution for providing the tag cost of below one cent (1¢). It was also discussed that only a fully printable chipless tag structure may satisfy the tag cost expectancy. Then the conventional approaches of time and frequency domain systems were reviewed and their final capabilities, based on a fully printable tag structure, were comprehensively investigated. It was shown that these two main approaches fail to address the expected content capacity based on a fully printable tag. All the new techniques and novel ideas openly available to date on chipless RFID systems, were also reviewed. It was shown that irrespective of some claims for providing high data encoding capacity based on a printable and low cost tag, there is no such a product available on the market. This suggested that these new techniques are in the research phase and industry is waiting for a product to provide reliable performance in a real scenario. Potential advantages of the proposed image-based system, specifically regarding the tag cost and content capacity, were introduced. All the prominent potentials of the system were considered from the tag and the reader viewpoint.

In **Chapter 3**, the idea of EM-imaging has been proposed as a novel idea for data encoding purpose on a chipless RFID tag. It first highlighted the main difference between the proposed approach of EM-imaging and other conventional techniques in RFID systems on a fully or partly illumination perspective of the tag surface. It was shown that the EM-imaging of the chipless RFID tag is technically possible at the 60 GHz and higher bands. The technical and regulatory situations of the 60 GHz band were also reviewed. The new idea of polarisation rotation instead of signal level criteria was proposed for the chipless RFID application. Then the novel idea of a strip line and a meander line as effective polarisers were introduced and

the working basis of these two elements based on diffraction theory and resonance was presented. It was shown that a well-designed strip and meander lines are capable of providing high cross-polar backscattered signal in the certain frequency bands. This unique aspect of the strip and meander lines suggested them as an effective EM-polariser. A comprehensive study on diffraction theory based on Kobayashi potential approach was provided to disclose the working basis of these two EM-polarisers.

The fabrication process of the proposed strip line and meander lines EM-polarisers was discussed in **Chapter 4**. These two EM-polarisers were fabricated through two different technologies: the costly but accurate approach of a photolithographic process and through inexpensive approach of printing. In photolithographic process, an annealed copper with a high quality substrate were utilised, while in printing process, the conductive ink was used to print the tag on a paper substrate. These two fabricated tags were then measured to disclose their final performance. The results of measurements rejected the idea of resonance-based approach for data encoding purpose. Instead, the new idea of on/off data encoding algorithm was proposed based on the printed tag performance. This new data encoding algorithm accommodated all the potentials and limitations of the printed tag structure as the final shape of the tag at its commercial stage.

The actual performance of the proposed printed polariser-based tag was then considered in **Chapter 5**. First, an analytical model of the reading scenario for the chipless RFID system was developed based on the radar theory. It was shown that the co-polar based systems are very vulnerable to changes in the reading zone and they require frequent system calibrations. In contrast, the proposed cross-polar system was very robust towards the multipath interference, the tag movement, and other changes in the reading zone. The analytical model results were then confirmed through different measurement scenarios. The reading process of the printed tag was not affected in a severe multipath and clutter interferences. Moreover, a printed tag was attached to a bottle of water and aluminum can contains liquid. It was shown that the system is successfully capable of decoding the attached tags to these highly reflective objects. The effect of tag bending and the barrier were also considered in the measurement process. It was shown that the system is very robust to a bent tag due to its miniaturised size. Also the secure identification is possible as many types of barriers didn't affect the reading of printed tag. Based on the successful measurement results, it was concluded that the proposed

tag structure provides a very robust, reliable and fully practical solution for industrial applications.

The reader antenna was introduced in **Chapter 6**. First, the technical and operational necessities of the reader antenna for the proposed technique of the image-based chipless RFID system were reviewed. It was concluded the "off-the-shelf" products on the mm-wave range of 60 GHz were not suitable for the demanded specifications by the proposed technique. Then, an array of DSPD antennas was proposed to satisfy the technical requirements of the EM-imaging. The prototype antenna was designed and fabricated on Taconic TLX-8 substrate. The substrate was characterised using the SIW resonant technique at 60 GHz. The array was fabricated through standard printed circuit board (PCB) technology and then tested. The array adequately covered the whole frequency range of operation 57-64 GHz while it provided a uniform radiation pattern in the azimuth direction with a limited pattern on the elevation angle. The measured CPL of the array was below -20 dB when it was attached to its very large connector. The measured gain of the array was 5.5-7 dBi over the entire frequency range of operation, while the whole array size including the connector was 22 × 14 mm. The compact and simple structure of the array suggested it as a suitable antenna for many applications in the mm-wave region for low range wireless communication systems.

The SAR theory was reviewed in **Chapter 7** as it was a mandatory approach for imaging due to some technical requirements. The range and azimuth image resolutions were introduced and their relations with the system parametres such as frequency of operation, available bandwidth, reading range, and the synthetic aperture size were explained. It was shown that a fine range resolution is not achievable due to the limited available frequency band. Therefore, only the azimuth resolution was proposed for the data encoding purpose. The tag shape was designed based on the azimuth resolution only. Then the EM-images of some prototype tags with different data encoding capacity were shown. The effect of the aperture size on the final EM-image of the tag was also considered. The final achieved tag image through SAR technique acquires 5 mm azimuth resolution. This image resolution defined 2 bits/cm^2 as the final data encoding capacity of the proposed system. A tag with 8.5 cm length encoded 17 bits of data while the tag width was only 1 cm. This proved that more than 93 bits is feasible for a credit card size tag.

Finally, the limitation of the proposed technique for relative movement of the reader and the tag was considered in the **Chapter 8** of this dissertation. The requirement for the relative

movement of the reader and the tag was addressed through the novel idea of the MIMO-based array antenna that didn't need any complex system. The theoretical fundamentals of the MIMO-based array antenna were discussed and it was shown that how a MIMO antenna can be related to a virtual array antenna. This idea was matured and finally a fixed array of 55 elements was suggested to provide a fast imaging approach for the chipless RFID system. The tag image through this new approach showed satisfactory resolution to encode the tag data while it suffered from azimuth resolution and noisier image.

In summary, it can be concluded that the main objective of the research for proposing a new approach for data encoding in a chipless RFID system has been successfully fulfilled. While the new approach considered most of the practical limitations of the chipless RFID systems in industry, the suggested approach provided noticeable data encoding capacity on a fully printable tag. The research may open a new field of study for other researcher to expand the potential advantageous of imaging approach for the chipless RFID and for other similar applications.

9.3 Future work

Chipless RFID systems are almost a new area of research. Considering the wide area of applications for chipless RFID systems, there are various demands on data capacity, reading range, reliable content, secure identifications, and anti-collision requirements. The proposed mm-wave image-based chipless tag satisfies some of the most important requirements; data encoding requirements, low cost, and reliable reading process. However, there are areas that have to be completed to provide an industry ready product based on the EM-imaging technique.

First, it should be noted that irrespective of the proven results for the image-based system, it is necessary to provide the required hardware for the system completion. All the measurements and signal processing in this research were based on the usage of the PNA and computer based signal processing. Therefore, the system completion is the first priority of this work.

There are however other areas which require further research activities. The optimisation of the MIMO-based array antenna for fast imaging as described at the end of Chapter 8 is one

example. The other two areas which can be specified as the future work are introduced in the following sections.

9.3.1 Three level-based encoding

Based on the discussions carried out in this dissertation, an on/off data encoding algorithm was proposed based on the technical and practical limitations. In the proposed approach, 5 EM-polarisers are used to create a high cross-polar component in the backscattered signal. All the measurements and signal processing were based on this assumption. As it verified by measurements, this working basis provides 12-15 dB received power level difference between the reflection from a column of 5 polarisers and no polariser case. This power level difference suggests a very reliable data encoding in real environment considering the system robustness to multipath interference. This issue can be easily verified by clear image of the tag with various contents in Chapter 8. However, it is possible to propose a three level encoding instead of two level based system. This means that X number of polarisers can define one level of signal, the X/2 number of polarisers relates to the second level and no polariser means the third level of data encoding. However, the system reliability will be sacrificed for the enhanced data encoding capacity. Addressing this issue, one may utilise 10 polarisers on each column instead of initial five polarisers. This provides a fair trade off between the tag width and the tag data encoding capacity. Figure 9-1 shows these two encoding algorithms and their differences.

In the three-level encoding, the difference between each state should be about 9-10 dB, while in the two-level encoding, as shown before 12-15 dB is the cross-polar power difference. The author has started working on signal processing based on the three-level encoding however, the result is not finalised yet. Hence this issue shall be considered as the future aspect of the proposed technique.

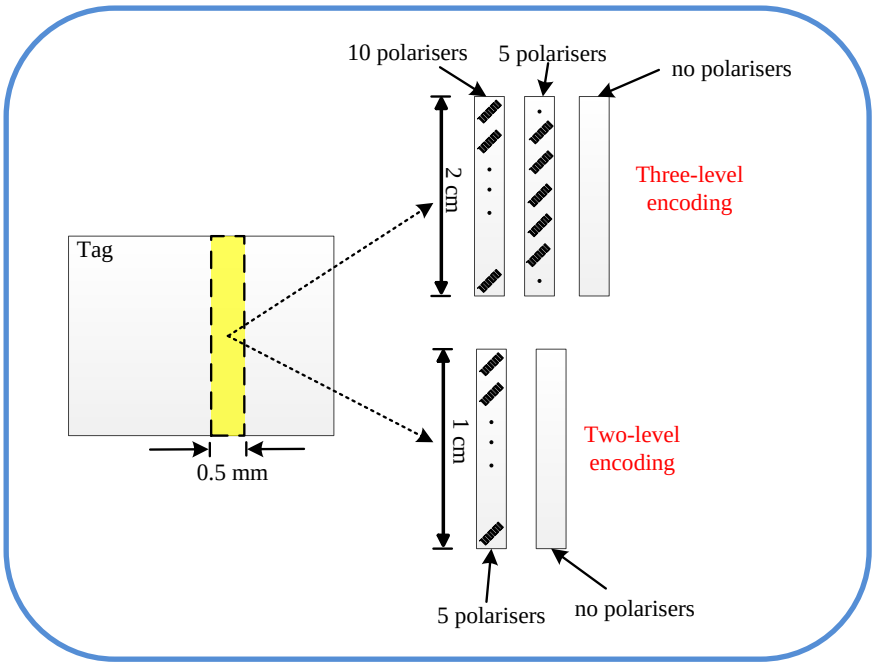

Figure 9-1 Two and three level encoding algorithms.

9.3.2 Tag orientation sensitivity

The proposed approach of the image-based chipless RFID system is based on the cross-polar component in the backscattered signal due to the polariser-based tag. As disclosed in Chapter 3, the strip line and meander line act as effective polarisers if the incident E-field maintains 45° angle with the polarisers main axis. Otherwise, the performance of these EM-polarisers would be different than what normally expected. In this regard, all the measurements, simulation and signal processing results shown in the preceding chapters are based on 45° orientation between the EM-polarisers and the incident E-field as shown in Figure 9-2(a). To evaluate the effect of tag miss-orientation on the system performance, the polariser on the tag surface is rotated at an arbitrary angle θ as shown in Figure 9-2(b). Various oriented tags are simulated and the results are shown in Figure 9-3. It is clear from the figure that the tag mis-orientation affects the received signal level in certain extent but with a detectable pattern. This is due to the reduction of the resonance factor on the cross-polar components. Obviously, reduction of the received signal directly affects the system performance. It is important to mention that the value in the Figure 9-3 shows the received E-field level for one single EM-polariser. The related power reduction hence is double of what is shown in Figure 9-3. Based on the measured values outlined in Chapter 4, Figure 4-7, the received power level of a column of five EM-polarisers is 12-15 dB more than that of no polariser case. Therefore, for tag orientation angles more than 20°, the received signal level

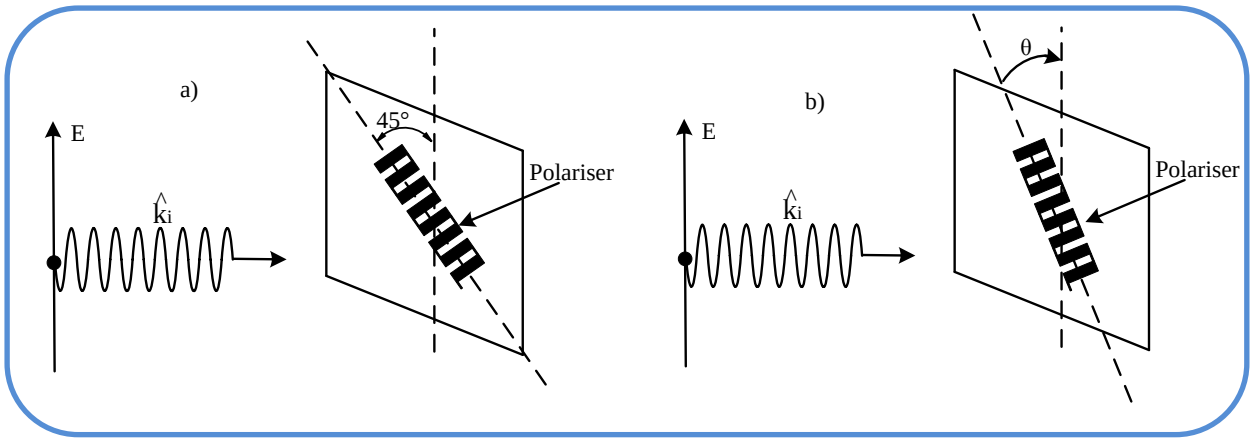

Figure 9-2 Tag orientation, a) correct angle of 45°, b) mis-oriented tag angle of θ°.

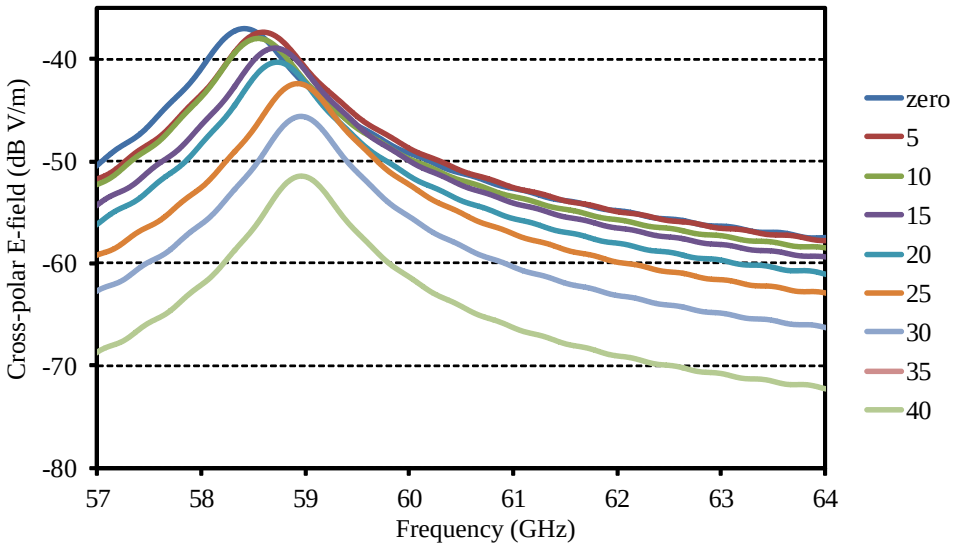

Figure 9-3 Effect of tag orientation on received signal level.

drops to more than 5 dB and hence the system capability for detection of the column of EM-polarisers will be severely affected as shown in Figure 9-4.

The suggested solution for providing more robust system to the tag orientation, is the usage of circular polarisation rather than the linear polarised interrogation signal. The entire proposed theory to date was based on the linear polarisation scheme of the Tx and Rx antennas at the reader side. The EM-polariser on the tag surface rotates the linear polarisation to its orthogonal direction. However, if the incident signal has circular polarisation, the EM-polariser again rotates it to the orthogonal direction. This means that a right hand circular polarisation (RHCP) is converted to the left hand circular polarisation (LHCP) and vice versa.

This provides insensitive system respect to the tag rotation. However, it should be mentioned that the range and azimuth resolution of the final tags EM-image shall be also considered with this new system arrangement. This means that the definition of the range and azimuth resolutions will be different and hence a new configuration is required. Obviously, the designed array of DSPD would not be suitable anymore for the new circularly polarised (CP) system and hence new CP antennas are required.

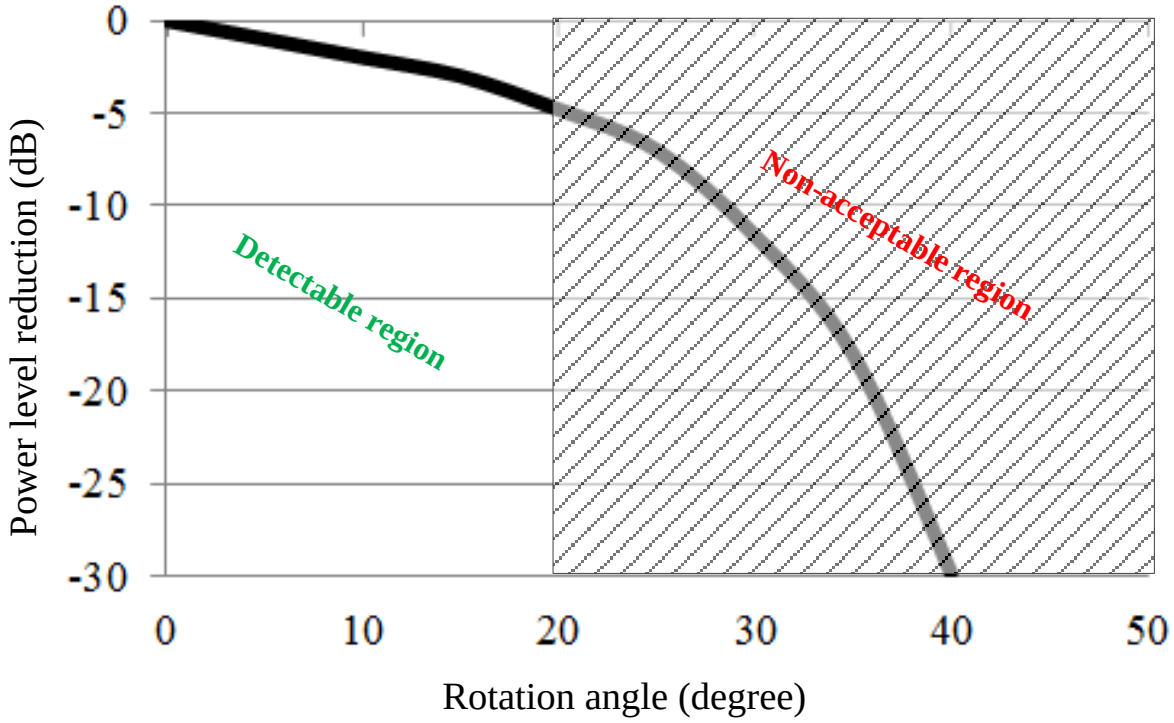

Figure 9-4 System degradation due to tag mis-orientation effect.

REFRENCES

[1] P.Harrop and R.Das, "Printed and Chipless RFID Forecasts, Technologies & Players 2009-2029," IDTechEx, USA, 2009.

[2] BiQRious. (2015). *QR Code Capacity*. Available: http://qrcodetracking.com/qr-code-capacity/

[3] *Barcode FAQ & Tutorial*. Available: http://www.idautomation.com/barcoding4beginners.html

[4] C. Turcu, *Current Trends and Challenges in RFID*: InTech, 2011.

[5] T.Lotlikar, R.Kankapurkar, A.Parekar, and A.Mohite, "Comparative study of Barcode, QR-code and RFID System," *International Journal Computer Technology & Applications,,* vol. 4, pp. 817-821, 2013.

[6] E.Arendarenko, "A study of comparing RFID and 2D barcode tag technologies for pervasive mobile applications," Master, Department of Computer Science and Statistics, University of Joensuu, 2009.

[7] G. White, G.Gardiner, G. P. Prabhakar, and A. Razak, "A comparison of barcoding and RFID technologies in practice," *Journal of Information, Information Technology and Organizations,* vol. 2, pp. 119-132, 2007.

[8] Cartman. (Feb 2015). *Asset Tracking: RFIDs, Barcodes or QR Codes?* Available: https://www.webcheckout.net/blog/rfid-asset-tracking/

[9] A. Campbell. (2011). *QR Codes, Barcodes and RFID: What's the Difference?* Available: http://smallbiztrends.com/2011/02/qr-codes-barcodes-rfid-difference.html

[10] Cisco. (2015). *Internet-of-everything*. Available: http://www.cisco.com/c/r/en/anz/internet-of-everything-ioe/tomorrow-starts-here/index.html

[11] S.Preradovic and N.Karmakar, "Chipless RFID, Bar Code of the Future," *IEEE Microwave magazine,* vol. 11, pp. 87-97, 2010.

[12] R. R. Fletcher. (2002). *Low-cost electromagnetic tagging: Design and implementation. Ph.D. thesis*. Available: www.media.mit.edu/physics/publications/theses/97.02.fletcher.pdf

[13] S.Preradovic, "Chipless RFID System for Barcode Replacement," PhD, ECSE, Monash University, 2009.

[14] V.Chawla and D. S. Ha, "An overview of passive RFID " *Communications Magazine, IEEE* vol. 45.

[15] P. Harrop. (2006). *The Price-Sensitivity Curve for RFID*. Available: http://www.printedelectronicsworld.com/articles/the-price-sensitivity-curve-for-rfid-00000488.asp?sessionid=1

[16] S.Preradovic, I.Balbin, N.C.Karmakar, and G.F.Swiegers, "Multiresonator-Based Chipless RFID System for Low-Cost Item Tracking," *IEEE Transactions on Microwave Theory and Techniques,* vol. 57, 2009.

[17] T. Singh, S. Tedjini, E. Perret, and A. Vena, "A Frequency Signature Based Method for the RF Identification of Letters," in *2011 IEEE international conference on RFID*, 2011.

[18] A.Vena, E.Perret, and S. Tedjini, "Chipless RFID Tag Using Hybrid Coding Technique," *IEEE Transactions on Microwave Theory and Techniques,* vol. 59, 2011.

[19] C. S. Hartmann, "A Global SAW ID Tag with Large Data Capacity," in *IEEE ULTrasonic Symposium*, 2002.

[20] C.Mandel, B.Kubina, M.Schüßler, and R.Jakoby, "Metamaterial-inspired Passive Chipless Radio-frequency Identification and Wireless Sensing," *Annals of telecommunications,* vol. 68, pp. 385-399, 2013.

[21] C.Mandel, B.Kubina, M.Schussler, and R.Jakoby, "Group-delay Modulation with Metamaterial-inspired Coding Particles for Passive Chipless RFID," presented at the RFID-TA, Nice, 2012.

[22] S. Shrestha, M.Balachandran, M.Agarwal, and V.V.Phoha, "A Chipless RFID Sensor System for Cyber Centric Monitoring Applications," *IEEE Transactions on Microwave Theory and Techniques,* vol. 57, 2009.
[23] J.R.Costa, B.Lima, and C.A.Fernandes, "Compact Beam-Steerable Lens Antenna for 60-GHz Wireless Communications," *IEEE Transactions on Antenna and Propagation,* vol. 57, p. 8, 2009.
[24] H.El Matbouly, N.Boubekeur, and F.Domingue, "A Novel Chipless Identification Tag Based on a Substrate Integrated Cavity Resonator " *IEEE Microwave and Wireless Components Letters,* vol. 23, 2013.
[25] C.M.Nijas, R.Dinesh, U.Deepak, A.Rasheed, S.Mridula, K.Vasudevan*, et al.*, "Chipless RFID Tag Using Multiple Microstrip Open Stub Resonators," *IEEE Transactions on Antenna and Propagation,* vol. 60, pp. 4429-4432, 2012.
[26] Y.F.Weng, S.W.Cheung, T.I.Yuk, and L. Liu, "Design of Chipless UWB RFID System Using A CPW Multi-Resonator," *IEEE Antenna and Propagation Magazine, ,* vol. 55, 2013.
[27] M.Zomorrodi and N.C.Karmakar, "An Array of Printed Dipoles at 60 GHz " in *IEEE International Symposium on Antennas and Propagation*, Memphis, Tennessee, USA, July-2014, pp. 73-74.
[28] M.Zomorrodi and N.Karmakar, "A Low Cost Wideband Printed Dipole Array Antenna for 60 GHz Image-Based Chipless RFID Reader," *IEEE Antennas and Propagation Magazine,* vol. Accepted on Jan2015, p. 13, 2015.
[29] S.Gupta, B.Nikfal, and C.Caloz, "Chipless RFID System Based on Group Delay Engineered Dispersive Delay Structures," *IEEE Antenna and Wireless Propagation letters,* vol. 10, pp. 1366-1368, 2011.
[30] R.Rezaiesarlak and M.Manteghi, "Complex-Natural-Resonance-Based Design of Chipless RFID Tag for High-Density Data," *IEEE transactions on Antenna And Propagation* vol. 62, 2014.
[31] ACMA, "60 GHz Band, Millimetre Wave Technology," 2004.
[32] S.K.Yong, "Introduction to 60 GHz," Samsung Electronics 2011.
[33] S.Yong and C.Chong, "An Overview of Multi Giga bit Wireless through Millimeter Wave Technology: Potentials and Technical Challenges," *EURASIP Journal on Wireless Communications and Networking,* p. 10, 2007.
[34] S.Yong, P.Xia, and A.V.Garcia, *60 GHz Technology for Gbps WLAN and WPAN*: John&Wiley, 2011.
[35] D. L. Brock, "The Electronic Product Code (EPC)," Auto-ID center, massachusetts institute of technology(MIT)2001.
[36] M.Zomorrodi, N.C.Karmakar, and S.G.Bansal, "Introduction of Electromagnetic Image-based Chipless RFID System " in *Intelligent Sensors, Sensor Networks and Information Processing, ISSNIP-2013*, Melbourne, 2013, pp. 443-448.
[37] M.Zomorrodi and N.C.Karmakar, "On the Usage of Diffraction Effect for Chipless RFID Systems," in *Australian Microwave Symposium (AMS)*, Melbourne, Australia, June 2014.
[38] (2015). Available: www.satoaustralia.com
[39] M.Zomorrodi and N.C.Karmakar, "Cross-RCS Based, High Data Capacity, Chipless RFID System," in *International Microwave Symposium (IMS-2014)*, Tampa Bay, Flordia, US, 2014.
[40] M.Zomorrodi and N.C.Karmakar, "Cross-Polarized Printable Chipless RFID Tag with Superior Data Capacity," in *European microwave week, EuMW2014*, Rome, Italy, 2014.
[41] T.Pisello, "The ROI of RFID in the Supply Chain," *RFID Journal internet article,* 2006.
[42] U. o. Sanfrancisco. (Feb 2015). *RFID Technology Boosts Walmart's Supply Chain Management*. Available: http://www.usanfranonline.com
[43] D. A. Hodges and H. G. Jackson, *Analysis and Design of Digital Integrated Circuits* 2nd ed. New York, USA: McGraw-Hill, 1988.
[44] J. R. Baker, H. W. Li, and D. E. Boyce, *CMOS Circuit Design, Layout and Simulation*. New York, USA: IEEE Press, 1998.

[45] M. S. Bhuiyan, R.E. Azim, and N. Karmakar, "A Novel Frequency Reused Based ID Generation Circuit for Chipless RFID Applications," in *Asia-Pacific Microwave Conference (APMC)*, Melbourne, Australia, 2011, pp. 1470-1473.

[46] I. Balbin and N.C.Karmakar, "Phase-Encoded Chipless RFID Transponder for Large-Scale Low-Cost Applications," *IEEE Microwave and Wireless Components Letters,,* vol. 19, pp. 509-511, AUGUST 2009.

[47] Md. Aminul Islam and N.C.Karmakar, "A Novel Compact Printable Dual-Polarized Chipless RFID System," *IEEE Transactions on Microwave Theory and Techniques,* vol. 60, pp. 2142-2151, July 2012.

[48] A. Ramos, A. Lazaro, D. Girbau, and R. Villarino, "Time-domain Measurement of Time-coded UWB Chipless RFID Tags," *Progress In Electromagnetics Research,* vol. 116, 2011.

[49] Z. Lu, S. Rodriguez, H. Tenhunen, and Z. Li-Rong, "An Innovative Fully Printable RFID Technology Based on High Speed Time-domain Reflections," in *High Density Microsystem Design and Packaging and Component Failure Analysis*, 2006, pp. 166-170.

[50] V.P Plessky and L.M.Reindl, "Review on SAW RFID Tags," *IEEE Transactions on Ultrasonics, Ferroelectrics, and Frequency Control,* vol. 57, pp. 14-23, 2010.

[51] C. Mandel, M. Schüßler, M. Maasch, and R. Jakoby, "A Novel Passive Phase Modulator Based on LH Delay Lines for Chipless Microwave RFID Applications," in *IEEE MTT-S International Microwave Workshop on Wireless Sensing, Local Positioning, and RFID*, Crotia, 2009.

[52] F.J.H.Martínez, F.Paredes, and G.Zamora, "Printed Magnetoinductive-Wave (MIW) Delay Lines for Chipless RFID Applications," *IEEE Transactions on Antennas and Propagation* vol. 60, 2012.

[53] A.Chamarti and K.Varahramyan, "Transmission Delay Line Based ID Generation Circuit for RFID Applications," *IEEE Microwave and Wireless Components Letters,* vol. 16, pp. 588-590, Nov. 2006.

[54] M.Sch¨ußler, C.Damm, M.Maasch, and R.Jakoby, "Performance Evaluation of Left-Handed Delay Lines for RFID Backscatter Applications," in *Microwave Symposium Digest,* , 2008.

[55] J.Vemagiri, A.Chamarti, M.Agarwal, and K.Varahramyan, "Transmission Line Delay-Based Radio Frequency Identification (RFID) tag," *Microwave and Optical Technology Letters,* vol. 49, p. 1900, 2007.

[56] (14 July 2014). *RF SAw Inc.* Available: http://www.rfsaw.com

[57] S.Preradovic, I.Balbin, N.C.Karmakar, and G.Swiegers, "Chipless Frequency Signature Based RFID Transponders," in *1st European Wireless Technology Conference*, Amsterdam 2008, pp. 302-305.

[58] D.Girbau, J.Lorenzo, A.Lázaro, C.Ferrater, and R.Villarino, "Frequency-Coded Chipless RFID Tag Based on Dual-Band Resonators," *IEEE Antennas and Wireless Propagation Letters,* vol. 11, 2012.

[59] F.Costa, S.Genovesi, and A.Monorchio, "A Chipless RFID Based on Multiresonant High-Impedance Surfaces," *IEEE Transactions on Microwave Theory and Techniques,* vol. 61, 2013.

[60] S.Mukherjee and G.Chakraborty, "Chipless RFID Using Stacked Multilayer Patches," in *Applied Electromagnetics Conference (AEMC), 2009* Kolkata, 2009.

[61] M. Glickstein, "Firewall Protection for Paper Documents, ," *RFID Journal internet article,* 2004.

[62] K. C. Jones, "Invisible RFID Ink Safe For Cattle And People, Company Says," *InformatioWeek,* 2007.

[63] St. Louis, "SOMARK's Chipless RFID Ink Tattoo Field Demo Brings the Company Closer to Launch," 2008.

[64] S.Kim, A.Georgiadis, A.Collado, and M.M. Tentzeris, "An Inkjet-Printed Solar-Powered Wireless Beacon on Paper for Identification and Wireless Power Transmission Applications," *IEEE transactions on microwave theory and techniques,* vol. 60.

[65] I.Jalaly and I.D.Robertson, "RF Barcodes Using Multiple Frequency Bands," in *International Microwave Symposium Digest, IEEE MTT-S* 2005.
[66] I.Balbin, "Chipless RFID transponder design," PhD, Monash Univeristy, 2010.
[67] H.S.Jang, W.G. Lim, K.S. Oh, S.M. Moon, and J.W. Yu, "Design of Low-Cost Chipless System Using Printable Chipless Tag With Electromagnetic Code," *IEEE Microwave and Wirless Components letters,* vol. 20, 2010.
[68] B.A.Munk, *Frequency Selective Surfaces, Theory and Design*: John Wiley & Sons Inc, 2000.
[69] M. G. Pettus, "RFID system utilizing parametric reflective technology " USA Patent, 2005.
[70] S.Särkkä, V. E, V. Viikari, M.Huusko, and K. Jaakkola, "Phase-Based UHF RFID Tracking With Nonlinear Kalman Filtering and Smoothing " *IEEE Sensors Journal,* vol. 12, 2012.
[71] P. V.Nikitin, R.Martinez, S.Ramamurthy, H.Leland, G.Spiess, and K. V. S. Rao, "Phase Based Spatial Identification of UHF RFID Tags," presented at the IEEE RFID, 2010.
[72] A.Vena, E.Perret, and S.Tedjini, "Chipless RFID Tag Using Hybrid Coding Technique," *IEEE Trans. on Microwave Theory and Tech. ,* vol. 59, 2011.
[73] Md. S. Bhuiyan, A.Azad, and N.Karmakar, "Dual-band Modified Complementary Split Ring Resonator (MCSRR) Based Multi-resonator Circuit for Chipless RFID Tag " in *IEEE- Intelligent Sensors, Sensor Networks and Information Processing,*, Melbourne,Australia, 2013.
[74] M. Soumekh, *Synthetic Aperture Radar signal processing with MATLAB algorithms*. USA: John Wily and Sons 1999.
[75] P.Treleaven and J.Wells, "3D Body Scanning and Healthcare Applications," *IEEE Computer Society,* vol. 40, p. 28, 2007.
[76] S. Oka, H. Togo, N. Kukutsu, and T. Nagatsuma, "Latest Trends in Millimetre-Wave Imaging technology," *Progress In Electromagnetics Research Letters,,* vol. 1, pp. 197–204, 2008.
[77] A. A. Bakar, "Design of Ultra-Wideband Microwave Imaging System for Breast Cancer Detection and Its Assessment Using Heterogeneous Breast Phantoms," PhD, School of Information Technology and Electrical Engineering, The University of Queensland, Brisben, March 2012.
[78] F. Ahmad, M.G. Amin, and S. A. Kassam, "Synthetic Aperture Beamformer for Imaging Through a Dielectric Wall," *IEEE Transactions on Aerospace and Electronic Systems,* vol. 41, 2005.
[79] N.Karmakar, R.Kosowatta, P.Kalansuriya, and R. E-Azim, *Chipless RFID Reader signal Processing*: Artech House Publishing, 2013.
[80] M.Skolnic, *Radar Handbook*, 3rd ed.: McGraw-Hill, 2008.
[81] G.L.Charvat, *A Low-Power Radar Imaging System*: Michigan State University, 2007.
[82] M.Zomorrodi and N.Karmakar, "Novel MIMO-based Technique for EM-imaging of Chipless RFID " in *International microwave synposium (IMS-2015), 17-22 May 2015*, Phoenix, USA.
[83] U. 6400. (2015). *60 GHz transciver*. Available: http://www.siliconimage.com/
[84] C.M.Ta and B.N. Wicks, "Issues in the Implementation of a 60GHz Transceiver on CMOS," in *IEEE International Workshop on Radio-Frequency Integration Technology(RFIT)*, Rasa Sentosa Resort, USA, 2007, pp. 135 - 140
[85] M.Zomorrodi and N. Karmakar, "A Low Cost Wideband Printed Dipole Array Antenna for 60 GHz Image-Based Chipless RFID Reader"," *IEEE Antennas and Propagation Magazine,* 2014.
[86] E.Md.Amin, Md.S.Bhuiyan, N.C.Karmakar, and B.Winther-Jensen, "Development of a Low Cost Printable Chipless RFID Humidity Sensor," *IEEE Sensors Journal,* vol. 14, pp. 140-149, 2014.
[87] C. A. Wiley, "Synthetic Aperture Radars: A Paradigm for Technology Evolution," *IEEE Transactions on Aerospace and Electronic Systems,,* vol. AES-21, p. 4, May 1985.
[88] JPL. Available: http://southport.jpl.nasa.gov/
[89] A.T.Blischack and M.Manteghi, "Embeded Singularity chipless RFID Tags," *IEEE transactions on Antenna And Propagation,* vol. 59, Nov2011 2011.

[90] N. C. Karmakar, *Handbook of Smart Antennas for RFID Systems*. Singapore: John Wiley, 2010.
[91] ITU-R, "Rec.p 676-9, Attenuation by Atmospheric Gases," International Telecommunication Union, Geneva2012.
[92] C.Koh, "The Benefits of 60 GHz Unlicensed Wireless Communications," YDI Company, USA.
[93] ITU, *Radio Regulation*. Geneva: ITU, 2012.
[94] N.Guo, R.C.Qiu, Sh.S.Mo, and K.Takahashi, "60-GHz Millimeter-Wave Radio: Principle, Technology, and New Results," *EURASIP Journal on Wireless Comm. and Networking,* 2007.
[95] W. Buchar, N. Karmakar, and M.Zomorrodi, "MIMO-Based Technique for Chipless RFID EM-Imaging at 60 GHz," Grant proposal Xerox, USASep 2014.
[96] Available: http://www.kurz.de
[97] M. H.Williams, "Diffraction by a Finitie Strip," *Oxford Journals, Mathematics & Physical Sciences,* vol. 35, 1980.
[98] M.C.Heaton, P.J.Joseph, and R.L.Haupt, "Unifrom Theory of Diffraction Analysis for Conductive Strips with Constant and Tapered Resistive Loads," in *Antennas and Propagation Society International Symposium,* , 1991, p. 4.
[99] U.Y.Ziya, "Physical Optics Theory for the Scattering of Waves by an Impedance Strip," *Optics Communications,* vol. 284, p. 1760, 2010.
[100] R.G.Kouyoumjian and P.H.Pathak, "A Unifm Geometrical Theory of Diffraction for an Edge in a Perfectly Conducting Surface," *Proceeding of the IEEE,* vol. 62, 1974.
[101] S.W.Lee, "Comparison of Uniform Asymptotic Theory and Ufimtsev's Theory of Electromagnetic Edge Diffraction," *IEEE Transactions on Antennas and Propagation,* vol. 25, 1977.
[102] T.Griesser and C.A.Balanis, "Backscatter Analysis of Dihedral Corner Reflectors Using Physical Optics and the Physical Theory of Diffraction," *IEEE Transactions on Antennas and Propagation,* vol. 35, 1987.
[103] R.Mittra, Y.Rahmat-Samii, and W. L. Ko, "Spectral Theory of Diffraction," *Applied Physic,* vol. 10, 1976.
[104] V.C.Monk and F.W.Sedenquist, "High-Frequency Radar Modeling," Advanced Sensors Directorate Research, Development, and Engineering Center, Alabama1995.
[105] J.B.keller, "One Handred Years of Diffraction Theory," *IEEE Transactions on Antennas and Propagation,* vol. AP-33, p. 4, 1985.
[106] A.Imran and Q.A.Naqvi, "Diffraction of Electromagnetic Plane Wave from a Slit in a PEMC Plane," *Progress In Electromagnetics Research* vol. 8, 2009.
[107] M.A.Imran, "Diffraction of Electromagnetic Plane Waves from Strips and Slits Using the Method of Kobayashi Potential," PhD Thesis, Quaid-I-Azam University, Islam Abad, 2010.
[108] A.K.Bhattacharyya and T.J.Chwalek, "Analysis of Multilayered Meander Line Polarizer," *International Journal of Microwave and Millimeter-Wave Computer-Aided Engineering,* vol. 7, pp. 442-454, 1997.
[109] L.Young, L.A.Robinson, and C.A.Hacking, "Meander-line Polarizer," *IEEE Transactions on Antennas and Propagation,* May-1973.
[110] R.S.Chu and K.Lee, "Analytical Model of a Multilayered Meander-Line Polarizer Plate with Normal and Oblique Plane-Wave Incidence," *IEEE Transactions on Antennas and Propagation,* vol. 35, p. 652, 1987.
[111] M.Mazur and W.Zieniutycz, "Multi-layer Meanderline Polarizer for Ku-band," in *Microwave, Radar and wireless communications(MIKON-2000)*, p. 78.
[112] F.Jian, "The Optimum Designing Method for Wide Bandwidth Meander-line Circular Polarizer " in *Antennas, Propagation and EM Theory, ISAPE 2000*, pp. 10-13.
[113] ACMA, "LIPD Regulation," 2011.
[114] (Sep 2014). Available: http://www.satoaustralia.com/

[115] W.Wiesbeck and D.Kahny, "Single Reference, Three Target Calibration and Error Correction for Monostatic Plarimetric Free Space Measurements," *Proceedings of the IEEE,* vol. 79, pp. 1551-1558, 1991.
[116] A.Vena, E.Perret, and S.Tedjni, "A Depolarizing Chipless RFID Tag for Robust Detection and Its FCC Compliant UWB Reading System," *IEEE Transactions on Microwave Theroy and Technique,* vol. 61, pp. 2982-2995, 2013.
[117] (2014, Oct 2014). *Vector network analyser*. Available: http://www.agilent.com
[118] J.Siden, P.Jonsson, T.Olsson, and G.Wang, "Performance Degradation of RFID System Due to the Distortion in RFID Tag Antenna," in *Microwave and Telecommunication Technology,*, Sevastopol,Ukraine, 2001, pp. 371-373.
[119] ACMA, "Radiocommunications (Low Interference Potential Devices) Class Licence 2000," ACMA, Canberra2011.
[120] Nokia. (14 Oct 2014). *Radio Link Systems Nokia MetroHopper 58 GHz*. Available: www.comlab.hut.fi/studies
[121] (14 Oct 2014). *Terabeam product*. Available: http://www.proxim.com/
[122] A.Nesic, S.Jovanovic, and V.Brankovic, "Design of Printed Dipoles Near The Third Resonance," in *Antennas and Propagation Society International Symposium,* , Atlanta, GA, USA 1998, pp. 928-931.
[123] R.B.Waterhouse, D.Novak, A.Nirmalathas, and C.Lim, "Broadband Printed Sectorized Coverage Antennas for Millimeter-Wave Wireless Applications," *IEEE Transactions on Antennas and Propagation,* vol. 50, pp. 12-16, 2002.
[124] W.Menzel, "A 40 GHz Printed Array Antenna," in *Digest*, 1980, pp. pp. 225-226.
[125] C.Peixeiro, P.Dufrane, and Y.Gullerme, "Microstrip Patch Antennas for a Mobile Communications System at 60 GHz," in *Antennas and Propagation Society International Symposium, AP-S. Digest* Baltimore, MD, USA 1996
[126] T.G.Ma and S.K.Jeng, " A Printed Dipole Antenna with Tapered Slot Feed for Ultrawide Band Applications,," *IEEE Transactions on Antennas and Propagation,* vol. 53, pp. 3833–3839, 2005.
[127] M.Scott, "A Printed Dipole for Wide-Scanning Array Application," in *IEEE 11th Int. Conference on Antennas and Propagation*, 2001, pp. 37-40.
[128] Y.Ho.Suh and K.Chang, "A New Millimeter-Wave Printed Dipole Phased Array Antenna Using Microstrip-Fed Coplanar Stripline Tee Junctions," *IEEE Transactions on Antennas and Propagation,* vol. 52, pp. 2019-2027, Aug 2004.
[129] V.Brankovic and A.Nesic, "Wide Band Printed Phase Array Antenna for Microwave and mm-Wave Applications," US Patent, March 2000.
[130] R.A.Alhalabi and G.M.Rebeiz, "High-Efficiency Angled-Dipole Antennas for Millimeter-Wave Phased Array Applications," *IEEE Transactions on Antennas and Propagation,* vol. 56, p. 7, 2008.
[131] Y.C.Chiou, R.A.Alhalabi, and G.M.Rebeiz, "High-Efficiency 60 GHz Dipole-Box Antennas," in *Antennas and Propagation Society International Symposium (APSURSI),* , 2010.
[132] P.Kalansuriya, N.CKarmakar, and E. Viterbo, "On the Detection of Frequency-Spectra-Based Chipless RFID Using UWB Impulsed Interrogation," *IEEE Transactions on Microwave Theory and Techniques,,* vol. 60, 2012.
[133] Taconic, "Taconic laminate material guide," ed, 2014.
[134] R. Anita and M.V.C.Kumar, "Analysis of Triangular Microstrip Patch Antenna for Different Antenna," in *JREAT International Journal of Research in Engineering & Advanced Technology*, 2013.
[135] S.Dey and N.C. Karmakar, "Design of Novel Super Wide Band Antennas close to the Small Antenna Limitation Theory " in *Microwave Symposium (IMS), 2014 IEEE MTT-S International* Tampa, FL, 2014, pp. 1-4.

[136] H.R.Fettermana, T.C.L.G.Sollnera, P.T.Parrisha, D.Parkera, H.Mathewsa, and P.E.Tannenwalda, "Printed Dipole Millimeter Antenna for Imaging Array Applications," *Electromagnetics,* vol. 3, pp. 209-215, 1983.
[137] D.M.Pozar, "Considerations for Millimeter Wave Printed Antennas," *IEEE Transactions on Antennas and Propagation,* vol. 31, No 5, p. 8, 1983.
[138] P.Katehi and N.Alexopoulos, "On the Effect of Substrate Thickness and Permittivity on Printed Circuit Dipole Properties " *IEEE Transactions on Antennas and Propagation,* vol. 31, p. 6, Jan 1983.
[139] W.Hong and K.Wu, "94 GHz Substrate Integrated Monopulse Antenna Array," *IEEE Transactions on Antennas and Propagation,* vol. 60, pp. 121-129, 2011.
[140] D.E.Zelenchuk, V.Fusco, G.Goussetis, A.Mendez, and D.Linton, "Millimeter-Wave Printed Circuit Board Characterization Using Substrate Integrated Waveguide Resonators," *IEEE Transactions on Microwave Theory and Technique,* vol. 60, Oct 2012.
[141] M.Bozzi and L.Perregrini, "Modeling of Conductor, Dielectric, and Radiation Losses in Substrate Integrated Waveguide by the Boundary Integral-Resonant Mode Expansion Method," *IEEE Transactions on Microwave Theory and Techniques,* vol. 56, pp. 3153-3161, 2008.
[142] J.Sheen, "Comparisons of Microwave Dielectric Property Measurements by Transmission/Reflection Techniques and Resonance Techniques " *Measurement Science and Technology,* vol. 20, 2009.
[143] W.L.Stutzman and G.A.Thiele, *Antenna Theory and Design*: John Wiley&Sons, 1981.
[144] C.A.Balanis, *Antenna Theory Analysis and Design*, Third ed.: John Wiley&Sons, 2005.
[145] G.Y.Chen and J.Sh.Sun, "A Printed Dipole Antenna with Microstrip Tapered Balun," *Microwave and Optical Technology Letters,* vol. 40, pp. 344-346, 20 Feb 2004.
[146] R.J. P.Douvilie and D.S.James, "Experimental Study of Symetric Microstrip Bends and Their Compensation," *IEEE Transactions on Microwave Theory and Technique* vol. 26, p. 175, 1978.
[147] S.M.Roy, "Development of a Frequency Encoded Chipless RFID Tag," PhD, ECSE, Monash University, 2008.
[148] R.L.Haupt, *Antenna Arrays, A Computational Approach*. Pennsylvania State University, State College, Pennsylvania: John Wiley&Sons, Inc, Publication, 2010.
[149] D. M. Pozar, *Microwave Engineering*, Third ed.: John Wiley&Sons, 2005.
[150] J. Coonrod, "Comparing Microstrip and CPW Performance," *Microwave Journal,* vol. 55, pp. 74-82, July 2012.
[151] S. Microwave. *1.85 mm connectors*.
[152] (2013). *SouthWest Microwave*. Available: www.southwestmicrowave.com
[153] *Ainfoinc Company*. Available: http://www.ainfoinc.com
[154] W.Carrara, R.Goodman, and R.Majewski, *Spotlight Synthetic Aperture Radar Signal Processing Algorithm*. Boston,: Artesch House, 1995.
[155] L. Martin. *3 dimensional radar*. Available: http://www.lockheedmartin.com.au/us/products/ground-based-air-surveillance/3delrr.html
[156] A.Vettore, S.Ponte, and N.Crocetto, "Space-Based Surface Change Detection with Differential SAR Interferometry: Potentials and Preliminary Investigations," in *Symposium on geospatial theory, processing and applications*, Ottawa, Canada, 2002.
[157] L.J.Cutrona, "A Comparision of Techniques for Achieving Fine Azimuth Resolution," *IRE Transactions on Military Electronics,* vol. MIL-6, pp. 119-121, 1962.
[158] M. A. Islam, "PhD Transfer Report, Compact Printable Chipless RFID System Using Polarization Diversity," Monash University, Melbourne2010.
[159] "Brochure on RFID-Radar™ System," T. S. P. Ltd, Ed., ed. Johannesburg,South Africa, 2011.
[160] A. Jamod, V. D. R. Gopu, and Y. S. Rao, "Matlab based SAR signal processor for educational use," in *Geoscience and Remote Sensing Symposium (IGARSS), 2012 IEEE International* MUNICH, 2012, pp. 5318 - 5321

[161] R. Bamler, "A comparision of Range-doppler and wavenumber domain SAR focusing algorithm," *IEEE Transactions on Geoscience And Remote Sensing,* vol. 30, 1992.
[162] A.AV.Uppuluri and R.J.Jost, "Matlab-based ERS SAR Data Acquisition and Processing Software for Classroom use," in *IEEE International Radar Conference*, 2004.
[163] M.Zomorrodi, "Improved Genetic Algorithm approach for Phased Array Radar Design," in *The Asia-Pacific Microwave Conference, APMC*, melbourne, Australia, 2011, pp. 1850-1854.
[164] Y.Yu, P.G. M. Baltus, A.Graauw, E. der Heijden, and C.S.Vaucher, "A 60 GHz Phase Shifter Integrated With LNA and PA in 65 nm CMOS for Phased Array Systems," *IEEE Jornal of Solid-State Circuits,* vol. 45, 2010.
[165] J. Li and P. Stoica, *MIMO Radar Signal Processing*: JohnWiley& Sons, NY, USA, 2008.
[166] W. Q. Wang, "Virtual Antenna Array Analysis for MIMO Synthetic Aperture Radars," *International Journal of Antennas and Propagation, Hindawi Publishing Corporation,* vol. 2012, p. 10, 2012.
[167] A. M. Haimovich, R. S. Blum, and L. J. Cimini, "MIMO radar with widely separated antennas," *IEEE Signal Processing Magazine,* vol. 25, pp. 116-129, 2008.
[168] X. Zhuge and A. G. Yarovoy, "A sparse aperture MIMO-SAR based UWB imaging system for concealed weapon detection," *IEEE Transactions on Geoscience and Remote Sensing,* vol. 49, pp. 509-518, 2011.
[169] correl Bill, "Efficient Spotlight SAR MIMO Linear Collection Configurations," *IEEE journal of selected topics in signal processing,* vol. 4, p. 7, Feb 2010.
[170] D. R. Fuhrmann, J. P. Browning, and M. Rangaswamy, "Signaling strategies for the hybrid MIMO phased-array radar," *IEEE Journal on Selected Topics in Signal Processing,* vol. 4, pp. 66-78, 2010.
[171] Lincoln Laboratory, "Practical phased array antenna," Massachusetts Institute of Technology (MIT), Boston,2014.
[172] M.Zomorrodi, "A phased array antenna design with Genethic algorithm," MSc., Electrical Engineering school, K.N.Toosi, Tehran, Iran, 2000.
[173] Y. Rahmat-Samii and E. Michielssen, *Electromagnetic Optimization by Genetic Algorithms*: Wiley, 1999.